Coupled Thermo-Hygro-Chemical Modelling of Self-healing Processes in Cementitious Materials

ADRIANA SILVIANA CHITEZ

Thesis submitted in candidature for the degree of Doctor of Philosophy at Cardiff University

2014

Acknowledgements

The research reported in this thesis was carried out at Cardiff School of Engineering, Cardiff University and was financially supported in a form of a Doctoral Training Grant by Cardiff University, the EPSRC and the finite element company LUSAS; this is gratefully acknowledged.

Firstly, I would like to thank my mother and grandmother who have borne my long absence with incredible patience. I am aware that this period was pretty hard for you, but I deeply appreciate your endless moral support and encouragement during my study.

I am also grateful to Iulia Mihai for her precious counsel regarding this research position and also to Professor Tony Jefferson and Professor Bob Lark for selecting me and accepting the role of principal and secondary supervisors. I am greatly indebted to Tony Jefferson who offered me his generous help, guidance and confidence during the difficult moments of this PhD, the work would not have been accomplished without his efforts and careful review of my manuscript.

I would also like to wholeheartedly thank Robert Davies who did the experimental work related to the crack recovery (all the data used to simulate the autogenous self-healing processes is taken from his measurements). I will treasure forever your warm friendship and unconditional help during and outside the working hours.

In addition, I wish to thank the laboratory technical staff Carl Wadsworth and Ian King for their assistance with the aggregate absorption experiment and also to my friends within and outside the department who made my stay in Cardiff pleasant and exciting. Denise, Sean, Shukri, Waleed, Toby, Chuansan, Adina, Silviu, Irina, Panos and Laura I will always remember the good times that we had.

Last, but certainly not the least, I would like to thank God for this wonderful opportunity of doing such a challenging job. This thesis is dedicated to the memory of my beloved father who was and continues to be my greatest supporter.

Va multumesc tuturor.

DECLARATION

This work has not previously been accepted in substance for any degree and is not concurrently submitted in candidature for any degree.

Signed.....(candidate) Date.....

STATEMENT 1

This thesis is being submitted in partial fulfilment of the requirements for the degree of PhD.

Signed.....(candidate) Date.....

STATEMENT 2

This thesis is the result of my own independent work/investigation, except where otherwise stated. Other sources are acknowledged by explicit references.

Signed.....(candidate) Date.....

STATEMENT 3

I hereby give consent for my thesis, if accepted, to be available for photocopying and for interlibrary loan, and for the title and summary to be made available to outside organisations.

Signed.....(candidate) Date.....

Summary

This thesis presents details of a numerical programme of study on the themo-hygro-chemical (*THC*) processes occurring during the self-healing of cementitious materials.

A comprehensive *THC* model, which is mechanistic in nature, is proposed and implemented in the framework of the finite element method. The aim of this model is to develop a useful computational tool that is capable of realistically predicting damage recovery in terms of the crack filling observed under specific environmental conditions. The early age and long term behaviour of the cementitious materials is simulated by solving a boundary value problem which couples moisture-temperature-ion transport mechanisms by means of mass and enthalpy balance equations. The model assumes that all the transport processes occur at the capillary pore level and that the self-healing is driven by ongoing hydration. In this context, attention is focused on developing an innovative microstructural model that can predict the quantitative evolution of the capillary porosity. The microstructural model is based on an existing colloidal classification of the water forms present in the clinker hydrates, on hydration kinetics principles and on the stoichiometry of the Portland cement. The effect of the aggregate absorption on the capillary porosity is also examined.

Firstly, the adopted theoretical considerations regarding the transport of moisture and temperature in cement-based materials are validated by comparing the numerical findings of the *TH* component with the reported results of three different sets of drying experiments. Then the *THC* model is applied to the simulation of a crack recovery experiment undertaken at Cardiff University. In both cases the proposed model was found to capture the essential characteristics of the thermo-hygro-chemical behaviour of cementitious materials.

Nomenclature

Symbols:

A_k , A_p , A_v	material constants
A_1 - A_3	material constants
A_λ , A_Γ	material parameters
$A_{specimen}$	area of the specimen
a	material constant
B	Blaine specific surface area
B_v , B_1 - B_4	material constants
b , b_1 - b_3	material parameters
C	integrand of the elemental secant capacitance matrix
C_p^π	specific heat capacity of phase π
$C_{\eta\_X}^j$	material coefficient of the j porosity computed with the X method
C_Γ	integrand of the hydration component of $\boldsymbol{F_e}$
$\hat{\boldsymbol{C}}$	global secant capacitance matrix
c	initial mass of cement per unit volume of material
c_v	concentration of the vapour phase
c_{FA}^j	j porosity coefficient accounting for the fly ash
c , c_η , c_1 , c_2	material constants
D_c	diffusion coefficient
D_{disp}^{ij}	tensor of hydrodynamic dispersion
D_{eff}	effective diffusion coefficient
D_{mol}	molecular diffusivity coefficient
D_{v0}	diffusion coefficient of vapour at reference temperature and pressure
D_X	diffusion coefficient controlling the hydration X
div	divergence
E	activation energy of the reaction
$\boldsymbol{F_e}$	vector of elemental body and boundary “forces”

F_q	integrand of the boundary condition component of $\boldsymbol{F_e}$
$\hat{\boldsymbol{F}}$	global load vector
f , f_B , f_D	arbitrary functions
f_{cap}^{ult}	volume fraction of capillary pores at the end of hydration
f_{conv}	conversion factor of the time
f_g	integrand of the gravitational component of $\boldsymbol{F_e}$
f_i	weight/mass ratio of i
f_s	Knudsen effect coefficient
$\boldsymbol{g}$	gravity vector
$grad$	gradient
H_i	heat release/specific enthalpy of i
H_c	heat of hydration of cement at complete hydration
H_{tot}	total heat release at complete reaction of cementitious material
h_{FA}	heat of hydration of the fly ash
h_x	distance in x direction
h_y	distance in y direction
$itime$	step number
$i1 \ldots i4$	saturation intervals
J_i^j	j flux of i
K	integrand of the elemental secant hydraulic conductivity matrix
K_X	order of reaction of mineral X
$\hat{\boldsymbol{K}}$	global secant hydraulic conductivity matrix
k_{iw}^0	intrinsic permeability of the matured paste
$k_{i\pi}$	intrinsic permeability coefficient of π
$k_{r\pi}$	hysteretic relative permeability of π
k_X	rate constant of the hydration of the mineral X
k_π	permeability of the medium with respect to π
M_l	mass of liquid phase
M_s	mass of dry solid (unreacted cement + precipitated material)
M_π	molar mass of π
m	material constant

m_{dry}	mass of the dry sample
m_{loss}	relative weight loss
m_p	fully saturated moisture content
$m_{specimen}$	mass of the specimen
m_{solid}	mass of the solid skeleton
m_{totH_2O}	mass of the total liquid phase
$m_w^{gel \rightarrow cap}$	mass of water expelled from the gel pores into the capillary pores
m_X	mass percentage of mineral X
$m_X^{depl\,/\,prec\_Y}$	mass of depleted/precipitated X during the hydration of Y
$m_X^{depl\,/\,prec\_STZ}$	mass of depleted/precipitated X during the Z hydration stage of X
$m_{X\_STZ1BRZ2}^{depl\_Y}$	mass of depleted X during the $Z2$ branch of the $Z1$ hydration stage of the mineral Y
$\dot{m}_\pi$	mass rate or sink/source term of π
$\dot{m}_\pi^i$	sink/source term of π due to i
N	shape function
$\boldsymbol{N}$	vector of shape function
n	time step
$\bar{\boldsymbol{n}}$	unit normal vector to the boundary flux
ne	number of finite elements
nn	number of nodes of a finite element
$nstop_X^{STZ}$	time step at which the Z hydration stage of X stops
$nstop_X$	time step at which all the stages of the hydration of X stops
p_{atm}	atmospheric pressure
p_c	capillary pressure
p_v^{sat}	water vapour saturation pressure
p_π	pressure of the fluid phase π
Q_h	rate of heat generation
q_π	imposed flux of phase π
$\bar{q}^\pi$	heat flux of phase π
r	residual proportion of the fully saturated moisture content when the concrete first hardens

r_0	the initial moisture content as a proportion of m_p
R	ideal gas constant
R_{ck}	average radius of the clinker minerals
RH	relative humidity
RH_{cr}	critical relative humidity
$t_{X,0}^{D}$	initiation time of the diffusion controlled hydration of the mineral X
t_X^I	duration of the induction period of the mineral X
S_w^j	water saturation degree corresponding to the j porosity
S_{w0}	initial degree of saturation
S_π	degree of saturation with respect to the phase π
$\boldsymbol{S}_w$	water degree of saturation vector
t_0	initial time
t_p	time in hours at which peak absorption is reached
T	temperature
T_{cr}	critical temperature of water
T_{env}	temperature of the surrounding environment
T_r , T_{ref}	reference temperature
T_0	initial temperature
T^π	temperature of phase π
$\boldsymbol{T}$	temperature vector
t	time
V_i	volume of i
V_i^{ult}	volume of water form i at the end of hydration
V_{mix}	volume of the mix
$V_s(\Gamma)$	volumetric strain due to shrinkage
$V_{specimen}$	volumetric of the specimen
V_{voids}^{ult}	volume of voids at the end of hydration
$\bar{v}^{\alpha\pi}$	mass-averaged velocity of phase π with respect to phase α
$\bar{v}^\pi$	mass-averaged velocity of phase π
W	weight function
w_i	mass of i per unit volume of material

$w_{i1..i4}$	mass of water per unit volume of material consumed during the saturation interval $i1 \ldots i4$
$\left(\frac{w}{c}\right)^{*}$, $\left(\frac{w}{c}\right)_{eff}$, $\frac{w}{c}$	lowest/effective/initial water-cement ratio of the mix
w_i^{ult}	mass of water form i per unit volume of material at the end of hydration
w_{moist_loss}	relative moisture loss per unit exposed area
wc	water content
X	principal variable
z	vertical distance from the reference level
z_i	stoichiometric coefficient
α	basic constant
α_L, α_T	longitudinal/transversal dispersivity parameter
α_P	material parameter
β_P	order of the process
β_{sf}	hydration shape parameter
Δ^{SP}	retardation time accounting for the superplasticizer
$\boldsymbol{\Delta\hat{C}}$	global tangent capacitance matrix
ΔH_h	heat of hydration
ΔH_P	heat of precipitation
ΔH_v	heat of evaporation
$\boldsymbol{\Delta\hat{K}}$	global hydraulic conductivity matrix
Δt	time increment
δ_{ij}	the Kronecker delta
δ_π	transfer coefficient of phase π
$\boldsymbol{\delta\Phi}$	increment of the global vector of unknowns
$\boldsymbol{\Phi}$	global vector of principal variables
Γ, Γ_{PC}	degree of hydration of the Portland cement
Γ_X	degree of hydration of the mineral X
Γ_X^D	critical degree of hydration of the mineral X
Γ_X^I	degree of hydration of the mineral X at the end of the induction period
Γ_{q_e}	boundary of the elemental domain
Γ_{qi}	i^{th} boundary of the domain

Γ_{ult}	degree of hydration at the end of hydration
Γ_0	percolation threshold of the degree of hydration
η	porosity
η_j	j type porosity
$\hat{\eta}$	local parametric coordinate
η_0	initial porosity
λ_{dry}^{eff}	effective thermal conductivity of a completely desaturated material
λ_T^{eff}	effective thermal conductivity of the moist material
λ_T^{π}	effective thermal conductivity of phase π
λ_{T_0}	effective thermal conductivity at reference temperature
μ_{chem}	chemical potential
μ_w^{pure}	viscosity of pure water
μ_{π}	viscosity of the fluid phase π
Θ	parameter of the finite difference approximation
τ_X	characteristic time of the hydration of the mineral X
τ_{sf}	hydration time parameter
τ_{sf}^{SP}	hydration time parameter of the superplasticizer
ρ_{dry}	apparent density
ρ_i	intrinsic phase averaged density of i
ρ_{loss}	average density loss
$\rho_{v_{env}}$	water vapour density in the surrounding environment
ρ_w^{tot}	intrinsic phase-averaged total water density
$\rho_{\pi} h^{\pi}$	heat source term of phase π
$\rho_{\pi} R_H^{\pi}$	exchange of energy due to phase conversion and mechanical interactions of phase π
$\overline{\rho C}_p$	heat storage capacity of the porous medium
$\overline{\rho}_w^{cap}$	phase-averaged capillary water density
$\overline{\rho}_{\pi}$	phase-averaged density of phase π
$\overline{\rho}_{\pi} C_p^{\pi}$	heat capacity of phase π

Ω	domain
Ω_e	elemental domain
ω	concentration of the solute
$\boldsymbol{\omega}$	concentration vector
ω_{env}	concentration of solute in the surrounding environment
ω_0	initial concentration
$\hat{\xi}$	local parametric coordinate
$\boldsymbol{\Psi}$	residual vector
ψ_G	gravitational potential
ψ_m^π	matric potential of phase π
ψ_t^π	total potential of phase π
∇	gradient
"$\cdot$", $\frac{D}{Dt}$	derivative with respect to time
$\left[\sum_l \left(\dot{m}_l H_l\right)\right]_\pi$	exchange term of phase π accounting for the latent heat of evaporation and chemical interactions

Subscripts/Superscripts/Abbreviations:

A	advection
ASR	alkali-silica reaction
$AW + ILW + IGW$	absorbed + interlayer + intragranular water
AW	absorbed water
ASTM	American Society for Testing and Materials
a	air
agg	aggregate (fine + coarse)
$a / d \_ agg$	absorption/desorption in/from the aggregates
b	binder
B	Bouny
BO	name of cement composition and concrete mix
CBW	chemical bound water
CD	conduction
CO	name of cement composition and hardened cement paste

CW	capillary water
C_2S	belite
C_3A	aluminate
C_3S	alite
C_4AF	aluminoferrite
C-S-H	calcium silicate hydrate gel
c, cem	cement
$cagg$	coarse aggregates
cap	capillary
$concr$	concrete
cw	combined water (effective gel water + *CBW*)
D	diffusion
DD	diffusion-dispersion
des	desorption from the gel network
ESEM	environmental scanning electron microscope
ea	entrapped air
$edry$	external drying
FA	fly ash
$FA-CaO$	fly ash calcium oxide
FEM	finite element method
FE1, FE2	types of finite elements
$fagg$	fine aggregate
$freeCaO$	free calcium oxide
GEM	Generalized Effective Media
$GGBF$	ground-granulated blast-furnace slag
GW	gel water
g	gas
H	name of cement composition and concrete mix
HC1	hydration curve 1
HC2	hydration curve 2
HPC	high-performance concrete
h	hydrated material
hyd	hydration
ITZ	interfacial transition zone
L	name of cement composition and concrete mix
LGP	large gel pores

M	name of cement composition and concrete mix
MgO	magnesium oxide
N	Neville
P	precipitated material
PC1, PC2	name of investigated cement composition
RVE	representative volume element
$seal$	sealed conditions
SCM	supplementary cementing materials
SEM	scanning electron microscope
SGP	small gel pores
SH	name of investigated cement composition
SHCC	hardening cementitious composite
SO_3	sulphur trioxide
SP	superplasticizer
$SSRC$	solid skeleton of the reacted clinker
STOICH_HC2	proposed microstructural model
TH	thermo-hygral
THC	thermo-hygro-chemical
THM	thermo-hygro-mechanical
tot	total
s	solid matrix
UCP	unhydrated cement particle
ult	end of hydration
v	vapour water
w	water/capillary water
wv	moisture
w/c	water cement ratio
XRD	X-ray Diffraction
π	material phase
ω	solute
$\eta\_B\ \&\ C$	according to Baroghel-Bouny and Chaussadent
$\eta\_N\ \&\ B$	according to Neville and Brooks
η_S	stoichiometry-based

Contents

Chapter 1. Introduction

1.1 Background of Research

Cementitious or cement-based materials are fine powder minerals that react with water to form a plastic mass, called cement paste, that hardens in time and binds together aggregate particles. They contain mainly Portland cement, but may also include mineral admixtures like fly ash, Ground Granulated Blastfurnace Slag (*GGBS*), and Pozzolanic materials. If sand and coarse aggregate are present in the mix, concrete is produced.

Imposing structural masterpieces such as the Colloseum, the Panthenon and the Pont du Gard bridge aqueduct were erected in Europe during the Roman Empire using a primitive cementitious mix that incorporated a volcanic sand called pozzolana. This material was not widely available and this may explain why, for many centuries after the fall of the Roman Empire, stone and brick masonry were the dominant building materials. Shaeffer (1992) reports that the use of cementitious mortars became fashionable again in the eighteenth-century, when Francois Cointeraux discovered that the addition of a cement-based binder into a mix of the ancient pisé made the compaction process unnecessary. Moreover, the discovery in 1824 of Portland cement by Joseph Aspin was the first step in the development of modern cementitious binding agents. Since then, concrete and mortars have continuously gained ground in Europe and cement has now become the most widely used man-made structural material (U. S. Geological Survey, 2009). To confirm this statement, information about the main world producers of cements, gathered by the European Cement Association in (Cembureau, 2014), is given in Table 1.1. According to this report, the global cement production was expected to increase from 3.7 billion tonnes in 2012 to 4 billion tonnes in 2013.

Concrete represents an artificial unsaturated sedimentary rock that contains pores (empty and/or filled with moisture) and solid mass. The skeleton matrix can be decomposed into three main parts according to the size of its constitutive components. Hydrates are found at the nanoscale, unreacted cement particles at the microscale and fine and coarse aggregates at the mesoscale.

Cement production° (Million tonnes)									
Country	**2001**	**2006**	**2007**	**2008**	**2009**	**2010**	**2011**	**2012**	**2013p**
China	661.0	1 236.8	1 361.2	1 388.4	1 644.0	1 881.9	2 063.2	2 137.0	2 359.0
India	102.9	159.0	170.5	185.0	205.0	220.0	270.0	239.0	272.0
European Union	225.8	264.8	271.0	251.8	201.3	191.0	195.5	159.2	157.2
USA	88.9	98.2	95.5	86.3	63.9	65.2	68.6	74.0	77.0
Brazil	39.4	41.4	45.9	51.6	51.7	59.1	63.0	68.0	71.9
Turkey	30.0	47.4	49.3	51.4	54.0	62.7	63.4	63.8	70.8
Russian Federation	28.7	54.7	59.9	53.5	44.3	50.4	56.1	53.0	55.6
Japan	75.9	69.9	67.8	63.0	54.9	51.7	51.5	59.2	61.7
Korea, Rep. of	52.0	49.2	52.2	51.7	50.1	47.4	48.2	46.9	47.3
Saudi Arabia	20.0	27.0	30.3	37.4	37.8	42.5	48.0	43.0	48.0
Indonesia	31.1	33.0	35.0	38.5	36.9	39.5	45.2	53.5	47.0
Mexico	33.2	37.9	38.8	37.1	35.1	34.5	35.4	36.2	37.0
Germany	32.1	33.6	33.4	33.6	30.4	32.3	33.5	32.4	31.5
Italy	39.8	47.8	47.5	43.3	36.4	34.4	33.1	26.2	23.1
France	19.1	22.0	22.1	21.2	18.1	18.0	19.4	18.0	17.5
Canada	12.1	14.3	15.1	13.7	11.0	12.4	12.0	12.5	12.1
Argentina	5.5	8.9	9.6	9.7	9.4	10.4	11.6	10.7	11.9
South Africa	8.4	13.1	13.7	13.4	11.8	10.9	11.2	13.8	14.9
Australia	6.8	9.2	9.2	9.4	9.2	8.3	8.6	9.8	10.5
United Kingdom	11.9	12.1	12.6	10.5	7.8	7.9	8.5	7.9	8.2

Notes: ° Cement production including cement produced with imported clinker
p: Provisional figures

Table 1.1 Main world cement producers – the G20 Group according to Cembureau (2014)

The voids, on the other hand, initially appear because of the chemical shrinkage that occurs during hydration. The configuration of the pore network (size and pore distribution) changes continuously and is influenced, amongst other things, by external environment or boundary conditions that cause damage. It is worth mentioning at this point that the cement-based materials are quasi-brittle. They behave satisfactorily under compression, but cannot withstand high tension forces. For this reason, steel reinforcing bars or fibres are usually embedded in the mass of the material to prevent tensile failure. Nevertheless, this solution does not prevent the development of the microcracks and implicitly, the increase in porosity. If damaged concrete is exposed to harmful environmental conditions, such as drying-wetting cycles, high temperatures or corrosion agents, the associated increase in moisture and heat flow can result in shrinkage or swelling. When these volume variations are restrained, further cracking can occur and the durability and strength of the material can be dramatically reduced. The water tightness of concrete, which is essential in the case of dams, storage tanks, nuclear reactors and disposal facilities for radioactive waste, becomes compromised. Moreover, an infiltrating fluid may chemically attack the reinforcement and weaken the structural elements. Repair and maintenance work is frequently needed to address

these problems, but sometimes even the most advanced inspection and remediation techniques are unable to improve the performance of the deteriorated structures. Furthermore, monitoring and maintenance programmes are fairly expensive; for example in Figure 1.1 two sets of statistics, released in 2013 and 2014, show that in all British public and private construction projects, repair and maintenance costs were 44.8% and 47.5% of the expenditure on new works, of which concrete structures form a large proportion.

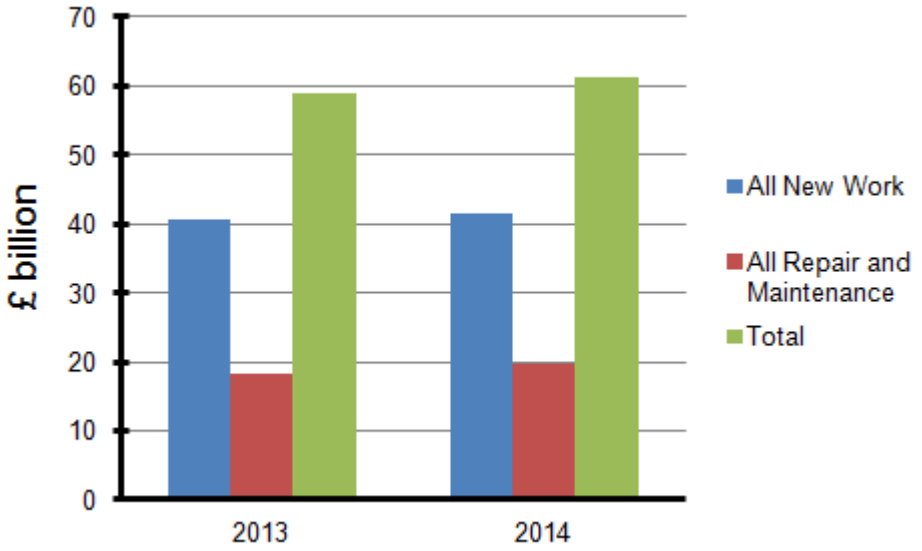

Figure 1.1 The expenditure on the construction works in Great Britain taken from (Office for National Statistics, 2013) and (Office for National Statistics, 2014)

Last but not least, it must be stated that the production of cementitious materials has considerable environmental impact. The exhaust products, released from the chemical reactions of the raw materials and from the combustion of fuels, include carbon and sulphur dioxide, nitrogen oxides and dust. CO_2 emissions are considered to be the most harmful of all and are evaluated to be in order of 5-7% of the total carbon dioxide global production (Joseph et al., 2009).

Recent trends in concrete mix design indicate that it is possible to obtain engineered cementitious materials capable of adapting to the environment. In short, these new and smart materials are able to heal cracks naturally, by continuous hydration, or artificially, by releasing a healing agent into the damaged zone. Many experimental investigations, showing the benefits of using self-healing cementitious materials, have been reported in the literature, but few investigations have been carried out on the numerical modelling of these self-healing processes. The current thesis seeks to address

precisely this issue by proposing a model that replicates the self-healing of ordinary cementitious materials.

1.2 Overall Motivation of Research

The motivation for this study consists in the desire to find a numerical approach that can assess the most efficient concrete mix design in terms of achieving the most effective and rapid autogenous healing of cracks. The proposed thermo-hygro-chemical (*THC*) model is formulated so that it can predict crack recovery capacities for different initial water - binder ratios and predict drying and hydration behaviour for different curing and exposure conditions. This will enable comprehensive, successful and cost-effective healing strategy to be developed and implemented in structural elements.

In the current thesis the objectives of the main body of research are as follows:

1. Develop a reliable theoretical model for the coupled transport of moisture and temperature that is capable of simulating the early-age and long term thermo-hygral (*TH*) behaviour of ordinary cementitious materials;
2. Integrate a microstructural model into the proposed *TH* framework in order to realistically reproduce the hydration reaction and the evolution of the pore network;
3. Investigate the coupled *TH* model under different curing conditions and compare the results with experimental findings;
4. Couple the theoretical principles describing the reactive transport of solutes to the *TH* model and thereby develop a novel *THC* model for the self-healing of cement-based materials;
5. Simulate by means of the finite element method, the self-healing process and validate the results against laboratory data.

1.3 Outline of the Thesis

This thesis is divided into 7 Chapters and 2 Appendices. Chapter 2 presents the overview of the most recent theories applicable for simulating the thermo-hygro-chemical behaviour of ordinary cementitious materials. Attention is directed especially towards the representation of the hydration kinetics and towards the understanding of the multiple physical and chemical processes occurring in unsaturated conditions. This

chapter also provides a brief description of existing numerical models as well as giving information on the healing techniques that are usually applied to cement-based materials.

The theoretical formulations necessary for the development of a comprehensive *THC* model are included in Chapter 3. The constitutive laws necessary for predicting the filling of a crack and the entropy and moisture evolutions within the building material considered are enumerated and discussed.

Chapter 4 focuses specifically on the fundamental aspects of the finite element modelling method by which a computer code is created. This part of the thesis gives insight into the procedure adopted for the spatial and temporal discretisations.

In Chapter 5 a microstructural model for the cementitious materials is proposed. Its results in terms of volume fraction variation of reactants and reaction products are validated with numerical data found in the literature. The volume fractions of the liquid phase are then used to formulate porosity functions required in the *TH* model and a comparison between these functions and the reported results found in other research works is done.

The validation of the *TH* model is described in Chapter 6. The accuracy of the thermo-hygral computer code is evaluated via three main examples that simulate self and external desiccation processes of cement pastes and concrete mixes with different water - binder ratios.

In Chapter 7 the application of the finite element method to the modelling of the self-healing process in an ordinary mortar is presented. A quantitative analysis of the amount of precipitated material is carried out and the results are compared to experimental data to confirm the efficiency of the model.

Finally, Chapter 8 enumerates the general conclusions and suggests future research trends in this area.

Chapter 2. Literature Review

2.1 Introduction

Cementitious materials have been among the most widely used building materials in civil engineering for decades. Various researchers have investigated both experimentally and numerically the physical processes occurring from the moment when the binder and the water are mixed up until the hydration reaction ceases. This study proposes a mathematical apparatus for simulating self-healing of ordinary cement-based materials and therefore the coupled thermo-hygro-chemical (*THC*) behaviour of the material needs to be considered. Implicitly, it is significant to grasp the importance of the kinetics of the hydration reactions, since the inner structure of the hardened paste varies considerably in time. In the current chapter, a selective review of the important aspects related to the *THC* modelling, found in various research studies, will be conducted.

Section 2.2 presents the chemical facets of the cement paste hardening. Attention is focused on describing the stages of the hydration kinetics of ordinary Portland cement and on establishing a set of reactions able to provide in time the hydrates identified in the reported chemical analyses.

The fundaments of the physical phenomena pertinent to the early age and long term behaviour of cement-based materials are covered in Section 2.3. The main constitutive laws related to drying and to the transport mechanisms of fluids, dissolved species and heat are listed in this section as they are formulated.

In section 2.4 the most recent numerical models utilized for simulating the complex behaviour of unsaturated cementitious materials are reviewed. All the examples revolve around the idea of crystal precipitation and are chosen in order to exemplify how this chemical process is dealt with from the computational point of view.

Section 2.5 is dedicated to the self-healing of cracks in cement paste or concrete structures. The classification of this phenomenon is succeeded by the quest of establishing the nature of the filler (i.e. the material that fills a crack).

The description of the existing models related to the self-healing is found in section 0. Attention is directed mainly to the numerical solutions proposed for quantifying the ongoing hydration.

The last section presents the summary and the conclusions of the above mentioned examinations.

2.2 Hydration of Ordinary Cementitious Materials

The hydration reaction is a complex process that occurs at the microscopic level of the cement powder. Its result is the formation of reaction products that will ensure the skeleton solidification. The complexity of the process resides in the intricacy of the chemical composition of Portland cement that leads initially to the appearance of an unstable chemical system with varying physical and chemical properties. The hydration is intimately linked to the characterisation of the cement paste from the thermo-hygral point of view and it is crucial that the progress of these thermo-hygro processes be included in a model aimed at simulating the behaviour of hydrated cementitious materials in time.

2.2.1 Chemical Composition of Portland Cement

The Portland cement is a mixture of 4 main impure minerals: alite, belite, aluminate and aluminoferrite representing 90-95 wt% of the total amount of the Portland cement (Illston and Domone, 2010) and other chemical species remnant from the clinkering and grinding processes. Although impure, these minerals are denoted by the same shorthand notation as the pure minerals, as can be seen in Table 2.1.

The minerals are the result of a burning process in rotary kilns, at extremely high temperatures, where the raw materials providing the source of calcium, silicon, aluminium and iron, react with each other and with the atmospheric oxygen to form oxide compounds. There are 4 main oxides in the composition of the clinker phases which are listed in Table 2.2 together with some residual compounds found in minor quantities (Illston and Domone 2010).

In order to improve the workability of the paste, gypsum is also added to the clinker before grinding.

Table 2.1 Common reactants and hydrates in the cement powder

Chemical name	**Mineral name**	**Cement notation**
tricalcium silicate	alite	C_3S
dicalcium silicate	belite	C_2S
tricalcium aluminate	aluminate	C_3A
tetracalcium aluminoferrite	aluminoferrite	C_4AF
calcium sulfate dihydrate	gypsum	$C\bar{S}H_2$
hexacalcium aluminate trisulfate 32-hydrate/AFt phase	ettringite	$C_6A\bar{S}_3H_{32}$
tetracalcium aluminate monosulfate 12-hydrate/AFm phase	–	$C_4A\bar{S}H_{12}$
calcium hydroxide	portlandite	CH
tetracalcium aluminate 13-hydrate	–	C_4AH_{13}
tricalcium aluminate 6-hydrate	hydrogarnet	C_3AH_6
tricalcium aluminoferrite 6-hydrate	impure hydrogarnet	$C_3(A,F)H_6$
AF_t phase	–	$C_6(A,F)\bar{S}_3H_{32}$
AF_m phase	–	$C_4(A,F)\bar{S}H_{12}$
impure iron (III) hydroxide	–	$(F,A)H_3$
calcium sulfate hemihydrate	bassanite	$C\bar{S}H_{0.5}$

Table 2.2 Common oxides in the cement powder

Chemical formula	Cement chemistry notation	Chemical name	Percentages by weight
principal oxides			
CaO	C	quicklime	60–67%
SiO_2	S	silicon dioxide/silica	17–25%
Al_2O_3	A	aluminium (III) oxide/alumina	3–8%
Fe_2O_3	F	iron (III)/ferric oxide	0.5–6%
minor cement constituents			
Na_2O		sodium oxide	
K_2O		potassium oxide	
MgO		magnesium oxide	
SO_3	$\overline{S}$	sulphur trioxide	
K_2SO_4		alkali sulphate	
Na_2SO			
free CaO			

2.2.2 Characterisation of the Hydration Kinetics

Although in the last 70 years a considerable number of both experimental and numerical studies have been published, the controlling mechanisms of hydration kinetics still remain controversial. Bullard et al. (2011) admit that the development of the hydration rate and its translation into a numerical algorithm -model similar to the ones used in geomechanics, is hampered by the inability of to isolating -isolate the individual chemical reactions. Even though advances in the understanding of gel nucleation and dissolution of alite are substantial, Bullard acknowledges that further research is needed on the chemistry of aluminate and gypsum hydration. The scope of the current thesis is not to elucidate the mechanisms of the hydration of cement paste. Nevertheless, a brief overview of the latest discoveries is required in order to provide the background of the model adopted for the evolution of the microstructure of the material.

Three main processes control the rate of reaction: (1) the dissolution of cement, (2) the diffusion of dissociated ions toward the precipitation sites and (3) the nucleation and growth of the new products. The dissolved ions continuously accumulate during the initial reaction period (Taylor, 1997; Bullard et al., 2011) until the dissolution rate decelerates very quickly (**the period of slow reaction**). Some authors report that the decrease is due to the appearance of a metastable barrier of calcium silicate hydrate

(*C-S-H*) (Stein and Stevels, 1964; Jennings and Pratt, 1979; Livingston et al., 2001), while others identify the crystallisation of a superficially, little soluble hydroxylated layer on the surface of the grain (Damidot et al., 1990; Garrault-Gauffinet and Nonat, 1999; Garrault et al., 2005). The period of slow reaction is followed by the **acceleration period,** when the nucleation and growth of the hydrates occur. At this point, it should be mentioned that the scope of the majority of the published studies is confined solely to *C-S-H* precipitation, despite the fact that all the four main clinker compounds react in the presence of water. Hubler et al. (2011) explain the acceleration period by a heterogeneous nucleation on the surfaces of pre-existing nanoparticles in conjunction with an aggregation process. Gartner (1997), on the other hand, points to the formation of a tobermorite-like or jennite-like structure. His study suggests that, after nucleation, silicate tetrahedral attach to the perimeter of the existing embryo and creates sheets of silicate chains which incorporate between them the calcium and hydroxyls ions. The experimental data demonstrate that the rate of growth, intimately linked to the reaction activity, reduces in time. Several hypothesis have been put forward on this **deceleration period**: the lack of water and space for the new hydrates, the excessive size of the still unhydrated minerals or the transition towards a diffusion rate control transport of free ions. The last hypothesis is based on the substantial amount of laboratory evidence which shows that the deposition of the low-density products develops right next to the anhydrous particles, whilst the precipitation of hydrates takes place much further away from these particles (Hadley et al., 2000; Kjellsen and Lagerblad, 2007; Gallucci et al., 2010). Bullard et al. (2011), however, are not entirely convinced of such behaviour and state that if the - diffusion driven transport ever occurs, it proceeds well after the impingement of different domains of the growing hydrates, when the heat release approaches zero.

2.2.3 Chemical Reactions in Hydrated Portland Cements

Knowledge about the behaviour of cement in the presence of water is largely based on the individual hydration of each mineral, either in a pure state or as a clinker compound, and thus it overlooks the interaction between the dissociated species of the principal constituents. Despite this drawback, the above mentioned approach is widely accepted by the science community since it is the least complex and it provides a good estimate of the holistic behaviour of the Portland cement (Mindess et al., 2003). Up to now, different researchers have proposed distinct sets of chemical reactions for the hydration of the same mineral. Some common features related to the nature of the products and their chemical stability can be distinguished though, especially when

decoding the shape of the calorimetric curve (see Figure 2.1). The following part of the thesis will be dedicated to the review of the stoichiometry of cement hydration. Under the assumption of a fully saturated paste, the main stages of cement-water reaction will be highlighted. It is noted that Table 2.1 gives the names of the common minerals encountered in cement chemistry that are used in the remainder of this thesis.

2.2.3.1 *Rehydration of Gypsum*

Gypsum is the raw material added in order to hinder the so called “set flash” of Portland cement, that leads to a quick setting of the paste due to the reaction between C_3A and water. The exothermic process that occurs during the cement manufacture (70 - 200°C) may partially dehydrate the gypsum (Taylor, 1997). The new compounds are the hemihydrates or the γ-$CaSO_4$ (“soluble anhydrite”), which differ essentially in the number of water molecules found in their structure. The experimental work performed by Fujii and Kondo (1986) demonstrated that $C\bar{S}H_{0.5}$ reconverts into $C\bar{S}H_2$ in about four hours if the paste contains only water and hemihydrate in a weight ratio equal to 0.4. The corresponding chemical reaction describing the rehydration is (Singh and Middendorf, 2007):

$$C\bar{S}H_{0.5} + 1.5H \rightarrow C\bar{S}H_2 \tag{2.1}$$

All the calcium sulphate phases are highly soluble and dissolute rapidly in the pore solution (at most 24 hours) into calcium and sulphate (Taylor, 1997). These ions will react later on with two of the existing clinker minerals.

2.2.3.2 *Hydration of Aluminate*

The hydration path of aluminate, the most soluble mineral of the clinker mix (Jennings and Thomas, 2009), takes place in multiple stages depending largely on the amount of sulphate ions (SO_4^{2-}) sourcing from the dissociated gypsum. Initially, the impure ettringite is formed (Taylor, 1997; Mindess et al., 2003):

$$C_3A + 3C\bar{S}H_2 + 26H \rightarrow C_6A\bar{S}3H_{32} \tag{2.2}$$

This hydrate is composed of loose packed hexagonal rods which adhere to the surface of aluminate grains (Scrivener and Pratt, 1984). In a preliminary phase, it absorbs free sulphate ions from the pore solution, but later on, due to a dynamic imbalance, the

SO_4^{2-} are released again in the liquid (Minard et al., 2007). Analysing the calorimetric curve, Bullard et al. (2011) reported that the ion liberation generates the second peak of the heat histogram which arises sometime between 20 and 30h after mixing (see Figure 2.1).

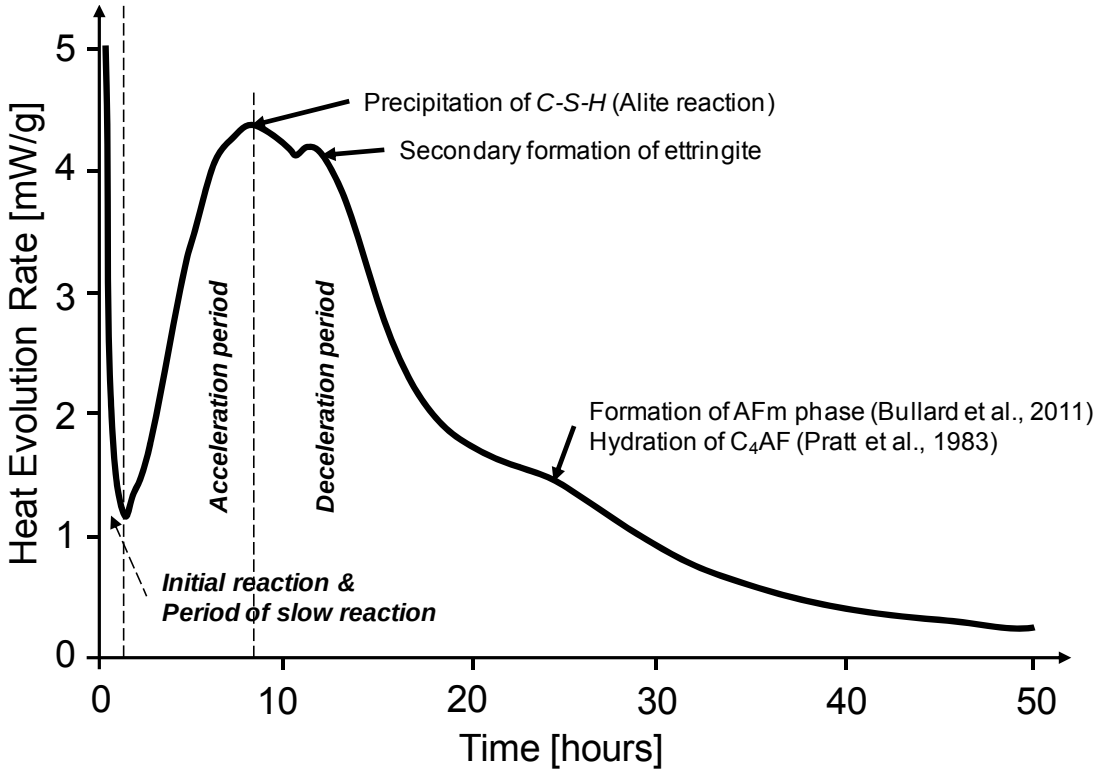

Figure 2.1 Typical isothermal calorimetric curve of an ordinary Portland cement adjusted from (Bullard et al., 2011)

Due to its instability in the absence of sulphate ions, the AF_t starts to dissolve and react with the remnant aluminate and water according to the reaction given in equation (2.3) (Taylor, 1997; Mindess et al., 2003). This represents the second stage of hydration of the aluminate.

$$2C_3A + C_6A\overline{S}_3H_{32} + 4H \rightarrow C_4A\overline{S}H_{12} \tag{2.3}$$

A low broad peak appears in the calorimetric curve (see Figure 2.1) as the AF_m phase precipitates. Mindess et al. (2003) admits that if the supply of sulphate ions is slower than the rate of ettringite formation, the mono- may appear prior to the trisulphoaluminate. Mindess et al. (2003) and Jennings and Thomas (2009) point out, in addition, that it is common to also find hydrogarnet in the hardened paste, even though the molar ratio $C\overline{S}H_2/C_3A$ is not zero. This is possible because of the high reactivity of aluminate which enables the reaction chain:

$$2C_3A + 21H \rightarrow C_4AH_{13} + C_2AH_8 \rightarrow 2C_3AH_6 + 9H \quad (2.4)$$

The monosulphoaluminate from reaction (2.3) is also an unstable compound. Mindess et al. (2003) suggest that if the amount of aluminate, portlandite and water is sufficient, the third stage of aluminate hydration takes place, leading to the depletion of AF_m:

$$C_3A + C_4A\overline{S}H_{12} + CH + 12H \rightarrow 2C_3A(C\overline{S},CH)H_{12} \quad (2.5)$$

On the other hand, Taylor (1997) mentions that C_4AH_{13} can also be identified in the composition of hydrated aluminate. This product, precipitated as a result of equation (2.6), characterises therefore the situation when AF_m is depleted before the total consumption of C_3A:

$$C_3A + CH + 12H \rightarrow C_4AH_{13} \quad (2.6)$$

2.2.3.3 *Hydration of Alite and Belite*

Alite is the most encountered mineral in the cement powder (40-70%) and its hydration activity is much more intense than the activity of belite (Jennings and Thomas, 2009; Mindess et al., 2003). The stoichiometry of the hydration of these two phases has been widely investigated (Fujii and Kondo, 1974; Locher, 1966; Peterson et al., 2005) and the conclusion from these studies is that the reaction products are almost similar, although their formation and accumulation is strongly related to the specific rate of each reaction. The difference between these phases is mainly attributed to the amount of water measured within the gel structure, which was slightly greater when probing the alite (Kantro et al., 1966; Brouwers, 2004). The precipitation of calcium silicate hydrate gel and of portlandite generates, in 4 to 8 hours, the main peak present in the calorimetric curve of the Portland cement (see Figure 2.1). Tennis and Jennings (2000) mention the following chemical reactions for completely saturated hydrates:

$$C_3S + 5.3H \rightarrow C_{1.7}SH_4 + 1.3CH \quad (2.7)$$

$$C_2S + 4.3H \rightarrow C_{1.7}SH_4 + 0.3CH \quad (2.8)$$

The hydrated gel in this case has a CaO/SiO_2 ratio equal to 1.7 in contrast to 1.5 reported by Mindess et al. (2003) and Peterson et al. (2005). Regarding this discrepancy, it should be mentioned that Locher (1966) performed a set of tests on C_3S pastes in which he has shown that the lime content in the *C-S-H* varies with the amount of initial mix water and with the degree of hydration. According to his data, in pastes with a considerable water content (≥ 0.6 g H_2O/g C_3S), the ratio varies between 1.4 to

1.6. The rest of the pastes are richer-in-lime calcium silicate hydrates having a CaO/SiO_2 ratio that can reach 2.3.

2.2.3.4 *Hydration of Aluminoferrite*

The hydration of aluminoferrite is comparable in complexity to the hydration of the aluminate phase, but is slower and more exothermic (Mindess et al., 2003; Taylor, 1997). Again, the presence of SO_4^{2-} is crucial in setting the reaction path, but this time the aluminium ions alternate in the crystalline structure of the precipitated products with iron ions. As long as gypsum is available, the chemical reaction proceeds as in equation (2.9), while in its absence, the reaction (2.10) takes place (Jennings and Thomas, 2009; Mindess et al., 2003):

$$0.75C_4AF + 3C\overline{S}H_2 + 27.5H \rightarrow C_6(A,F)\overline{S}_3H_{32} + 0.5(F,A)H_3 \quad (2.9)$$

$$1.5C_4AF + C_6(A,F)\overline{S}_3H_{32} + 7H \rightarrow 3C_4(A,F)\overline{S}H_{12} + (F,A)H_3 \quad (2.10)$$

Regarding the hydration of the ferrite phase, in the model of Tennis and Jennings (2000) for the structure of calcium silicate hydrate, only impure hydrogarnet is formed:

$$C_4AF + 2CH + 10H \rightarrow 2C_3(A,F)H_6 \quad (2.11)$$

In contrast with C_3A, the reaction rate of C_4AF is slower and according to Pratt et al. (1983) it is visible in the form of the less distinctive third shoulder of the typical calorimetric curve. In his textbook, Taylor (1997) states that the exothermic feature of both C_3A and C_4AF hydrations is given in a larger extent by the reaction of the anhydrous with water and not by the subsequent stages of precipitation.

2.3 Physical Processes in Unsaturated Ordinary Cementitious Materials

The hygro-thermal characterisation of cementitious materials is centred around the transient transport mechanisms within the material that dictate implicitly the saturation state of the material. These processes, “rediscovered” and extensively investigated during the last 80 years, alter the behaviour of cement/concrete pastes over time by changing the saturation state (Otieno et al., 2010). The effects are in the majority of cases detrimental: leaching (Gawin et al., 2008), chloride or carbonation-induced corrosion (Baroghel-Bouny et al., 2011; Otieno et al., 2010), freeze and thaw (Jacobsen and Sellevold, 1996). The entire body of literature agrees that, in cement-based materials, the substances being transported through the pore network have a

much more complex structure than in the majority of much more elaborated mobility capacity than in the preponderance of the porous materials because of the continuous change in shape and diameter of pores during hydration (Xi et al., 1994). The air, water or dissolved ions found in the pore network travel in time from one location to the other driven by gradients in different potentials (e.g. pressure, temperature, chemical concentration).

2.3.1 Drying of Cementitious Materials

The movement of liquid and gaseous phases within cement-based materials causes the moisture content to decrease, which is accentuated during hydration by self-desiccation, as can be seen in Figure 2.2 (Kim and Lee, 1999; Kang et al., 2012). Lura et al. (2003) link the initiation of autogenous drying to the moment when chemical shrinkage ceases to be totally converted into an external volume change and the stiffness of the newly formed hydrates is capable of sustaining the compression arising from the internal fluid menisci. The tests performed by Kim and his co-workers revealed the fact that for concretes with low water-cement (*w/c*) ratios, which have denser microstructures than ordinary concretes, the rate of fluid transfer is hindered, while the autogenous drying is enhanced. They also showed that in concretes with low *w/c* ratios the rate of moisture diffusion is much lower than that of concretes with high *w/c* ratios.

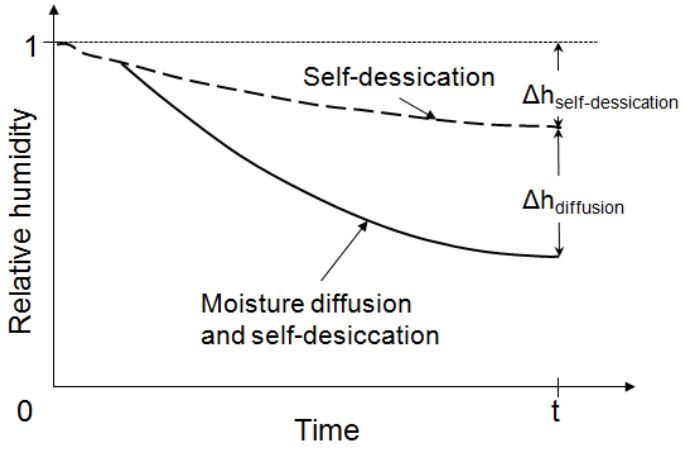

Figure 2.2 Schematic representation of drying according to Kim and Lee (1999)

2.3.2 Transport Mechanisms of Fluids in Cementitious Materials

When speaking about the numerical modelling of moisture transfer, there are two main schools of thought, each of which has a different perspective. The first, known as the mechanistic approach, considers and examines individually the various causes that enable the movement of the aqueous and vapour phases. The second is more

phenomenological and is based on the assumption that a single flux term describes all the possible transport phenomena. The following sections will present the physical aspects of the transport mechanisms in cementitious materials in the context of these two perspectives.

2.3.2.1 *Advection*

Scherer (1990), a proponent of the mechanistic approach, reports in his review dedicated to the theory of drying that once a liquid/vapour interface is present, the evaporation process triggers the movement of liquid due to an imbalance in energy. The liquid water is pulled away from the saturated zones towards the empty void areas to impede the energy increase of the system and so, a water pressure driven gradient is generated. Many researchers share the same opinion and describe the flux by means of Darcy's law (Koniorczyk and Gawin, 2012; Bary et al., 2012; Gawin et al., 2011b; Baroghel-Bouny et al., 2011; Davie et al., 2014):

$$J_{\pi}^{A} = -\frac{k_{\pi}}{\mu_{\pi}} \nabla p_{\pi} \tag{2.12}$$

where: J_{π}^{A} represents the advective flux of the fluid, k_{π} is the permeability of the medium with respect to the fluid, μ_{π} is the viscosity and p_{π} is the pressure of the fluid. Scherer (1990) suggests that the law is suitable even for transport in small pores as long as the liquid phase remains in a funicular state (Figure 2.3.a). Difficulties arise when the drying front reaches the gel pore level and the water is found mostly in the absorbed layer. The permeability decreases and, at low relative humidity, the movement of water becomes diffusive in nature due to the disjoining pressures which predominate (Figure 2.3.b).

Although extensive research has been carried out on water permeability in cementitious materials, no single experimental procedure is able to adequately cover and identify all the transformations that occur in the internal structure of the material, especially those that occur in early age cementitious materials. Aldea et al. (1999) and

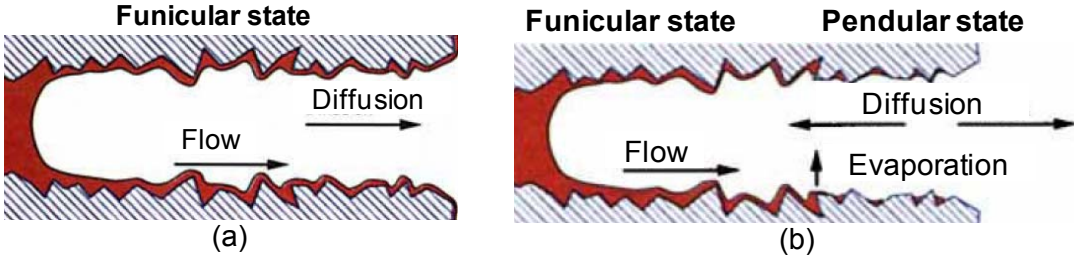

Figure 2.3 Transport mechanisms in pores from (Scherer, 1990):

(a) funicular and (b) funicular and pendular state

Marsavina et al. (2009) conclude that permeability is related to porosity, in undamaged concrete, and to crack properties, in damaged concrete. When the amount of cracking becomes significant, Rodriguez and Doug Hooton (2003), Poursaee and Hansson (2008) and Jaffer and Hansson (2008) have found that the permeability increases by several orders of magnitude. Martys (1995) conducted a survey on direct and indirect methods of measuring the permeability and reported that the values for cement-based materials are much smaller than for other porous materials such as most rocks or soils: 10^{-22} m^2 for high strength cement pastes and 10^{-18} m^2 for typical concrete. In addition, he acknowledged that the unsaturated state reduces this magnitude even more by a factor known as the hysteretic relative permeability, $k_{r\pi}$:

$$k_{\pi} = k_{i\pi} k_{r\pi} \tag{2.13}$$

where $k_{i\pi}$ is the intrinsic permeability coefficient.

In their numerical analyses, which examined the significance of several permeability values and functions, Davie et al. (2012) showed that having an accurate expression for the relative permeability is crucial. According to their investigation, it is difficult to establish precisely the order of magnitude of the permeability coefficients for a specific material type since “different formulations could result in the prediction of apparently different intrinsic permeabilities for the same concrete”. Therefore, in current *THC* models, the trend is to calibrate these parameters rather than to use standardised values.

2.3.2.2 *Diffusion*

In the case of cementitious materials, the interstitial liquid is an electrolyte solution. In these circumstances the evaporation creates a local imbalance of concentration that triggers the diffusion of vapour in order to maintain the equilibrium (Scherer, 1990; Li et al., 2009). The movement of the gaseous phase of water is described by Fick’s law:

$$J_v^D = -D_c \nabla c_v = -\frac{D_c c_v}{RT} \nabla \mu_{chem} \tag{2.14}$$

where: J_v^D symbolizes the diffusive flux, D_c is the diffusion coefficient, c_v is the concentration of the vapour phase, R is the ideal gas constant, T is the temperature and μ_{chem} is the chemical potential.

The phenomenological approach, mentioned in the beginning of section 0, treats diffusion as a physical process (Di Luzio and Cusatis, 2009; Li et al., 2009; Xi et al., 1994; Kang et al., 2012). No attempt is made to differentiate between various water states and a unique moisture flux term, integrated in a unique mass conservation equation, is used. Di Luzio and Cusatis (2009) and Xi et al. (1994) state that diffusion is a combination of molecular, Knudsen and surface diffusion which becomes active between specific relative humidities and pore size intervals. The diffusive flux adopted, preserves the mathematical pattern given in equation (2.14). Di Luzio and Cusatis (2009) account for the variation of water/cement ratio and of relative humidity. They indicate that at low humidities, the transport capacity is constant whereas at high humidities, it increases. Li et al. (2009), on the other hand, consider that the phase change of water is instantaneous and prefer to express the diffusive flux in terms of a relative humidity gradient.

2.3.3 Transport Mechanisms of Chemical Species in Cementitious Materials

In cementitious materials, the interstitial fluid contains molecules or charged chemical species that may interact with each other and with the solid. Various dissolved ions were identified in the pore solutions: Ca^{2+}, Na^{+}, K^{+}, Cl^{-}, OH^{-}, $SiO_4H_2^{2-}$, $SiO_4H_3^{-}$, $SiO_7H_4^{2-}$, $SiO_4H_2^{2-}$, SO_4^{2-}, $Al(OH)_4^{-}$, AlO_2^{-} (Baroghel-Bouny, 1994; Samson, 2003; Baur et al., 2004; Bullard et al., 2010; Wan et al., 2013). When describing the transport of solute in cement-based materials, the majority of the existing studies refer to the movement of ions. One frequent approach is to consider a mobile multiple ionic system (Barbarulo et al., 2000; Baroghel-Bouny et al., 2011; Koniorczyk, 2012). The second, does not account explicitly for the movement of individual ions, but considers a generalised flux for all the chemical species of interest (Koniorczyk and Gawin, 2008; Pesavento et al., 2012). Either way, the principal hygro/chemical potentials are the combined advective, diffusive (molecular and thermal) and dispersive fluxes (Gawin et al., 2008; Koniorczyk and Gawin, 2008; Baroghel-Bouny et al., 2011; Sedighi, 2011; Koniorczyk, 2012; Pesavento et al., 2012).

The dissolved ions are transported mainly by the water flow, so the essential advective mechanisms are the same as those described above in section 2.3.2.1. The advective flux is altered only by the concentration of the chemical species under consideration and by the capacity of the cementitious materials to behave like a semi-permeable membrane (Jennings and Pratt, 1979; Koniorczyk and Gawin, 2008; Hou et al., 2013).

The study on solution concentrations by Double et al. (1978) shows, for example, that the hydrate which is formed around the alite surface, allows the transport of dissociated calcium ions, but blocks the movement of silicate ions. The diffusion of the solute, on the other hand, is triggered by other physical phenomena as will be detailed below. In her investigation of chloride ingress, Baroghel-Bouny coupled the chemical and electrical potentials by means of the modified Nernst-Planck equation (Baroghel-Bouny et al., 2011). Because of the Coulombic interactions (Boudreau et al., 2004), this equation represents, in fact, an extension of Fick's law. In Baroghel-Bouny's study, the ionic diffusion depends upon the gradient of concentration, the electrical field and the gradient of chemical affinity due to a highly concentrated salt solution. This approach has a widespread use for both cement-based materials and clays (Barbarulo et al., 2000; Boudreau et al., 2004; Samson et al., 2005). Some authors take it to a more complex level adding the Soret effect that considers the influence of temperature gradient upon diffusion (Sedighi, 2011). A simplified expression of the diffusive flux is presented in (Gawin et al., 2008), where the migration of the Ca^{2+} ions is described by the traditional Fick's law expressed in terms of a concentration gradient. The diffusion coefficient in this case is defined using a five parameter electrolyte diffusion model formulated initially by Onsager and Fuoss (1931) and applied later to cementitious materials by Kuhl and Meschke (2003, 2007). When investigating the diffusivity of multispecies solutions, (Baroghel-Bouny et al., 2011) found that the physico-chemical properties of the solvent and the solution, produce preferential flow paths for each cation and anion.

It is worth mentioning that some studies refer to hydrodymanimc dispersion as the third type of transport mechanism of a solute (Bear and Bachmat, 1991; Sedighi, 2011). Although from the mathematical point of view its expression is similar to Fick's law, the specific nature of this movement resides in merging the effects of mechanical dispersion and molecular diffusion. Bear and Bachmat (1991) state that dispersivity is manifested in both longitudinal and transverse flow directions due to the variation of molecular velocities along the pore cross-section and also from one pore to the other. Koniorczyk and Gawin (2008, 2012), on the other hand, prefer to use a single term to describe simultaneously the diffusive and dispersive fluxes. The tensor of hydrodynamic dispersion combines the coefficients of molecular and mechanical dispersion, but also of molecular diffusion:

$$D_{disp}^{ij} = \alpha_T \left|\overline{v}^{ws}\right| \delta_{ij} + \left(\alpha_L - \alpha_T\right) \frac{\overline{v}_i^{ws} \overline{v}_j^{ws}}{\left|\overline{v}^{ws}\right|} + \eta S_w D_{mol} \delta_{ij} \tag{2.15}$$

where: D_{disp}^{ij} represents the tensor of hydrodynamic dispersion, α_T and α_L are the transverse and the longitudinal dispersivity parameters, $\left|\overline{v}^{ws}\right|$ symbolises the absolute velocity of the water phase, δ_{ij} is the Kronecker delta, η represents the porosity, S_w is the water degree of saturation and D_{mol} is the molecular diffusivity coefficient.

2.3.4 Transport Mechanisms of Heat in Cementitious Materials

The thermal performance of structures made of cementitious materials and subjected to extreme environmental temperature has been investigated in detail. Koniorczyk and Gawin (2012) and Davie et al. (2010) demonstrate that a theory developed for extreme boundary conditions is suitable for both characterising the early age behaviour or the chemical degradation under normal thermal conditions. Regarding the transport of energy in cement-based materials, the convection, the conduction and the latent heat of vaporisation are usually considered, while the radiation is commonly disregarded. Heat conduction obeys Fourier's law:

$$J_T^{CD} = -\lambda_T^{eff} \nabla T \tag{2.16}$$

in which λ_T^{eff} is the effective thermal conductivity that invariably changes with temperature (Davie et al., 2012), but also with the saturation degree and with the porosity (Gawin et al., 2006) or with the amount of water lost during dehydration (Bary et al., 2012). The heat convection, enabled by the bulk movement of both liquid and gaseous phases, is influenced by the permeability of the porous medium with respect to the existing fluids (Gawin et al., 2006; Sedighi, 2011; Pesavento et al., 2012; Bary et al., 2012). Gawin et al. (2011a) state that for a moderate temperature range, both conductive and convective components are active, but above the critical point of water, the conduction predominates and the convection can be omitted. Davie et al. (2010), on the other hand, obtain satisfactory results even when they disregard the convective flux in the problem describing the *TH* behaviour at low temperatures. The heat transfer is usually a rapid phenomenon. In their investigation dedicated to the study of creep and shrinkage in concrete structures, Acker and Ulm (2001) remark that the thermal diffusion occurs much more quickly than the drying of cement.

2.4 Developments in Thermo-Hygro-Chemical Models for Cementitious Materials

A review of existing coupled *THC* models is presented below, which follows on naturally from the preceding discussion on transport mechanisms in cement-based materials. Koniorczyk (2012) and Koniorczyk and Gawin (2012) developed a finite element code for salt crystallisation in concrete structures using five macroscopic balance equations for enthalpy, linear momentum and the mass of dry-air, moisture and salt. The numerical simulation is built on previous work on cementitious materials subjected to elevated temperatures (Gawin et al., 1999; Gawin et al., 2006) or on the leaching of calcium ions (Gawin et al., 2008; Gawin et al., 2009). The governing equations for moisture and dry-air take into account the variation in time of the saturation degrees and of the density of the phase considered, in addition to the change of porosity caused by variations of temperature and by the deformation of solid skeleton. The transport mechanisms considered are the advection of water, vapour and dry air in conjunction with the diffusion of the gaseous phases. Similar terms describe the variation of the amount of salt, but in this case, a dispersive flux composed of mechanical dispersion and molecular diffusion is employed. Besides self-desiccation, the authors subjected a number of specimens to external drying which triggered the movement of salt from the core to the surface. The salt phase change occurs by means of a Freundlich non-equilibrium isotherm, where the kinetics of crystallisation incorporates two stages: the dissolution of the salt crystals during the partly saturated state with respect to salt and the precipitation of the reaction product during the saturated state. The supersaturation ratio, computed using the Pitzer model, is the parameter that makes the switch between these two processes. Koniorczyk and his co-workers acknowledge that salt formation is an exothermic process. Therefore, in the enthalpy balance equation, apart from the conductive and convective flows, separate terms for the heat release of the precipitation reaction and also of the vaporisation are accounted for.

The *HC* model created by Baroghel-Bouny et al. (2011), used to investigate the isothermal coupled moisture-ion transport, is based on the Darcian and Fickian flows of bulk water, vapours and dry air. The innovation in their investigation resides in the fact that Baroghel-Bouny et al. use different expressions to define the relative permeability with respect to the liquid and gaseous phases. In their opinion, the traditional analytical relationship proposed in Van Genuchten (1980) is suited solely to absorption and thus, the numerical derivation given in Mualem (1976) is preferred in the case of the liquid

phase. Moreover, the experimental data gathered from desorption tests shows that below 40% water saturation degree, the relative permeability decreases dramatically and thus, the advection may be neglected. The diffusive transport of ions is characterised by the Nernst-Planck equation and is driven by the diffusion under concentration gradient, the movement under chemical activity effects and the migration under (local) electrical field. Baroghel-Bouny's model includes the mass balance equations for four chemical species (Cl^-, OH^-, Na^+ and K^+) and considers only the binding of the chloride ions. The physical absorption of Cl^- to the existing *C-S-H* proceeds via a Freundlich type binding isotherm and the instantaneous precipitation of Friedel's salt.

In a distinct series of papers, Bary et al. (2008), de Morais et al. (2009) and Bary et al. (2012) describe simulations of coupled water flow and heat transfer in concrete structures (plain or reinforced) subjected to high temperature. The data collected from the experimental simulation program MAQBETH were validated by means of a simplified *THM* model. The computational technique neglected the existence of the dry air by eliminating its corresponding mass balance equation, but took into account the presence of cracks. A single mass balance equation for both vapour and bulk water phases was employed. The porosity change due to the dehydration process was accounted for and the transport mechanisms were represented exclusively by the advective flux. Regarding this precise term, it should be mentioned Bary et al. (2008) formulated a Generalized Effective Media (*GEM*), which can be used to compute an overall permeability coefficient. The coefficient depends upon the permeability of the undamaged material and upon the permeability of the cracks.

In 2012, Pesavento et al. published a thermo-hygro-chemical model, also based on the mechanics of multiphase porous media (Pesavento et al., 2012). Its purpose was to analyse the alkali-silica reaction (*ASR*) that generates an amorphous swelling gel that compresses the already existing solid skeleton. The authors though cast doubt on the nature of the gel-water combination mechanism and do not clarify if the water molecules chemically react or are absorbed. The proposed mass balance equation of moisture has a similar form as that given by Gawin et al. (2011a), but a mass sink term is introduced to account for the consumption of H_2O molecules during the formation of the alkali-silica gel. This mass sink, which considers the loss of the swelling capacity due to the aging of the material, is proportional to the overall normalized gel formation rate. The progress of the alkali-silica gel accumulation follows the thermodynamics of chemical reactions proposed by Steffens et al. (2003) and is proportional to an empirically determined water combination coefficient that expresses the variability of

the reaction with the water saturation degree. In Pesavento et al.'s model, the volume averaged enthalpy balance equation includes convective and conductive heat transfers, but excludes any contribution from the *ASR*.

2.5 Self-healing in Cementitious Materials

Due to the widespread interest in materials that recover after being damaged, the healing capacity of hardened cement and concrete pastes has become a central issue for many researchers. The phenomenon of crack repair was discussed for the first time in the scientific literature by Turner (1937), but experimental research on this phenomenon has greatly expanded in the last 15 years. The starting point for inducing and enhancing crack healing were the laboratory investigations conducted by Dry (1994). Since then, an impressive amount of experimental work has been undertaken and different approaches propounded.

2.5.1 Classification

Recently, Van Tittelboom and De Belie (2013) provided an extensive description of the existing structural recovery mechanisms and identified three main groups of self-healing techniques. The first two, called capsule and vascular based self-healing, are very similar and work by damage or temperature activation. These two are categorised as autonomic healing techniques, where the material is intentionally designed to have an increased repair potential (Schlangen and Joseph, 2009). The operating principle is simple: spherical and cylindrical shells, embedded in the paste (capsule based approach), or tubular elements connecting the interior and the exterior of the structure (vascular based approach), release – upon breakage – single or multi-component healing agents which react in specific environmental conditions and fill the openings. The third technique, on the other hand, known as intrinsic self-healing, is based on the chemical reactions that take place exclusively between the components of the cementitious matrix. In this case, the recovery is enabled by autogenous healing (basic or improved) or by healing in the polymer modified concrete. From the point of view of human interference, the mechanism of self-healing is either "active" – when it requires intervention or "passive smart" (Li et al., 1998).

In the forthcoming chapters a method for the numerical simulation of autogenous healing mechanisms will be proposed and therefore only this type of structural recovery

will be reviewed in the next paragraphs. For additional information on the other types of self-healing mechanisms, the following references are recommended (Li and Yang, 2008; Joseph et al., 2010; Van Tittelboom and De Belie, 2013; Schlangen and Sangadji, 2013).

2.5.2 Autogenous Healing

It is generally agreed that the crucial compounds for autogenous healing are the water and the unreacted cement (Lauer and Slate, 1956; Neville, 2002; Granger et al., 2007; Van Tittelboom and De Belie, 2013). The degree of efficiency increases if continuous, total wetting (100% relative humidity) is maintained (Lauer and Slate, 1956). Initially, Turner (1937) described the healing process as an ongoing hydration of remnant clinker and also as an intercrystallisation of the fractured crystals. Later on, other petrographic results confirmed the presence of calcium hydroxide produced by the hydration of alite or belite, but also revealed the formation of calcium carbonate (Lauer and Slate, 1956; Wagner, 1974). In this context Edvardsen (1999) stated that calcite precipitation is “almost the sole cause for the autogenous healing”. Clear (1985), on the other hand, claimed that the small cavities are clogged by debris based on observations that indicated a reduced amount of $CaCO_3$ for young concrete and a substantial quantity of carbonate in late stages of curing. The current trend in the cement industry further complicates the situation because modern mixes contain additional cementitious materials that often contribute to autogenous healing. However, in engineered strain hardening cementitious composite (*SHCC*), containing polyvinyl alcohol fibres and local waste materials (blast furnace slag + limestone powder), Qian et al. (2009) report that the principal filler after 28 days is still the calcite. Hence, it seems that previous investigators have failed to reach a consensus on the nature of the fill product. Nevertheless, the latest tendency, consistent with the opinion of Neville (2002), is to consider that autogenous healing of ordinary cementitious materials is achieved by continuous hydration in the first weeks, when the amount of unreacted cement is rather high, and by carbonation thereafter (Van Tittelboom and De Belie, 2013). This hypothesis is sustained also by the results of Jacobsen et al. (1995) and Granger et al. (2007), who found that the composition of the new precipitate, sampled at 12 and 20 weeks after casting, was mainly *C-S-H*.

From the physical point of view, the ongoing reaction between clinker and H_2O molecules improves the transport and the mechanical properties of the hardened cement paste, diminished previously by internal shrinkage, creep or any external

loading. Tests show a decrease of water permeability (Edvardsen, 1999; Hearn and Morley, 1997; Hearn, 1998; Neville, 2002), a return of the global stiffness to the pre-damage value and a potential regain of compressive and flexural strengths (Jacobsen et al., 1995; Pimienta and Chanvillard, 2004; ter Heide and Schlangen, 2007; Granger et al., 2007). Amongst the material properties considered in these investigations, the greatest degree of recovery was in water tightness. Granger et al. (2007) consider that the reaction products bridge cracks easily, but that the arrangement of the new crystals does not possess the same sturdiness as that of the original matrix. Some of the factors influencing the efficiency of autogenous healing and their effects are listed below:

- the mix may contain chemical components that expand during carbonation or moisture ingress (Hosoda et al., 2009; Sisomphon et al., 2011),
- a low *w/c* ratio augments the volume fraction of unreacted cement grains,
- the heat treatment accelerates the hydration kinetics (Neville, 2002; Granger et al., 2007),
- the sustained compression across the plane of the crack amplifies the repair potential (Ngab and Nilson, 1981).

The accretion of new hydrates from the opposing surfaces of a crack leads to a satisfactory degree of healing only if the crack opening is sufficiently small. In Table 2.3, some reported values of healable crack widths are given.

Table 2.3 Experimental results of self-healing

Cracking method	Autogenous healing conditions	Type of mix	Validation of self-healing	Crack width [µm]	Experimental results	Reference
four point bending	cracked sample cured in water for 28 days	fiber reinforced strain hardening cementitious composite + local waste material + byproduct	*ESEM* investigation	10-60 >60	100% healed partially healed	(Qian et al., 2009)
-	cracked sample exposed to water flow	-	permeability test	200	50% healed completely after 7 weeks	(Edvardsen, 1999)
preloading to 70% and 90% of compressive strength	cracked sample cured in water for 30 days	self-consolidated concrete + high volume fly ash/low lime fly ash	compressive strength	-	4% recovery	Şahmaran et al., 2008)
freeze/thaw cycles in water	cracked sample cured in water for 3 months	6 different concrete mixes	resonance frequency compressive strength	-	85-98% recovery 4-5% recovery	(Jacobsen and Sellevold, 1996)
splitting tensile test	cracked sample exposed to water flow at T=20°C for 336 hours	high-performance concrete (*HPC*) with *w/c*=0.37	permeability test	50 100 150	fall of initial flow rate to ≈ 2% fall of initial flow rate to ≈ 6% fall of initial flow rate to ≈ 15%	(Reinhardt and Jooss, 2003)

2.6 Numerical Models on Autogenous Healing

There have been a limited number of numerical studies on autogenous healing. The ability of these models to realistically describe the relevant processes at a large scale is rather limited. The most frequently reported computational approach was developed by a team of researchers from Delft University of Technology who have used the HYMOSTRUC model (van Breugel, 1991) to find the distribution of the unreacted cement particles and have simulated further hydration considering diffusion and thermodynamic principles. In the HYMOSTRUC model, cement particles are represented by spherical elements dispersed in an aqueous medium and hydrate in a two stage process simulated using boundary and diffusion controlled mechanisms. In a preliminary phase, ter Heide (2005) modelled autogenous healing with bridging particles that filled the existing gaps between clusters of hydrates. These clusters are the result of the expansion of unhydrated cement particles (*UCP*) and are modelled using HYMOSTRUC. The transition to self-healing is done by incorporating the bar and the ribbon models developed by Lokhorst (1999) and Koenders (1997). The clusters, converted into a set of horizontal bars, are bridged by vertical elements when a size criterion is satisfied. Ye and van Breugel (2007) upgraded HYMOSTRUC to allow for a 3D analysis and concluded that there exists a considerable potential for the self-healing of microcracks even in the case of one year old specimens. In the following years, Huang and Ye (2011, 2012) and Huang et al. (2013) published a set of articles which describe the simulation of further hydration, enabled by the breaking of embedded water capsules, using thermodynamic principles and that account for diffusion of both unhydrated cement grains and hydrated products formed before cracking. Initially, they investigated autogenous healing using a 3D model, in which there was a prescribed percentage of anhydrous cement particles. The micrometric analysed area, comprising two crack surfaces and a crack space filled with *C-S-H*, *UCP* and pore phases, was divided into 1 μm x 1 μm x 1 μm voxels. At each iteration step, the concentration of each voxel was calculated using the Fickian type transport mechanism of dissociated ions. The same computational algorithm was used in Huang and Ye (2012), but this time the microstructure of the cement paste before cracking was given by HYMOSTRUC 3D. In Huang et al. (2013) the following improvements were carried out: a non-flat crack surface was assumed, the inner *C-S-H* did not contribute to the intrinsic material recovery and the leaching of Ca^{2+} was assessed.

In 2007, another group of researchers, also based at Delft University, focused their attention on expressing the capacity of self-healing by estimating the amount and

distribution of remnant unhydrated cement in the interfacial transition zone (*ITZ*) and in the bulk paste (He et al., 2007). In their simulation system, named SPACE, created by Stroeven and Stroeven (1999), they dynamically generated in a container a 3D distribution of unhydrated cement nuclei and described the reaction between clinker and water roughly as in HYMOSTRUC. Their conclusion, predominantly qualitative, stated that the fine cement types produce an increased surface area density of the *UCP* in the *ITZ*, which can be further related to the probability of crack filling. A more quantitative evaluation of structural repair was presented by He (2010). In this article, the author predicts the optimum location of the crack with respect to the distance between two aggregate particles, such that the healed crack width is a maximum. A different set of self-healing studies centred on the investigation of two possible cracking modes was performed in (Lv and Chen, 2012) and (Lv and Chen, 2013). Again, spherical unhydrated particles were randomly distributed in a cubic representative volume element and the volume of hydrated product per area of crack surface was estimated by means of probabilistic calculus. The hydration kinetics followed an empirical law of thickness expansion based on the measurements of Kondo and Ueda (1968) and Knudsen (1980). The proposed curve, however, varied solely with time and ignored the nature of nuclei, the surface density and the external environment (curing temperature and water content). The efficiency of self-healing was calculated and shown explicitly only for a dome-like cracks (Lv and Chen, 2013).

The mechanical recovery of the cracked cement paste is discussed by Remmers and de Borst (2008) *and* Hilloulin et al. (2013). The first two authors propose a finite element model to describe the three principal stages of the self-healing: the cracking, the transport of material and the filling of the cracks. Although attention is focused mainly on the simulation of fracture, Remmers and de Borst are among the first to introduce the momentum and mass balance equations for a fluid-saturated porous medium in order to advance a macroscale level numerical self-healing strategy. No consideration is given to the chemical reactions, but instead, the fluid pressure is assumed to initiate the healing mechanism. In the authors' view, at a certain time moment (unspecified in the paper), the crack rebonding occurs by adding a strength and stiffness increment of the interface to the constitutive relation that governs the crack opening. Hilloulin et al. (2013) solve a hydro-mechanical cellular problem in a *RVE* and estimate the partial volumes of the hydrates that have precipitated after water penetration. The evolution of a homogenous Young's modulus is then obtained by applying a self-consistent scheme. The filling material has an explicit chemical composition and its quantity is computed from a set of clinker-water reactions and from the evolution of the degree of hydration. The stages of the normalized chemical affinity

(dissolution, nucleation and diffusion-controlled phase) are highlighted and the characteristic time of reaction given by the Arrhenius law influences the rate of hydration.

2.7 Conclusions

This chapter presented a state-of-the-art review of the understanding and modelling of thermo-hygro-chemical behaviour and of the hydration kinetics of cementitious materials in relation to the autogenous healing phenomenon. There is not yet agreement on the mechanisms that govern the autogenous filling of cracks, but there is agreement in a large and growing body of literature that the structural recovery is due to the ongoing hydration of the *UCP*. Recent theoretical and experimental findings show that the hydrates are formed during a multistage process. Regarding the stoichiometry of these reactions, there is a consensus among scientists, mainly driven by pragmatism, that the interactions between the ions of the four clinker phases can be neglected and that only the stoichiometries of the individual minerals need be considered.

Researchers agree that the fluids are generally subjected to drying, advection and diffusion. The drying via self-desiccation, triggers the appearance of pores within the mix. The advective flow depends on the microstructure of the material including the quantity of empty pores, cracks and the liquid phase form, while the diffusive flow depends on the *w/c* ratio and the relative humidity within the pores. The heat transfer mechanisms, on the other hand, consist of convection, conduction and vaporisation. The chemical behaviour of cementitious materials deals, besides hydration, with the transport of dissolved ions inside the porous medium. This movement is due to advection, diffusion and dispersion. The diffusion, in this case, couples the chemical and the electrical potentials and produces differential flows if multiple ions are considered.

It was also highlighted that the existing models, related to the autogenous healing, are formulated mostly without coupling between thermal, hygral and chemical components. The only study in which such an approach is mentioned, concentrates more on crack formation and fails to propose a comprehensive solution for transport processes and self-healing. Thus, the need to develop a computational code able to rigorously represent all the *THC* aspects is justified.

Chapter 3. Theoretical Formulation

3.1 Introduction

The third chapter of this thesis brings to the fore the interactions between the hygral, thermal and chemical components of the computational model that simulates autogenous healing of cement-based materials. The major aim of this chapter is to present the mathematical framework necessary to analyse the behaviour of this type of porous material.

Section 3.2 is dedicated to the theoretical formulation of the hydration kinetics of the cement powder. The focus is mainly on two aspects. The first is the estimation of the water forms populating the porous network at various size scales that enables the determination of the porosity functions. The second is the computation of the rate of heat generation which follows closely the hydration approach advanced by Schindler and Folliard (2005).

The transport mechanisms characterising the moisture phase are dealt with in the subsequent section 3.3. The two governing differential equations pertinent to the masses of liquid and vapour are expressed with respect to the solid skeleton and then the flow parameters included in these relationships are defined highlighting the diversity of the fluxes considered.

The principles regarding the simulation of the reactive transport are presented in section 3.4. An overall mass balance law is formulated for a single solute accounting for all the chemical elements carried by the interstitial liquid that will combine and heal the cracks. Three distinctive fluxes: advection, molecular diffusion and dispersion dictate the movement of ions, while a sink/source term based on a Freundlich type isotherm is utilized to represent the production of the hydrates.

Section 3.5 presents the transport mechanisms encountered during the heat transfer. The macroscopic energy balance equation for the entire porous medium is derived and some simplifying assumptions are made. The governing relationships employed in this equilibrium equations are listed and defined.

Finally, section 3.6 resumes the theoretical aspects presented in detail up to that point and stresses the innovations introduced in the current *THC* model.

3.2 Hydration Kinetics

In a number of papers the hydration degree is defined as the ratio between the mass of hydrated material at time t and the mass of hydrated material at theoretical complete hydration (Gawin et al., 2006). However, the present work uses the definition suggested by Schindler and Folliard (2005) which originates from the calorimetric analysis of the cement hydrolysis. According to these authors, the hydration curve may also be determined by tracking in time the ratio between $H(t)$ - the heat released at time t and H_{tot} - the total heat released when all the cement has reacted.

$$\Gamma(t) = \frac{H(t)}{H_{tot}} \tag{3.1}$$

Theoretically, the hydration degree should range between 0 – at the initiation of the crystallisation process – and 1 – at the cessation of any chemical activity. In practice however, a value equal to unity may never be reached and instead a smaller computed ultimate degree of hydration needs to be considered.

Consideration of hydration kinetics enables the characterisation of the cement hardening process from hygral, thermal and chemical point of view. The stages of the reaction, the nature of the resultant chemical products, the development and evolution of the porous medium together with the advancement of the heat release are all related to the progress of the hydration and have to be included in a holistic *THC* model.

3.2.1 Evolution of the Hydration Degree

Portland cement is composed of polymineralic grains dominated by impure C_3S that fluctuates usually between 40–70% by weight (Jennings and Thomas, 2009). The reaction kinetics of alite consist of three distinctive steps (Taylor, 1997; Fujii and Kondo, 1974) which are extrapolated in this study to all the remaining minerals in a similar manner to that described in Bernard et al. (2003). A short description of these stages is presented below together with the formulae characterising the time evolution of the hydration degree in which the subscript X refers to one of the four possible clinker minerals existing within the cement powder.

1. **The induction period**. Throughout this initial step the outermost layers of the clinker mineral dissociate into constitutive ions. The remaining grains are covered with

3 to 4 layers of absorbed water molecules (Fujii and Kondo, 1974) and the hydrolysis advances with a constant reaction rate given by the equation:

$$\Gamma_X(t) = \frac{\Gamma_X^I}{t_X^I} t \tag{3.2}$$

where Γ_X^I is the degree of hydration threshold at the end of the induction period, t_X^I is the duration of the induction period and t is the current time.

2. **The nucleation and growth controlled hydration**. During this interval the volume of hydrates increases considerably and fills the capillary pores. The crystallisation kinetics is described by an Avrami type equation (Bernard et al., 2003):

$$\Gamma_X(t) = 1 - \exp\left\{-\left[k_X(t - t_X^I)\right]^{K_X}\right\} \tag{3.3}$$

where k_X is the rate constant equal to the product of K_X and the characteristic time τ_X, whilst K_X is a parameter giving the order of reaction.

3. **Diffusion controlled hydration**. According to Fujii and Kondo (1974), once a critical hydration degree is exceeded, the reaction enters a final phase where the already formed precipitates coat the unhydrated grains and reduce the free movement of the dissociated ions. The expression proposed for the reaction advancement beyond this point reads:

$$\Gamma_X(t) = 1 - \left(-\frac{\sqrt{2D_X}}{R_{ck}} \sqrt{t - t_{X,0}^D} + \sqrt[3]{1 - \Gamma_X^D} \right)^3 \tag{3.4}$$

in which Γ_X^D is the critical hydration degree, $t_{X,0}^D$ denotes the initiation time of the diffusion controlled hydration, R_{ck} represents the average radius of the clinker phases and D_X is the diffusion coefficient controlling the final hydration stage.

3.2.2 Evaluation of Water Forms in Hardened Cement Pastes

Many properties of cement-based materials, including the mechanical and mass transport potentials, originate from the nanostructure level of the hydrated paste. The reaction between cement and water gives rise to a complex physical and chemical structure which comprises a range of hydration products, pores and unreacted cement grains. During the hydrolysis, the liquid phase is stored in a multitude of locations that vary in dimension and intensity of the attraction forces between the H_2O molecules. This leads to the existence of several aqueous phases with distinctive thermodynamic properties.

3.2.2.1 *Classification of Water Forms*

This section provides a summary of the author's interpretation of the colloidal model proposed by Jennings (2008), which deals with the classification of the water forms in cement paste and, in particular, in calcium silicate hydrate gels. A brief description of these water phases, used to determine some of the hygral characteristics of the current numerical model, is presented in the following paragraphs along with a schematic illustration given in Figure 3.1.

The *C-S-H* gel represents a nanometric non-crystalline product that incorporates solid particles and pores. Depending on the saturation state of the paste, the pores are either full of water or partially empty. Because of their location, these voids are generally termed gel pores and, to the first approximation, form the so-called gel porosity. However, the behaviour of the water in the largest gel voids is more like the behaviour of the water in the capillary network. Thus, these voids are included in the capillary porosity rather than in the gel porosity.

Jennings states that the silicate globule – the basic unit block of the *C-S-H* gel – has a platelet shape and an internal sheet like structure similar to that of tobermorite and jennite. It comprises Ca^{2+}, Si^{2+} and O^{2-} ions which constitute the **solid skeleton of the reacted clinker** (*SSRC*), OH^- groups strongly bound to the solid skeleton representing the **non-evaporable/chemically bound water** (*CBW*) and water molecules frequently called **globular evaporable water**, that can be slowly removed during medium to extreme drying conditions. The potentially mobile aqueous phase is situated in intraglobular pores and in interlayer spaces, both less than 1nm in size. According to their specific location, these liquid phases will be referred from now on as **intraglobular** (*IGW*) and **interlayer water** (*ILW*), respectively. The globular evaporable water is subjected to strong adsorption forces, has a high density (1.2 to 2 mg/m^3) and collapses the globule when it is removed.

The silicate globules are surrounded by **adsorbed water** (*AW*) with the same thermodynamic behaviour as the globular evaporable water. During hydration, the globules pack in flocs ranging between 30 to 60 nm in size that have variable densities and that encapsulate **small gel pores** (*SGP*) (1-3 nm) filled with **constrained water**. This aqueous form together with the sum of the adsorbed, interlayer and intraglobular water represents the effective **gel water** which in this study is taken into account when assessing the gel porosity. The **large gel pores** (*LGP*), on the other hand, are between 3 to12 nm in diameter and separate two neighbouring globule flocs. They contain H_2O

molecules that form a meniscus at the interface with the gaseous phase and behave similarly to the bulk/capillary water situated outside the gel boundaries.

As far as the capillary network is concerned, its presence is due to the colloidal precipitates that are too dense to fill all the available space and that entrap regions of pore solution during the short-term syneresis. After the setting of the paste though, the newly created non-gel phases restrain the contraction of the solid network in the absence of heat treatment, thus preventing further syneresis. Thereafter, the volume of the capillary pores begins to decrease as a consequence of the ongoing hydration.

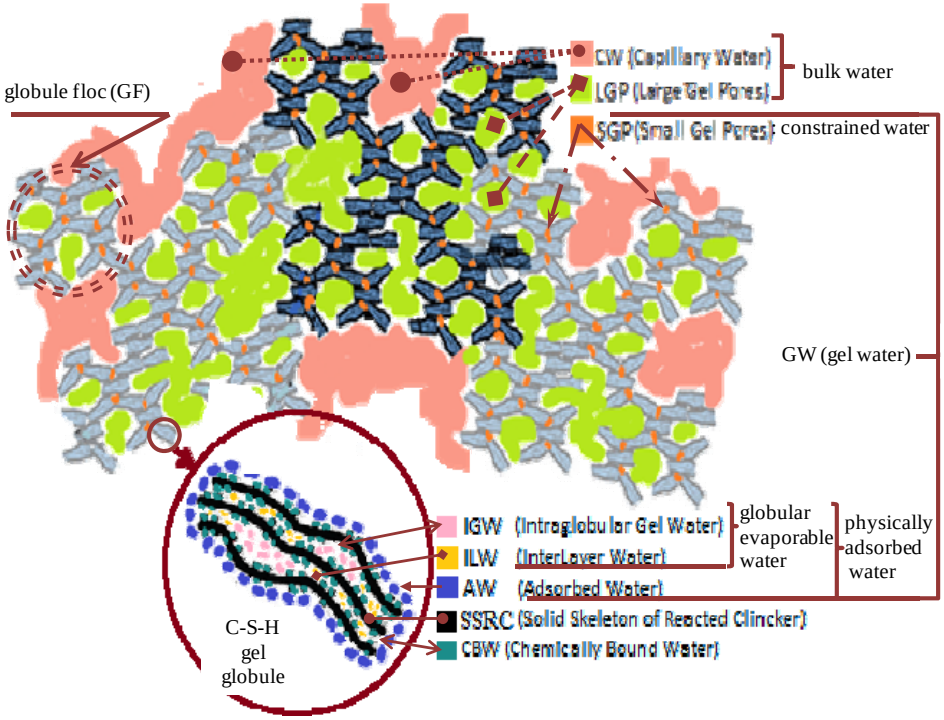

Figure 3.1 Representation of water forms within the *C-S-H* gel according to Jennings (2008)

Before moving to the next section, it should be mentioned that, in the current investigation, the classification of the water forms corresponding to the *C-S-H* gel was also extended to the reaction products resulting from the hydration of aluminate and aluminoferrite. The following section provides the mass fractions associated with these water forms.

3.2.2.2 *Estimation of Mass Fractions of the Water Forms*

Returning to the theoretical considerations enumerated in section 3.2.1, the function representing the degree of hydration pertinent to a specific clinker compound is:

$$\Gamma_X(t)=\begin{cases}\dfrac{\Gamma_X^I}{t_X^I}t & ,t<t_X^I\\ \Gamma_X^I+1-\exp\left\{-\left[k_X\left(t-t_X^I\right)\right]^{K_X}\right\} & ,t_X^I\le t<t_{X,0}^D\\ 1-\left(-\dfrac{\sqrt{2D_X}}{R_{ck}}\sqrt{t-t_{X,0}^D}+\sqrt[3]{1-\Gamma_X^D}\right)^3 & ,t_{X,0}^D\le t\end{cases} \tag{3.5}$$

where in order to satisfy the continuity condition $t_{X,0}^D$ has the expression:

$$t_{X,0}^D=t_X^I+\frac{\left[-\ln\left(\Gamma_X^I-\Gamma_X^D+1\right)\right]^{\frac{1}{K_X}}}{k_X} \tag{3.6}$$

Following the approach adopted by Bernard et al. (2003), the hydration degree of the Portland cement can be computed as a weighted average of these individual hydration degrees:

$$\Gamma_{PC}(t)=\frac{\sum_X\left(m_X\Gamma_X(t)\right)}{\sum_X m_X} \tag{3.7}$$

in which m_X is the mass percentage of the clinker mineral X and Γ_X is its corresponding degree of hydration.

In order to evaluate the masses per unit volume of material of each water form present in the paste, a numerical algorithm is proposed based on reaction stoichiometry. Firstly, the duration required to reach theoretical complete hydration ($\Gamma_{PC}(t)=1$) is computed and then partitioned in small time steps. For each temporal division, the individual hydration curve (3.5) provides a mass of consumed clinker used to calculate afterwards the depleted amount of water in compliance with the chemical reactions from Appendix A, Table A. 1. It is necessary to draw attention to the fact that Powers and Brownyard (1948), Tennis and Jennings (2000) and Jennings (2008) acknowledge that the variation of the water saturation degree of the medium decreases the number of water moles within the hydrates, which is interpreted here as a decrease in the stoichiometric coefficients. Jennings suggests that in the case of *C-S-H*, distinct water forms are expelled from their location during four relative humidity intervals delimited in terms of water content by four H_2O mole thresholds and implicitly by four stoichiometric

numbers. These intervals, denoted in this thesis by *i*1, *i*2, *i*3 and *i*4, correspond to ≈0%, (0%, 11%], (11%, 40%] and (40%, 60%], respectively and are also preserved for the rest of the precipitates. For these other hydrates however, the stoichiometry is adjusted according to the available experimental data, as can be seen in Appendix A, Table A. 2. By solving the chemical reactions, the values w_{i1}, w_{i2}, w_{i3}, and w_{i4} (the quantities of water per unit volume of material consumed at 60%, 40%, 11% and ≈0% *RH*, repectively) are estimated. The masses of *LGP*, *SGP*, *AW+ILW+IGW* and *CBW* per unit volume of material are then found by using the relationships in (3.8):

$$\begin{aligned} w_{LGP}(t) &= w_{i4}(t) - w_{i3}(t) & \qquad w_{AW+ILW+IGW}(t) &= w_{i2}(t) - w_{i1}(t) \\ w_{SGP}(t) &= w_{i3}(t) - w_{i2}(t) & \qquad w_{CBW}(t) &= w_{i1}(t) \end{aligned} \tag{3.8}$$

The proposed algorithm employs an iterative procedure applied to each clinker mineral that aims to mathematically simulate a multistage chemical phenomenon involving the potential interactions between both intermediate precipitates and reactants. It is thus necessary at this point to clarify some numerical aspects regarding the modelling of the reactions. The hydration of alite and belite is a one stage process controlled solely by the available quantity of the solid reactant. In this case, the iteration stops when the accumulated mass of consumed C_3S and C_2S surpasses their initial amounts. The reactions involving the aluminate and aluminoferrite, on the other hand, are more complex and occur in three phases. In the primer stage, the presence of gypsum influences the precipitation path. If $C\overline{S}H_2$ is the first to be depleted, the hydration enters in the second phase. Otherwise, due to the absence of C_3A and/or C_4AF, the reaction ceases completely. A similar pattern holds during the second phase of hydration, but this time gypsum is replaced by $C_6A\overline{S}_3H_{32}$ (for the aluminate) or by $C_6(A,F)\overline{S}_3H_{32}$ (for the aluminoferrite). In the third stage, the portlandite precipitated from alite and belite is consumed. In the case of C_3A, two simultaneous reactions which have the same reaction rates occur, while in the case of C_4AF a single hydrolysis takes place. It should also be added that at each time step, the amount of available CH is compared to the required amount. If the formed portlandite is insufficient, the hydration Stage 3 of C_3A and C_4AF is not simulated. More details about the numerical algorithm are presented in the form of pseudo codes in Appendix A, Figure A. 1 to Figure A. 2.

3.2.3 Estimation of the Ultimate Degree of Hydration

Another parameter characterising the reaction kinetics is the ultimate degree of hydration, Γ_{ult} , which represents the final stage reached by the chemical process. The stoichiometric based algorithm presented above is able to determine this value which depends on the chemical and physical features of the cement paste/concrete mix. Theoretically, Γ_{ult} should be equal to one, but in the majority of cases there is either insufficient water with respect to the initial unhydrated quantity of cement and/or there is not enough space required for full crystal nucleation. Powers (1964) states that although the chemical equilibrium is not reached, the reaction may stop before the complete consumption of clinker compounds and thus the following expression for the ultimate degree of hydration is applicable:

$$\Gamma_{ult} = \frac{\left(\frac{w}{c}\right)_{eff}}{\left(\frac{w}{c}\right)^{*}} \leq 1 \tag{3.9}$$

where $\left(\frac{w}{c}\right)_{eff}$ is the effective water-cement ratio of the mix (takes into account the water absorption of the aggregate) and $\left(\frac{w}{c}\right)^{*}$ denotes the lowest water-cement ratio that would permit complete hydration. This last term is equal to:

$$\left(\frac{w}{c}\right)^{*} = \frac{w_{i4}}{c} \leq 1 \tag{3.10}$$

3.2.4 Porosity

As will be seen in the forthcoming section 3.3.1, explaining the governing balance equations employed in the *THC* model, the capillary and total porosities play a crucial role in the mathematical description of the flow problems (moisture and heat). The capillary porosity includes all the voids that may store the water forms that have the same behaviour as the bulk water. On the other hand, the total porosity equals to the sum of capillary and gel porosities. As previously stated, the emergence in the mass of the hardened cement paste of encapsulated capillary pores is triggered during the syneresis process. In time though, the volume of these large size interstices decreases especially when C_3S and C_2S begin to hydrate (Jennings, 2008; Cook and Hover,

1999). Throughout the syneresis, the chemical shrinkage predominates and is converted almost exclusively into an external volume change. Therefore, the degree of water saturation remains constant and close to 1. In order to numerically capture this effect, the expression of the porosity for this short time period is given by:

$$\eta_j(\Gamma) = \frac{w - \Gamma \sum_i w_i^{ult}}{w - \Gamma_0 \sum_i w_i^{ult}} \eta_j(\Gamma_0) \quad , \Gamma < \Gamma_0 \tag{3.11}$$

where j stands for the porosity type (capillary or gel), w is the mass of the mix water per unit volume of material, w_i^{ult} is the mass of the component i of the gel water at the end of hydration per unit volume of material (i = *CBW*, *AW+ILW+IGW*, *SGW*) and Γ_0 is the percolation threshold of the degree of hydration. When this limit is surpassed, the paste starts to gain stiffness. The chemical shrinkage begins to be restrained by the hydration products and empty voids form within the mix (Lura et al., 2003). In addition, the aggregate (if unsaturated) absorbs part of the bulk water (Buenfeld and Okundi, 1999).

For $\Gamma \geq \Gamma_0$ the porosity has the same general form as in (Neville and Brooks, 1987) and follows the principles of Powers' model (Powers and Brownyard, 1948). Its expression is estimated from the quantity of cement paste constituents at the end of hydration, considering that the reaction products advance proportionally with the overall hydration degree from (3.7). Experimental evidence suggests an essentially linear relationship between porosity and degree of hydration (Neville and Brooks, 1987; Young and Hansen, 1987; Halamickova et al., 1995; Cook and Hover, 1999). In the current investigation the adopted formula for porosity uses the above considerations and the quantities of the water forms obtained from the iterative stoichiometric algorithm:

$$\eta_j(\Gamma) = \frac{V_w + V_{ea} - \left[V_s(\Gamma) + \Gamma \sum_i V_i^{ult} \right]}{V_c + V_w + V_{ea} + \sum V_{agg} + \sum V_{SCM}} \quad , \Gamma \geq \Gamma_0 \tag{3.12}$$

In this relationship V_w, V_{ea}, V_c, V_{agg} and V_{SCM} are the volumes of mix water, entrapped air , mix cement, aggregate and supplementary cementing materials (*SCM*), $V_s(\Gamma)$ is the volumetric strain due to shrinkage and V_i^{ult} is the volume of the component i of the gel water at the cessation of hydration. Making use of the initial water cement ratio and also of the densities, (3.12) may be rearranged to give:

$$\eta_j(\Gamma) = \frac{\frac{w}{c}\frac{c}{\rho_w} + V_{ea} - \left[V_s(\Gamma) + \Gamma \sum_i \frac{w_i^{ult}}{\rho_i}\right]}{\frac{c}{\rho_c} + \frac{w}{c}\frac{c}{\rho_w} + V_{ea} + \sum V_{agg} + \sum V_{SCM}} \quad , \Gamma \geq \Gamma_0 \tag{3.13}$$

where ρ_w, ρ_c and ρ_i are the densities of bulk water, cement and component i of the gel water, respectively. Multiplying top and bottom by $\frac{\rho_w}{c}$, (3.13) leads to:

$$\eta_j(\Gamma) = \frac{\frac{w}{c} + \frac{\rho_w V_{ea}}{c} - \left[V_s(\Gamma)\frac{\rho_w}{c} + \Gamma \cdot C_{\eta\_S}^j\right]}{\frac{\rho_w}{\rho_c} + \frac{w}{c} + \frac{\rho_w V_{ea}}{c} + \frac{\rho_w \sum V_{agg}}{c} + \frac{\rho_w \sum V_{SCM}}{c}} \quad , \Gamma \geq \Gamma_0 \tag{3.14}$$

in which $C_{\eta\_S}^j$ is a material coefficient corresponding to the porosity type j.

The volumetric strain is determined experimentally, but can be neglected if drying takes place under sealed conditions, since it is relatively small (≈ 1300 μstrains for ordinary cement and ≈ 200 μstrains for ordinary concrete at ≈ 700 days from casting (Baroghel-Bouny, 1994)). $C_{\eta\_S}^j$, on the other hand, is obtained using the reaction stoichiometry and quantifies the amount of water excluded from the j type porosity at complete theoretical hydration:

$$C_{\eta\_S}^{cap} = \frac{\rho_w}{c} \sum_i \frac{w_i^{ult}}{\rho_i} \tag{3.15}$$

$$C_{\eta\_S}^{tot} = \frac{\rho_w}{c} \frac{w_{CBW}^{ult}}{\rho_{CBW}} \tag{3.16}$$

3.2.5 Rate of Heat Generation

In order to quantify the variation in time of the rate of heat generation, this thesis uses the definition of the hydration degree suggested by Schindler and Folliard (2005) and presented in equation (3.1):

Schindler and Folliard's general hydration model is employed in order to calculate the magnitude of several enthropy based physical properties. The model has a large applicability and is capable of predicting the in-place temperature variation of various cement types (including mixes that incorporate supplementary cementing materials like

fly ash (*FA*) and/or ground-granulated blast-furnace slag cement (*GGBF*)). The rate of heat generation develops according to the relationship:

$$Q_h = \frac{d\left(H(t)\right)}{dt} = \frac{d\left(H_{tot}\Gamma(t)\right)}{dt} = H_{tot}\dot{\Gamma} \tag{3.17}$$

where $\dot{\Gamma}$ represents the rate of the degree of hydration. In Schindler and Folliard's approach, the overall hydration degree function is obtained by fitting the experimental data recorded during the semi-adiabatic calorimetric probing of various cement types. Its expression has the form:

$$\Gamma(t) = \Gamma_{ult}\exp\left[-\left(\frac{\tau_{sf}}{f_{conv}\cdot t}\right)^{\beta_{sf}}\right] \tag{3.18}$$

where Γ_{ult} is the ultimate degree of hydration, τ_{sf} and β_{sf} are hydration time and shape parameters while f_{conv} is a conversion factor based on Arrhenius' rate theory and dependent upon temperature. Carino and Lew (2001) proposed the following relationship for this last term:

$$f_{conv}(T) = \exp\left[\frac{E}{R}\left(\frac{1}{T_r}-\frac{1}{T}\right)\right] \tag{3.19}$$

in which E is the activation energy of the reaction, T_r is the reference temperature equal to 294.1°K and T is the concrete temperature corresponding to the chronological time t. The formulae for the parameters τ_{sf}, β_{sf} and E, as well as the total heat of reaction H_{tot}, account for the fact that the cement is a multiphase material which undergoes more than one reaction during hydration. The effect of the chemical species is embodied in the forthcoming relationships by the weight ratio of component i in terms of total cement content denoted here by f_i. Using multivariate Regression Analysis, Schindler and Folliard (2005) obtained the following expressions for β_{sf} and τ_{sf}:

$$\beta_{sf} = 181.4\cdot f_{C_3A}^{0.146}\cdot f_{C_3S}^{0.227}\cdot B^{-0.535}\cdot f_{SO_3}^{0.558}\cdot\exp\left(-0.647\cdot f_{GGBF}\right) \tag{3.20}$$

$$\tau_{sf} = 66.78\cdot f_{C_3A}^{-0.154}\cdot f_{C_3S}^{-0.401}\cdot B^{-0.804}\cdot f_{SO_3}^{-0.758}\cdot\exp(2.187 f_{GGBF} + 9.5 f_{FA} f_{FA-CaO}) + \tau_{sf}^{SP} \tag{3.21}$$

where B is the specific surface area of the cement obtained with Blaine's method (m^2/kg) and τ_{sf}^{SP} is the hydration time parameter given in (3.22) which takes into account the effect of the superplasticizer (*SP*) by means of the retardation time Δ^{SP}:

$$\tau_{sf}^{SP} = \Delta^{SP}\left[-\ln\left(\frac{0.14\frac{w}{c}}{\Gamma_{ult}}\right)\right]^{\frac{1}{\beta_{sf}}} \tag{3.22}$$

The activation energy depends on the chemical composition and on the fineness of the mix:

$$E = 22100 \cdot \left[1 - 1.05 \cdot f_{FA} \cdot \left(1 - \frac{f_{FA-CaO}}{0.40}\right) + 0.40 \cdot f_{GGBF}\right] \cdot f_{C_3A}^{0.3} \cdot f_{C_4AF}^{0.25} \cdot B^{0.35} \tag{3.23}$$

Returning to the equation (3.17), the total heat of reaction at full hydration equals to:

$$H_{tot} = c\ \left[H_c \cdot f_{cement} + 461 \cdot f_{GGBF} + h_{FA} \cdot f_{FA}\right] \tag{3.24}$$

where c is the initial mass of cement per unit volume of material, h_{FA} is the heat of hydration of the fly ash and H_c represents the heat of hydration of cement at complete hydration. This last term takes into account the contribution of each clinker mineral and other oxides and is equal to:

$$H_c = 500 f_{C_3S} + 260 f_{C_2S} + 866 f_{C_3A} + 420 f_{C_4AF} + 624 f_{SO_3} + 1186 f_{freeCaO} + 850 f_{MgO} \tag{3.25}$$

Deriving (3.18) in terms of chronological time and using (3.17), (3.24) and (3.25), the expression for the rate of heat generation of an ordinary Portland cement ***without any additions*** becomes (Schindler and Folliard, 2005):

$$Q_h = c \cdot H_c \cdot f_{cement} \cdot \Gamma \cdot \left(\frac{\tau_{sf}}{t}\right)^{\beta_{sf}} \frac{\beta_{sf}}{t} \frac{1}{\left\{\exp\left[\frac{E}{R}\left(\frac{1}{T_r} - \frac{1}{T}\right)\right]\right\}^{\beta_{sf}}} \tag{3.26}$$

3.3 Moisture Flow

In cementitious materials the moisture flow comprises the transport of the water and vapour phases. Individual mass balance equations will be derived below for inclusion in the *THC* model. Moreover, the main transfer mechanisms will be highlighted and their mathematical representation, capable of simulating the autogenous healing of cement-based materials, will be provided.

3.3.1 Governing Differential Equation for Moisture Flow

For a given material phase (π) the generalised expression of the macroscopic volume averaged mass balance equation has the form (Lewis and Schrefler, 1998):

$$\frac{D^{\pi}\overline{\rho}_{\pi}}{Dt} + \overline{\rho}_{\pi} div\left(\overline{v}^{\pi}\right) = \dot{m}_{\pi} \tag{3.27}$$

where $\frac{D^{\pi}}{Dt}$ is the material time derivative with respect to phase π, $\overline{\rho}_{\pi}$ stands for the phase-averaged density, $\overline{v}^{\pi}$ is the mass-averaged velocity and $\dot{m}_{\pi}$ signifies the sink/source term accounting for phase change. The phase-averaged density represents the mass of phase π per volume of the entire porous medium and has the mathematical expression:

$$\overline{\rho}_{\pi} = \eta S_{\pi} \rho_{\pi} \tag{3.28}$$

in which η is the porosity, while S_{π} and ρ_{π} are the degree of saturation and the intrinsic phase averaged density, respectively. The vapour and the dry air are miscible (Dalton's law: $p_g = p_v + p_a$) and therefore it is commonly agreed that they share the same volume fraction ηS_g, S_g being the degree of saturation with respect to the gaseous phase (vapour + dry air). In the current thesis the approach adopted by de Morais et al. (2009) is used and therefore, the mass balance of the dry air is neglected. For the water vapour, equation (3.27) becomes:

$$\frac{D^{v}\overline{\rho}_{v}}{Dt} + \overline{\rho}_{v} div\left(\overline{v}^{v}\right) = \dot{m}_{v} \tag{3.29}$$

while for the liquid water phase the equation is:

$$\frac{D^{w}\overline{\rho}_{w}}{Dt} + \overline{\rho}_{w} div\left(\overline{v}^{w}\right) = \dot{m}_{w} \tag{3.30}$$

In order to account for the coexistence of dry air and vapour within the gas phase, the material time derivative $\frac{D^{v}\overline{\rho}_{v}}{Dt}$ changes into $\frac{D^{g}\overline{\rho}_{v}}{Dt}$ according to:

$$\frac{D^{g}\overline{\rho}_{v}}{Dt} = \frac{D^{v}\overline{\rho}_{v}}{Dt} + grad\left(\overline{\rho}_{v}\right)\overline{v}^{gv} \tag{3.31}$$

where $\overline{v}^{gv}$ is the relative velocity of phase v with respect to phase g. But $\overline{v}^{gv}$ can be decomposed into:

$$\overline{v}^{gv} = \overline{v}^{g} - \overline{v}^{v} = -\overline{v}^{vg} \tag{3.32}$$

$\overline{v}^{g}$ and $\overline{v}^{v}$ being the velocities of the phases g and v, respectively. Therefore, substituting (3.32) into (3.31) and (3.31) into (3.29), the mass conservation equation of the water vapour written with respect to the gaseous phase is:

$$\frac{D^{g}\overline{\rho}_{v}}{Dt} + \left[grad\left(\overline{\rho}_{v}\right)\overline{v}^{vg} + \overline{\rho}_{v} div\left(\overline{v}^{vg}\right)\right] + \overline{\rho}_{v} div\left(\overline{v}^{g}\right) = \dot{m}_{v} \tag{3.33}$$

Moreover, the above relationship can be further simplified as in (3.35) if the equality (3.34) is applied:

$$grad\left(\overline{\rho}_{v}\right)\overline{v}^{vg} + \overline{\rho}_{v} div\left(\overline{v}^{vg}\right) = div\left(\overline{\rho}_{v}\overline{v}^{vg}\right) \tag{3.34}$$

$$\frac{D^{g}\overline{\rho}_{v}}{Dt} + div\left(\overline{\rho}_{v}\overline{v}^{vg}\right) + \overline{\rho}_{v} div\left(\overline{v}^{g}\right) = \dot{m}_{v} \tag{3.35}$$

In order to solve the moisture flow problem and to implement it in a numerical model, it is necessary to write all the mass balance equations with respect to the same material phase. If the solid skeleton is chosen as the common reference, $\frac{D^{g}\overline{\rho}_{v}}{Dt}$ and $\frac{D^{w}\overline{\rho}_{w}}{Dt}$ are replaced by:

$$\frac{D^{g}\overline{\rho}_{v}}{Dt} = \frac{D^{s}\overline{\rho}_{v}}{Dt} - grad\left(\overline{\rho}_{v}\right)\overline{v}^{sg} \tag{3.36}$$

$$\frac{D^{w}\overline{\rho}_{w}}{Dt} = \frac{D^{s}\overline{\rho}_{w}}{Dt} - grad\left(\overline{\rho}_{w}\right)\overline{v}^{sw} \tag{3.37}$$

The relative velocities of the gas and water with respect to the solid skeleton ($\overline{v}^{sg}$ and $\overline{v}^{sw}$) can be dissociated in a similar manner as in (3.32). The resulting expressions of $\overline{v}^{w}$ and $\overline{v}^{g}$ are then substituted into equations (3.30) and (3.33), in which the relationships (3.36) and (3.37) are also introduced and the following equalities are obtained:

$$\frac{D^{s}\overline{\rho}_{v}}{Dt} + \overline{\rho}_{v} div\left(\overline{v}^{s}\right) - \left[grad\left(\overline{\rho}_{v}\right)\overline{v}^{sg} + \overline{\rho}_{v} div\left(\overline{v}^{sg}\right)\right] + div\left(\overline{\rho}_{v}\overline{v}^{vg}\right) = \dot{m}_{v} \tag{3.38}$$

$$\frac{D^{s}\overline{\rho}_{w}}{Dt} + \overline{\rho}_{w} div\left(\overline{v}^{s}\right) - \left[grad\left(\overline{\rho}_{w}\right)\overline{v}^{sw} + \overline{\rho}_{w} div\left(\overline{v}^{sw}\right)\right] = \dot{m}_{w} \tag{3.39}$$

Grouping the terms in the squared brackets according to a vector identity analogous to (3.34), the two mass balance equations finally become:

$$\frac{D^s\overline{\rho}_v}{Dt}+\overline{\rho}_v div\left(\overline{v}^s\right)+\underbrace{div\left(\overline{\rho}_v\overline{v}^{gs}\right)}_{\substack{ADVECTION\\FLUX}}+\underbrace{div\left(\overbrace{\overline{\rho}_v\overline{v}^{vg}}^{J_v^D}\right)}_{\substack{DIFFUSION\\FLUX}}=\dot{m}_v \tag{3.40}$$

$$\frac{D^s\overline{\rho}_w}{Dt}+\overline{\rho}_w div\left(\overline{v}^s\right)+\underbrace{div\left(\overbrace{\overline{\rho}_w\overline{v}^{ws}}^{J_w^A}\right)}_{\substack{ADVECTION\\FLUX}}=\dot{m}_w \tag{3.41}$$

Before employing this system of equations to examine the moisture flow in cementitious materials, it should be stated that the model uses the capillary water saturation degree, S_w^{cap}, as the hygral variable. The first consequence of this is that all the existing fluxes (diffusion and advection), expressed in (3.40) and (3.41), occur at the capillary pore level. In this context the precise formula of $\overline{\rho}_w$ becomes:

$$\overline{\rho}_w=\overline{\rho}_w^{cap}=\eta_{cap}S_w^{cap}\rho_w \tag{3.42}$$

The second implication concerns the physical meaning of the right hand side term in equations (3.40) and (3.41). While $\dot{m}_v$ represents the source of water vapour due to vaporisation, $\dot{m}_w$ accounts simultaneously for the depletion of the liquid phase due to evaporation ($\dot{m}_v$), hydration ($\dot{m}_w^{hyd}$) and water adsorption/desorption by the aggregate ($\dot{m}_w^{a/d\_agg}$) and for the water supply in the capillary pores due to the desorption of the gel network ($\dot{m}_w^{des}$):

$$\dot{m}_w=-\dot{m}_v-\dot{m}_w^{hyd}-\dot{m}_w^{a/d\_agg}+\dot{m}_w^{des} \tag{3.43}$$

Some clarification related to this last source term is needed at this point. During drying, the evaporation successively empties the capillary pores until the desiccation front reaches the gel interstices. In these circumstances, the mass balance equation (3.41) can no longer be applied because S_w^{cap} is null. Experimental evidence though, suggests that the phase change of water continues to manifest even beyond this moment (Scherer, 1990). The current thesis accounts for the ongoing desiccation by assuming that after a critical relative humidity level, RH_{cr}, estimated to be somewhere between 40-50% (Baroghel-Bouny, 2007; Jennings, 2008; Illston and Domone, 2010), both globular evaporable and chemically bound water, denoted here by $m_w^{gel\rightarrow cap}$, feed the capillary pores. The mass of supplied aqueous phase is:

$$m_w^{des} = \begin{cases} \dfrac{\partial m_w^{gel \to cap}}{\partial RH} & ,\forall RH \le RH_{cr} \\ 0 & ,\forall RH > RH_{cr} \end{cases} \tag{3.44}$$

where the expression of $m_w^{gel \to cap}$ derives from the definition of the water content, wc, given by Baroghel-Bouny et al. (1999):

$$m_w^{gel \to cap} = m_{dry} \cdot wc = m_{dry} \cdot \eta_{cap} \frac{\rho_w}{\rho_{dry}} S_w^{cap} \tag{3.45}$$

In the above relationship m_{dry} stands for the mass of the dry sample, ρ_{dry} is the ratio between m_{dry} and the total volume of the paste and S_w^{cap} is a sorption isotherm obtained by fitting experimental measurements (see equation (3.66)). Using these terms, the rate of water intake by the capillary network may be expressed as:

$$\dot{m}_w^{des} = \begin{cases} \dfrac{\partial m_w^{des}}{\partial S_w^{cap}} \dot{S}_w^{cap} & ,\forall RH \le RH_{cr} \\ 0 & ,\forall RH > RH_{cr} \end{cases} \tag{3.46}$$

Considering now the water consumed by the hydration process, its rate equals the product of the ultimate quantity of the gel water (computed using the stoichiometric model) and the time derivative of the degree of hydration:

$$\begin{gathered} \dot{m}_w^{hyd} = \sum_i \left(w_i^{ult} \right) \dot{\Gamma} \\ i \in \left\{ SGP,\, AW + ILW + IGW,\, CBW \right\} \end{gathered} \tag{3.47}$$

The rate of absorption/desorption by the aggregate is a sink/source term that accounts for the transport of liquid water towards and from the pores of the aggregate during drying. Often, aggregates used in concretes are in an air-dry state and have interstices comparable to – or larger than – those found in *C-S-H* gels (Neville and Brooks, 1987). This means in theory that, depending on the level of the relative humidity reached in the proximity of the aggregate particle, bulk water can be absorbed from and subsequently expelled into the capillary network (Buenfeld and Okundi, 1999). However, after a few hours, the hydrated cement paste creates a protective layer of gel products on the surface of the aggregate and hinders the further transport of water (Neville and Brooks, 1987; Verbeck and Landgren, 1960). In general, the coarse aggregate is significantly more absorbent than the sand (fine aggregate), particularly if crushed limestone is used. In this thesis, an experimental procedure, described in Chapter 5, was carried on in order to evaluate $\dot{m}_w^{a/d\_agg}$.

3.3.2 Mechanisms of Liquid Water Flow

Having defined the governing moisture mass conservation equations, the thesis will now move on to detail the mathematical expressions used for the dominant mechanisms facilitating the movement of the aqueous phase within the porous medium. The velocity of the water with respect to the solid phase obeys Darcy's law and is proportional to the hydraulic permeability k_w and to the gradient of the total water potential ψ_t^w:

$$\bar{v}^{ws} = -\frac{k_w}{\eta_{cap} S_w^{cap}} \nabla \psi_t^w \tag{3.48}$$

Among the mechanisms capable of generating the transfer of water from one point to the other, the matric and gravitational potentials, ψ_m^w and ψ_G, are dominant. Thus:

$$\psi_t^w = \psi_m^w + \psi_G \tag{3.49}$$

According to Sedighi (2011), the matric potential encompasses in its meaning the capillary action together with the absorption effect exerted on the water molecules by the London-van der Walls forces and the chemical binding process. As long as there exists a continuous wetting fluid, the matric potential equals the water pressure p_w. If the interstices of the porous medium are partially filled by water, a difference in pressure develops across the interface separating the gas and the liquid:

$$p_c = p_a - p_w \tag{3.50}$$

where p_c and p_a are the capillary and the air pressures. An equilibrium relation given by Kelvin's law exists between the capillary water and the water vapour:

$$-\frac{p_c}{\rho_w}\frac{M_w}{RT} = \ln\left(\frac{p_v}{p_v^{sat}}\right) = \ln(RH) \tag{3.51}$$

in which M_w is the molar mass of liquid water, p_v represents the water vapour pressure, p_v^{sat} is the water vapour saturation pressure and RH is the relative humidity. The variation of p_v^{sat} follows Antoine's equation and depends solely on temperature:

$$p_v^{sat}(T) = 10^{b_1 - \frac{b_2}{b_3 + T}} \tag{3.52}$$

where b_1, b_2 and b_3 are material parameters. Hence, in funicular saturation state, the matric potential is described by:

$$\psi_m^w = p_w = p_g - p_c \tag{3.53}$$

However, in the case of pendular state, there is just a very thin film of H_2O molecules surrounding the cement grains and the amount of both vapour and dry air overrides the amount of the liquid phase. The water and capillary pressures are meaningless from the physical point of view. The matric potential is obtained in these circumstances after integrating the differential of the Gibbs function for vapour from p_v^{sat} to p_v (Lewis and Schrefler, 1998):

$$\psi_m^w = \left(\frac{M_w}{RT}\right)^{-1} \ln\left(\frac{p_v}{p_v^{sat}}\right) \tag{3.54}$$

This matric potential, if multiplied by $-\rho_w$, equals to the expression of p_c derived from the equation (3.51). In (Gawin et al. 2006a) the capillary pressure is redefined according to the above observation and the relationship presented in (3.55) is employed along the whole moisture content range.

$$p_c = -\rho_w \left(\frac{M_w}{RT}\right)^{-1} \ln\left(\frac{p_v}{p_v^{sat}}\right) = -\rho_w \left(\frac{M_w}{RT}\right)^{-1} \ln(RH) \tag{3.55}$$

The water density (ρ_w) is temperature dependent and is assumed to obey the Thiesen-Scheel-Diesselhorst equation (McCutcheon et al., 1993):

$$\rho_w(T) = 1000 \cdot \left[1 - \frac{(T + 288.9414)}{508929.2(T + 68.12963)}(T - 3.9863)^2\right] \tag{3.56}$$

The second mechanism producing liquid movement has a smaller impact in comparison with the matric potential and, as a result, some researchers simply ignore it (Baroghel-Bouny et al., 2011; de Morais et al., 2009). However, in the proposed analysis the gravitational potential is taken into account.

$$\psi_G = \rho_w \boldsymbol{g} \tag{3.57}$$

In which $\boldsymbol{g}$ is the gravitational acceleration.

The formulae for the other terms in equation (3.48), that have not been defined so far, are given in the following paragraphs. Numerical investigations such as those conducted by de Morais et al. (2009), Gawin et al. (2011a), Baroghel-Bouny et al.

(2011) and Koniorczyk (2012) have shown that the hydraulic permeability is proportional to the intrinsic (k_{iw}) and the relative permeability (k_{rw}) of the liquid and inverse proportional to the aqueous viscosity, μ_w:

$$k_w = \frac{k_{iw} k_{rw}}{\mu_w} \tag{3.58}$$

In this thesis k_{iw} is obtained by superposing the relationships reported in (Gawin et al., 1999, 2006a) and is dependent upon both hydration degree and temperature as it is illustrated in Figure 3.2. The formula (3.59), adopted in here, accounts for the effect of the intrinsic permeability of the matured paste k_{iw}^0, for the reference temperature T_{ref} = 273.15 °K, for the atmospheric pressure p_{atm} and for the material constants A_k, A_Γ and A_p. It can be seen that during a normal positive temperature range (T<373.15°K), k_{iw} may vary up to 2 orders of magnitude throughout the hydration process.

$$k_{iw} = k_{iw}^0 10^{A_k (T - T_{ref}) + A_\Gamma (1-\Gamma)} \left(\frac{p_g}{p_{atm}} \right)^{A_p} \tag{3.59}$$

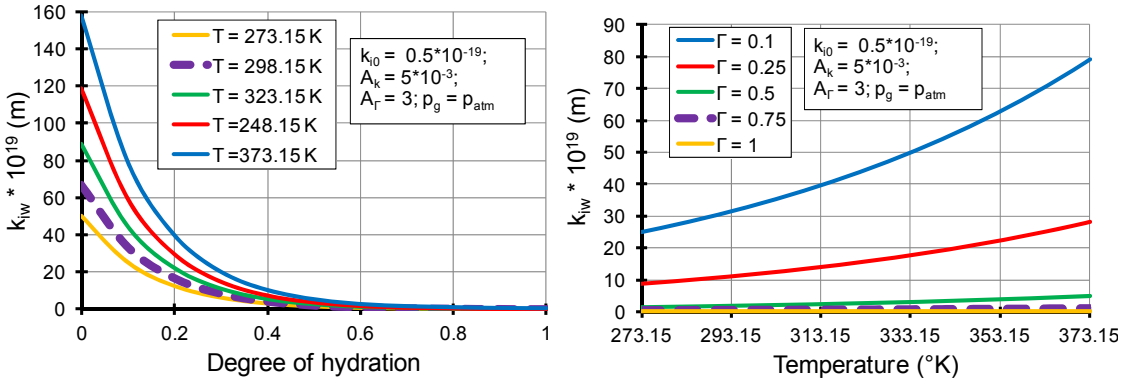

Figure 3.2 Variation of k_{iw} with (a) degree of hydration and (b) temperature

Concerning the relative permeability with respect to the water phase, a number of numerical expressions have been given in the literature. Among these are: the formula given by Mualem's model valid for both adsorption and desorption processes (Baroghel-Bouny et al., 2011), the formula based on the irreducible saturation (Gawin et al., 1999) and the overall permeability function advanced in the Generalised Effective Media approach that considers the contribution of the cracks (Bary et al., 2012). The relationship employed in the current work uses the reactive transport models for cementitious materials and was originally proposed by van Genuchten (Koniorczyk, 2012; de Morais et al., 2009; Gawin et al., 2008):

$$k_{rw} = \sqrt{S_w^{cap}} \left\{ 1 - \left[1 - \left(S_w^{cap} \right)^{\frac{1}{m}} \right]^m \right\}^2 \tag{3.60}$$

where m is a material constant. The variation of the relative water permeability with the capillary water saturation degree is plotted in Figure 3.3 (a).

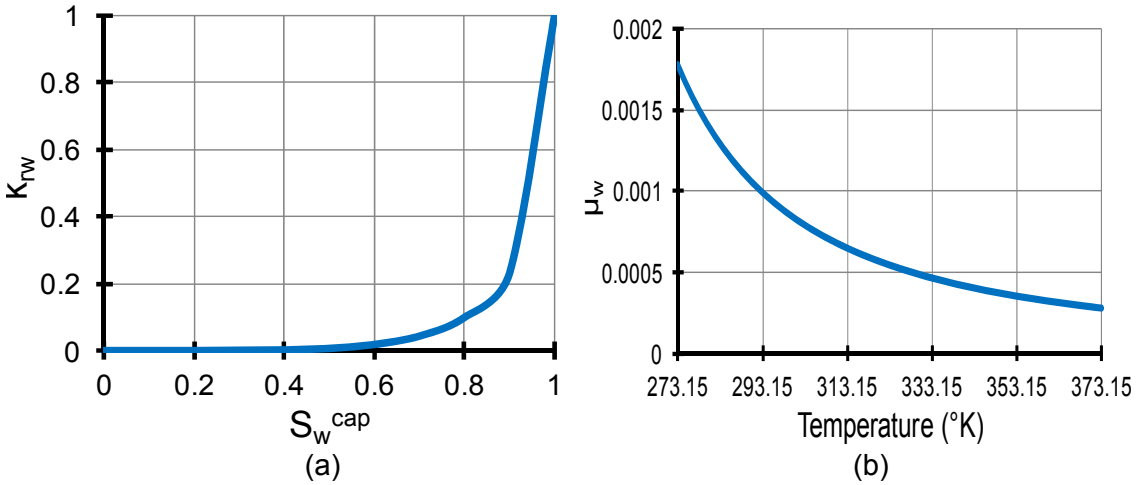

Figure 3.3 Variation of (a) k_{rw} and (b) μ_w

Last but not least, the magnitude of the viscosity of the pore liquid is generally agreed to vary both with temperature and concentration of the solute. Koniorczyk and Gawin (2008) suggested equation (3.61) when studying the influence of NaCl on moisture and energy transfer, whilst Baroghel-Bouny et al. (2011) adopted the extended Jones-Dole equation from (3.62) to analyse the isothermal coupled moisture–ion transport in cementitious materials:

$$\mu_w(T,\omega) = \mu_w^{pure}(T) \cdot \left(1 + A_1\omega - A_2\omega^2 + A_3\omega^3\right) \tag{3.61}$$

$$\mu_w(T,\omega) = \mu_w^{pure}(T) \cdot \left(1 - B_1\omega^{\frac{1}{2}} + B_2\omega - B_3\omega^{\frac{3}{2}} + B_4\omega^2\right) \tag{3.62}$$

In these two relationships, ω represents the concentration of the solute (kg salt / kg solution), the parameters A_1, A_2, A_3 and B_1, B_2, B_3, B_4 stand for material constants, while the function $\mu_w^{pure}(T)$ describes the change of viscosity of pure water with temperature. The latter term has been identified as the major contributing factor for the evolution of μ_w in the early age of cement hydration. Therefore, in the current numerical simulation, which is focused on the autogenous healing phenomenon, the formula used by Gawin et al. (1999), depicted in Figure 3.3 (b) and valid for 273 < T < 373°K, is employed:

$$\mu_w(T) = \mu_w^{pure}(T) = 0.6612 \cdot (T - 229)^{-1.562} \tag{3.63}$$

Summarising all the above information, the specific discharge due to the advection of the water phase can be replaced in the mass balance equation in the form:

$$\bar{v}^{ws} = -\frac{1}{\eta_{cap} S_w^{cap}} \frac{k_w k_{rw}}{\mu_w} \left(\nabla p_w + \rho_w \boldsymbol{g} \right) = -\frac{1}{\eta_{cap} S_w^{cap}} \frac{k_w k_{rw}}{\mu_w} \left(\nabla p_g - \nabla p_c + \rho_w \boldsymbol{g} \right) \quad (3.64)$$

Before passing to the next section it must be also noted that a relationship between the two hygric parameters S_w^{cap} and p_c is needed in order to solve the mass balance equations from section 3.3.1. At present however, there is no purely analytical formula to describe such relationship and instead experimental data are used to develop the so called 'capillary curves'. The disadvantage with cement-based materials is that because of their weak permeability, the capillary curve cannot be obtained directly via drainage or suction as for rocks and sands. Baroghel-Bouny et al. (1999) carried out an alternative experimental procedure which led to a 'sorption curve' expressed in terms of weight loss versus relative humidity. Desorption tests on 1.5 year old ordinary concrete and cement paste specimens were performed and an s-shaped function was proposed based on the derivations of Van Genuchten (1980):

$$p_c\left(S_w\right) = a\left[\left(\frac{1}{S_w}\right)^b - 1\right]^{\frac{b-1}{b}}, \; b = \frac{1}{m} \quad (3.65)$$

The curve relates the total liquid water saturation to the capillary pressure and was derived using mature concrete samples in which the hydration reactions were effectively complete. This means that during the early age drying, when the porous network has not yet stabilised, the above capillary curve needs to be adjusted in order to give a realistic estimation. In the current thesis, the function ϖ takes into consideration the impact of porosity development upon the capillary curve. Thus, the equation (3.65) is modified into:

$$p_c\left(S_w, T, \Gamma\right) = \varpi\left(\Gamma\right) a \frac{\gamma\left(T\right)}{\gamma\left(T_0\right)} \left[\left(\frac{1}{S_w^{cap}}\right)^b - 1\right]^{\frac{b-1}{b}} \quad (3.66)$$

that also accounts for the effect of temperature upon the capillary curve (Edlefsen and Andersen, 1943; Cleall, 1998). The expressions of γ is:

$$\gamma\left(T\right) = 0.1171 - 0.00001516 \cdot T \quad (3.67)$$

whilst ϖ is equal to:

$$\varpi(\Gamma) = \left(\frac{\eta_{cap}(\Gamma)}{\eta_{cap}(\Gamma_{ult})} \right)^{c_\eta} \tag{3.68}$$

c_η being a material parameter.

The early-age properties of the desorption tests are difficult to measure and there is no available experimental evidence to validate equation (3.66). However, this relationship is comparable to the capillary curve proposed by Sciumè et al. (2013), which is also dependent on the hydration degree. Therefore it was decided to use (3.66) in the *TH* component in the self-healing model.

The validity of the capillary curve for the whole moisture spectrum is another point of debate. During the hygroscopic moisture range there is enough water in the pores to have a liquid-gas interface and therefore to have a real capillary pressure. But the evaporation triggered by the decrease of vapour pressure successively empties the pores until the desiccation front reaches very small voids filled with an insufficient number of water molecules to create a meniscus. This stage corresponds to the critical gel point (RH_{cr}), which represents the moment when the gel water begins to be expelled from the gel pores. At this *RH* level the physical meaning of capillary pressure, and implicitly the applicability of the capillary curve, is questionable. However, experimental evidence suggests that the phase change of water continues to manifest even after this point and Gawin et al. (2006a) propose that a water potential, similar in form to that used for the capillary pressure, controls further desiccation. In this thesis it is acknowledged the fact that other drying mechanisms become operational below a certain moisture limit, but it is considered that on the basis of the work of Powers and Brownyard (1948), Feldman (1973) and Jennings (2008) it is justify the use of a capillary curve below the critical *RH* level. In brief, it is assumed that when water starts to be removed from the gel pores, it does not immediately change phase, but feeds the capillary network with liquid water and thus maintains the liquid-gas interface.

3.3.3 Mechanisms of Water Vapour Flow

The relationship (3.40) describing the conservation equation of the water vapour accounts for the transfer of the gaseous phase that occurs by both advection and diffusion. The transport due to the bulk motion of this fluid is sustained by the matric potential, written below as a product of the permeability of the porous medium with respect to the gaseous phase, k_g and the gas pressure gradient ∇p_g:

$$\bar{v}^{gs} = -k_g \nabla p_g \tag{3.69}$$

In the current thesis it is assumed that the combined dry-air vapour mix is always at atmospheric pressure ($p_g = p_{atm}$) and vapour diffuses through the gas phase. Gardner et al. (2008) have found that the time to reach steady state of the gas flow is relatively short and would be negligible in comparison with the time scale of drying shrinkage. In the absence of rapidly changing temperature gradients, they consider that the current assumption is valid and thus the $\bar{v}^{gs}$ term is neglected in equation (3.40).

The diffusive flow, on the other hand, is assumed to obey Fick's law (de Morais et al., 2009):

$$\bar{v}^{vg} = -\frac{1}{\eta_{cap} S_g} \rho_g \frac{M_a M_w}{\left(M_g\right)^2} D_{eff} \nabla\left(\frac{p_v}{p_g}\right) \tag{3.70}$$

where M_a, M_w and M_g are the molar mass of dry air, liquid water and gas and D_{eff} denotes the effective diffusion coefficient. This expression can be simplified as follows if it is assumed that $M_a = M_g$ and if ρ_g is written in terms of p_g via the ideal gas law:

$$\bar{v}^{vg} = -\frac{1}{\eta_{cap} S_g} p_g \frac{M_w}{RT} D_{eff} \nabla\left(\frac{p_v}{p_g}\right) \tag{3.71}$$

The movement of the vapour species is intimately linked to the development of the internal structure of the paste, as can be easily seen in the formula for the effective diffusion coefficient (Gawin et al., 2011):

$$D_{eff} = \eta_{cap} \left(S_g\right)^{A_v} f_s D_{v0} \left(\frac{T}{T_{ref}}\right)^{B_v} \left(\frac{p_{atm}}{p_g}\right) \tag{3.72}$$

In the above relationship A_v and B_v are material constants, f_s represents the structure coefficient accounting for the Knudsen effect that considers the number of collisions of the H_2O molecules with the solid skeleton and D_{v0} is the diffusion coefficient of the water vapour in the air at reference temperature and pressure. It is evident from Figure 3.4 that D_{eff} increases with temperature and reduces with the saturation of the porous network.

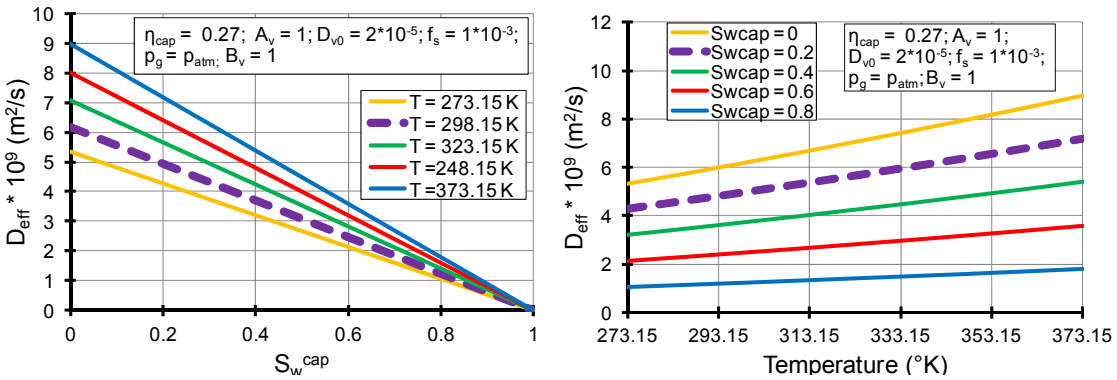

Figure 3.4 Variation of D_{eff} with (a) S_w^{cap} and (b) temperature

3.4 Reactive Transport

The autogenous healing of cementitious materials during the first few months is caused by the continuous hydration of the unreacted clinker (Jacobsen et al., 1995; Granger et al., 2007). The cement grains dissociate in the presence of pore water and release various ions that are transported and accumulate inside the porous medium. When the concentration of these electrically charged particles reaches a supersaturation state, a chemical reaction takes place and the new hydrates start to crystallise filling the existing voids. In a cement-based material, the amount of a chemical species in the pore solution can be traced spatially and temporally via a mass balance equation written in terms of the solute under consideration:

$$\frac{D^{\omega}\overline{\rho}_{\omega}}{Dt} + \overline{\rho}_{\omega} div\left(\overline{v}^{\omega}\right) = -\dot{m}_{\omega} \tag{3.73}$$

In this case, the phase-averaged density ($\overline{\rho}_{\omega}$) refers to the dissociated ions and is equal to $\omega\eta_{cap}S_w^{cap}\rho_w$ where ω represents the mass of unreacted cement per mass of solution in the capillary pores. The other undefined terms, $\overline{v}^{\omega}$ and $\dot{m}_{\omega}$, stand for the velocity of the solute and for the sink/source term integrating all the chemical processes occurring within the capillary network. By successively changing the material derivative ($\omega \rightarrow w \rightarrow s$), (3.73) becomes:

$$\frac{D^{s}\overline{\rho}_{\omega}}{Dt} + \overline{\rho}_{\omega} div\left(\overline{v}^{s}\right) + \underbrace{div\left(\overline{\rho}_{\omega}\overline{v}^{ws}\right)}_{\substack{ADVECTION\\FLUX}} + \underbrace{div\left(\overline{\rho}_{\omega}\overline{v}^{\omega w}\right)}_{\substack{DIFFUSION\ -DISPERSION\\FLUX}} = -\dot{m}_{\omega} \tag{3.74}$$

The first transport mechanism appearing in the above relationship is similar to the bulk movement of the water phase because it is driven by the relative velocity of the liquid

with respect to the solid skeleton. Therefore, the constitutive laws mentioned in section 3.3.2 remain valid even for the advective flow of the unhydrated cement grains.

The second transport mechanism describes two distinct types of movement driven by the gradient of concentration ω and mathematically described by the extended linear Fick's law (Koniorczyk, 2012):

$$\overline{\rho}_{\omega}\overline{v}^{\omega w} = J_{\omega}^{DD} = -\rho_{w}\left(D_{mdisp}^{ij} + D_{mdiff}^{ij}\right)\nabla\omega \tag{3.75}$$

D_{mdisp}^{ij} is a diffusion function that accounts for the mechanical and molecular hydraulic dispersion that enables the movement of chemical particles under a concentration difference and is dependent upon the longitudinal and transversal dispersion coefficients, α_L and α_T (Bear and Bachmat, 1991):

$$D_{mdisp}^{ij} = \alpha_T\left|\overline{v}^{ws}\right|\delta_{ij} + \frac{\overline{v}_i^{ws}\overline{v}_j^{ws}}{\left|\overline{v}^{ws}\right|}\left(\alpha_L - \alpha_T\right) \quad , \delta_{ij} = \begin{cases} 1, & i = j \\ 0 & i \neq j \end{cases} \tag{3.76}$$

Defined by Koniorczyk (2010) as "the effect of the microscopic variations of velocity near the considered point", the molecular diffusion D_{mdiff}^{ij} has the formula:

$$D_{mdiff}^{ij} = \eta_{cap}S_w^{cap}D_{mol}\delta_{ij} \quad , \delta_{ij} = \begin{cases} 1, & i = j \\ 0 & i \neq j \end{cases} \tag{3.77}$$

in which D_{mol} is the molecular diffusion coefficient.

In the proposed model the sink/source term in equation (3.74) accounts mainly for the precipitation of *C-S-H* gel. In essence, this process is analogous to other numerical chemical transformations found in the literature that simulate either the salt crystallisation (Koniorczyk, 2010; Koniorczyk, 2012), the salt ingress (Baroghel-Bouny et al., 2011), the alkali-silica reaction (Pesavento et al., 2012) or the leaching of Ca^{2+} ions (Gawin et al., 2008). Therefore, it was decided in the current thesis to adapt these existing theories for the formation of the filling hydrates. The precipitates that result during autogenous healing develop in the empty spaces according to a Freundlich type isotherm which assumes thermodynamic equilibrium between the dissolved and the crystallised material:

$$m_{\omega} = \underbrace{\left(\alpha_P S_w^{cap}\omega^{\beta_P}\right)}_{Freundlich}\rho_w\eta_{cap} \tag{3.78}$$

In the above formula, α_P is a parameter that depends on the binder composition and β_P is the order of the process. The sink/source term $\dot{m}_\omega$ is therefore the derivative of the equation (3.78).

3.5 Heat Transfer

The thermal effect is coupled to the hygric flow by adding a macroscopic energy balance equation to the algebraic system composed of equations (3.40) and (3.41). Conventionally, for the phase π of a cementitious paste, the governing relationship describing the heat flow reads (Lewis and Schrefler, 1998):

$$\overline{\rho}_\pi C_p^\pi \frac{D^\pi T^\pi}{Dt} = \rho_\pi h^\pi + \rho_\pi R_H^\pi - div\left(\overline{q}^\pi\right) - \left[\sum_l \left(\dot{m}_l H_l\right)\right]_\pi \tag{3.79}$$

where $\overline{\rho}_\pi C_p^\pi$, T^π and $\overline{q}^\pi$ represent the heat capacity, the temperature and the heat flux of the considered phase, $\rho_\pi R_H^\pi$ is the exchange of energy due to phase conversion and mechanical interactions, $\rho_\pi h^\pi$ denotes the heat source term and $\left[\sum_l \left(\dot{m}_l H_l\right)\right]_\pi$ is the exchange term accounting for the latent heat of evaporation and chemical interactions. The heat flux is described by Fourier's law:

$$\overline{q}^\pi = -\lambda_T^\pi \nabla\left(T^\pi\right) \tag{3.80}$$

in which λ_T^π is the effective thermal conductivity of phase π.

By means of a procedure resembling the algorithm utilized for the mass balance equations of moisture, equation (3.79) will be formulated in terms of the derivative of the solid phase. Furthermore, since the model assumes that all the material phases are in thermodynamic equilibrium, their corresponding temperatures are all equal to T. Hence, the individual entropy equilibrium equations become:

$$\overline{\rho}_s C_p^s \frac{D^s T}{Dt} = \rho_s h^s + \rho_s R_H^s - div\left(-\lambda_T^s \nabla T\right) - \left[\sum_l \left(\dot{m}_l H_l\right)\right]_s \tag{3.81}$$

$$\overline{\rho}_w C_p^w \left[\frac{D^s T}{Dt} + v^{ws} \nabla T\right] = \rho_w h^w + \rho_w R_H^w - div\left(-\lambda_T^w \nabla T\right) - \left[\sum_l \left(\dot{m}_l H_l\right)\right]_w \tag{3.82}$$

$$\overline{\rho}_g C_p^g \left[\frac{D^s T}{Dt} + v^{gs} \nabla T \right] = \rho_g h^g + \rho_g R_H^g - div\left(-\lambda_T^g \nabla T\right) - \left[\sum_l \left(\dot{m}_l H_l \right) \right]_g \tag{3.83}$$

But, as in geomechanics, the heat source terms, $\rho_\pi h^\pi$, are ignored and the total balance of energy exchange between all the phases, $\sum_\pi \left(\rho_\pi R_H^\pi \right)$ is null (Lewis and Schrefler, 1998). Hence, adding (3.81), (3.82) and (3.83), the heat transfer equation for the entire porous medium which considers a reactive transport reads:

$$\overline{\rho C}_p \frac{D^s T}{Dt} + \underbrace{\left(\overline{\rho}_w C_p^w v^{ws} + \overline{\rho}_g C_p^g v^{gs} \right) \nabla T}_{\substack{CONVECTIVE \\ HEAT}} = \underbrace{div\left(\lambda_T^{eff} \nabla T \right)}_{\substack{CONDUCTIVE \\ HEAT}} - \left(\dot{m}_v \Delta H_v + \dot{m}_P \Delta H_P + \dot{m}_h \Delta H_h \right) \tag{3.84}$$

where $\overline{\rho C}_p = \sum_\pi \left(\overline{\rho}_\pi C_p^\pi \right)$ stands for the heat storage capacity of the porous medium, $\lambda_T^{eff} = \sum_\pi \lambda_T^\pi$ represents the effective thermal conductivity of the moist material, ΔH_v, ΔH_P and ΔH_h are the heat of evaporation, precipitation and hydration, respectively, while $\dot{m}_v$, $\dot{m}_P$ and $\dot{m}_h$ are the mass rates of evaporated water, precipitates and hydrated material, respectively. Some remarks are needed at this point. Firstly, de Morais et al. (2009) and Bary et al. (2012) considered that the energy transfer enabled by the bulk movement of the fluids can be neglected. Secondly, when simulating the autogenous healing, the precipitated material coincides with the hydrates and implicitly the heat of hydration matches the heat of precipitations. Thus, equation (3.84) simplifies into:

$$\overline{\rho C}_p \frac{D^s T}{Dt} - div\left(\underbrace{\lambda_T^{eff} \nabla T}_{J_T^{CD}} \right) + \left(\dot{m}_v \Delta H_v + Q_h \right) = 0 \tag{3.85}$$

where Q_h, defined earlier in (3.26), is the heat release accounting for the combined precipitation and hydration processes.

As stated previously, in this work the author has considered the reactive transport of cementitious materials and accounted for the distinct physical properties of all the water forms translated mainly in different density values. Thus the following expression of the thermal storage capacity was used:

$$\begin{aligned} \overline{\rho C}_p = {} & \left(1 - \eta_{tot}\right) \rho_s C_p^s + \eta_{cap} S_w^{cap} \rho_w C_p^w + \eta_c S_g \rho_v \left(C_p^v - C_p^a \right) + \\ & + \eta_{cap} S_g \rho_a C_p^a + w_{cw}^{ult} \Gamma C_p^{cw} + \eta_{tot} S_P \rho_P C_p^P \end{aligned} \tag{3.86}$$

where ρ_s and C_p^s are the density and specific heat capacity of the solids, w_{cw}^{ult} and C_p^{cw} are the mass of combined water phases (*SGP* + *AW* + *ILW* +*IGW* + *CBW*) per unit volume of the paste at the end of hydration and its corresponding heat capacity, while ρ_p and C_p^P are the density and specific heat capacity of the precipitated material. In the case of a concrete mix, the properties of the solid obey the adjusted law of mixtures as given by Bentz (2007):

$$C_p^s = C_p^{concr} = \sum_i \left(C_p^i f_i \right) \tag{3.87}$$

where f_i denotes the mass fraction of the component i (c = cement, $fagg$ = fine aggregate, $cagg$ = coarse aggregate, $GGBF$ = ground-granulated blast-furnace slag, FA = fly ash and SP = superplasticizer). A comparable relationship, based on the masses per unit volume and the volumes of each component, is applied to compute ρ_s

$$\rho_s = \frac{c + w_{fagg} + w_{cagg}}{V_c + V_{fagg} + V_{cagg}} \tag{3.88}$$

Regarding the effective thermal conductivity of a completely desaturated material, Harmathy (1970) states that, in normal conditions, it varies linearly with temperature. Gawin et al. (1999) propose the following thermal dependency:

$$\lambda_{dry}^{eff} = \lambda_{T_0} \left[1 + A_\lambda \left(T - T_{ref} \right) \right] \tag{3.89}$$

in which λ_{T_0} is the effective thermal conductivity at reference temperature and A_λ is a material parameter. At the same time, the effective thermal conductivity in a system with fluctuant moisture content is equal to:

$$\lambda_T^{eff} = \lambda_{dry}^{eff} \left[1 + \frac{4 M_l}{M_s} \right] \tag{3.90}$$

where M_l is the mass of the total liquid phase and M_s is the mass of the dry solid (unreacted cement and precipitated material):

$$M_l = \eta_{tot} \rho_w^{tot} S_w^{tot} \tag{3.91}$$

$$M_s = \left(1 - \eta_{tot} \right) \rho_s \tag{3.92}$$

In the above two relationships, ρ_w^{tot} represents the intrinsic phase-averaged total water density obtained from equation (3.93), that considers the contribution of all the water forms, while S_w^{tot} is the total saturation degree calculated with relation (3.94).

$$\rho_w^{tot} = \left\{ \frac{\Gamma \sum_i \frac{w_i^{ult}}{\rho_i} + (1-\Gamma) \cdot \sum_j \frac{w_j^{ult}}{\rho_j}}{\Gamma \sum_i w_i^{ult} + (1-\Gamma) \sum_j w_j^{ult}} \right\}^{-1} \qquad \begin{matrix} i \in \{SGP,\, AW + ILW + IGW,\, LGP\} \\ j = CW \end{matrix} \tag{3.93}$$

$$S_w^{tot} = \frac{\eta_{cap}}{\eta_{tot}} S_w^{cap} + \frac{\Gamma \cdot \sum_i V_i}{\eta_{ott} V_{mix}} \qquad i \in \{SGP, AW + ILW + IGW\} \tag{3.94}$$

Finally, it is noted that the phase change in enthalpy due to vaporisation manifests below the critical temperature of water, T_{cr} = 647.3°K and is a result of the difference between the specific enthalpies of vapour and liquid water. The Watson formula provided in (Gawin et al., 2011a) describes its evolution:

$$\Delta H_v = H_v - H_w = \begin{cases} 2.672 \cdot 10^5 \left(T - T_{cr}\right)^{0.38} & ,T < T_{cr} \\ 0 & ,T \geq T_{cr} \end{cases} \tag{3.95}$$

3.6 Summary

The purpose of the present chapter was to give the underlying scientific principles behind the thermo-hygro-chemical model for the autogenous healing of cement-based materials. The governing equations largely follow those given in the theoretical formulations of *THM* models (Lewis and Schrefler, 1998; Gawin et al., 2006; de Morais et al., 2009), but focus on the transfer within the capillary network. The hygric variable encountered in the mass balance equation of the liquid phase is the capillary water saturation degree and the phase changes are assumed to occur exclusively inside the capillary pores. This implies that the sink/source term embodies, in addition, the water absorption of the aggregate from the capillary network and the water release from the gel pores into the capillary interstices at low relative humidities. In terms of entropy balance, the rate of the released total heat is computed from the hydration model proposed by Schindler and Folliard (2005), in which the hydration degree depends on temperature according to the Arrhenius' rate theory. Schindler and Folliard's model captures the change in the chemical composition of the cement and it is adjusted here to allow for the presence of the superplasticizers.

One of the main contributions of this chapter is the stoichiometric algorithm based on the colloid model proposed by Jennings (2008), that is incorporated in order to estimate the porosity function as well as the ultimate degree of hydration. This formulation accounts for the three main stages of the hydration reaction mentioned by Fujii and Kondo (1974) and Bernard et al. (2003) and evaluates the water forms existing within the voids of the cement paste considering the interaction between the clinker phases and the intermediate hydrates. The proposed expression for the porosity comprises two components. The first accounts for the plastic behaviour of the cement paste during the time interval limited by the percolation hydration degree and thereupon leads to a constant and close to 1 value of the water saturation degree. The second component complies with the traditional models for porosity evaluation and employs predominantly the data of the stoichiometric algorithm.

The proposed *THC* model accounts for the reactive transport occurring during the autogenous healing of the cementitious materials. An individual mass balance equation considering the transport of solute and the crystallisation of hydrates was added to the algebraic system. The transfer of a generic solute that comprises a number of electrically charged particles takes place by advection, diffusion and dispersion. The sink/source term, which represents the chemical reactions, is based on a Freundlich type isotherm that establishes a thermodynamic balance between the reactants and the precipitates. In the present analysis, the self-healing phenomenon affects the porosity function due to the production of the filling material. Implicitly flow parameters such as hydraulic conductivity, diffusion and dispersion coefficients as well as the heat storage capacity change because of the crack recovery.

Chapter 4. Numerical Formulation

4.1 Introduction

Having defined in the previous chapter the differential equations describing the transport mechanisms in cement-based materials and the laws governing the physical and chemical processes occurring during autogenous healing, the author will now move on to discuss the numerical procedure that gives the solution of the derived system of equations. The numerical methods employed for simulating the transport of heat, moisture and solute in porous media was dealt with in several investigations including Lewis and Schrefler (1998), Gawin et al. (2006b) and Koniorczyk (2012). The literature provides two main computational techniques which can be classified as uncoupled and coupled solutions. The first, cited by Lewis and Schrefler (1998) in the case of surface subsidence analysis, reduces the model complexity by solving separately the governing equations. In contrast, the coupled procedures are suited for modelling a situation in which none of the fields can be solved separately and none of the variables can be eliminated (Zienkiewicz and Chan, 1989). Because of the strong interaction between humidity, temperature and crack recovery, the latter approach is selected in the current investigation and is detailed in this chapter.

A spatial discretisation, by means of the finite element method (*FEM*), is used to solve the non-linear system, while time discretisation, achieved using the finite difference technique, estimates the time derivatives. Section 4.2 sets the boundary value problem pertinent to the autogenous healing of cement and introduces the basic concepts behind the *FEM*. Section 4.3 deals with the numerical technique that provides the temporal discretisation. In this part of the chapter, a Newton-Raphson incremental iterative scheme for solving the nonlinear system of equations is described. Finally, section 4.4 highlights some important information related to the selected numerical formulations.

4.2 Spatial Discretisation

Before detailing the topic of this part of the thesis, a few remarks need to be made. The current investigation is aimed solely at the simulation of coupled thermo-hygro-chemical processes of the self-healing of the cracks. The mechanical component is not

taken into account and therefore the divergence of the velocity of the solid skeleton, $div\left(\overline{v}^{s}\right)$ in the equations (3.40), (3.41) and (3.74) is neglected. Additionally, the author adopts in this study the assumption cited in Chapter 3 which states that the gas pressure equals the atmospheric pressure. This leads to the removal of the term $div\left(\overline{\rho}_{v}\overline{v}^{gs}\right)$ from equation (3.40).

4.2.1 Formulation of the Boundary Value Problem

The governing balance equations describing the thermo-hygral behaviour of the cementitious materials, which have been previously presented in Chapter 3, are summarized below using the shorthand notations listed in the Nomenclature section.

$$\dot{\overline{\rho}}_{w} + \nabla J_{w}^{A} + \dot{m}_{v} + \dot{m}_{w}^{hyd} + \dot{m}_{w}^{a/d\_agg} - \dot{m}_{w}^{des} = 0 \tag{4.1}$$

$$\dot{\overline{\rho}}_{v} + \nabla J_{v}^{D} - \dot{m}_{v} = 0 \tag{4.2}$$

$$\dot{\overline{\rho}}_{\omega} + \nabla J_{\omega}^{A} + \nabla J_{\omega}^{DD} + \dot{m}_{\omega} = 0 \tag{4.3}$$

$$\overline{\rho C}_{p}\dot{T} + \nabla J_{T}^{CD} + \dot{m}_{v}\Delta H_{v} - Q_{h} = 0 \tag{4.4}$$

Adding equations (4.1) (4.1) and (4.2), the vapour mass term ($\dot{m}_{v}$) is eliminated and a simpler formulation for moisture balance is obtained:

$$\dot{\overline{\rho}}_{w} + \dot{\overline{\rho}}_{v} + \nabla J_{w}^{A} + \nabla J_{v}^{D} + \dot{m}_{w}^{hyd} + \dot{m}_{w}^{a/d\_agg} - \dot{m}_{w}^{des} = 0 \tag{4.5}$$

However, from the relationship (4.1) it can be immediately verified that:

$$\dot{m}_{v} = -\left(\dot{\overline{\rho}}_{w} + \nabla J_{w}^{A} + \dot{m}_{w}^{hyd} + \dot{m}_{w}^{a/d\_agg} - \dot{m}_{w}^{des}\right) \tag{4.6}$$

which is substituted into the entropy conservation law (4.4) to give:

$$\overline{\rho C}_{p}\dot{T} + \nabla J_{T}^{CD} - \left(\dot{\overline{\rho}}_{w} + \nabla J_{w}^{A} + \dot{m}_{w}^{hyd} + \dot{m}_{w}^{a/d\_agg} - \dot{m}_{w}^{des}\right)\Delta H_{v} - Q_{h} = 0 \tag{4.7}$$

Hence, the system to be solved (that has three principal variables S_{w}, T and ω and an internal variable Γ) becomes:

$$\dot{\overline{\rho}}_{w} + \dot{\overline{\rho}}_{v} + \nabla J_{w}^{A} + \nabla J_{v}^{D} + \dot{m}_{w}^{hyd} + \dot{m}_{w}^{a/d\_agg} - \dot{m}_{w}^{des} = 0 \tag{4.8}$$

$$\overline{\rho C}_{p}\dot{T} + \nabla J_{T}^{CD} - \left(\dot{\overline{\rho}}_{w} + \nabla J_{w}^{A} + \dot{m}_{w}^{hyd} + \dot{m}_{w}^{a/d\_agg} - \dot{m}_{w}^{des}\right)\Delta H_{v} - Q_{h} = 0 \tag{4.9}$$

$$\dot{\overline{\rho}}_{\omega} + \nabla J_{\omega}^{A} + \nabla J_{\omega}^{DD} + \dot{m}_{\omega} = 0 \tag{4.10}$$

The initial conditions which are imposed set the values of the unknowns at time t_{0} in all points of the domain:

$$S_{w} = S_{w0} \;\; T = T_{0} \;\; \omega = \omega_{0} \;\; on \;\; \Omega \bigcup \Gamma_{q} \tag{4.11}$$

The boundary conditions, on the other hand, are of Cauchy's type:

$$\left(J_w^A + J_v^D\right)\cdot\overline{\boldsymbol{n}} - q_{wv} - \delta_{wv}\left(\rho_v - \rho_{v_{env}}\right) = 0 \quad on\ \Gamma_{q1} \tag{4.12}$$

$$\left(J_T^{CD} - J_w^A \Delta H_v\right)\cdot\overline{\boldsymbol{n}} - q_T - \delta_T\left(T - T_{env}\right) = 0 \quad on\ \Gamma_{q2} \tag{4.13}$$

$$\left(J_\omega^A + J_\omega^{DD}\right)\cdot\overline{\boldsymbol{n}} - q_\omega - \delta_\omega\left(\omega - \omega_{env}\right) = 0 \quad on \quad \Gamma_{q3} \tag{4.14}$$

where $\overline{\boldsymbol{n}}$ is the unit normal vector to the boundary flux, the two sets (q_{wv}, q_T, q_ω) and (δ_{wv}, δ_T, δ_ω) are the imposed fluxes and transfer coefficients of the moisture, heat and precipitated material, respectively, $\rho_{v_{env}}$, T_{env} and ω_{env} are the water vapour density, temperature and concentration of precipitated material in the undisturbed environmental phases and Γ_{q1}, Γ_{q2} and Γ_{q3} form the boundary of the domain $\Gamma_q = \Gamma_{q1} \bigcup \Gamma_{q2} \bigcup \Gamma_{q3}$.

4.2.2 Finite Element Discretisation

Due to the nature of the constitutive relations listed in Chapter 3, the boundary value problem defined above is always nonlinear. Therefore, its solution is commonly deduced by means of a numerical procedure that takes the form of the finite element method (Lewis and Schrefler, 1998; Gawin et al., 2006; Koniorczyk, 2012). A concise description of essential *FEM* theory is provided to explain the numerical algorithms implemented in the computer code, but further background may be found in (Zienkiewicz et al., 2013). In broad terms the finite element process consists in minimising the residual obtained after substituting some approximate functions (see equation (4.15)) into the partial differential equation and into the boundary conditions.

$$\boldsymbol{X} \cong \sum_{i=1}^{nn} N_i X_i = \boldsymbol{N}^T \boldsymbol{X} \tag{4.15}$$

where nn represents the number of nodes corresponding to the particular finite elements into which the domain is divided, i is the point at which both the shape function N and the principal variables X are evaluated, whilst "T" denotes the transpose of the vector. The finite element method splits the domain into multiple subcomponents (Ω_e and Γ_{q_e}) and uses for each material phase the weighted residual method which multiplies the integral statements applied over Ω and over Γ_q with some arbitrary functions W. In the end, the discrete components are assembled according to the relationship:

$$\int_{\Omega} W f_D(\boldsymbol{X}) d\Omega + \int_{\Gamma} W f_B(\boldsymbol{X}) d\Gamma = \sum_{e=1}^{ne} \left(\int_{\Omega_e} W f_D(\boldsymbol{X}) d\Omega_e + \int_{\Gamma_{q_e}} W f_B(\boldsymbol{X}) d\Gamma_{q_e} \right) \tag{4.16}$$

The above $f_D(\boldsymbol{X})$ and $f_B(\boldsymbol{X})$ functions represent, at this stage, unspecified governing equations and boundary conditions, while ne is the parameter that specifies the number of finite elements. Having in mind the configuration of the current boundary value problem, the weight functions satisfy the following:

$$\begin{cases} W, \ for\, \Omega_e \\ -W, \ for\, \Gamma_{q_e} \end{cases} \tag{4.17}$$

4.2.2.1 *Development of the Integral Statement*

In the case of the autogenous healing of cement based materials, the above mentioned spatial discretisation, applied to a single finite element, leads to the following integral statements:

$$\begin{aligned} &\int_{\Omega_e} W \left(\dot{\bar{\rho}}_w + \dot{\bar{\rho}}_v + \nabla J_w^A + \nabla J_v^D + \dot{m}_w^{hyd} + \dot{m}_w^{a/d\_agg} - \dot{m}_w^{des} \right) d\Omega_e - \\ &- \int_{\Gamma_{q1_e}} W \left[\left(J_w^A + J_v^D \right) \cdot \overline{\boldsymbol{n}} - q_{wv} - \delta_{wv} \left(\rho_v - \rho_{v_{env}} \right) \right] d\Gamma_{q1_e} = 0 \end{aligned} \tag{4.18}$$

$$\begin{aligned} &\int_{\Omega_e} W \left[\overline{\rho C}_p \dot{T} + \nabla J_T^{CD} - \left(\dot{\bar{\rho}}_w + \nabla J_w^A + \dot{m}_w^{hyd} + \dot{m}_w^{a/d\_agg} - \dot{m}_w^{des} \right) \Delta H_v - Q_h \right] d\Omega_e - \\ &- \int_{\Gamma_{q2_e}} W \left[\left(J_T^{CD} - J_w^A \Delta H_v \right) \cdot \overline{\boldsymbol{n}} - q_T - \delta_T \left(T - T_{env} \right) \right] d\Gamma_{q2_e} = 0 \end{aligned} \tag{4.19}$$

$$\begin{aligned} &\int_{\Omega_e} W \left(\dot{\bar{\rho}}_\omega + \nabla J_\omega^A + \nabla J_\omega^{DD} + \dot{m}_\omega \right) d\Omega_e - \\ &- \int_{\Gamma_{q3_e}} W \left[\left(J_\omega^A + J_\omega^{DD} \right) \cdot \overline{\boldsymbol{n}} - q_\omega - \delta_\omega \left(\omega - \omega_{env} \right) \right] d\Gamma_{q3_e} = 0 \end{aligned} \tag{4.20}$$

If the properties of the divergence operator are considered, these relationships can be rearranged as follows:

$$\begin{aligned} &\int_{\Omega_e} W \left(\dot{\bar{\rho}}_w + \dot{\bar{\rho}}_v + \dot{m}_w^{hyd} + \dot{m}_w^{a/d\_agg} - \dot{m}_w^{des} \right) d\Omega_e + \int_{\Omega_e} W \nabla \left(J_w^A + J_v^D \right) d\Omega_e - \\ &- \int_{\Gamma_{q1_e}} W \left[\left(J_w^A + J_v^D \right) \cdot \overline{\boldsymbol{n}} \right] d\Gamma_{q1_e} + \int_{\Gamma_{q1_e}} W \left[q_{wv} + \delta_{wv} \left(\rho_v - \rho_{venv} \right) \right] d\Gamma_{q1_e} = 0 \end{aligned} \tag{4.21}$$

$$\int_{\Omega_e} W\left[\overline{\rho C}_p \dot{T} - \left(\dot{\bar{\rho}}_w + \dot{m}_w^{hyd} + \dot{m}_w^{a/d\_agg} - \dot{m}_w^{des}\right)\Delta H_v - Q_h\right] d\Omega_e + \\ + \int_{\Omega_e} W\nabla\left(J_T^{CD} - J_w^A \Delta H_v\right) d\Omega_e - \\ - \int_{\Gamma_{q2_e}} W\left[\left(J_T^{CD} - J_w^A \Delta H_v\right)\cdot \overline{\boldsymbol{n}}\right] d\Gamma_{q2_e} + \int_{\Gamma_{q2_e}} W\left[q_T + \delta_T\left(T - T_{env}\right)\right] d\Gamma_{q2_e} = 0 \tag{4.22}$$

$$\int_{\Omega_e} W\left(\dot{\bar{\rho}}_\omega + \dot{m}_\omega\right) d\Omega_e + \int_{\Omega_e} W\nabla\left(J_\omega^A + J_\omega^{DD}\right) d\Omega_e - \\ - \int_{\Gamma_{q3_e}} W\left[\left(J_\omega^A + J_\omega^{DD}\right)\cdot \overline{\boldsymbol{n}}\right] d\Gamma_{q3_e} - \int_{\Gamma_{q3_e}} W\left[q_\omega + \delta_\omega\left(\omega - \omega_{env}\right)\right] d\Gamma_{q3_e} = 0 \tag{4.23}$$

It is convenient at this point to obtain the weak form of these equations by performing an integration by parts of the $\int_{\Omega_e} W\nabla J_i^j d\Omega_e$ terms, based on the Gauss-Green Divergence Theorem (Zienkiewicz et al., 2013). The second-order derivatives, included in the ∇J_i^j gradients, transform into first-order derivatives allowing the cancellation of the boundary defined integrals containing the flux terms:

$$\int_{\Omega_e} W\left(\dot{\bar{\rho}}_w + \dot{\bar{\rho}}_v + \dot{m}_w^{hyd} + \dot{m}_w^{a/d\_agg} - \dot{m}_w^{des}\right) d\Omega_e + \\ + \int_{\Gamma_{q1_e}} W\left[\left(J_w^A + J_w^D\right)\cdot \overline{\boldsymbol{n}}\right] d\Gamma_{q1_e} - \int_{\Omega_e} \nabla W\left(J_w^A + J_w^D\right) d\Omega_e - \\ - \int_{\Gamma_{q1_e}} W\left[\left(J_w^A + J_v^D\right)\cdot \overline{\boldsymbol{n}}\right] d\Gamma_{q1_e} - \int_{\Gamma_{q1_e}} W\left[q_{wv} + \delta_{wv}\left(\rho_v - \rho_{venv}\right)\right] d\Gamma_{q1_e} = 0 \tag{4.24}$$

$$\int_{\Omega_e} W\left(\overline{\rho C}_p \dot{T} - \left(\dot{\bar{\rho}}_w + \dot{m}_w^{hyd} + \dot{m}_w^{a/d\_agg} - \dot{m}_w^{des}\right)\Delta H_v - Q_h\right) d\Omega_e + \\ + \int_{\Gamma_{q2_e}} W\left[\left(J_T^{CD} - J_w^A \Delta H_v\right)\cdot \overline{\boldsymbol{n}}\right] d\Gamma_{q2_e} - \int_{\Omega_e} \nabla W\left(J_T^{CD} - J_w^A \Delta H_v\right) d\Omega_e - \\ - \int_{\Gamma_{q2_e}} W\left[\left(J_T^{CD} - J_w^A \Delta H_v\right)\cdot \overline{\boldsymbol{n}}\right] d\Gamma_{q2_e} - \int_{\Gamma_{q2_e}} W\left[q_T + \delta_T\left(T - T_{env}\right)\right] d\Gamma_{q2_e} = 0 \tag{4.25}$$

$$\int_{\Omega_e} W\left(\dot{\bar{\rho}}_\omega + \dot{m}_\omega\right) d\Omega_e + \\ + \int_{\Gamma_{q3_e}} W\left[\left(J_\omega^A + J_\omega^{DD}\right)\cdot \overline{\boldsymbol{n}}\right] d\Gamma_{q3_e} - \int_{\Omega_e} \nabla W\left(J_\omega^A + J_\omega^{DD}\right) d\Omega_e - \\ - \int_{\Gamma_{q3_e}} W\left[\left(J_\omega^A + J_\omega^{DD}\right)\cdot \overline{\boldsymbol{n}}\right] d\Gamma_{q3_e} - \int_{\Gamma_{q3_e}} W\left[q_\omega + \delta_\omega\left(\omega - \omega_{env}\right)\right] d\Gamma_{q3_e} = 0 \tag{4.26}$$

The simplified system of integrals becomes:

$$\underbrace{\int_{\Omega_e} W\left(\dot{\bar{\rho}}_w + \dot{\bar{\rho}}_v + \dot{m}_w^{hyd} + \dot{m}_w^{a/d\_agg} - \dot{m}_w^{des}\right) d\Omega_e}_{I_{wv}} - \underbrace{\int_{\Omega_e} \nabla W\left(J_w^A + J_w^D\right) d\Omega_e}_{II_{wv}} - \int_{\Gamma_{q1_e}} W\left[q_{wv} + \delta_{wv}\left(\rho_v - \rho_{v_{env}}\right)\right] d\Gamma_{q1_e} = 0 \tag{4.27}$$

$$\underbrace{\int_{\Omega_e} W\left[\overline{\rho C}_p \dot{T} - \left(\dot{\bar{\rho}}_w + \dot{m}_w^{hyd} + \dot{m}_w^{a/d\_agg} - \dot{m}_w^{des}\right)\Delta H_v - Q_h\right] d\Omega_e}_{I_T} - \underbrace{\int_{\Omega_e} \nabla W\left(J_T^{CD} - J_w^A \Delta H_v\right) d\Omega_e}_{II_T} - \int_{\Gamma_{q2_e}} W\left[q_T + \delta_T\left(T - T_{env}\right)\right] d\Gamma_{q2_e} = 0 \tag{4.28}$$

$$\underbrace{\int_{\Omega_e} W\left(\dot{\bar{\rho}}_\omega + \dot{m}_\omega\right) d\Omega_e}_{I_\omega} - \underbrace{\int_{\Omega_e} \nabla W\left(J_\omega^A + J_\omega^{DD}\right) d\Omega_e}_{II_\omega} - \int_{\Gamma_{q3_e}} W\left[q_\omega + \delta_\omega\left(\omega - \omega_{env}\right)\right] d\Gamma_{q3_e} = 0 \tag{4.29}$$

In order to express equations (4.27) to (4.29) in matrix form, the phase-averaged densities in the I type integrals are decomposed into separate components that highlight the principal variables and their derivatives. As was discussed in Chapter 3, the phase-averaged densities are functions of S_w, T, Γ and ω and thus, the expression of the representative $\dot{\bar{\rho}}_\pi$ term is:

$$\dot{\bar{\rho}}_\pi = \frac{\partial \bar{\rho}_\pi}{\partial S_w}\dot{S}_w + \frac{\partial \bar{\rho}_\pi}{\partial T}\dot{T} + \frac{\partial \bar{\rho}_\pi}{\partial \Gamma}\dot{\Gamma} + \frac{\partial \bar{\rho}_\pi}{\partial \omega}\dot{\omega} \tag{4.30}$$

At the same time the derivative of m_ω previously defined in equation (3.78) gives:

$$\dot{m}_\omega = \alpha_P \omega^{\beta_P} \rho_w \eta \dot{S}_w + \alpha_P S_w \omega^{\beta_P} \eta \frac{\partial \rho_w}{\partial T}\dot{T} + \alpha_P S_w \omega^{\beta_P} \rho_w \frac{\partial \eta}{\partial \Gamma}\dot{\Gamma} + \alpha_P S_w \eta \beta_P \omega^{\beta_P - 1} \rho_w \dot{\omega} \tag{4.31}$$

The adopted spatial discretisation facilitates an expression for the time derivative of the unknowns similar to (4.15):

$$\dot{\boldsymbol{X}} \cong \sum_{i=1}^{nn} N_i \dot{X}_i = \boldsymbol{N}^T \dot{\boldsymbol{X}} \tag{4.32}$$

Thus, recalling the equations (3.46) and (3.47), the terms I_i (i = wv, T and ω) from (4.27) to (4.29) yield:

$$I_{wv} = \int_{\Omega_e} W \left[\begin{array}{c} \left(\frac{\partial \overline{\rho}_w}{\partial S_w} + \frac{\partial \overline{\rho}_v}{\partial S_w} \right) \boldsymbol{N}^T \dot{\boldsymbol{S}}_{\boldsymbol{w}} + \left(\frac{\partial \overline{\rho}_w}{\partial T} + \frac{\partial \overline{\rho}_v}{\partial T} \right) \boldsymbol{N}^T \dot{\boldsymbol{T}} + \left(\frac{\partial \overline{\rho}_w}{\partial \Gamma} + \frac{\partial \overline{\rho}_v}{\partial \Gamma} \right) \dot{\Gamma} + \\ + \left(\frac{\partial \overline{\rho}_w}{\partial \omega} + \frac{\partial \overline{\rho}_v}{\partial \omega} \right) \boldsymbol{N}^T \dot{\boldsymbol{\omega}} + \sum_i \left(w_i^{ult} \right) \dot{\Gamma} + \dot{m}_w^{a/d\_agg} - \frac{\partial m_w^{des}}{\partial S_w} \boldsymbol{N}^T \dot{\boldsymbol{S}}_{\boldsymbol{w}} \end{array} \right] d\Omega_e \quad (4.33)$$

$$I_T = \int_{\Omega_e} W \left[\begin{array}{c} \overline{\rho C}_p \boldsymbol{N}^T \dot{\boldsymbol{T}} - \left(\frac{\partial \overline{\rho}_w}{\partial S_w} \boldsymbol{N}^T \dot{\boldsymbol{S}}_{\boldsymbol{w}} + \frac{\partial \overline{\rho}_w}{\partial T} \boldsymbol{N}^T \dot{\boldsymbol{T}} + \frac{\partial \overline{\rho}_w}{\partial \Gamma} \dot{\Gamma} + \frac{\partial \overline{\rho}_w}{\partial \omega} \boldsymbol{N}^T \dot{\boldsymbol{\omega}} \right) \Delta H_v - \\ - \left(\sum_i \left(w_i^{ult} \right) \dot{\Gamma} + \dot{m}_w^{a/d\_agg} - \frac{\partial m_w^{des}}{\partial S_w} \boldsymbol{N}^T \dot{\boldsymbol{S}}_{\boldsymbol{w}} \right) \Delta H_v - Q_h \end{array} \right] d\Omega_e \quad (4.34)$$

$$I_\omega = \int_{\Omega_e} W \left[\begin{array}{c} \left(\frac{\partial \overline{\rho}_\omega}{\partial S_w} \boldsymbol{N}^T \dot{\boldsymbol{S}}_{\boldsymbol{w}} + \frac{\partial \overline{\rho}_\omega}{\partial T} \boldsymbol{N}^T \dot{\boldsymbol{T}} + \frac{\partial \overline{\rho}_\omega}{\partial \Gamma} \dot{\Gamma} + \frac{\partial \overline{\rho}_\omega}{\partial \omega} \boldsymbol{N}^T \dot{\boldsymbol{\omega}} \right) + \\ + \alpha_P \omega^{\beta_P} \rho_w \eta \boldsymbol{N}^T \dot{\boldsymbol{S}}_{\boldsymbol{w}} + \alpha_P S_w \omega^{\beta_P} \eta \frac{\partial \rho_w}{\partial T} \boldsymbol{N}^T \dot{\boldsymbol{T}} + \\ + \alpha_P S_w \omega^{\beta_P} \rho_w \frac{\partial \eta}{\partial \Gamma} \dot{\Gamma} + \alpha_P S_w \eta \beta_P \omega^{\beta_P - 1} \rho_w \boldsymbol{N}^T \dot{\boldsymbol{\omega}} \end{array} \right] d\Omega_e \quad (4.35)$$

In the theoretical considerations presented at the beginning of section 3.3.3, the gas pressure was assumed to be equal to the atmospheric pressure. This means that it is constant in space and hence the conductivity flux yields:

$$J_w^A = k_w \rho_w \left(\nabla p_c + \rho_w \boldsymbol{g} \right) \quad (4.36)$$

But having in mind the link between p_c and S_w, the spatial differential of the capillary pressure in terms of the variables considered equals:

$$\nabla p_c = \nabla \left[p_c \left(S_w, T, \Gamma \right) \right] = \frac{\partial p_c}{\partial S_w} \nabla S_w + \frac{\partial p_c}{\partial T} \nabla T + \frac{\partial p_c}{\partial \Gamma} \nabla \Gamma \quad (4.37)$$

In this expression, the spatial derivative of the hydration degree is replaced by equation (4.38) which is consistent with the hydration model proposed by Schindler and Folliard (2005).

$$\nabla \Gamma = \nabla \Gamma \left(T \right) = \frac{\partial \Gamma}{\partial T} \nabla T \quad (4.38)$$

Regarding the diffusive flux of the water vapours, the spatial invariability of the gas pressure implies that:

$$J_v^D = -D_{eff} \nabla \rho_v = -D_{eff} \frac{M_w}{RT} \nabla p_v \quad (4.39)$$

in which:

$$\nabla p_v = \nabla \left[p_v \left(S_w, T \right) \right] = \frac{\partial p_v}{\partial S_w} \nabla S_w + \frac{\partial p_v}{\partial T} \nabla T \quad (4.40)$$

For the precipitated material, the diffusive-dispersive flux is employed in its condensed shape:

$$\begin{aligned} J_{\omega}^{DD} &= -\rho_w D_{mdd}^{ij} \nabla \omega \\ D_{mdd}^{ij} &= D_{mdisp}^{ij} + D_{mdiff}^{ij} \end{aligned} \tag{4.41}$$

while the advective flux develops into:

$$J_{\omega}^{A} = k_w \rho_{\omega} \left[\frac{\partial p_c}{\partial S_w} \nabla S_w + \left(\frac{\partial p_c}{\partial T} + \frac{\partial p_c}{\partial \Gamma} \frac{\partial \Gamma}{\partial T} \right) \nabla T + \rho_w \boldsymbol{g} \right] \tag{4.42}$$

Finally, the conductive heat flux found in the entropy balance equation is given by:

$$J_{T}^{CD} = -\lambda_T^{eff} \nabla T \tag{4.43}$$

As a result, the terms II_i (i = m , T and ω) can be rewritten in the following form, if the approximation (4.15) is taken into consideration:

$$II_{wv} = \int_{\Omega_e} \nabla W \left[\begin{array}{c} k_w \rho_w \left(\frac{\partial p_c}{\partial S_w} \nabla \left(\boldsymbol{N}^T \boldsymbol{S_w} \right) + \left(\frac{\partial p_c}{\partial T} + \frac{\partial p_c}{\partial \Gamma} \frac{\partial \Gamma}{\partial T} \right) \nabla \left(\boldsymbol{N}^T \boldsymbol{T} \right) + \rho_w \boldsymbol{g} \right) - \\ - D_{eff} \frac{M_w}{RT} \left(\frac{\partial p_v}{\partial S_w} \nabla \left(\boldsymbol{N}^T \boldsymbol{S_w} \right) + \frac{\partial p_v}{\partial T} \nabla \left(\boldsymbol{N}^T \boldsymbol{T} \right) \right) \end{array} \right] d\Omega_e \tag{4.44}$$

$$II_{T} = \int_{\Omega_e} \nabla W \left[\begin{array}{c} - \lambda_T^{eff} \nabla \left(\boldsymbol{N}^T \boldsymbol{T} \right) - \\ - k_w \rho_w \left(\frac{\partial p_c}{\partial S_w} \nabla \left(\boldsymbol{N}^T \boldsymbol{S_w} \right) + \left(\frac{\partial p_c}{\partial T} + \frac{\partial p_c}{\partial \Gamma} \frac{\partial \Gamma}{\partial T} \right) \nabla \left(\boldsymbol{N}^T \boldsymbol{T} \right) \right) \Delta H_v \\ - k_w \rho_w \rho_w \boldsymbol{g} \Delta H_v \end{array} \right] d\Omega_e \tag{4.45}$$

$$II_{\omega} = \int_{\Omega_e} \nabla W \left[\begin{array}{c} k_w \rho_{\omega} \left(\frac{\partial p_c}{\partial S_w} \nabla \left(\boldsymbol{N}^T \boldsymbol{S_w} \right) + \left(\frac{\partial p_c}{\partial T} + \frac{\partial p_c}{\partial \Gamma} \frac{\partial \Gamma}{\partial T} \right) \nabla \left(\boldsymbol{N}^T \boldsymbol{T} \right) + \rho_w \boldsymbol{g} \right) - \\ - \rho_w D_{mdd}^{ij} \nabla \left(\boldsymbol{N}^T \boldsymbol{\omega} \right) \end{array} \right] d\Omega_e \tag{4.46}$$

Using I_i and II_i in equations (4.27) to (4.29) and extracting common factors when possible, the weak form of the integral statements becomes:

$$\begin{aligned}
&\int_{\Omega_e} W \begin{bmatrix} \left(\frac{\partial \overline{\rho}_w}{\partial S_w} + \frac{\partial \overline{\rho}_v}{\partial S_w} - \frac{\partial m_w^{des}}{\partial S_w}\right) \boldsymbol{N}^T \dot{\boldsymbol{S}}_{\boldsymbol{w}} + \\ + \left(\frac{\partial \overline{\rho}_w}{\partial T} + \frac{\partial \overline{\rho}_v}{\partial T}\right) \boldsymbol{N}^T \dot{\boldsymbol{T}} + \\ + \left(\frac{\partial \overline{\rho}_w}{\partial \omega} + \frac{\partial \overline{\rho}_v}{\partial \omega}\right) \boldsymbol{N}^T \dot{\boldsymbol{\omega}} \end{bmatrix} d\Omega_e + \\
&+ \int_{\Omega_e} W \left[\left(\frac{\partial \overline{\rho}_w}{\partial \Gamma} + \frac{\partial \overline{\rho}_v}{\partial \Gamma} + \sum_i \left(w_i^{ult} \right) \right) \dot{\Gamma} \right] d\Omega_e + \\
&+ \int_{\Omega_e} \nabla W \begin{bmatrix} \left(-k_w \rho_w \frac{\partial p_c}{\partial S_w} + D_{eff} \frac{M_w}{RT} \frac{\partial p_v}{\partial S_w} \right) \nabla \left(\boldsymbol{N}^T \boldsymbol{S}_{\boldsymbol{w}} \right) + \\ + \left(-k_w \rho_w \left(\frac{\partial p_c}{\partial T} + \frac{\partial p_c}{\partial \Gamma} \frac{\partial \Gamma}{\partial T} \right) + D_{eff} \frac{M_w}{RT} \frac{\partial p_v}{\partial T} \right) \nabla \left(\boldsymbol{N}^T \boldsymbol{T} \right) \end{bmatrix} d\Omega_e + \\
&+ \int_{\Omega_e} W \dot{m}_w^{a/d_agg} d\Omega_e - \\
&- \int_{\Omega_e} \nabla W \left(\rho_w k_w \rho_w \boldsymbol{g} \right) d\Omega_e - \int_{\Gamma_{q1_e}} W \left[q_{wv} + \delta_{wv} \left(\rho_v - \rho_{v_{env}} \right) \right] d\Gamma_{q1_e} = 0
\end{aligned} \tag{4.47}$$

$$\begin{aligned}
&\int_{\Omega_e} W \begin{bmatrix} \left(-\frac{\partial \overline{\rho}_w}{\partial S_w} + \frac{\partial m_w^{des}}{\partial S_w} \right) \Delta H_v \boldsymbol{N}^T \dot{\boldsymbol{S}}_{\boldsymbol{w}} + \\ + \left(\overline{\rho C}_p - \frac{\partial \overline{\rho}_w}{\partial T} \Delta H_v \right) \boldsymbol{N}^T \dot{\boldsymbol{T}} + \\ + \left(-\frac{\partial \overline{\rho}_w}{\partial \omega} \Delta H_v \right) \boldsymbol{N}^T \dot{\boldsymbol{\omega}} \end{bmatrix} d\Omega_e + \int_{\Omega_e} W \left[-\left(\sum_i \left(w_i^{ult} \right) + \frac{\partial \overline{\rho}_w}{\partial \Gamma} \right) \Delta H_v \right] \dot{\Gamma} d\Omega_e + \\
&+ \int_{\Omega_e} \nabla W \begin{bmatrix} \left(k_w \rho_w \frac{\partial p_c}{\partial S_w} \Delta H_v \right) \nabla \left(\boldsymbol{N}^T \boldsymbol{S}_{\boldsymbol{w}} \right) + \\ + \left(\lambda_T^{eff} + k_w \rho_w \left(\frac{\partial p_c}{\partial T} + \frac{\partial p_c}{\partial \Gamma} \frac{\partial \Gamma}{\partial T} \right) \Delta H_v \right) \nabla \left(\boldsymbol{N}^T \boldsymbol{T} \right) \end{bmatrix} d\Omega_e + \\
&+ \int_{\Omega_e} W \left(-Q_h - \dot{m}_w^{a/d_agg} \Delta H_v \right) d\Omega_e - \\
&- \int_{\Omega_e} \nabla W \left(-\rho_w k_w \rho_w \boldsymbol{g} \right) \Delta H_v d\Omega_e - \int_{\Gamma_{q2_e}} W \left[q_T + \delta_T \left(T - T_{env} \right) \right] d\Gamma_{q2_e} = 0
\end{aligned} \tag{4.48}$$

$$\begin{aligned}
&\int_{\Omega_e} W \begin{bmatrix} \left(\frac{\partial \overline{\rho}_\omega}{\partial S_w} + \alpha_P \omega^{\beta_P} \rho_w \eta\right) \boldsymbol{N}^T \dot{\boldsymbol{S}}_{\boldsymbol{w}} + \\ \left(\frac{\partial \overline{\rho}_\omega}{\partial T} + \alpha_P S_w \omega^{\beta_P} \eta \frac{\partial \rho_w}{\partial T}\right) \boldsymbol{N}^T \dot{\boldsymbol{T}} + \\ + \left(\frac{\partial \overline{\rho}_\omega}{\partial \omega} + \alpha_P S_w \eta \beta_P \omega^{\beta_P - 1} \rho_w\right) \boldsymbol{N}^T \dot{\boldsymbol{\omega}} \end{bmatrix} d\Omega_e + \\
&+ \int_{\Omega_e} W \left(\frac{\partial \overline{\rho}_\omega}{\partial \Gamma} + \alpha_P S_w \omega^{\beta_P} \rho_w \frac{\partial \eta}{\partial \Gamma}\right) \dot{\Gamma} d\Omega_e + \\
&+ \int_{\Omega_e} \nabla W \begin{bmatrix} \left(-k_w \rho_\omega \frac{\partial p_c}{\partial S_w}\right) \nabla\left(\boldsymbol{N}^T \boldsymbol{S}_{\boldsymbol{w}}\right) + \\ + \left(-k_w \rho_\omega \left(\frac{\partial p_c}{\partial T} + \frac{\partial p_c}{\partial \Gamma} \frac{\partial \Gamma}{\partial T}\right)\right) \nabla\left(\boldsymbol{N}^T \boldsymbol{T}\right) + \\ + \rho_w D_{mdd}^{ij} \nabla\left(\boldsymbol{N}^T \boldsymbol{\omega}\right) \end{bmatrix} d\Omega_e - \\
&- \int_{\Omega_e} \nabla W \left(\rho_w k_w \rho_w \boldsymbol{g}\right) d\Omega_e - \int_{\Gamma_{q3_e}} W \left[q_\omega + \delta_\omega \left(\omega - \omega_{env}\right)\right] d\Gamma_{q3_e} = 0
\end{aligned} \tag{4.49}$$

This set of equations may be summarised in a concise matrix notation as:

$$\begin{aligned}
&\int_{\Omega_e} W \left(C_{11} \boldsymbol{N}^T \dot{\boldsymbol{S}}_{\boldsymbol{w}} + C_{12} \boldsymbol{N}^T \dot{\boldsymbol{T}} + C_{13} \boldsymbol{N}^T \dot{\boldsymbol{\omega}}\right) d\Omega_e + \\
&+ \int_{\Omega_e} \nabla W \left(K_{11} \nabla\left(\boldsymbol{N}^T \boldsymbol{S}_{\boldsymbol{w}}\right) + K_{12} \nabla\left(\boldsymbol{N}^T \boldsymbol{T}\right) + K_{13} \nabla\left(\boldsymbol{N}^T \boldsymbol{\omega}\right)\right) d\Omega_e + \\
&+ \int_{\Omega_e} W \left(C_{\Gamma 1} \dot{\Gamma} + \dot{m}_w^{a/d-agg}\right) d\Omega_e - \int_{\Omega_e} \nabla W f_{g1} d\Omega_e - \int_{\Gamma_{q1_e}} W F_{q1} d\Gamma_{q1_e} = 0
\end{aligned} \tag{4.50}$$

$$\begin{aligned}
&\int_{\Omega_e} W \left(C_{21} \boldsymbol{N}^T \dot{\boldsymbol{S}}_{\boldsymbol{w}} + C_{22} \boldsymbol{N}^T \dot{\boldsymbol{T}} + C_{23} \boldsymbol{N}^T \dot{\boldsymbol{\omega}}\right) d\Omega_e + \\
&+ \int_{\Omega_e} \nabla W \left(K_{21} \nabla\left(\boldsymbol{N}^T \boldsymbol{S}_{\boldsymbol{w}}\right) + K_{22} \nabla\left(\boldsymbol{N}^T \boldsymbol{T}\right) + K_{23} \nabla\left(\boldsymbol{N}^T \boldsymbol{\omega}\right)\right) d\Omega_e + \\
&+ \int_{\Omega_e} W \left[C_{\Gamma 2} \dot{\Gamma} + \left(-Q_h - \dot{m}_w^{a/d-agg} \Delta H_v\right)\right] d\Omega_e - \int_{\Omega_e} \nabla W f_{g2} d\Omega_e - \int_{\Gamma_{q2_e}} W F_{q2} d\Gamma_{q2_e} = 0
\end{aligned} \tag{4.51}$$

$$\begin{aligned}
&\int_{\Omega_e} W \left(C_{31} \boldsymbol{N}^T \dot{\boldsymbol{S}}_{\boldsymbol{w}} + C_{32} \boldsymbol{N}^T \dot{\boldsymbol{T}} + C_{33} \boldsymbol{N}^T \dot{\boldsymbol{\omega}}\right) d\Omega_e + \\
&+ \int_{\Omega_e} \nabla W \left(K_{31} \nabla\left(\boldsymbol{N}^T \boldsymbol{S}_{\boldsymbol{w}}\right) + K_{32} \nabla\left(\boldsymbol{N}^T \boldsymbol{T}\right) + K_{33} \nabla\left(\boldsymbol{N}^T \boldsymbol{\omega}\right)\right) d\Omega_e + \\
&+ \int_{\Omega_e} W C_{\Gamma 3} \dot{\Gamma} d\Omega_e - \int_{\Omega_e} \nabla W f_{g3} d\Omega_e - \int_{\Gamma_{q3_e}} W F_{q3} d\Gamma_{q3_e} = 0
\end{aligned} \tag{4.52}$$

where:

$$C_{11} = \frac{\partial \overline{\rho}_w}{\partial S_w} + \frac{\partial \overline{\rho}_v}{\partial S_w} - \frac{\partial m_w^{des}}{\partial S_w} \qquad K_{11} = -k_w \rho_w \frac{\partial p_c}{\partial S_w} + D_{eff} \frac{M_w}{RT} \frac{\partial p_v}{\partial S_w}$$

$$C_{12} = \frac{\partial \overline{\rho}_w}{\partial T} + \frac{\partial \overline{\rho}_v}{\partial T} \qquad K_{12} = -k_w \rho_w \left(\frac{\partial p_c}{\partial T} + \frac{\partial p_c}{\partial \Gamma} \frac{\partial \Gamma}{\partial T} \right) + D_{eff} \frac{M_w}{RT} \frac{\partial p_v}{\partial T}$$

$$C_{13} = \frac{\partial \overline{\rho}_w}{\partial \omega} + \frac{\partial \overline{\rho}_v}{\partial \omega} \qquad K_{13} = 0$$

$$C_{21} = \left(-\frac{\partial \overline{\rho}_w}{\partial S_w} + \frac{\partial m_w^{des}}{\partial S_w} \right) \Delta H_v \qquad K_{21} = k_w \rho_w \frac{\partial p_c}{\partial S_w} \Delta H_v$$

$$C_{22} = \overline{\rho C}_p - \frac{\partial \overline{\rho}_w}{\partial T} \Delta H_v \qquad K_{22} = \lambda_T^{eff} + k_w \rho_w \left(\frac{\partial p_c}{\partial T} + \frac{\partial p_c}{\partial \Gamma} \frac{\partial \Gamma}{\partial T} \right) \Delta H_v$$

$$C_{23} = -\frac{\partial \overline{\rho}_w}{\partial \omega} \Delta H_v \qquad K_{23} = 0$$

$$C_{31} = \frac{\partial \overline{\rho}_\omega}{\partial S_w} + \alpha_P \omega^{\beta_P} \rho_w \eta \qquad K_{31} = -k_w \rho_\omega \frac{\partial p_c}{\partial S_w}$$

$$C_{32} = \frac{\partial \overline{\rho}_\omega}{\partial T} + \alpha_P S_w \omega^{\beta_P} \eta \frac{\partial \rho_w}{\partial T} \qquad K_{32} = -k_w \rho_\omega \left(\frac{\partial p_c}{\partial T} + \frac{\partial p_c}{\partial \Gamma} \frac{\partial \Gamma}{\partial T} \right)$$

$$C_{33} = \frac{\partial \overline{\rho}_\omega}{\partial \omega} + \alpha_P S_w \eta \beta_P \omega^{\beta_P - 1} \rho_w \qquad K_{33} = \rho_w D_{mdd}^{ij}$$

$$f_{g1} = \rho_w k_w \rho_w \boldsymbol{g} \qquad F_{q1} = q_{wv} + \delta_{wv} \left(\rho_v - \rho_{v_{env}} \right) \qquad C_{\Gamma 1} = \frac{\partial \overline{\rho}_w}{\partial \Gamma} + \frac{\partial \overline{\rho}_v}{\partial \Gamma} + \sum_i \left(w_i^{ult} \right)$$

$$f_{g2} = -\rho_w k_w \rho_w \Delta H_v \boldsymbol{g} \qquad F_{q2} = q_T + \delta_T \left(T - T_{env} \right) \qquad C_{\Gamma 2} = -\left(\sum_i \left(w_i^{ult} \right) + \frac{\partial \overline{\rho}_w}{\partial \Gamma} \right) \Delta H_v$$

$$f_{g3} = \rho_\omega k_w \rho_w \boldsymbol{g} \qquad F_{q3} = q_\omega + \delta_\omega \left(\omega - \omega_{env} \right) \qquad C_{\Gamma 3} = \frac{\partial \overline{\rho}_\omega}{\partial \Gamma} + \alpha_P S_w \omega^{\beta_P} \rho_w \frac{\partial \eta}{\partial \Gamma}$$

4.2.2.2 *Weighting by the Galerkin Method*

The Galerkin method is applied in order to choose the W function (Galerkin, 1915). Consequently, the shape function $\boldsymbol{N}$ weights the integral of all the residuals. This option is preferred because, due to the multiplication between the shape function and its transpose, it generally results in symmetric matrices. Thus, from the last three equations mentioned in the previous subsection, the condensed elemental system of equations to be solved is:

$$\int_{\Omega_e} \boldsymbol{N} \begin{bmatrix} C_{11} & C_{12} & C_{13} \\ C_{21} & C_{22} & C_{23} \\ C_{31} & C_{32} & C_{33} \end{bmatrix} \boldsymbol{N}^T \begin{Bmatrix} \dot{\boldsymbol{S}}_w \\ \dot{\boldsymbol{T}} \\ \dot{\boldsymbol{\omega}} \end{Bmatrix} d\Omega_e + \\ + \int_{\Omega_e} \nabla \boldsymbol{N} \begin{bmatrix} K_{11} & K_{12} & K_{13} \\ K_{21} & K_{22} & K_{23} \\ K_{31} & K_{32} & K_{33} \end{bmatrix} \nabla \boldsymbol{N}^T \begin{Bmatrix} \boldsymbol{S}_w \\ \boldsymbol{T} \\ \boldsymbol{\omega} \end{Bmatrix} d\Omega_e = \begin{Bmatrix} \boldsymbol{F}_{1e} \\ \boldsymbol{F}_{2e} \\ \boldsymbol{F}_{3e} \end{Bmatrix} \tag{4.53}$$

The components of $\boldsymbol{F}_e$ are a combination of body (the integrals over Ω_e) and boundary (the integrals over Γ_{q_e}) "forces":

$$\boldsymbol{F}_{1e} = \int_{\Omega_e} \boldsymbol{N} \left(- C_{\Gamma 1} \dot{T} - \dot{m}_w^{a/d\_agg} \right) d\Omega_e + \int_{\Omega_e} \nabla \boldsymbol{N} f_{g1} d\Omega_e + \int_{\Gamma_{q1_e}} \boldsymbol{N} F_{q1} d\Gamma_{q1_e} \tag{4.54}$$

$$\boldsymbol{F}_{2e} = \int_{\Omega_e} \boldsymbol{N} \left[- C_{\Gamma 2} \dot{T} + \left(- Q_h - \dot{m}_w^{a/d\_agg} \Delta H_v \right) \right] d\Omega_e + \int_{\Omega_e} \nabla \boldsymbol{N} f_{g2} d\Omega_e + \int_{\Gamma_{q2_e}} \boldsymbol{N} F_{q2} d\Gamma_{q2_e} \tag{4.55}$$

$$\boldsymbol{F}_{3e} = \int_{\Omega_e} \boldsymbol{N} \left(- C_{\Gamma 3} \dot{T} \right) d\Omega_e + \int_{\Omega_e} \nabla \boldsymbol{N} f_{g3} d\Omega_e + \int_{\Gamma_{q3_e}} \boldsymbol{N} F_{q3} d\Gamma_{q3_e} \tag{4.56}$$

whilst the shape function vector is a differentiable function prescribed only in terms of coordinates. In the case of a 2D 4 noded finite element, $\boldsymbol{N}$ is expressed as follows:

$$\boldsymbol{N} = \begin{Bmatrix} N_1 \\ N_2 \\ N_3 \\ N_4 \end{Bmatrix} = \begin{Bmatrix} \frac{1}{4}\left(1 - \hat{\xi}\right)\left(1 - \hat{\eta}\right) \\ \frac{1}{4}\left(1 + \hat{\xi}\right)\left(1 - \hat{\eta}\right) \\ \frac{1}{4}\left(1 + \hat{\xi}\right)\left(1 + \hat{\eta}\right) \\ \frac{1}{4}\left(1 - \hat{\xi}\right)\left(1 + \hat{\eta}\right) \end{Bmatrix} \tag{4.57}$$

where $\hat{\xi}$ and $\hat{\eta}$, defined over [-1,1], are the local parametric coordinates isoparametrically "mapped" to the Cartesian coordinates by interpolation. Equation (4.53) can be condensed even more and extrapolated to the entire domain if an assembly procedure similar to the one showed in (4.16) is adopted. Its ultimate format, presented in (4.58), introduces:

$\boldsymbol{\Phi} = \begin{Bmatrix} \boldsymbol{S}_w \\ \boldsymbol{T} \\ \boldsymbol{\omega} \end{Bmatrix} = \begin{Bmatrix} \boldsymbol{\Phi}_1 \\ \boldsymbol{\Phi}_2 \\ \boldsymbol{\Phi}_3 \end{Bmatrix}$ – the global vector of unknowns,

$\hat{\boldsymbol{C}} = \begin{bmatrix} \hat{\boldsymbol{C}}_{11} & \hat{\boldsymbol{C}}_{12} & \hat{\boldsymbol{C}}_{13} \\ \hat{\boldsymbol{C}}_{21} & \hat{\boldsymbol{C}}_{22} & \hat{\boldsymbol{C}}_{23} \\ \hat{\boldsymbol{C}}_{31} & \hat{\boldsymbol{C}}_{32} & \hat{\boldsymbol{C}}_{33} \end{bmatrix}$ ($\hat{\boldsymbol{C}}_{ij} = \sum_{e=1}^{ne} \int_{\Omega_e} \boldsymbol{N} C_{ij} \boldsymbol{N}^T d\Omega_e$) – the global secant capacitance matrix,

$\hat{\boldsymbol{K}} = \begin{bmatrix} \hat{\boldsymbol{K}}_{11} & \hat{\boldsymbol{K}}_{12} & \hat{\boldsymbol{K}}_{13} \\ \hat{\boldsymbol{K}}_{21} & \hat{\boldsymbol{K}}_{22} & \hat{\boldsymbol{K}}_{23} \\ \hat{\boldsymbol{K}}_{31} & \hat{\boldsymbol{K}}_{32} & \hat{\boldsymbol{K}}_{33} \end{bmatrix}$ ($\hat{\boldsymbol{K}}_{ij} = \sum_{e=1}^{ne} \int_{\Omega_e} \boldsymbol{N} K_{ij} \boldsymbol{N}^T d\Omega_e$) – the global secant hydraulic conductivity matrix,

$\hat{\boldsymbol{F}} = \begin{Bmatrix} \boldsymbol{F}_1 \\ \boldsymbol{F}_2 \\ \boldsymbol{F}_3 \end{Bmatrix}$ ($\hat{\boldsymbol{F}}_i = \sum_{e=1}^{ne} \boldsymbol{F}_{ie}$) – the global the right-hand side load vector.

$$\hat{\boldsymbol{C}}\dot{\boldsymbol{\Phi}} + \hat{\boldsymbol{K}}\boldsymbol{\Phi} = \hat{\boldsymbol{F}} \tag{4.58}$$

Before ending this section it should also be stated that for the numerical integration of the above matrices, the Gauss-Legendre rules are employed. In a 2D domain, these rules, defined between the local parametric coordinates $-1 \le \hat{\xi} \le +1$ and $-1 \le \hat{\eta} \le +1$, operate with respect to four sampling points with the coordinates $\left(-\sqrt{3}^{-1}, -\sqrt{3}^{-1}\right)$, $\left(\sqrt{3}^{-1}, -\sqrt{3}^{-1}\right)$, $\left(\sqrt{3}^{-1}, \sqrt{3}^{-1}\right)$, $\left(-\sqrt{3}^{-1}, \sqrt{3}^{-1}\right)$ and the corresponding weights 1, 1, 1, 1. In this procedure, illustrated in equation (4.59), the surface integral of an arbitrary function f equals to the sum of the products between the values of the given integrand in the Gauss points and their weights (Zienkiewicz et al., 2013).

$$\int_{-1}^{+1}\int_{-1}^{+1} f(\hat{\xi}, \hat{\eta})\, d\hat{\xi} d\hat{\eta} = \sum_{i=1}^{4} f(\hat{\xi}_i, \hat{\eta}_i) W_i \tag{4.59}$$

4.3 Time Discretisation

The time derivative of the main variables is obtained from a generalised midpoint rule (Lewis and Schrefler, 1998):

$$\dot{\boldsymbol{\Phi}}_{n+\Theta} = \frac{1}{\Delta t}\left(\boldsymbol{\Phi}_n - \boldsymbol{\Phi}_{n\text{-}1}\right) \tag{4.60}$$

$$\boldsymbol{\Phi}_{n+\Theta} = (1-\Theta)\boldsymbol{\Phi}_{n\text{-}1} + \Theta\boldsymbol{\Phi}_n \tag{4.61}$$

in which $\boldsymbol{\Phi}_n$ and $\boldsymbol{\Phi}_{n\text{-}1}$ are the principal variables at the time steps t_n and $t_{n\text{-}1}$ ($t_n = t_{n\text{-}1} + \Delta t$; Δt is a time increment), whilst Θ represents a parameter ranging between 0 and 1. In the current investigation an implicit finite difference approximation

is chosen and thus Θ equals to unity. (4.61) is also applied to the forcing vector $\hat{\boldsymbol{F}}$ and so by replacing (4.60) into (4.58) it leads to:

$$\hat{\boldsymbol{C}}\frac{1}{\Delta t}\left(\boldsymbol{\Phi}_n-\boldsymbol{\Phi}_{n\text{-}1}\right)+\hat{\boldsymbol{K}}\boldsymbol{\Phi}_n=\hat{\boldsymbol{F}}_n \tag{4.62}$$

where $\hat{\boldsymbol{C}}$ and $\hat{\boldsymbol{K}}$ need to be evaluated for the current step n. Theoretically, the solution could be determined based on direct iteration:

$$\boldsymbol{\Phi}_n=\left(\hat{\boldsymbol{K}}\left(\boldsymbol{\Phi}_n\right)+\hat{\boldsymbol{C}}\left(\boldsymbol{\Phi}_n\right)\frac{1}{\Delta t}\right)^{-1}\left(\hat{\boldsymbol{F}}_n+\hat{\boldsymbol{C}}\left(\boldsymbol{\Phi}_n\right)\frac{1}{\Delta t}\boldsymbol{\Phi}_{n\text{-}1}\right) \tag{4.63}$$

However, due to the level of nonlinearity, it is impossible to embrace such an approach and instead a Newton-Raphson method is used. In this numerical scheme the above true root, $\boldsymbol{\Phi}_n$, is successively approximated by several values until the below residual $\boldsymbol{\Psi}$ is minimised.

$$\boldsymbol{\Psi}\left(\boldsymbol{\Phi}\right)=\hat{\boldsymbol{C}}\left(\boldsymbol{\Phi}-\boldsymbol{\Phi}_{n\text{-}1}\right)+\Delta t\left(\hat{\boldsymbol{K}}\boldsymbol{\Phi}-\hat{\boldsymbol{F}}\right) \tag{4.64}$$

in which $\hat{\boldsymbol{C}}$, $\hat{\boldsymbol{K}}$ and $\hat{\boldsymbol{F}}$ are evaluated at the approximated $\boldsymbol{\Phi}$. Consequently, within the current step n, a loop that computes the new $\boldsymbol{\Phi}_n$ and that breaks when the L2 norm of the residual reaches a certain specified tolerance is introduced. Mathematically, the reduction of the time approximation error is achieved by equating to 0 the truncated form of the Taylor's series expansion for the $\boldsymbol{\Psi}$ at the new value $\boldsymbol{\Phi}_n^{k+1}$, about the known:

$$\boldsymbol{\Psi}\left(\boldsymbol{\Phi}_n^{k+1}\right)\cong\boldsymbol{\Psi}\left(\boldsymbol{\Phi}_n^{k}\right)+\left[\frac{\partial\boldsymbol{\Psi}}{\partial\boldsymbol{\Phi}}\left(\boldsymbol{\Phi}_n^{k}\right)\right]\boldsymbol{\delta\Phi}_n^{k+1}=0 \tag{4.65}$$

The quantity required to revise the vector of variables within a loop step is:

$$\boldsymbol{\delta\Phi}_n^{k+1}=\left[\frac{\partial\boldsymbol{\Psi}}{\partial\boldsymbol{\Phi}}\left(\boldsymbol{\Phi}_n^{k}\right)\right]^{-1}\left(-\boldsymbol{\Psi}\left(\boldsymbol{\Phi}_n^{k}\right)\right) \tag{4.66}$$

and the revised $\boldsymbol{\Phi}_n$ equals to:

$$\boldsymbol{\Phi}_n^{k+1}=\boldsymbol{\Phi}_n^{k}+\boldsymbol{\delta\Phi}_n^{k+1} \tag{4.67}$$

The term $\dfrac{\partial\boldsymbol{\Psi}}{\partial\boldsymbol{\Phi}}$ denotes the Jacobian of the approximation error as follows:

$$\frac{\partial\boldsymbol{\Psi}_p}{\partial\boldsymbol{\Phi}_r}=\underbrace{\left\{\hat{\boldsymbol{C}}_{pr}+\sum_{t=1}^{nn}\sum_{s=1}^{3}\frac{\partial\hat{\boldsymbol{C}}^t_{ps}}{\partial\boldsymbol{\Phi}_r}D\Phi_{s_t}\right\}}_{\Delta\hat{\boldsymbol{C}}_{pr}}+\Delta t\underbrace{\left\{\hat{\boldsymbol{K}}_{pr}+\sum_{t=1}^{nn}\sum_{s=1}^{3}\frac{\partial\hat{\boldsymbol{K}}^t_{ps}}{\partial\boldsymbol{\Phi}_r}\Phi_{s_t}\right\}}_{\Delta\hat{\boldsymbol{K}}_{pr}}\qquad p,r\in[1,3] \tag{4.68}$$

In the above formula $D\Phi_{s_t}$ is the difference between the current and the previous value of the unknown Φ_{s_t}, while $\frac{\partial \hat{\boldsymbol{C}}^t_{ps}}{\partial \boldsymbol{\Phi}_r}$ and $\frac{\partial \hat{\boldsymbol{K}}^t_{ps}}{\partial \boldsymbol{\Phi}_r}$ are obtained numerically according to:

$$\frac{\partial \boldsymbol{X}^t}{\partial \boldsymbol{\Phi}_r} = \begin{bmatrix} \frac{\partial X_{1,t}}{\partial \Phi_{r_1}} & \frac{\partial X_{1,t}}{\partial \Phi_{r_2}} & \cdots & \frac{\partial X_{1,t}}{\partial \Phi_{r_{nn}}} \\ \frac{\partial X_{2,t}}{\partial \Phi_{r_1}} & \frac{\partial X_{2,t}}{\partial \Phi_{r_2}} & \cdots & \frac{\partial X_{2,t}}{\partial \Phi_{r_{nn}}} \\ \vdots & \vdots & & \vdots \\ \frac{\partial X_{nn,t}}{\partial \Phi_{r_1}} & \frac{\partial X_{nn,t}}{\partial \Phi_{r_2}} & \cdots & \frac{\partial X_{nn,t}}{\partial \Phi_{r_{nn}}} \end{bmatrix} \qquad r \in [1,3]$$

$$\begin{aligned} \frac{\partial X_{i,j}}{\partial \Phi_{1_v}} &= \frac{X_{i,j}\left(\Phi_{1_1}, \Phi_{1_2}, \cdots, \Phi_{1_v} + \Delta\Phi_1, \cdots, \Phi_{1_{nn}}, \boldsymbol{\Phi_2}, \boldsymbol{\Phi_3}\right) - X_{i,j}\left(\boldsymbol{\Phi_1}, \boldsymbol{\Phi_2}, \boldsymbol{\Phi_3}\right)}{\Delta\Phi_1} \\ \frac{\partial X_{i,j}}{\partial \Phi_{2_v}} &= \frac{X_{i,j}\left(\boldsymbol{\Phi_1}, \Phi_{2_1}, \Phi_{2_2}, \cdots, \Phi_{2_v} + \Delta\Phi_2, \cdots, \Phi_{2_{nn}}, \boldsymbol{\Phi_3}\right) - X_{i,j}\left(\boldsymbol{\Phi_1}, \boldsymbol{\Phi_2}, \boldsymbol{\Phi_3}\right)}{\Delta\Phi_2} \\ \frac{\partial X_{i,j}}{\partial \Phi_{3_v}} &= \frac{X_{i,j}\left(\boldsymbol{\Phi_1}, \boldsymbol{\Phi_2}, \Phi_{3_1}, \Phi_{3_2}, \cdots, \Phi_{3_v} + \Delta\Phi_3, \cdots, \Phi_{3_{nn}}\right) - X_{i,j}\left(\boldsymbol{\Phi_1}, \boldsymbol{\Phi_2}, \boldsymbol{\Phi_3}\right)}{\Delta\Phi_3} \end{aligned} \tag{4.69}$$

where $\boldsymbol{X}$ stands for either $\hat{\boldsymbol{C}}_{ps}$ or $\hat{\boldsymbol{K}}_{ps}$.

In this way, by replacing (4.68) into (4.66), one finally obtains equation (4.70) in which $\boldsymbol{\Delta}\hat{\boldsymbol{C}} = \begin{bmatrix} \boldsymbol{\Delta}\hat{\boldsymbol{C}}_{11} & \boldsymbol{\Delta}\hat{\boldsymbol{C}}_{12} & \boldsymbol{\Delta}\hat{\boldsymbol{C}}_{13} \\ \boldsymbol{\Delta}\hat{\boldsymbol{C}}_{21} & \boldsymbol{\Delta}\hat{\boldsymbol{C}}_{22} & \boldsymbol{\Delta}\hat{\boldsymbol{C}}_{23} \\ \boldsymbol{\Delta}\hat{\boldsymbol{C}}_{31} & \boldsymbol{\Delta}\hat{\boldsymbol{C}}_{32} & \boldsymbol{\Delta}\hat{\boldsymbol{C}}_{33} \end{bmatrix}$ and $\boldsymbol{\Delta}\hat{\boldsymbol{K}} = \begin{bmatrix} \boldsymbol{\Delta}\hat{\boldsymbol{K}}_{11} & \boldsymbol{\Delta}\hat{\boldsymbol{K}}_{12} & \boldsymbol{\Delta}\hat{\boldsymbol{K}}_{13} \\ \boldsymbol{\Delta}\hat{\boldsymbol{K}}_{21} & \boldsymbol{\Delta}\hat{\boldsymbol{K}}_{22} & \boldsymbol{\Delta}\hat{\boldsymbol{K}}_{23} \\ \boldsymbol{\Delta}\hat{\boldsymbol{K}}_{31} & \boldsymbol{\Delta}\hat{\boldsymbol{K}}_{32} & \boldsymbol{\Delta}\hat{\boldsymbol{K}}_{33} \end{bmatrix}$ are the tangent capacitance and hydraulic conductivity matrices.

$$\begin{aligned} \begin{Bmatrix} \boldsymbol{\delta\Phi_1} \\ \boldsymbol{\delta\Phi_2} \\ \boldsymbol{\delta\Phi_3} \end{Bmatrix}_n^{k+1} &= \begin{bmatrix} \frac{\partial \boldsymbol{\Psi_1}\left(\boldsymbol{\Phi}_n^k\right)}{\partial \boldsymbol{\Phi_1}} & \frac{\partial \boldsymbol{\Psi_1}\left(\boldsymbol{\Phi}_n^k\right)}{\partial \boldsymbol{\Phi_2}} & \frac{\partial \boldsymbol{\Psi_1}\left(\boldsymbol{\Phi}_n^k\right)}{\partial \boldsymbol{\Phi_3}} \\ \frac{\partial \boldsymbol{\Psi_2}\left(\boldsymbol{\Phi}_n^k\right)}{\partial \boldsymbol{\Phi_1}} & \frac{\partial \boldsymbol{\Psi_2}\left(\boldsymbol{\Phi}_n^k\right)}{\partial \boldsymbol{\Phi_2}} & \frac{\partial \boldsymbol{\Psi_2}\left(\boldsymbol{\Phi}_n^k\right)}{\partial \boldsymbol{\Phi_3}} \\ \frac{\partial \boldsymbol{\Psi_3}\left(\boldsymbol{\Phi}_n^k\right)}{\partial \boldsymbol{\Phi_1}} & \frac{\partial \boldsymbol{\Psi_3}\left(\boldsymbol{\Phi}_n^k\right)}{\partial \boldsymbol{\Phi_2}} & \frac{\partial \boldsymbol{\Psi_3}\left(\boldsymbol{\Phi}_n^k\right)}{\partial \boldsymbol{\Phi_3}} \end{bmatrix}^{-1} \begin{Bmatrix} -\boldsymbol{\Psi_1}\left(\boldsymbol{\Phi}_n^k\right) \\ -\boldsymbol{\Psi_2}\left(\boldsymbol{\Phi}_n^k\right) \\ -\boldsymbol{\Psi_3}\left(\boldsymbol{\Phi}_n^k\right) \end{Bmatrix} = \\ &= \left(\boldsymbol{\Delta}\hat{\boldsymbol{C}}\left(\boldsymbol{\Phi}_n^k\right) + \Delta t \boldsymbol{\Delta}\hat{\boldsymbol{K}}\left(\boldsymbol{\Phi}_n^k\right)\right)^{-1} \begin{Bmatrix} -\boldsymbol{\Psi_1}\left(\boldsymbol{\Phi}_n^k\right) \\ -\boldsymbol{\Psi_2}\left(\boldsymbol{\Phi}_n^k\right) \\ -\boldsymbol{\Psi_3}\left(\boldsymbol{\Phi}_n^k\right) \end{Bmatrix} \end{aligned} \tag{4.70}$$

Returning now to the equation (4.64), and having in mind the structure of its components, the partitioned expression of the time residual has the form:

$$\begin{Bmatrix} \boldsymbol{\Psi}_1(\boldsymbol{\Phi}) \\ \boldsymbol{\Psi}_2(\boldsymbol{\Phi}) \\ \boldsymbol{\Psi}_3(\boldsymbol{\Phi}) \end{Bmatrix} = \begin{bmatrix} \hat{\boldsymbol{C}}_{11} & \hat{\boldsymbol{C}}_{12} & \hat{\boldsymbol{C}}_{13} \\ \hat{\boldsymbol{C}}_{21} & \hat{\boldsymbol{C}}_{22} & \hat{\boldsymbol{C}}_{23} \\ \hat{\boldsymbol{C}}_{31} & \hat{\boldsymbol{C}}_{32} & \hat{\boldsymbol{C}}_{33} \end{bmatrix} \left(\begin{Bmatrix} \boldsymbol{\Phi}_1 \\ \boldsymbol{\Phi}_2 \\ \boldsymbol{\Phi}_3 \end{Bmatrix} - \begin{Bmatrix} \boldsymbol{\Phi}_1 \\ \boldsymbol{\Phi}_2 \\ \boldsymbol{\Phi}_3 \end{Bmatrix}_{n-1} \right) + \\ + \Delta t \left(\begin{bmatrix} \hat{\boldsymbol{K}}_{11} & \hat{\boldsymbol{K}}_{12} & \hat{\boldsymbol{K}}_{13} \\ \hat{\boldsymbol{K}}_{21} & \hat{\boldsymbol{K}}_{22} & \hat{\boldsymbol{K}}_{23} \\ \hat{\boldsymbol{K}}_{31} & \hat{\boldsymbol{K}}_{32} & \hat{\boldsymbol{K}}_{33} \end{bmatrix} \begin{Bmatrix} \boldsymbol{\Phi}_1 \\ \boldsymbol{\Phi}_2 \\ \boldsymbol{\Phi}_3 \end{Bmatrix} - \begin{Bmatrix} \hat{\boldsymbol{F}}_1 \\ \hat{\boldsymbol{F}}_2 \\ \hat{\boldsymbol{F}}_3 \end{Bmatrix} \right) \tag{4.71}$$

Figure 4.1 shows the pseudocode incorporated in the proposed *THC* model to solve the boundary value problem.

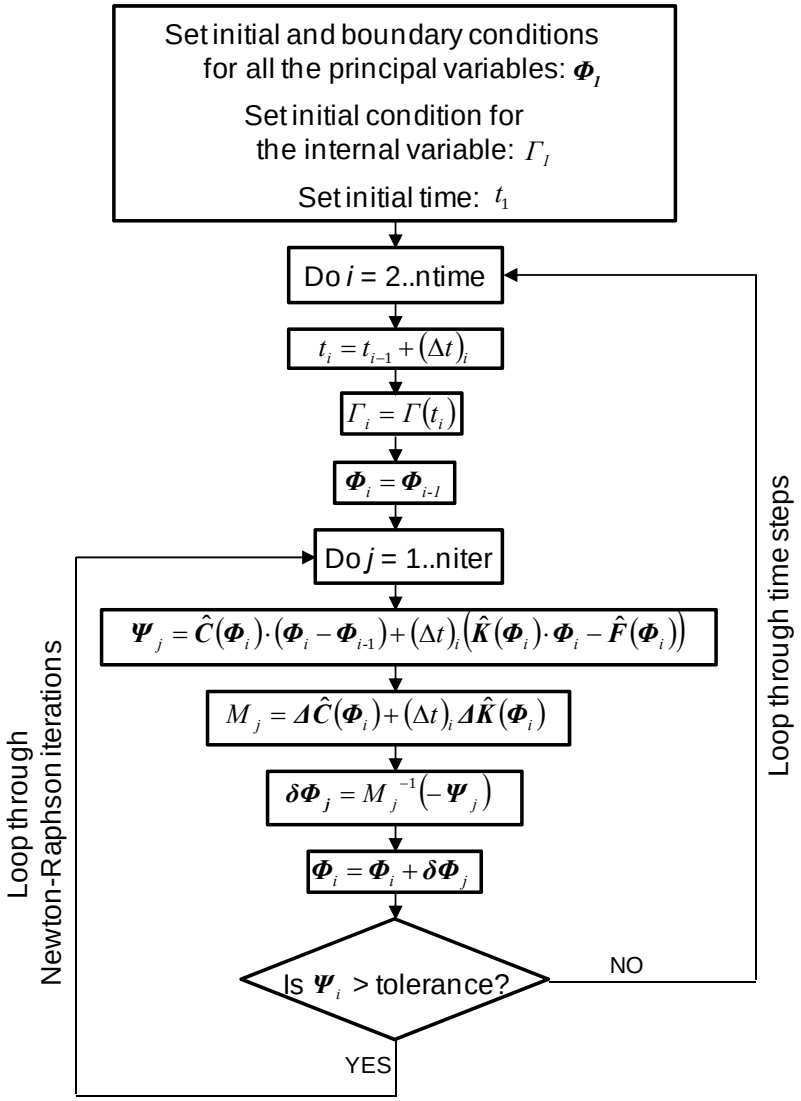

Figure 4.1 The pseudocode used to solve the boundary value problem

4.4 Summary

The numerical formulation used to find the temporal and spatial evolution of moisture, heat and concentration of the precipitates has been presented in this chapter. The

solution is obtained after solving a coupled system of equations by means of a finite element and a finite difference approximation. During the spatial discretisation, the continuum is split into non-overlaping subdomains over which the integrals corresponding to the Galerkin type weighted residual method are applied. The outcome represents a set of elemental matrix equations that are assembled to give a single set of non-linear ordinary first order differential equations with respect to time. Its variable is a single vector of unknowns that condenses the three principal variables characterising the moisture, temperature and chemical precipitation fields. The temporal discretisation is performed via an implicit forward finite difference approximation and the Newton-Raphson method. During a given time step, the initial value assigned to the vector of unknowns is updated iteratively until a convergence criterion is satisfied by an increment ensued from the truncated Taylor series expansion of the approximation error.

Chapter 5. Application and validation of the Microstructural Model and porosity function

5.1 Introduction

The proposed microstructural model *STOICH_HC2* traces the hydration kinetics of the Portland cement and replicates the quantitative evolution and chemical reactions of the mix constituents together with the transformation of the porous network. This is a stand-alone model able to provide a realistic development of the porosity function that is consistent with the sink term $\dot{m}_w^{hyd}$. Therefore, the results from *STOICH_HC2* are used as an input in all the subsequent numerical simulations presented in this thesis which predict the thermo-hygral behaviour of the cement-based materials subjected to various curing conditions.

The algorithm derived for replicating the development of the internal configuration of the cement paste provides information about the consumption and formation of the reactants and reaction products, the modification of the capillary and gel pore networks and also about the intensity of chemical shrinkage. The microstructural model incorporates a component defining the kinetics of the hydrolysis of the main clinker minerals that is further employed to solve the stoichiometry of the Portland cement hydration for four different saturation states. The resulting mass of consumed H_2O is used to quantify the ultimate degree of hydration and the water forms present in the gel hydrates. These liquid phases enable the computation of the capillary and total porosity functions that are needed in the *TH* and the *THC* formulation.

Section 5.2 deals with the validation of the *STOICH_HC2* model. First, the adopted hydration curve and stoichiometry are briefly specified. Then, data from two available plots found in the literature (Tennis and Jennings, 2000; Bernard et al., 2003) are considered for numerical comparison. These represent the numerically deduced variation of the relative volumes of the reacted cement phases with the hydration degree. In the first example the influence of the hydration curve is analysed by presenting an additional temporal distribution of hydrates obtained when using the

simplified hydration curve *HC1*, which takes into account only the nucleation and growth stage.

The validation of the adopted porosity function is described in Section 5.3. Some clarifying theoretical aspects needed to quantify the gel water forms and also the capillary and total porosities are introduced. Then, two porosity functions taken from the literature are presented. A set of predicted volume fractions, related to the gel water forms, are compared with existing experimental measurements. Also, stoichiometry-based porosity function is validated using data from the literature. Furthermore, this section presents a study on the influence of aggregates on the porosity development.

Finally, Section 5.4 provides the conclusions from the above work.

5.2 Application and Validation of the Microstructural Model

5.2.1 Introduction to examples

In the current microstructural model the evolution in time of the relative volumes of the reactants and reaction products is obtained by computing for each clinker phase the mass of mineral reacting during a given time step t. This mass is estimated by means of the hydration curve (3.5), taken from (Bernard et al., 2003) that considers the induction period, the nucleation and growth controlled hydration and the diffusive hydrolysis:

$$\Gamma_X(t) = \begin{cases} \dfrac{\Gamma_X^I}{t_X^I} t & ,t < t_X^I \\ \Gamma_X^I + 1 - \exp\left\{-\left[k_X (t - t_X^I)\right]^{K_X}\right\} & ,t_X^I \le t < t_{X,0}^D \\ 1 - \left(-\dfrac{\sqrt{2D_X}}{R_{ck}}\sqrt{t - t_{X,0}^D} + \sqrt[3]{1 - \Gamma_X^D}\right)^3 & ,t_{X,0}^D \le t \end{cases} \quad (3.5)$$

This curve will be referred from now on as *HC2* and its kinetic hydration parameters, defined in Chapter 3, are given in Appendix A, Table A. 3.

The quantity of the produced hydrates is calculated using the stoichiometric reactions from the Appendix A, Table A. 1 that account for the formation of *C-S-H*, CH, sulphoaluminates, sulphoaluminoferrites, C_4AH_{13}, $(F,A)H_3$, $C_3A(C\overline{S},CH)H_{12}$ and hydrogarnet. These stoichiometric equations in conjunction with the *HC2* curve form

the *STOICH_HC2* model which is validated in the following paragraphs. The numerical results in terms of relative volumes of reactants and hydrates are compared with the volume fractions estimated by Tennis and Jennings (2000) and Bernard et al. (2003).

5.2.2 Example 1: (Tennis and Jennings, 2000)

Tennis and Jennings (2000) have created a computational code for simulating the structure of the *C-S-H* gel using a set of chemical reactions that does not reflect the production of sulphoaluminoferrites, $(F,A)H_3$ and $C_3A(C\overline{S},CH)H_{12}$ which were reported in other research works (Jennings and Thomas, 2009; Mindess et al., 2003). They considered that the hydration curve (5.1), denoted from now on by *HC1*, is valid throughout the entire hydration process of each cement mineral*:*

$$\Gamma_X(t) = 1 - \exp\left\{-\left[k_X\left(\frac{t}{24} - t_X^I\right)\right]^{K_X}\right\} \tag{5.1}$$

where t is the hydration time (in hours), k_X is the rate constant, t_X^I is the initiation of the hydration in terms of time and K_X represents the reaction order. These parameters are listed in Appendix A, Table A. 3.

It must be noted that *HC1* disregards the induction period and the diffusion controlled hydration and, as Tennis and Jennings acknowledge, is “best suited to describing the nucleation and growth reactions” (Tennis and Jennings, 2000). In order to highlight the influence of the hydration curve on the proposed microstructural model, *HC1* will be employed in the current example in conjunction with the stoichiometric reactions from Table A. 1 to form the *STOICH_HC1* model. However, this version of the microstructural model will not be used to simulate the autogenous healing of cementitious materials and represents only a tool for validating *STOICH_HC2*.

Figure 5.1 and Table 5.1 illustrate the differences between the evolution of the reactions (individual or as a whole) when using *HC1* and *HC2*. All the degrees of hydration given by *HC1* are higher after the 10th day and therefore the hydrolysis is more rapid: in less than 60 days, between 91 and 100% of the reaction has occurred in the case of C_3A, C_3S and C_4AF. In contrast, when utilizing *HC2*, only 75% to 87% of the same three clinker phases have chemically combined with H_2O by the end of the 60th day. Furthermore, the slope of the *HC1* curves becomes more gentle after

approximately the 40th day, which means that for this type of hydrolysis, the amount of consumed/precipitated substance during a reference time interval Δt is smaller.

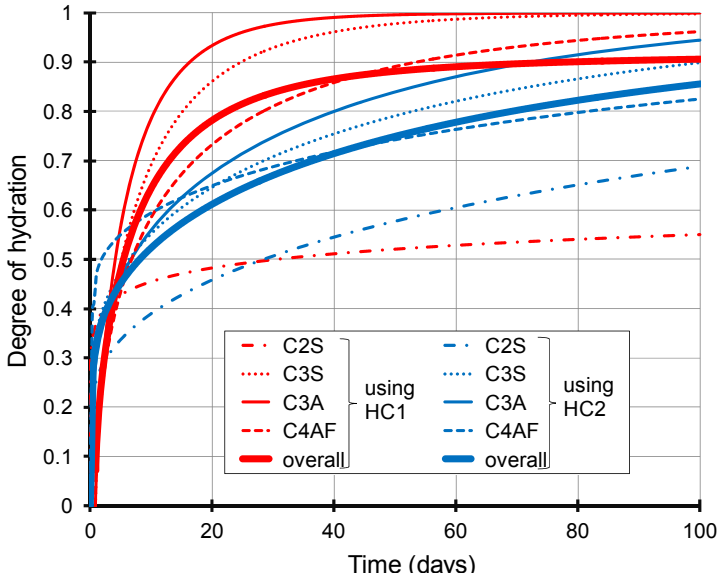

Figure 5.1 Hydration curves of the individual clinker minerals and of the overall cement paste according to *HC1* and *HC2*; water/cement ratio = 0.5

Table 5.1 Early-age behaviour of *HC1* and *HC2* functions

HC1		***HC2***	
Time interval [days]	Γ_X	**Time interval [days]**	Γ_X
0...0.2	$\Gamma_{C_4AF} > \Gamma_{C_3A} > \Gamma_{C_3S} > \Gamma_{C_2S}$	0...0.9	only C_2S reacts
0.2...8	$\Gamma_{C_4AF} > \Gamma_{C_3S} > \Gamma_{C_3A} > \Gamma_{C_2S}$	0.9...1.1	$\Gamma_{C_2S} > \Gamma_{C_4AF} > \Gamma_{C_3S} > \Gamma_{C_3A}$
8...15	$\Gamma_{C_4AF} > \Gamma_{C_3A} > \Gamma_{C_3S} > \Gamma_{C_2S}$	1.1...1.6	$\Gamma_{C_2S} > \Gamma_{C_4AF} > \Gamma_{C_3A} > \Gamma_{C_3S}$
15...21	$\Gamma_{C_3A} > \Gamma_{C_4AF} > \Gamma_{C_3S} > \Gamma_{C_2S}$	1.6...2.3	$\Gamma_{C_2S} > \Gamma_{C_3A} > \Gamma_{C_4AF} > \Gamma_{C_3S}$
>21	$\Gamma_{C_3A} > \Gamma_{C_3S} > \Gamma_{C_4AF} > \Gamma_{C_2S}$	2.3...3.2	$\Gamma_{C_2S} > \Gamma_{C_3A} > \Gamma_{C_3S} > \Gamma_{C_4AF}$
		3.2...3.9	$\Gamma_{C_3A} > \Gamma_{C_2S} > \Gamma_{C_3S} > \Gamma_{C_4AF}$
		3.9...4.9	$\Gamma_{C_3A} > \Gamma_{C_3S} > \Gamma_{C_2S} > \Gamma_{C_4AF}$
		>4.9	$\Gamma_{C_3A} > \Gamma_{C_3S} > \Gamma_{C_4AF} > \Gamma_{C_2S}$

Table 5.1 suggests that in the first part of the hydration reaction, *STOICH_HC1* and *STOICH_HC2* models will produce distinct evolutions of the volume fractions of the hydrates since according to the *HC1* curves, the most consumed minerals are C_4AF and C_3A, whilst according to the *HC2* curves, C_2S and C_3A are the most reactive compounds. Nevertheless, after the point exceeding Γ_X = 0.52 (for *HC1*) and 0.38 (for

HC2) until the end of the hydrolysis, the magnitude of the individual hydration degrees follow the same trend for both types of curves: $\Gamma_{C_3A} > \Gamma_{C_3S} > \Gamma_{C_4AF} > \Gamma_{C_2S}$.

5.2.2.1 *Model Data*

This example investigates the hydration of the average Type I Portland cement considered in (Tennis and Jennings, 2000). The reported mix, denoted here by *PC1*, has the mass characteristics and chemical composition given in Table 5.2 and Table 5.3.

Table 5.2 Mix characteristics of the investigated cement pastes and concretes

		PC1	***PC2***	***CO***	***BO***	***M***	***L***	***H***
$\frac{w}{c}$		0.500	0.500	0.348	0.487	0.400	0.280	0.680
c	[kg/m^3]	507	620	1501	353	423	310	541
w_{fagg}	[kg/m^3]	1519	1241	-	744	736	782	647
w_{cagg}	[kg/m^3]	-	-	-	1192	1016	955	1055
$\frac{w_{SP}}{c}$	%	-	-	-	-	0.5	-	2.0
ρ_c	[kg/m^3]	3168	3168	3168	3168	3150	3150	3150
ρ_{fagg}	[kg/m^3]	2560	2650	-	2650	2650	2650	2650
ρ_{cagg}	[kg/m^3]	-	-	-	2770	2770	2770	2770
ρ_{SP}	[kg/m^3]	-	-	-	-	2300	-	2300
ρ_{dry}	[kg/m^3]	-	-	1498	2290	2176	2046	2252
V_{ea}	[m^3/m^3]	0.003	0.025	0.005	0.005	0.051	0.051	0.048

The resulting masses of reactants and reaction products are transformed into volume fractions considering the densities specified in Appendix A, Table A. 4.

Table 5.3 Chemical composition of the investigated Portland cements

		PC1	*PC2*	*CO / BO*	*M / L / H*
f_{C_3A}	[%]	10.00	7.60	3.03	10.00
f_{C_3S}	[%]	55.00	54.30	57.28	57.00
f_{C_2S}	[%]	18.00	18.70	23.98	14.00
f_{C_4AF}	[%]	8.00	7.30	7.59	8.00
f_{SO_3}	[%]	–	–	2.04	3.50
f_{GGBF}	[%]	–	–	0	–
f_{FA}	[%]	–	–	0	–
f_{FA-CaO}	[%]	–	–	0	–
f_{MgO}	[%]	–	–	0.80	1.30
$f_{freeCaO}$	[%]	–	–	0.53	0.53
f_{cem}	[%]	–	–	100	99.50 / 0 / 98.00
f_{gypsum}	[%]	4.00	5.70	4.39	7.52
f_{inert}	[%]	5.00	4.80	3.73	3.48
B Blaine fineness	[m^2/kg]	–	–	311.6	358.0

5.2.2.2 *Results and Discussions*

Figure 5.2 illustrates the development of the relative volumes of the phases of the paste *PC1* versus the overall hydration degree when *STOICH_HC2* is employed. The capillary water existing in the porous medium is represented by the H_2O volume fraction, whilst the liquid phases encountered in the gel precipitates are implicitly included in the volume fractions of the hydrates. The plot shows that both the unreacted and the combined water vary linearly with the hydration degree. C_3S, C_3A, C_4AF and gypsum are depleted by the time Γ_{PC} reaches unity. All the three hydration stages of C_3A and C_4AF are reached. Stage 2 initiates at Γ_{PC} = 0.1 due to the exhaustion of the calcium sulphate. Stage 3, on the other hand, triggered by the depletion of the trisulphoaluminate and trisulphoaluminoferrite respectively, begins at Γ_{PC} = 0.32 for C_3A and at Γ_{PC} = 0.60 for C_4AF. It should be specified as well that only the second branch from Stage 3 is active during the last 26% of the overall hydration of the C_3A. The distribution given by the *STOICH_HC2* model overlaps in Figure 5.3 (a) with the numerical outcome computed by Tennis and Jennings (2000). In *STOICH_HC2* all the four minerals combine with H_2O as soon as they are mixed.

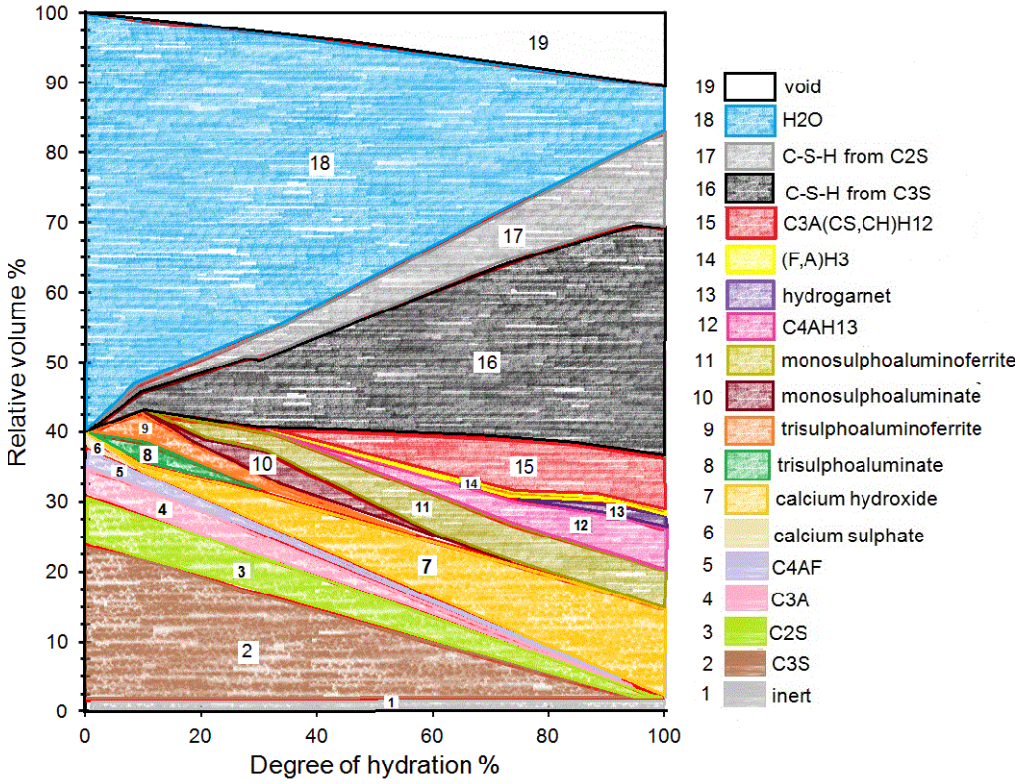

Figure 5.2 Evolution of the relative volumes of the phases of the *PC1* paste when using *STOICH_HC2*

This fact generates an evolution of the volume fractions less compliant with Tennis and Jennings' findings during Stage 1 and Stage 2, since the values presented by these researchers were computed using a *HC1* curve. However, after Γ_{PC} = 0.50 the results provided by the *STOICH_HC2* model begin to substantially approach the values cited in (Tennis and Jennings, 2000), especially in terms of water in the capillary pores. On the other hand, the distribution obtained when employing *STOICH_HC1* (Figure 5.3 (b)) follows more closely the findings published by Tennis and Jennings (2000) during Stages 1 and 2, but generates an overestimation of the capillary porosity and an underestimation of the gel products towards the complete hydration. This behaviour is due to the different stoichiometry used in (Tennis and Jennings, 2000).

Table 5.5 summaries part of the results calculated at Γ_{PC} = 1 and shows that there is a better match between *STOICH_HC2* and Tennis and Jennings' results in terms of capillary porosity, volume fraction of *C-S-H* and volume fraction of total gel hydrates.

(a)

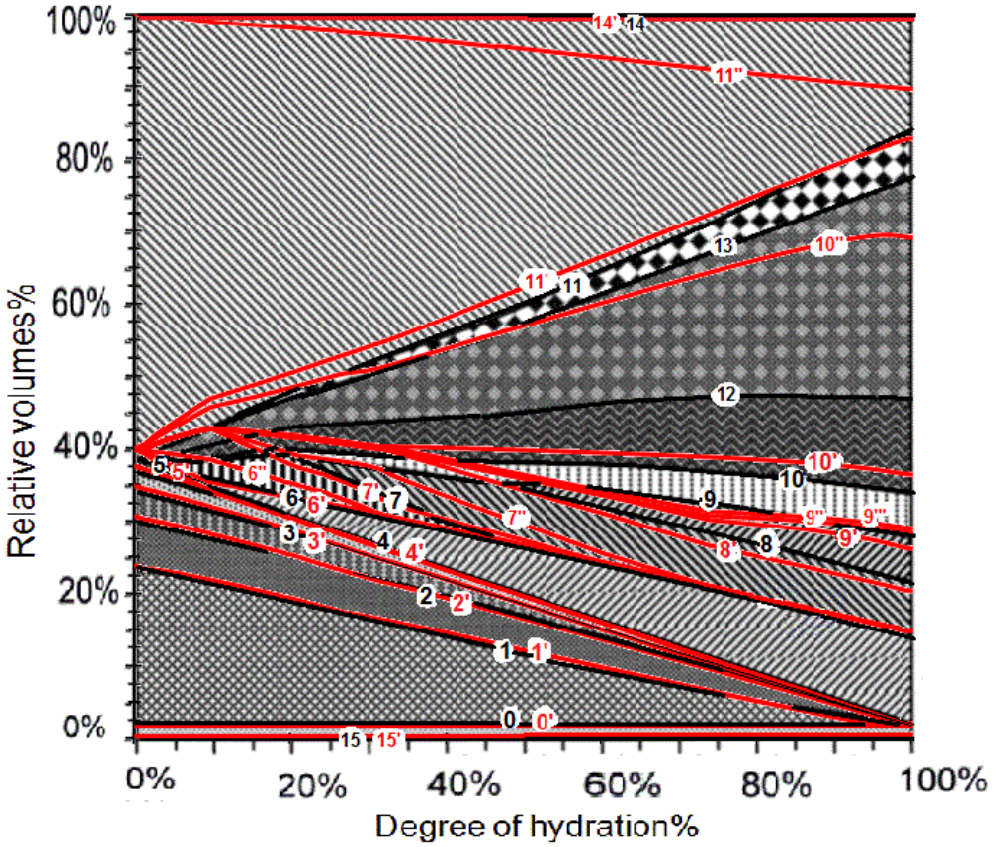

For legend see Table 5.4

(b)

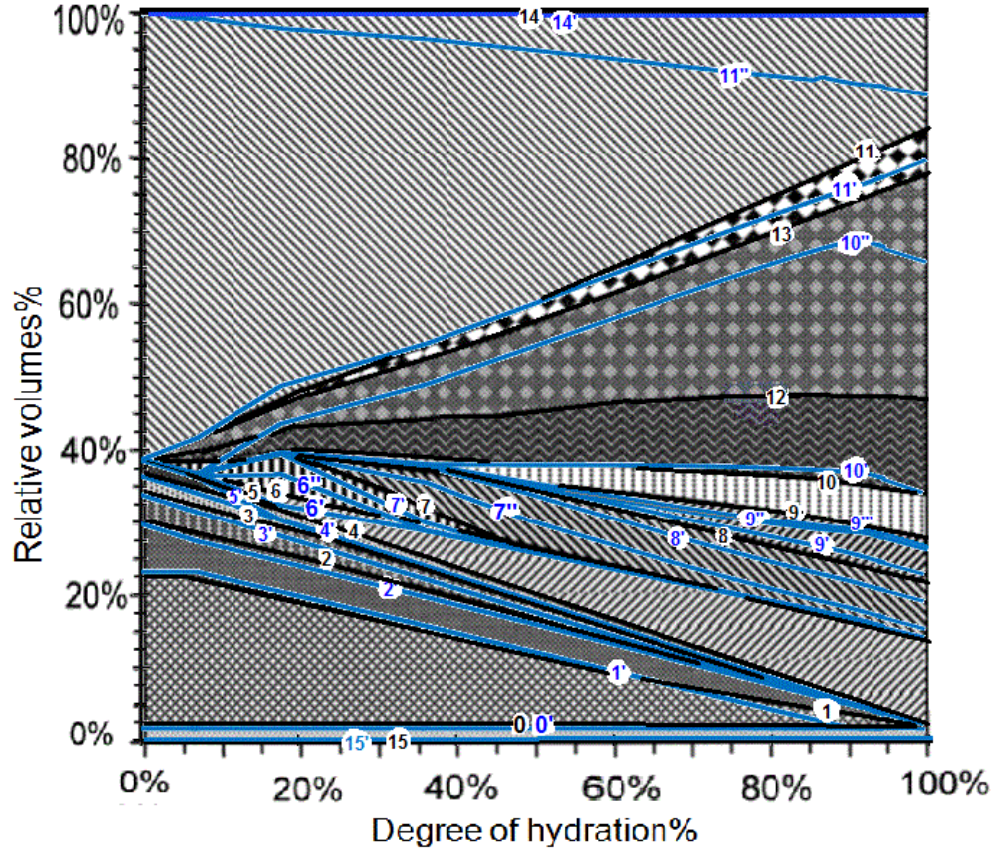

For legend see Table 5.4

Figure 5.3 Superposition of the hydration representation using data from (Tennis and Jennings, 2000) (black lines) and from the models (a) *STOICH_HC2* (red lines) and (b) *STOICH_HC1* (blue lines)

Table 5.4 Description of the legend of Figure 5.3

(Tennis and Jennings, 2000)		***STOICH_HC2* and *STOICH_HC1* models**	
Area between lines	**Hydration product**	**Area between lines**	**Hydration product**
15-0	inert material	15'-0'	inert material
0-1	C_3S	0'-1'	C_3S
1-2	C_2S	1'-2'	C_2S
2-3	C_3A	2'-3'	C_3A
3-4	C_4AF	3'-4'	C_4AF
4-5	$C\overline{S}H_2$	4'-5'	$C\overline{S}H_2$
4-6	CH	4'-6'	CH
6-7	trisulphoaluminate	6'-6''	trisulphoaluminate
		6''-7'	trisulphoaluminoferrite
7-8	monosulphoaluminate	7'-7''	monosulphoaluminate
		7''-8'	monosulphoaluminoferrite
8-9	C_4AH_{13}	8'-9'	C_4AH_{13}
9-10	hydrogarnet	9'-9''	hydrogarnet
		9''-9'''	$(F, A)H_3$
		9'''-10'	$C_3A(C\overline{S},CH)H_{12}$
10-12	high density *C-S-H*	10'-10''	*C-S-H* from hydration of C_3S
12-13	low density *C-S-H*	10''-11'	*C-S-H* from hydration of C_2S
13-11	*C-S-H* porosity		
11-14	capillary porosity	11'-11''	H_2O in capillary pores
		11''-14'	voids

Table 5.5 Comparison of ultimate volume fractions for the hydration of *PC1*

Volume fractions at Γ_{PC} = 1	***STOICH_HC2***	***STOICH_HC1***	**(Tennis and Jennings, 2000)**
capillary pores	0.18	0.25	**0.16**
C-S-H	0.47	0.43	**0.50**
total gel hydrates (*C-S-H* + aluminates+ aluminoferrites)	0.68	0.65	**0.70**

These three relative volumes are in fact sufficient to decide upon the efficiency of the proposed microstructural model because, for the evaluation of the capillary and gel porosities, solely the ultimate masses of the water forms are required. Thus it is reasonable to conclude that the *STOICH_HC2* model provides a good quantitative approximation of the pore network.

5.2.3 Example 2: (Bernard et al., 2003)

5.2.3.1 *Model Data*

The second example is taken from the work of Bernard et al. (2003), which examines the hydrolysis of the Type I ordinary Portland cement *PC2* described in Table 5.2 and Table 5.3. The hydration kinetics obey the principles of the *STOICH_HC2* model and are evaluated by means of the parameters provided in Appendix A, Table A. 3.

5.2.3.2 *Results and Discussions*

Under the above conditions, the evolution of the relative volumes in Figure 5.4 shows, on one hand, that Γ_{PC} = 0.17 and Γ_{PC} = 0.43 delineate the three stages of the hydration of C_3A and, on the other, that the reaction pattern of C_4AF stops in Stage 2 because the previously precipitated amount of $C_6(A,F)\overline{S}_3H_{32}$ is sufficient to consume all the remaining C_4AF.

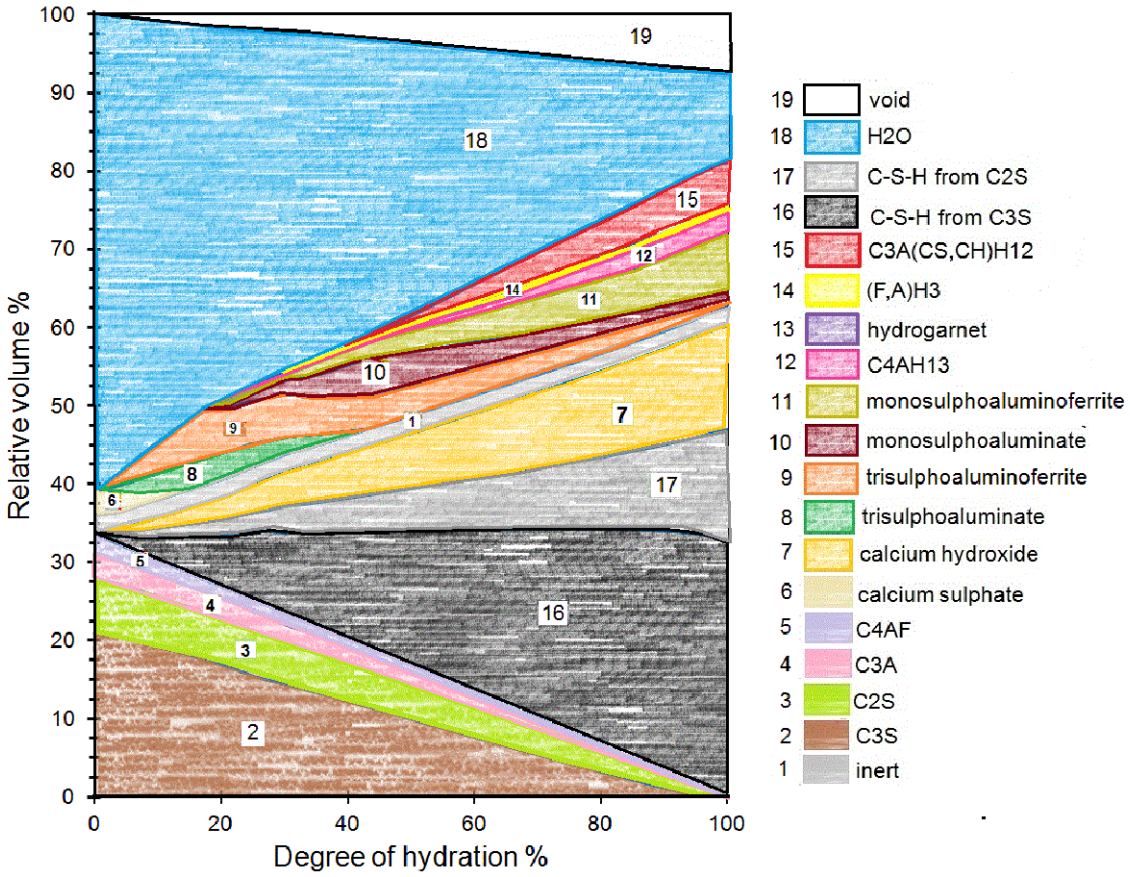

Figure 5.4 Evolution of the relative volumes of the phases of the *PC2* paste from *STOICH_HC2* highlighting all the phases

(b)

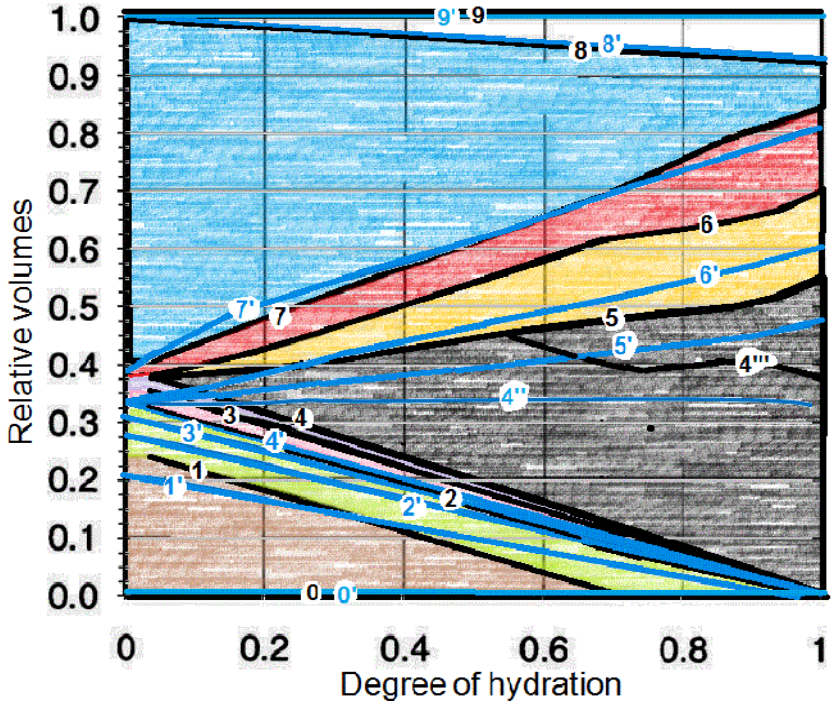

For legend see Table 5.6

Figure 5.5 Evolution of the relative volumes of the phases of the *PC2* paste from *STOICH_HC2* (blue lines) and from (Bernard et al., 2003) (black lines)

Table 5.6 Representation of hydration product development from Figure 5.5

(Bernard et al., 2003)		***STOICH_HC2***	
Area between lines	**Hydration product**	**Area between lines**	**Hydration product**
0-1	C_3S	0'-1'	C_3S
1-2	C_2S	1'-2'	C_2S
2-3	C_3A	2'-3'	C_3A
3-4	C_4AF	3'-4'	C_4AF
4-4'''	low density *C-S-H*	4'-4''	*C-S-H* from hydration of C_3S
4'''-5	high density *C-S-H*	4''-5'	*C-S-H* from hydration of C_2S
5-6	CH	5'-6'	CH
6-7	aluminates	6'-7'	gypsum + tri- and monosulphoaluminate + + tri- and monosulphoaluminoferrites + + hydrogarnet + C_4AH_{13} + $(F,A)H_3$ + + $C_3A(C\bar{S},CH)H_{12}$ +
7-8	H_2O	7'-8'	H_2O in capillary pores
8-9	voids	8'-9'	voids

If compared with Bernard et al.'s results (Figure 5.5), one can observe a slightly larger discrepancy in the variations of C_3S and aluminates, but a smaller difference for the formation of *C-S-H* and CH. These deviations are most likely related to the stoichiometric reactions, unspecified in Bernard et al. (2003). Despite this situation, the

fact that the current ultimate volume fraction of capillary pores (f_{cap}^{ult} = 0.19) matches reasonably the reported value (f_{cap}^{ult} = 0.14) justifies the conclusion that the overall capillary and gel water are well estimated by the *STOICH_HC2* model.

5.3 Application and Validation of porosity functions

5.3.1 Introduction to examples

5.3.1.1 *Adopted porosity function*

The proposed microstructural model enables the computation of the porosity function which is an essential parameter in the governing equilibrium equations, used in the *THC* model. As was pointed out previously, the numerical simulation of the hydration reaction suggests a linear dependency of both capillary and gel porosities on Γ_{PC}. In the following section equations (3.11) and (3.14) are put together into equation (5.2) in order to define the variation of the pore network through the entire hydrolysis of the Portland cement.

$$\eta_j(\Gamma)=\begin{cases} \dfrac{w-\Gamma\sum_i w_i^{ult}}{w-\Gamma_0\sum_i w_i^{ult}}\eta_j(\Gamma_0) & ,\Gamma<\Gamma_0 \\ \dfrac{\dfrac{w}{c}+\dfrac{\rho_w V_{ea}}{c}-\left[V_s(\Gamma)\dfrac{\rho_w}{c}+\Gamma\cdot C_{\eta\_S}^{j}\right]}{\dfrac{\rho_w}{\rho_c}+\dfrac{w}{c}+\dfrac{\rho_w V_{ea}}{c}+\dfrac{\rho_w\sum V_{agg}}{c}+\dfrac{\rho_w\sum V_{SCM}}{c}} & ,\Gamma\geq\Gamma_0 \end{cases} \tag{5.2}$$

This equation will be used in the current thesis to validate both the *TH* and *THC* models. The terms w_i^{ult} that represents the amount of water forms populating the gel structure of the hydrates at the end of hydration are evaluated, as was discussed in Chapter 3, using the colloid model presented in (Jennings, 2008). Jennings has correlated the liquid phases with the number of water moles remaining within the *C-S-H* during drying experiments and summarised his findings regarding the water distribution along a desiccation process in an isotherm similar to the one presented in Figure 5.6. Four main relative humidity intervals and their associated mole numbers, listed in Appendix A, Table A. 2, dictate the type of H_2O found within the hydrate. It should be remarked that although the desorption curve indicates 2.3 moles of H_2O at 11% *RH*, a

threshold equal to 2.1 is considered in the calculations since it is used by Jennings and Thomas (2009).

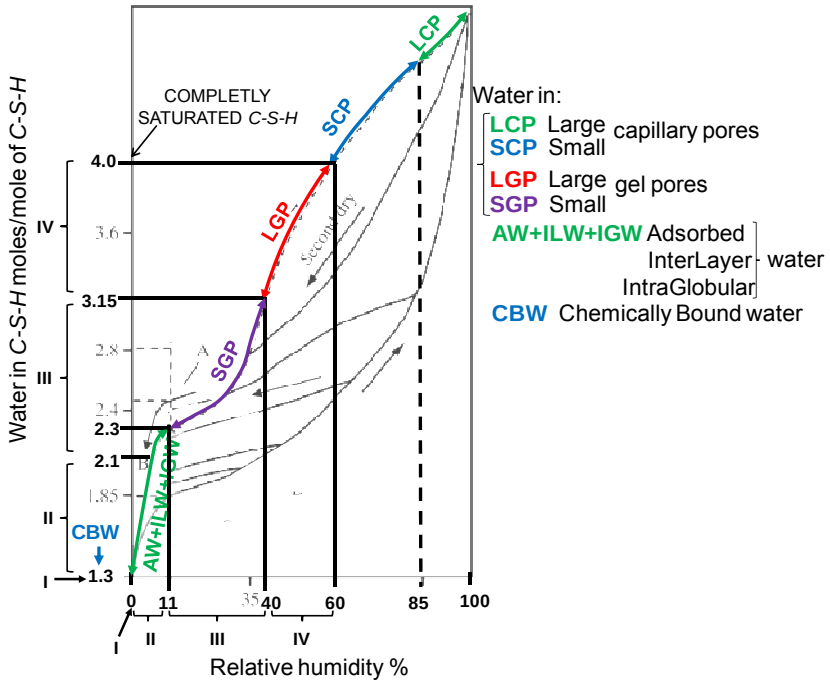

Figure 5.6 Distribution of the water forms within the *C-S-H* gel based on the data collected from (Jennings, 2008)

Regarding the $V_s(\Gamma)$ term, it should be said that the variations given in equations (5.3) and (5.4) where chosen for the investigated cement paste and concrete mixes, respectively. These relationships were obtained by fitting the laboratory measurements of the autogenous shrinkage performed in (Baroghel-Bouny, 1994).

$$V_s^{BO}(\Gamma)=\begin{cases}0 & ,0\le\Gamma<0.29\\ -40+140\Gamma & ,0.29\le\Gamma<0.76\\ -200+350\Gamma & ,0.76\le\Gamma<0.92\\ -1650+1920\Gamma & ,0.92\le\Gamma\le1\end{cases} \tag{5.3}$$

$$V_s^{CO}(\Gamma)=\begin{cases}0 & ,0\le\Gamma<0.48\\ -950+2000\Gamma & ,0.48\le\Gamma<0.91\\ -450+2100\Gamma^5 & ,0.91\le\Gamma\le1\end{cases} \tag{5.4}$$

5.3.1.2 *Alternative porosity functions*

In their textbook dedicated to the concrete technology Neville and Brooks (2003), derive the following capillary and total porosity functions based on the experimental data taken from Powers and Brownyard (1948) and presented here in Table 5.7:

$$\eta_j^{N\&B}(\Gamma) = \frac{\frac{w}{c} + \frac{V_{ea}}{c} - \Gamma \cdot C^j_{\eta\_N\&B}}{0.317 + \frac{w}{c} + \frac{V_{ea}}{c} + \frac{\sum V_{agg}}{c}} \tag{5.5}$$

where the superscript $N\&B$ shows that the formula was proposed by Neville and Brooks (2003), the subscript j represents the type of porosity (capillary or total), whilst the constants $C^j_{\eta\_N\&B}$ are equal to 0.36 for the capillary porosity and to 0.17 for the total porosity.

Table 5.7 Results of the *STOICH_HC2* model in terms of gel water forms

		PC1	***PC2***	***CO***	***BO***	**(Neville and Brooks, 2003)**
(1)	$\frac{w^{ult}_{CBW}}{c}$	0.165	0.169	0.173	0.173	**0.230**
(2)	$\frac{w^{ult}_{CBW} + w^{ult}_{AW+ILW+IGW}}{c}$	0.245	0.239	0.243	0.243	
(3)	$\frac{V^{ult}_{LGP} + V^{ult}_{SGP} + V^{ult}_{AW+ILW+IGW}}{V_{SSRC} + V^{ult}_{CBW} + {}^{ult}_{LGP} + V^{ult}_{SGP} + V^{ult}_{AW+ILW+IGW}}$	0.327	0.315	0.315	0.313	**0.280**
(4)	$\frac{V^{ult}_{voids}}{V_C}$	0.222	0.195	0.184	0.158	**0.185**

Baroghel-Bouny and Chaussadent, on the other hand, have found that for a specific cement paste and concrete mix (t.i. *CO* and *BO*, respectively, from Table 5.2 and Table 5.3), the capillary and total porosities $\eta_{cap}(\Gamma_{B\&C})$ and $\eta_{tot}(\Gamma_{B\&C})$ reach 5.2% and 30.3% at the degree of hydration $\Gamma^{CO}_{B\&C}$ = 0.76 and 5.8% and 12.2% at $\Gamma^{BO}_{B\&C}$ = 0.9, respectively (Baroghel-Bouny and Chaussadent, 1995). In the current investigation these values are employed in the linear relationship (5.6):

$$\eta_j^{B\&C}(\Gamma) = \left[\eta_j(\Gamma_{B\&C}) + \left(\eta_0 - \eta_j(\Gamma_{B\&C})\right)\frac{\Gamma_{B\&C} - \Gamma}{\Gamma_{B\&C}}\right]\frac{1}{100} \tag{5.6}$$

where the superscript $B\&C$ shows that the formula was proposed by Baroghel-Bouny and Chaussadent (1995) and η_0 is the initial volume fraction of the pore system.

5.3.2 Comparison of various estimates of water form quantities.

The cement mixtures enumerated in Table 5.2 and Table 5.3 are examined via the *STOICH_HC2* model for each saturation range. The masses of the water forms are

computed according to equation (3.8), while the volumes are estimated using the densities given in Appendix A, Table A. 2. The results are compared with data available in the literature (Neville and Brooks, 2003) in Table 5.7.

The row (1) estimates the quantity of combined water per mass of dry cement. After drying at 105°C, the normally cited average value equals to 0.23. This quantity exceeds the mass fraction of *CBW* (obtained after a D-drying – vacuum drying to the equilibrium vapour pressure above ice at – 79˚C (~ 6.7 x 10^{-2} Pa)), but if the *AW+ILW+IGW* is added (the *RH* approaches 11%), then the two values are comparable, as can be seen in row (2). The row (3) assesses the ratio between the volumes of gel water and cement gel. In this case the discrepancy in magnitude might be attributed to the liquid found in *LGP*. This water form populates the gel pores, but has a similar behaviour as the capillary water and so, during a desiccations experiment, part of it may be neglected. The last volume fraction given in (4) measures the chemical shrinkage built up due to the density difference between reactants and reaction products. In this instance, the ratio depends heavily on the densities of the reaction products considered.

5.3.3 Validation of the Porosity functions. Results and Discussion

Figure 5.7 depicts the progression of the stoichiometry and experimentally-based porosity functions for the *CO* and *BO* mixes. According to the *STOICH_HC2* model, the hydration of *CO* ceases at Γ_{PC} = 0.83 due to an insufficient water cement ratio, while the hydrolysis of *BO* reaches Γ_{PC} = 1. The resulting material coefficients are equal to $C_{\eta\_S}^{cap}$ = 0.237 and $C_{\eta\_S}^{tot}$ = 0.122 for *CO* and $C_{\eta\_S}^{cap}$ = 0.279 and $C_{\eta\_S}^{tot}$ = 0.144 for *BO*.

When comparing with Baroghel-Bouny and Chaussadent's results, the observed discrepancies appear because the considered pore radii limits for the capillary, gel and total porosities are different from the pore radii provided in Jennings' colloidal model. In their article, Baroghel-Bouny and Chaussadent assume the radii of the capillary pores to vary between 37 - 40Å and 60μm and the total porosity to include pores with radii from 10Å to 60μm. On the other hand, in the stoichiometry-based approach, the capillary system excludes *GW* (see Figure 3.1) and goes down to pores having the radius equal to 60Å, while the total porosity includes also the voids smaller than 5Å. It is therefore expected that the total porosity will be greater if equation (5.2) is used. If the total porosity is consistent with a demarcating pore radius of approximately 10Å, that is it disregards the chemically bound and half of the absorbed water, then the

updated stoichiometry-based function (5.2) (red long-dash double-dot lines) almost coincides with the porosity development from (Neville and Brooks, 1987) and is very close to that given by Baroghel-Bouny and Chaussadent (1995).

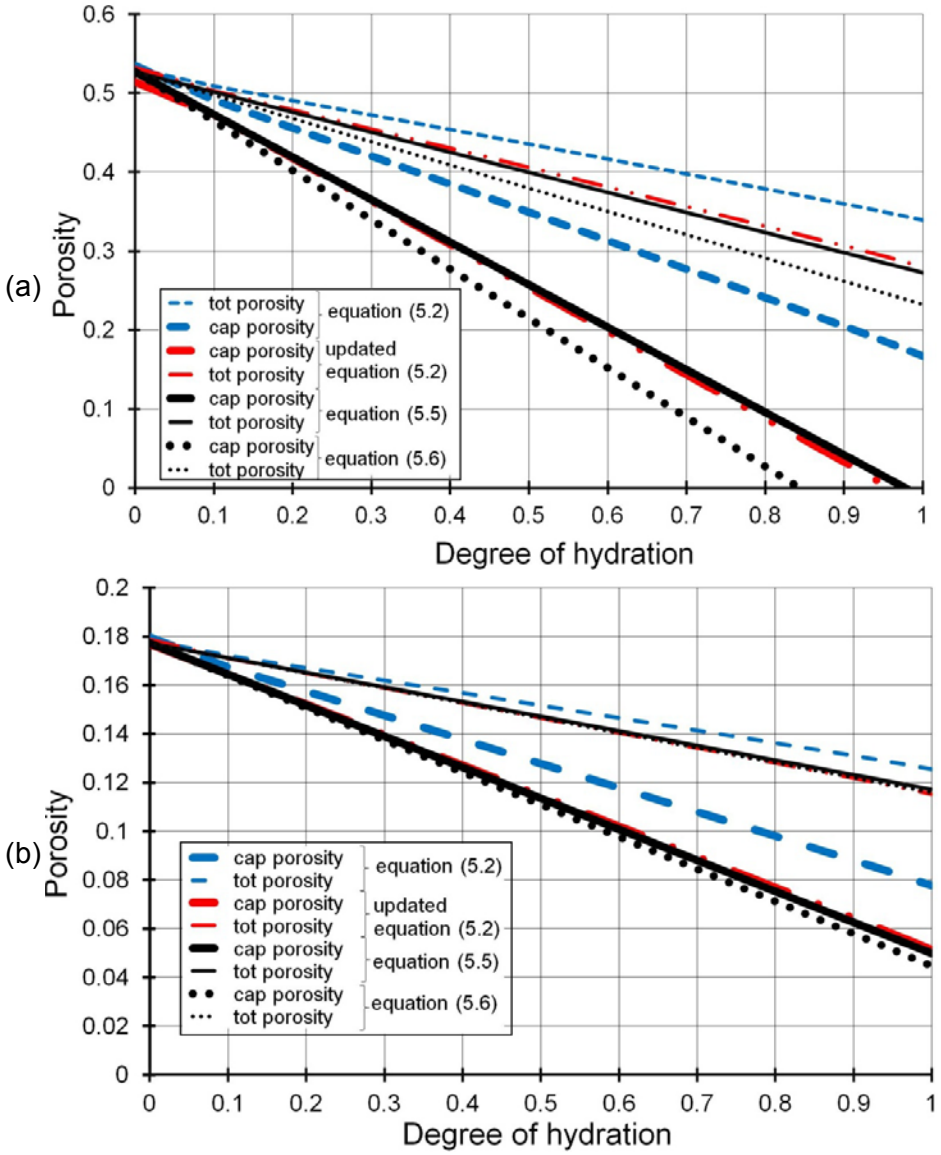

Figure 5.7 Porosity development for (a) *CO* and (b) *BO*

5.3.4 Impact of Aggregates on the Porosity Development

The current hygro-thermal model for concrete takes into account the contribution of the internal porosity of the aggregate on the behaviour of the investigated material. As was described in Chapter 3, in the current simulations the pores of the aggregates particles are modelled as water reservoirs that are filled with liquid during the first minutes of curing and then are emptied due to desiccation. This transfer takes place as long as the aggregate particle is not covered by a gel-like barrier. Detailed experimental data on the water absorption capacity of the aggregate embedded in the cement paste is

rather scarce in the literature. Therefore, a basic experimental study, focused on early-age behaviour, was performed in order to include in the modelling the effect of the aggregate absorption. 8 sets of samples comprising 6 to 7 oven-dried (for 24 hours) limestone particles with sizes between 10 and 14 mm, were weighed and immersed in 110 cm^3 steel containers, partially filled with a grout having the water/cement ratio = 0.5. The containers were then emptied at 1 hour intervals and the aggregate particles weighed after being cleaned with a cloth soaked in acetone. The last reading was taken at 8 hours because after that moment it was no longer possible to extract the individual particles without the use of impact tools. The whole procedure was repeated 3 times and the average results in terms of absorption percentages are displayed in Figure 5.8. The formation of the gel-like barrier is assumed to occur around Γ = 30%, which corresponds to approximately 24 hours. Thus, the decreasing trend of the absorption curve, shown in Figure 5.8, persists until the end of the first day of curing. After this point, the water is blocked in the aggregate pores, which means that the absorption is constant and that $\dot{m}_w^{a/d\_agg}$ – the rate of absorption/desorption by the aggregate – is zero.

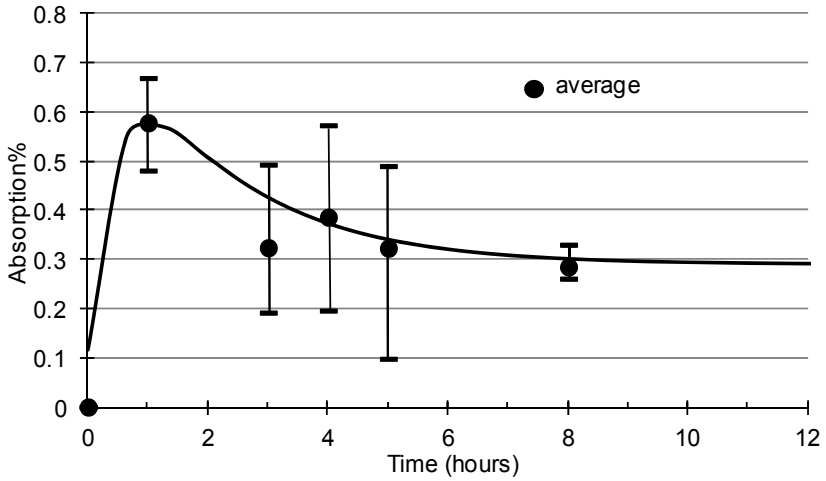

Figure 5.8 Water absorption of a representative coarse aggregate

The variation of aggregate water content, from the time of mixing, may be approximated using the formula given in equation (5.7):

$$m_w^{a/d\_agg}(t) = m_p \left\{ r_0 + \left[(r - r_0) + \alpha \exp\left(-c_1 \frac{t}{t_p} \right) \right] \left[1 - \exp\left(-c_2 \frac{t}{t_p} \right) \right] \right\} \qquad (5.7)$$

where m_p = 0.578 is the fully saturated moisture content, r = 0.5 represents the residual proportion of m_p present when the concrete first hardens, r_0 = 0 is the initial moisture content as a proportion of m_p, t_p = 1 is the time in hours at which peak absorption is reached, whilst c_1, c_2 and α are basic constant fixed at 0.5, 2.178 and

1.035, respectively.

The error bars in Figure 5.8 denote the considerable variability of the measured values. However, the amount of water penetrating the pores of the limestone particles may be considered second order in comparison with that used in hydration and thus the moderate inaccuracies in the derived aggregate sink-source function are unlikely to have a significant effect on overall computations of moisture content or porosity. Nevertheless, this may not be the case if a more absorbent aggregate was used.

5.4 Conclusions

This chapter presents and validates the theoretical considerations employed in the proposed microstructural model *STOICH_HC2*, which is able to simulate the hydration reaction of the ordinary Portland cements. *STOICH_HC2* considers the formation of aluminium-bearing compounds and accounts for the induction period, the nucleation and growth controlled hydration and the diffusive hydrolysis. These features permit the estimation of the ultimate degree of hydration which corresponds to the complete consumption of the capillary water. The microstructural model suggests a linear dependency of the capillary and total porosities with respect to the degree of hydration. The proposed functions account for the autogenous shrinkage and highlight the role of the masses of the water forms populating the gel structure. Moreover, the numerical model suggests that the capillary network comprises the effective capillary pores and also the large gel pores, while the gel network includes the small gel pores and the interstices containing the adsorbed, interlayer and intraglobular water. Under such conditions, the demarcation between the capillary and the gel pores is assumed to be at 60Å. The microstructural model considers also the amount of water absorbed/expelled from aggregate in the first hours after mixing. The comparison between the numerical and the experimental results demonstrates that *STOICH_HC2* emerges as a reliable quantitative predictor of the microstructure of Portland cements and can be used to provide the hygral input required when simulating the moisture and temperature transport within cementitious materials. The study is however limited by the lack of information on the reaction rate under sealed conditions, which slows down the hydration kinetics.

Chapter 6. Validation of Moisture and Temperature Transport in Cementitious Materials

6.1 Introduction

This part of the thesis presents a series of numerical simulations aimed at validating the moisture evolution of samples subject to different types of drying conditions by means of the finite element discretisation presented in Chapter 4. The *THC* model previously described can be split into two main sections: the first focuses on the transport processes of both fluids and heat, whilst the second couples the reactive transport of dissolved ions in the context of the autogenous healing of cementitious materials. The experimental conditions of the examples presented in this chapter inactivate the reactive transport component of the *THC* model and thus, the numerical results presented in this chapter are obtained by applying the spatial and temporal discretisation within a classic *TH* boundary value problem. This mathematical framework is constructed employing hygral data from the microstructural model which was introduced and validated in Chapter 5.

The moisture and temperature distributions given by the proposed *TH* model are compared in Section 6.2 with those from a series of laboratory investigated desiccation tests performed by Kim and Lee (1999), Baroghel-Bouny (1994) and Baroghel-Bouny et al. (1999). The materials considered, which are either hardened cement pastes or concretes with different water-cement ratios, are exposed from 3 to 24 months to both self-desiccation and external drying.

Conclusions from all the above work are provided in Section 6.3.

6.2 Validation of the Boundary Value Problem for Moisture and Heat Flows

In all the following numerical examples, there is a set of parameters employed in the governing balance equations which are common to all the analysed drying tests (see Table 6.1). Moreover, the imposed boundary conditions facilitate mainly unilateral flows of heat and moisture which allows the formulation of the boundary value problem in 1D.

Table 6.1 Common constants used in the Examples 1, 2 and 3

p_v^{sat} equation (3.52)	b_1		8.071	Antoine's law parameters
	b_2		1731	
	b_3		233.4	
$\overline{\rho C}_p$ equation (3.86)	C_p^c	[J/(°K*kg)]	840	Cerny and Rovnonikova (2002)
	C_p^{fagg}		835	
	C_p^{cagg}		920	
	C_p^{cw}		4180	
	$\left(C_p^v - C_p^{da}\right)$		1400	
	w_{cw}^{ult}	[kg/m3]	from *STOICH_HC2*	
D_{eff} equation (3.72)	A_v		1	Gawin et al. (1999)
	B_v		1.667	
	f_s		$1*10^{-3}$	
	D_{v0}	[m²/s]	$2*10^{-5}$	
λ_{dry}^{eff} equation (3.89)	λ_{T_0}	[W/(m*°K)]	1.7	Gawin et al. (1999)
	A_λ	[1/°K]	$5*10^{-4}$	
k_{iw} equation (3.59)	T_0	[°K]	273.2	Gawin et al. (1999)
	A_k		$5*10^{-3}$	
	A_p		1	
Rate of heat generation model (3.19), (3.22), (3.26)	Δ^{SP}	[hours]	3	
	T_r	[°K]	294.1	
	p_{atm}	[Pa]	$1.01325*10^5$	
	M_w	[kg/kmol]	18	
	R	[J/(°K*kmol)]	8314.47	

The optimum spatial discretisation is obtained after a mesh convergence study, performed with 2D 4-noded finite elements, which has provided the smallest number of finite elements giving reliable results with a minimum level of computational cost. This preliminary analysis showed that in the case of autogenous drying, the refinement of

the discretisation does not affect the numerical outcome. On the contrary, when exposing one side of the sample to the surrounding environment, it was found that the results are divergent until at least 20 bilinear elements are employed along the flow direction. Three representative mesh convergence studies are illustrated in Figure 6.1 to confirm these conclusions. In this plot the number in front of FE shows how many finite elements were used in the modelling.

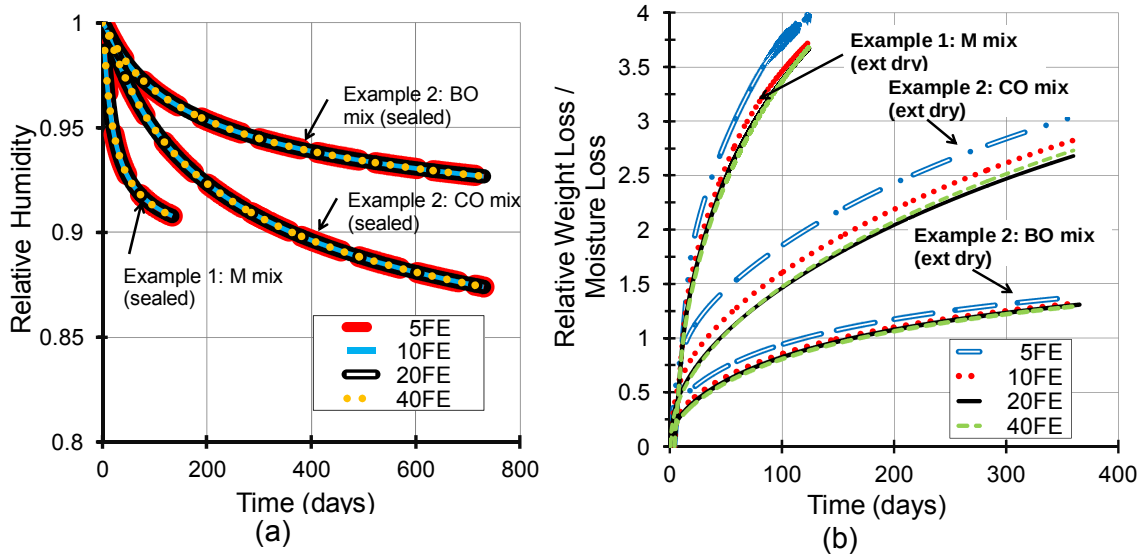

Figure 6.1 Variation of results depending on the number of finite elements used: (a) self-desiccation and (b) external drying;

6.2.1 Example 1: Self-desiccation of Ordinary Hardened Cement Pastes and Concretes

The *TH* boundary value solution is first applied to simulate the self-desiccation processes presented in (Baroghel-Bouny, 1994). In this case the inner relative humidity of the samples drops because of the cement hydration and as a consequence, the capillary porosity function and implicitly the capillary curve are the sole constitutive relationships controlling the intensity of the drying.

6.2.1.1 *Numerical Model Conditions*

A type I normal Portland cement is used to prepare the mixes *CO* (hardened cement paste) and *BO* (concrete). The chemical composition of the binder, computed with Bogue's formula, can be found in Table 5.3, whilst the mix characteristics are provided in Table 5.2. In this experiment, schematically represented in Figure 6.2 (a), no

exchange of moisture with the exterior is allowed, but heat transfer is permitted. The temperature of the environment is maintained constant at T = 21°C and the samples are placed in a sealed desiccator. The relative humidity is measured by means of a Vaisala thermohygrometer of ± 1% *RH* accuracy for a period of 2 years. In the absence of any information about the size of the specimen, a cube of 10 X 10 X 10 cm is considered during the numerical analysis.

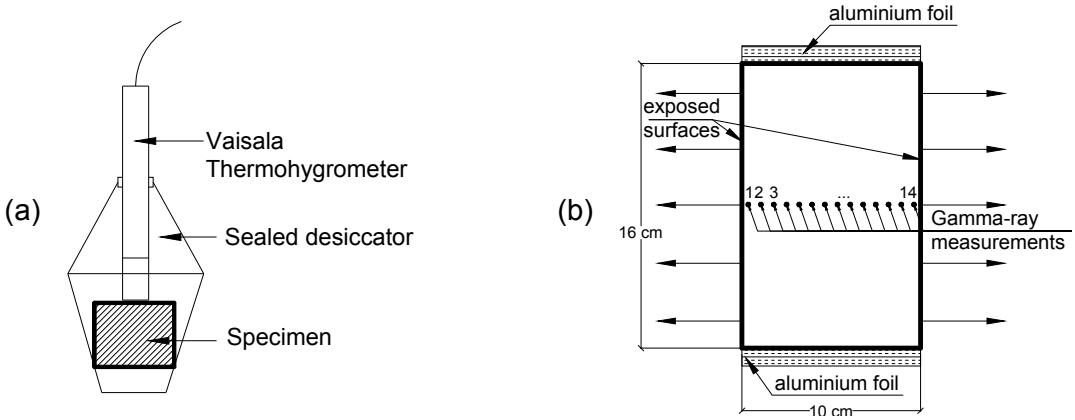

Figure 6.2 Experimental set-up for (a) the sealed and (b) the external drying

Table 6.2 Examples 1 and 2: Drying parameters of *CO* and *BO* mixes

			CO	BO
k_{iw} equation (3.58)	k_{iw}^0	[m^2]	6*10^{-22}	5*10^{-21}
	A_Γ		3	3
k_{rw} equation (3.59)	m		0.461	0.440
$p_c\left(S_w^{cap},\Gamma\right)$ equations (3.66), (3.68)	a	[MPa]	37.55	18.62
	b		2.168	2.275
	c_η		-11	-10
$\eta_j(\Gamma)$ equation (3.13)	w_{CBW}^{ult}	[kg/m^3]	219.9	60.99
	$w_{AW+ILW+IGW}^{ult}$	[kg/m^3]	89.21	24.65
	w_{SGP}^{ult}	[kg/m^3]	118.2	32.63
	w_{LGP}^{ult}	[kg/m^3]	95.71	26.41
	w_{CW}^{ult}	[kg/m^3]	0.075	27.24
	$C_{\eta\_S}^{cap}$		0.237	0.279
	$C_{\eta\_S}^{tot}$		0.122	0.144
equations (4.12), (4.13)	δ_{wv}	[m/s]	2.5*10^{-4}	2.5*10^{-4}
	δ_T	[W/(°K*m^2)]	8.3	4
Γ_{ult}			0.85	1

As was explained earlier, only the material constants employed in the functions $\eta_j(\Gamma)$ and $p_c\left(S_w^{cap},\Gamma\right)$ play an active role in the desiccation process. In Table 6.2, the parameters describing the change in porosity and Γ_{ult} are extracted from the *STOICH_HC2* model, while the coefficients defining the capillary curve are established by means of a "trial and error" procedure.

As was discussed in the previous section, the domain is split into 20 equally sized 4-noded planar elements. Variable time-steps are considered (see (6.1)) in the temporal discretisation and a $1*10^{-3}$ convergence tolerance is adopted for $\boldsymbol{\Psi}$ in the Newton-Raphson iterations.

$$\Delta t_{BO}=\begin{cases}360s, & 1<itime\le 48\\ 8640s, & 48<itime\le 400\\ 14400s, & 400<itime\end{cases}\qquad \Delta t_{CO}=\begin{cases}360s, & 1<itime\le 48\\ 4320s, & 48<itime\le 400\\ 8640s, & 400<itime\le 1000\\ 10800s, & 1000<itime\le 3000\\ 14400s, & 3000<itime\end{cases} \tag{6.1}$$

where $itime$ is the current number step. The initial values of the principal variables are T_0 = 294°K and $S_w^{cap}{}_0=\dfrac{\dfrac{w}{\rho_w}}{\dfrac{w}{\rho_w}+V_{ea}}$ = 0.99 (*CO*) / 0.97 (*BO*). The numerical analysis starts at Γ_0 ≈ 0 by taking the initial time equal to 1 second.

6.2.1.2 *Results and Discussion*

As shown in Figure 6.3 (a), the model predicts that the hydrolysis of *BO* is quicker than that of *CO*, but both slow down considerably after 300 days. This trend is followed inevitably by the porosity function – Figure 6.3 (b) – and implicitly by the water saturation degree – Figure 6.3 (c). Regarding the latter variable, it is interesting to notice that in the case of autogenous drying, an extremely small difference between the S_w^{cap} of *CO* and *BO* exists. This aspect clearly suggests that the intensity of the self-desiccation, quantified by the relative humidity, depends almost exclusively on the capillary curve. Baroghel-Bouny reports that during the two years of testing, the *RH* exceeds 0.87 for *CO* and 0.93 for *BO*. In these circumstances, if Kelvin's law is applied, the expected p_c cannot exceed 18.9 MPa for *CO* and 9.84 MPa for *BO*. For this

reason, the correlation between S_w^{cap} and p_c, depicted in Figure 6.4, needs to be provided by the capillary curve coefficients a, b and c_η.

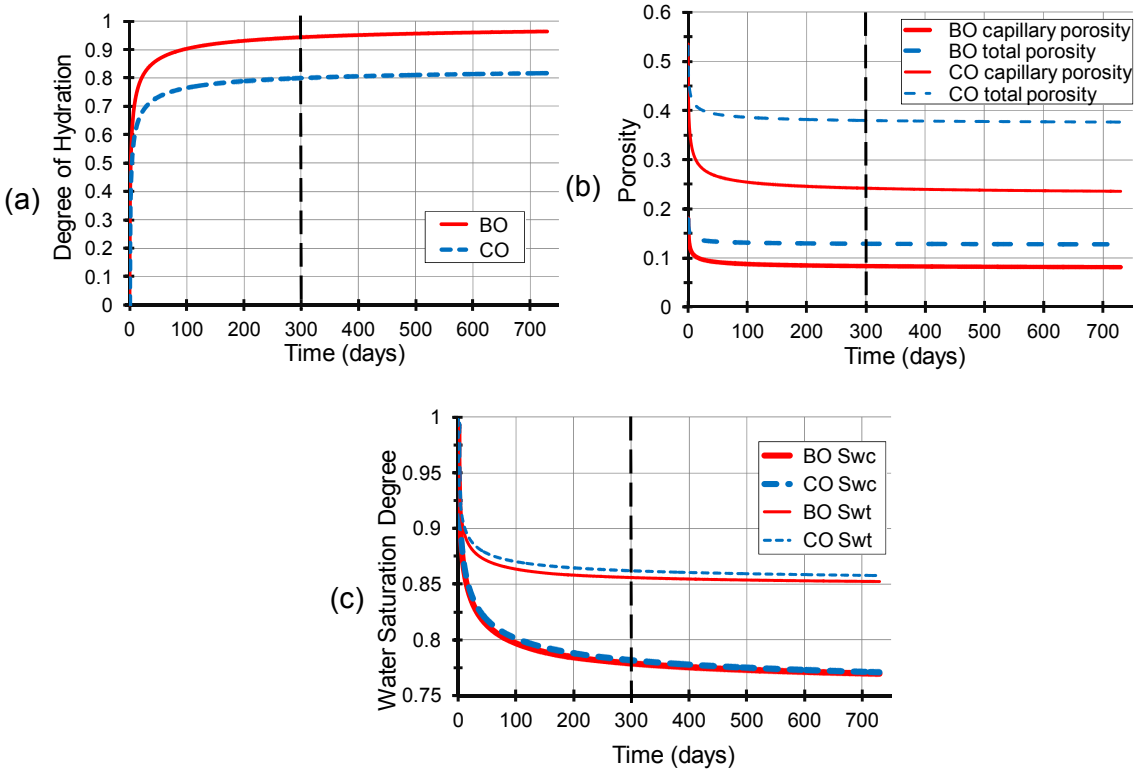

Figure 6.3 Example 1: Evolution of (a) degree of hydration, (b) porosity and (c) water saturation degree under sealed drying

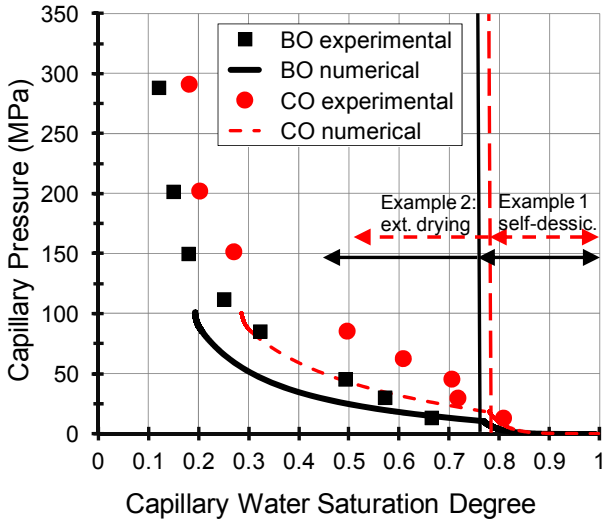

Figure 6.4 Examples 1 and 2: Capillary curves of *BO* and *CO*

The predictive capability of the model in terms of *RH* is generally reasonable during the testing period, the largest percentage error being observed in the case of *BO*. The comparison between the numerical and the experimental findings is plotted in Figure

6.5. The histogram (a) shows that for the cement paste, the modelled drying process is slightly more intense by the end of the 3rd month. Nevertheless, it can be remarked that in the first 70 days, the estimated relative humidity values are greater than the measured ones. For example, the *RH* values (experimental, numerical) at t = 18.24 days are (0.97,0.99), whilst at t = 180 days they equal to (0.93, 0.92). In time though, the simulated desiccation slows down in intensity and the percentage error decreases to 0.89% at 1 year and to 0.06% at 2 years. From the graph (b) of Figure 6.5, it can be seen that during the initial 3 months, the water consumption from the capillary network of the *BO* is mildly overestimated (the maximum *RH* percentage error being 1.86%).

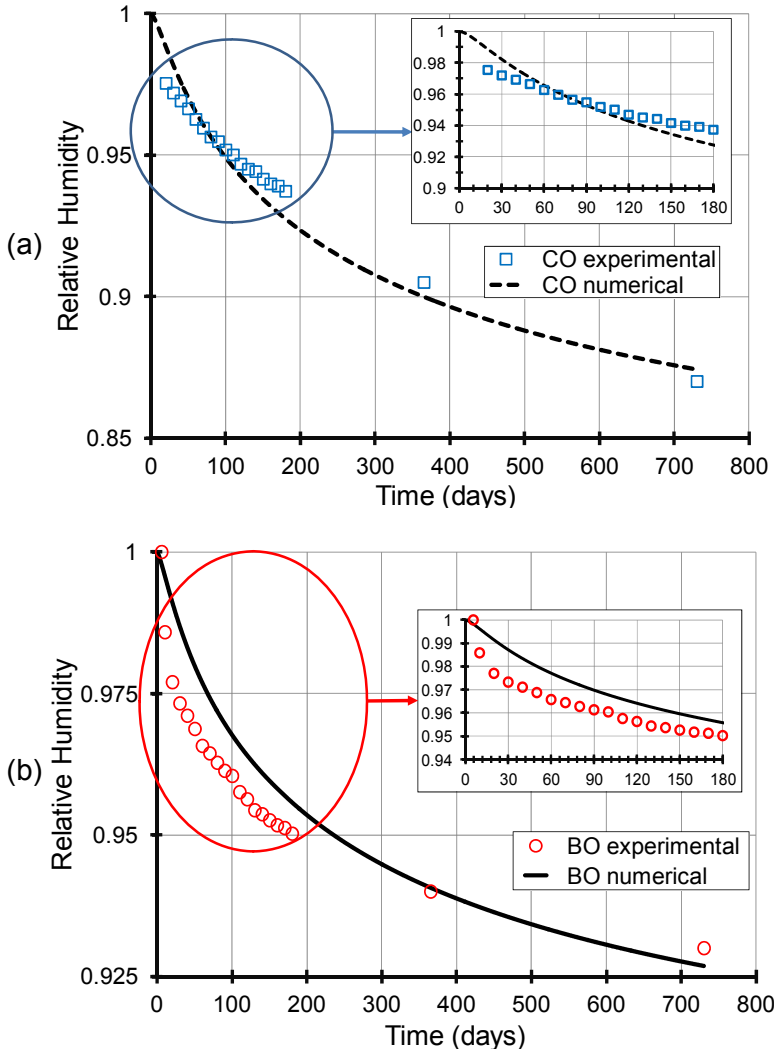

Figure 6.5 Example 1: Variation of *RH* of samples (a) *CO* and (b) *BO*

By analysing Baroghel-Bouny's data for the concrete sample, a striking observation emerges. Up to t = 6.5 days, a nearly constant relative humidity close to unity is measured that. This behaviour is understandable for concrete in the plastic state in which the percolation threshold hydration degree is not reached ($\Gamma \leq 0.1$). However, the duration given by the experiment is unexpectedly long since in 6 days, the degree

of hydration of an ordinary mix with 0.5 water-cement ratio is expected to be approximately around 0.60 (Tennis and Jennings, 2000), regardless of the curing conditions (Bentz et al., 1997). Therefore, since in the current investigation the porosity curve takes into consideration the percolation threshold, the desiccation initiates sooner, after only 4.3 hours. On the other hand, the proposed model produces a more optimistic forecast of the relative humidities in the long term. At 12 months the laboratory and numerical results are almost the same (0.940 versus 0.941), whilst at the end of the experiment (2 years) the values to be compared are 0.930 and 0.927.

6.2.2 Example 2: External Drying of Ordinary Hardened Cement Pastes and Concretes

The next validation example models the external drying of two specimens cured under sealed conditions for 2 years that are made of the previously investigated materials: *CO* and *BO* (Baroghel-Bouny et al., 1999). In their research work, Baroghel-Bouny and her collaborators determined the relative weight and density losses. Regarding the latter physical property, the values were obtained at 6, 62, 128 and 353 days using a gamma ray attenuation procedure applied in 14 positions along the length of the specimen.

In the present validation example, the following formula is used to compute the relative weight loss at t:

$$m_{loss}(t) = \frac{m_{specimen}(t_0) - m_{specimen}(t)}{m_{specimen}(t_0)} \cdot 100 \tag{6.2}$$

where the mass of the specimen, $m_{specimen}$, quantifies the mass of all the existing water phases (liquid and gaseous) and the mass of the solid matrix.

Regarding the second physical property, an average density loss is estimated according to:

$$\rho_{loss}(t) = \frac{\rho(t) - \rho(t_0)}{\rho(t_0)} \cdot 100 \tag{6.3}$$

$$\rho = \frac{m_{totH_2O} + m_{solid}}{\Delta V_{specimen}} \tag{6.4}$$

Equations (6.5) and (6.6) assess m_{totH_2O} and m_{solid} by taking into account the drying shrinkage of the cylinders.

$$m_{totH_2O} = \underbrace{\left[\underbrace{\eta_{cap} S_w^{cap} \rho_w}_{w_{cap}} + \underbrace{\left(w_{CBW}^{ult} + w_{AW+ILW+IGW}^{ult} + w_{SGP}^{ult} \right) \Gamma}_{w_{gel}} + \underbrace{\eta_{tot} \left(1 - S_w^{tot} \right) \rho_v}_{w_v} \right]}_{w_{totH_2O}} \Delta V_{specimen} \tag{6.5}$$

$$m_{solid} = \rho_{dry} \Delta V_{specimen} \tag{6.6}$$

In the above relationships $\Delta V_{specimen}$ denotes the difference between the initial volume of the specimens and the experimentally measured volumetric shrinkage reported in (Baroghel-Bouny, 1997) and presented here in Figure 6.6.

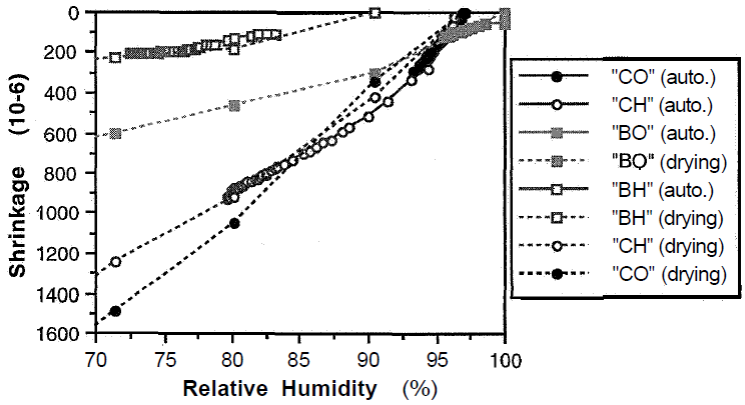

Figure 6.6 Measured shrinkage dependence on *RH* from (Baroghel-Bouny, 1997)

6.2.2.1 *Numerical Model Conditions*

The relative humidity instrumentation presented in Figure 6.2 (b) was applied to cylindrical samples having the dimensions Φ16 X 10 cm. The lateral surface of the specimens was wrapped with aluminium foil sheets, while the two ends were exposed to the environment conditions maintained at 50 ± 5% relative humidity and 20 ± 1°C. This experimental information was used to define the boundary conditions.

The modelling is done by considering the material parameters listed in Table 6.2. The same capillary curve as in the first example is employed because this test represents a continuation of the previous drying experiment. The open sides of the specimen enable advective transport mechanisms within the porous material whose parameters are determined by a trial and error technique. Once again 20 finite elements and a $1*10^{-3}$ convergence tolerance are used, but the time discretisation is now more refined as can be seen in equation (6.7).

$$\Delta t_{BO} = \begin{cases} 360s, & 1 < itime \le 48 \\ 2160s, & 48 < itime \le 400 \\ 4320s, & 400 < itime \le 1000 \\ 5400s, & 1000 < itime \le 2000 \\ 6170s, & 2000 < itime \le 3000 \\ 7200s, & 3000 < itime \end{cases} \qquad \Delta t_{CO} = \begin{cases} 360s, & 1 < itime \le 48 \\ 2160s, & 48 < itime \le 400 \\ 4320s, & 400 < itime \le 1000 \\ 5400s, & 1000 < itime \le 2000 \\ 7200s, & 2000 < itime \le 3000 \\ 8640s, & 3000 < itime \le 4000 \\ 10800s, & 4000 < itime \end{cases} \tag{6.7}$$

The simulation starts exactly from the end point of the first example. The initial temperature, capillary saturation degree, effective time and degree of hydration are hence T_0 = 294°K, $S_w^{cap}{}_0$ = 0.771 (*CO*) / 0.769 (*BO*), t_0 = 730 days and Γ_0 = 0.81 (*CO*) / 0.96 (*BO*).

6.2.2.2 *Results and Discussions*

Figure 6.7 (a) indicates an apparent stagnation of the hydration processes for both *CO* and *BO* and a considerable stabilisation of the porous network.

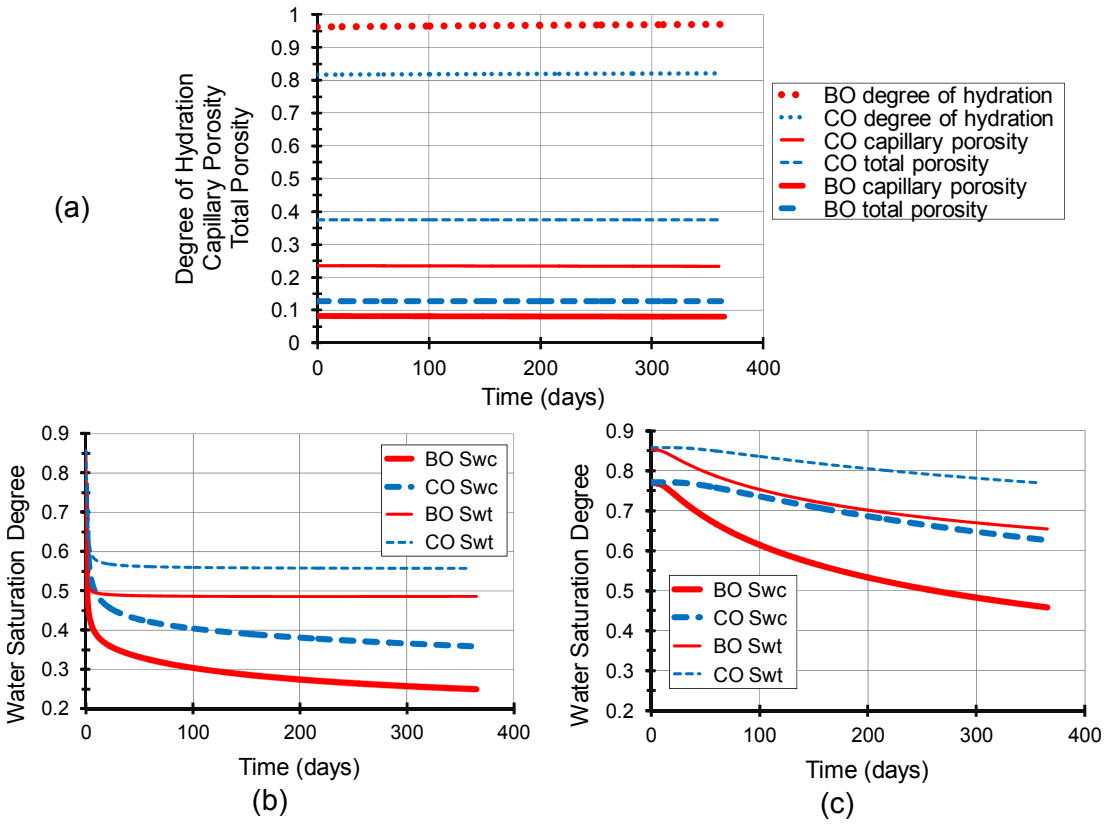

Figure 6.7 Example 2: Evolution of (a) degree of hydration and porosity and water saturation degrees at (b) 2.5mm and (c) 47.5mm

Figure 6.7 (b) and (c), on the other hand, show that the model is able to capture the different drying kinetics of the materials. One should remark that although at the

beginning of the simulation, both samples have in all their points a similar initial capillary water saturation degree, after about 360 days of external drying, the S_w^{cap} of the *BO* drops to 0.25 at the edge and 0.46 at the middle of the sample in comparison to the S_w^{cap} of the *CO* that reduces to 0.36 towards the exposed sides but is 0.63 at the core. In addition, the *TH* model highlights the importance of the advective flux of the liquid water in the external drying and confirms that the moisture flow in the cement paste is smaller than the flow in the concrete.

The validation of Example 2 continues with the presentation of the experimental and numerical plots of the relative weight and density losses (Figure 6.8 and Figure 6.9).

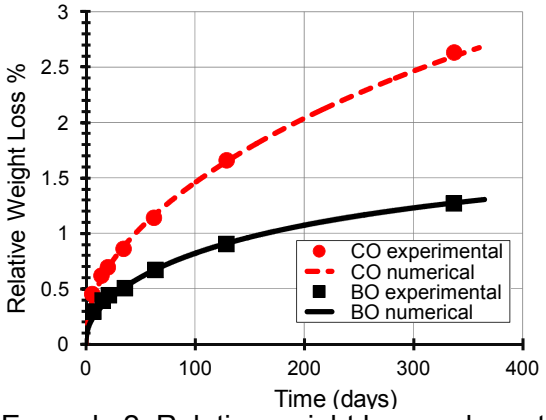

Figure 6.8 Example 2: Relative weight loss under external drying

The solution of the boundary value problem in terms of relative weight loss of both *CO* and *BO* closely matches the data reported by Baroghel-Bouny et al.. The largest difference – 0.37 (experimental) versus 0.46 (numerical) – occurs in the case of the hardened cement paste at 5.3 days. The changes in relative density loss, on the other hand, are slightly more difficult to exactly predict. The laboratory work suggests an irregular variation along the length of the specimens despite the symmetrically applied boundary conditions. The modelling fails to reproduce this behaviour, but it is promising to see that at least one of the two predicted moisture gradients is close to that measured. In the case of the hardened cement pastes, the amount of water remaining in the cylinders at the 128th and the 353rd day is less than expected for the right-hand side part of the specimen. However, the moisture distributions within the 6th and the 62nd day are much more satisfactory. The numerical simulation tends to perform better when the relative density loss of the *BO* is analysed. The most pronounced inaccuracies can be observed on the left-hand side of Figure 6.9, along the first 20 mm of the sample where the intensity of the drying process is underestimated during the last 3 sets of measurements.

(a)

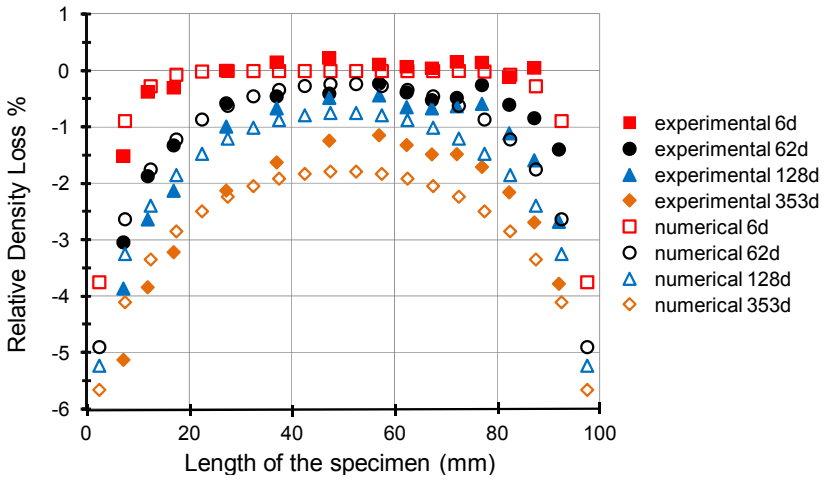

(b)

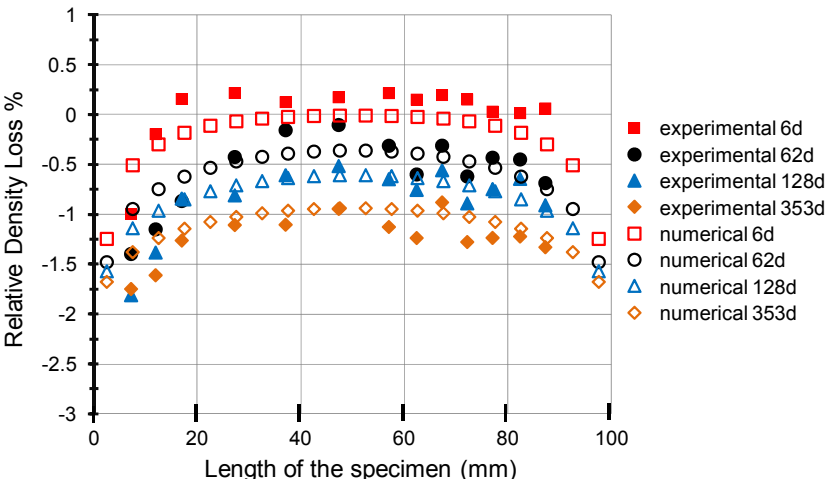

Figure 6.9 Example 2: Relative density loss under external drying along the sample: (a) *CO* and (b) *BO*

6.2.3 Example 3: Drying of Concrete Mixes with Different *w/c* Ratios

The last series of simulations are aimed at examining the efficiency of the proposed *TH* model in predicting the moisture change of three concretes with low, medium and high compressive strengths during different curing conditions. The example replicates the results taken from (Kim and Lee, 1999) in terms of relative humidity and moisture loss weight per unit exposed area (kg/m^2). In which concerns the computation of the latter physical property, the following relationship is used in the current findings:

$$w_{moist\_loss}(t) = \left[w_{totH_2O}(t_0) - w_{totH_2O}(t)\right] \cdot \frac{V_{specimen}}{A_{specimen}} \tag{6.8}$$

Kim and Lee (1999) provide no information related to the chemistry of the binder and a standard *ASTM* Type I cement composition taken from (Schindler and Folliard, 2005) is selected. The accuracy of the final numerical data is therefore influenced more than ever by the output from the *STOICH_HC2* model.

6.2.3.1 *Model Domain and Time Step Discretisation*

In Kim and Lee's paper, totally sealed specimens of 10 x 10 x 10 cm and drying specimens of 20 x 10 x 10 cm were demoulded after 1 day and moist-cured for another 3 days before testing. Paraffin wax was used as a seal material, but in the case of the drying specimens, one of the two 10 x 10 sides was left free to permit a uniaxial moisture flow. During the desiccation, the specimens were subjected to 50 ± 2% *RH* and 20 ± 1°C. The relative humidity values were measured by means of Vaisala HMP44 probes and Vaisala HMI41 indicators placed at 3, 7, and 12 cm from the exposed surface. The experimental set-up is illustrated in Figure 6.10.

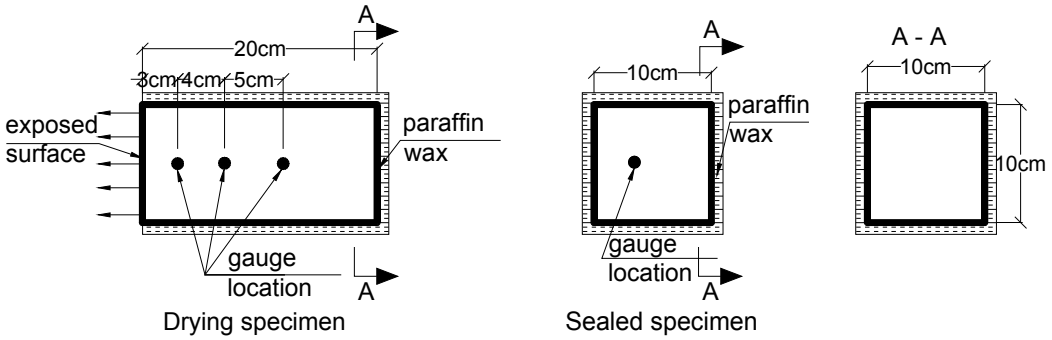

Figure 6.10 Experiment 3: Schematic representation of samples

Table 5.2 and Table 5.3 provide the necessary mix characteristics and mass percentages of the used clinker minerals. It is interesting to observe that the *STOICH_HC2* model forecasts an incomplete hydration of the high and medium strength concretes due to insufficient water. The ultimate Γ for these two mixes reaches only 0.63 and 0.93, respectively, whereas the low strength concrete has Γ_{ult} = 1. The coefficients of the capillary curve $p_c\left(S_w^{cap},\Gamma,T\right)$ are taken from the self-desiccation experiment simulated in Example 2, while the coefficients of the advective flux of the water phase are calibrated using a "trial and error" procedure. Table 6.3 lists the parameters specific to the example 3.

The analysis is performed with: 20 equally sized, 4-noded planar elements, $1*10^{-3}$ convergence tolerance for $\boldsymbol{\Psi}$ in the Newton-Raphson iterations and t_0 = 4 days.

Table 6.3 Example 3: Parameters characterising the drying of *M*, *L* and *H* mixes

Mix			M	L	H
k_{iw} equation (3.58)	k_{iw}^{0}*10^{20}	[m^2]	**7.5** | 4.0	**9.0** | 4.5	**3.5** | 1.3
	A_Γ		0.9	0.9	0.9
k_{rw} equation (3.59)	m		0.440	0.440	0.440
$p_c\left(S_w^{cap},\Gamma\right)$ equations (3.66), (3.68)	a	[MPa]	18.62	18.62	18.62
	b		2.275	2.275	2.275
	c_η		-7	-12.3	-11.5
$\eta_j(\Gamma)$ equations (3.13), (3.15)and (3.16)	w_{CBW}^{ult}	[kg/m3]	70.09	54.82	63.56
	$w_{AW+ILW+IGW}^{ult}$	[kg/m3]	28.85	21.91	25.75
	w_{SGP}^{ult}	[kg/m3]	38.82	29.39	34.31
	w_{LGP}^{ult}	[kg/m3]	31.43	23.79	27.77
	w_{CW}^{ult}	[kg/m3]	0	80.89	0
	$C_{\eta\_S}^{cap}$		0.271	0.285	0.190
	$C_{\eta\_S}^{tot}$		0.138	0.147	0.098
equations (4.12), (4.13)	δ_{wv}*10^4	[m/s]	9	5	4
	δ_T	[W/(°K*m^2)]	8.3	8.3	8.3
Γ_{ult}			0.93	1.00	0.63

The time-steps are equals to:

$$\Delta t_{seal}=\begin{cases}1200s, & 1<itime\le 48\\ 8640s, & 48<itime\le 400\\ 10800s, & 400<itime\end{cases}\qquad \Delta t_{edry}=\begin{cases}1200s, & 1<itime\le 48\\ 4320s, & 48<itime\le 1000\\ 5400s, & 1000<itime\le 1800\\ 8640s, & 1800<itime\end{cases} \tag{6.9}$$

The water absorption, occurring during the moist curing, is taken into account indirectly by means of the initial RH_0 – 0.999 (*L*) / 0.987 (*M*) / 0.970 (*H*) – reported by Kim and Lee (1999). The initial values of the principal variables are T_0 = 293 °K and

$$S_{w\ 0}^{cap}=\left[1+\left(\frac{1}{\left(\frac{\eta_{cap}(\Gamma_0)}{\eta_{cap}(\Gamma_{ult})}\right)^{c_\eta}}\frac{\xi_0}{\xi(T_0)}\left(-\frac{\rho_w(T_0)RT_0\ln(RH_0)}{M_w}\right)\frac{1}{a\cdot p_{atm}}\right)^{\frac{b}{b-1}}\right]^{-\frac{1}{b}}$$ = 0.73 (*L*) / 0.87 (*M*) / 1.00 (*H*) where Γ_0 equals to 0.80 (*L*) / 0.65 (*M*) / 0.44 (*H*).

6.2.3.2 *Results and Discussions*

Figure 6.11 shows that by the end of the testing period, both the hydrolysis of the clinker minerals and the formation of the capillary pores have almost reached their ultimate values. Regardless of the water-cement ratio, 91% of the reaction has taken place at 124 days after casting.

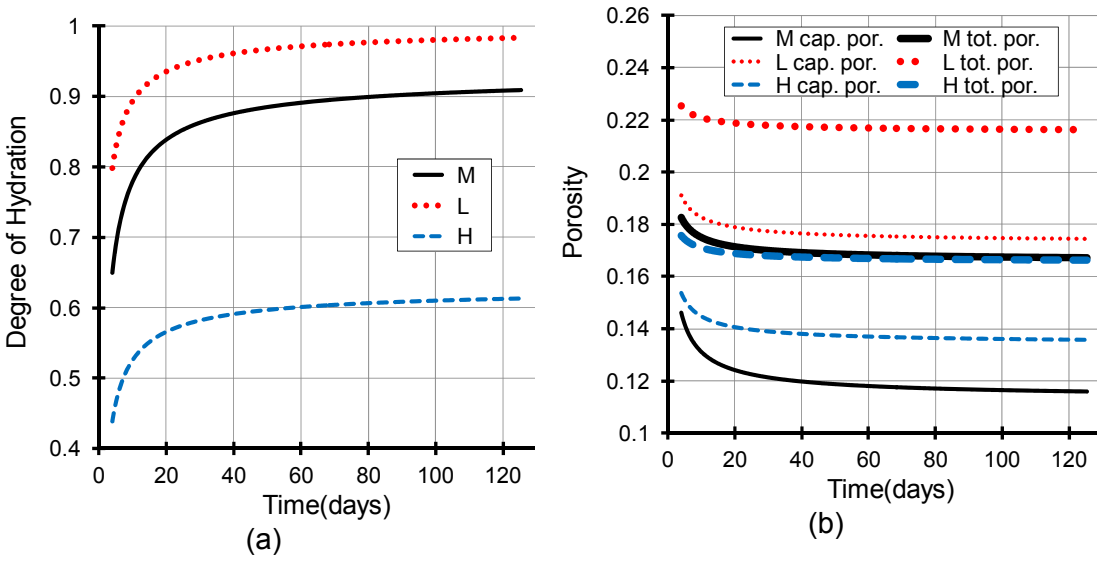

Figure 6.11 Example 3: Evolution of (a) degree of hydration and (b) porosity

In the case of the self-desiccation experiment, the distributions of the water saturation degrees depicted in Figure 6.12 (a) reflects the expected behaviour of the three types of concretes.

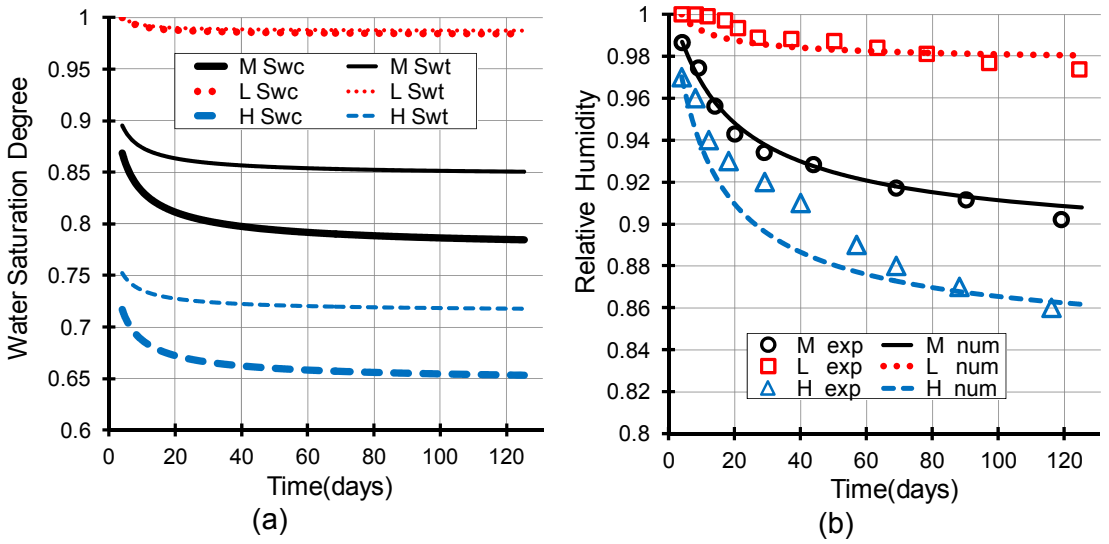

Figure 6.12 Example 3: Evolution of (a) water saturation degree and (b) relative humidity under sealed conditions

The specimen with the highest water-cement ratio has the slowest drying kinetics and loses only 2% of the capillary water. The numerically estimated inner relative humidities agree with the values reported by Kim and Lee (1999), as can be seen in Figure 6.12 (b), especially in the case of the *M* sample. However, the *TH* model is unable to predict the hindered self-desiccation during the first 20 days of the low strength concrete and it slightly overestimates the drying of the high strength concrete during the first 60 days.

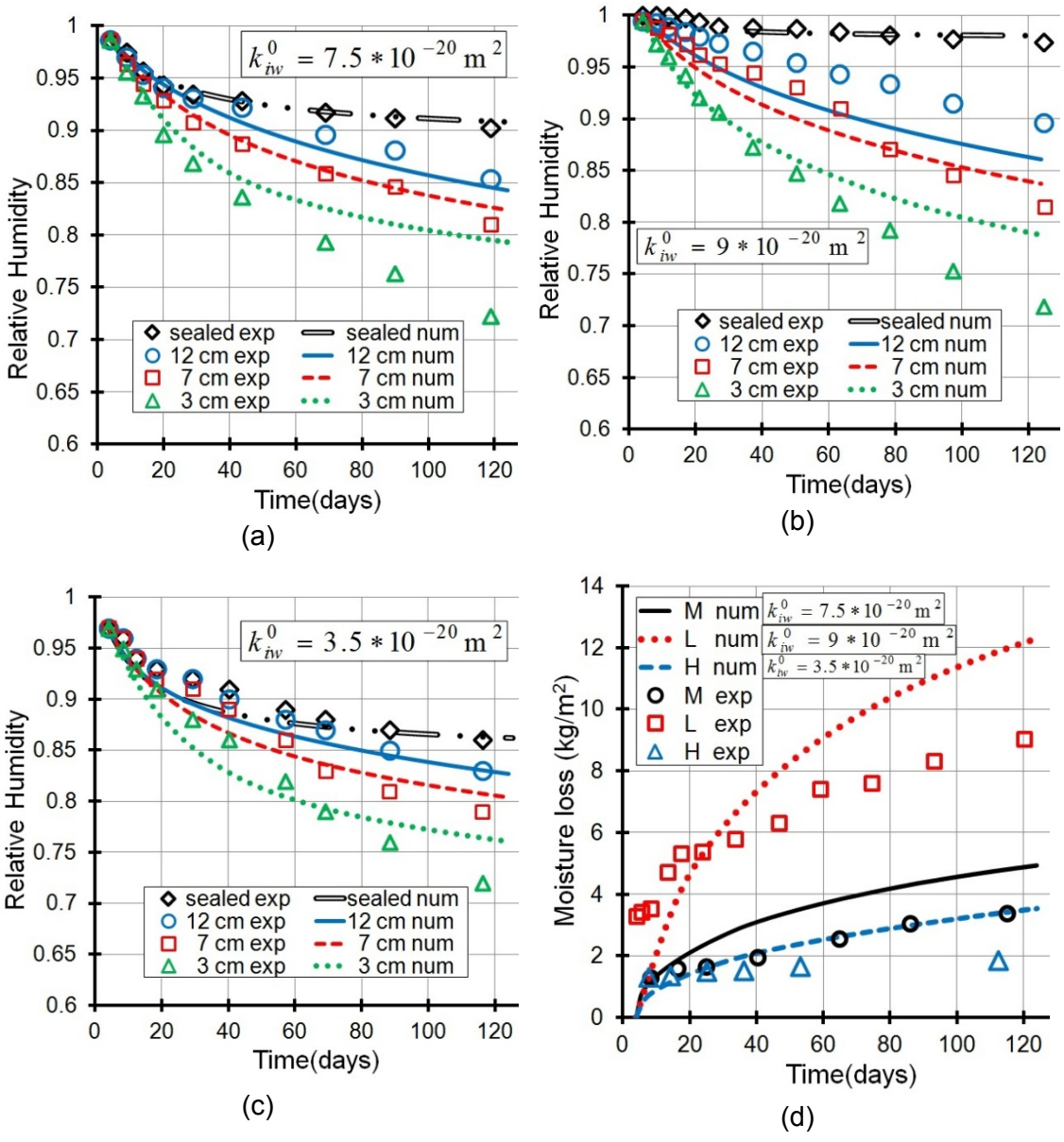

Figure 6.13 Example 3 – variant 1: Evolution of *RH*s and moisture losses; (a) *M*, (b) *L* and (c) *H*

Regarding the external drying, the values of the intrinsic permeability (shown in bold in Table 6.3) of the matured paste are initially considered and the results are plotted in Figure 6.13. The estimated drying evolutions capture the moisture gradients existing

along the specimens. The *RH* values measured at 7 and 12 cm from the free side of the sample are best predicted in the modelling of *M* and *H*, whilst the most satisfactory *RH*s at 3 cm are seen for the *L* concrete. Concerning the moisture loss, one can easily see that the results are not very close to the experimental data since the drying mechanisms are overall underestimated after approximately the 20th day.

This is the reason why an additional series of simulations was undertaken using the second set of k_{iw}^0 values.

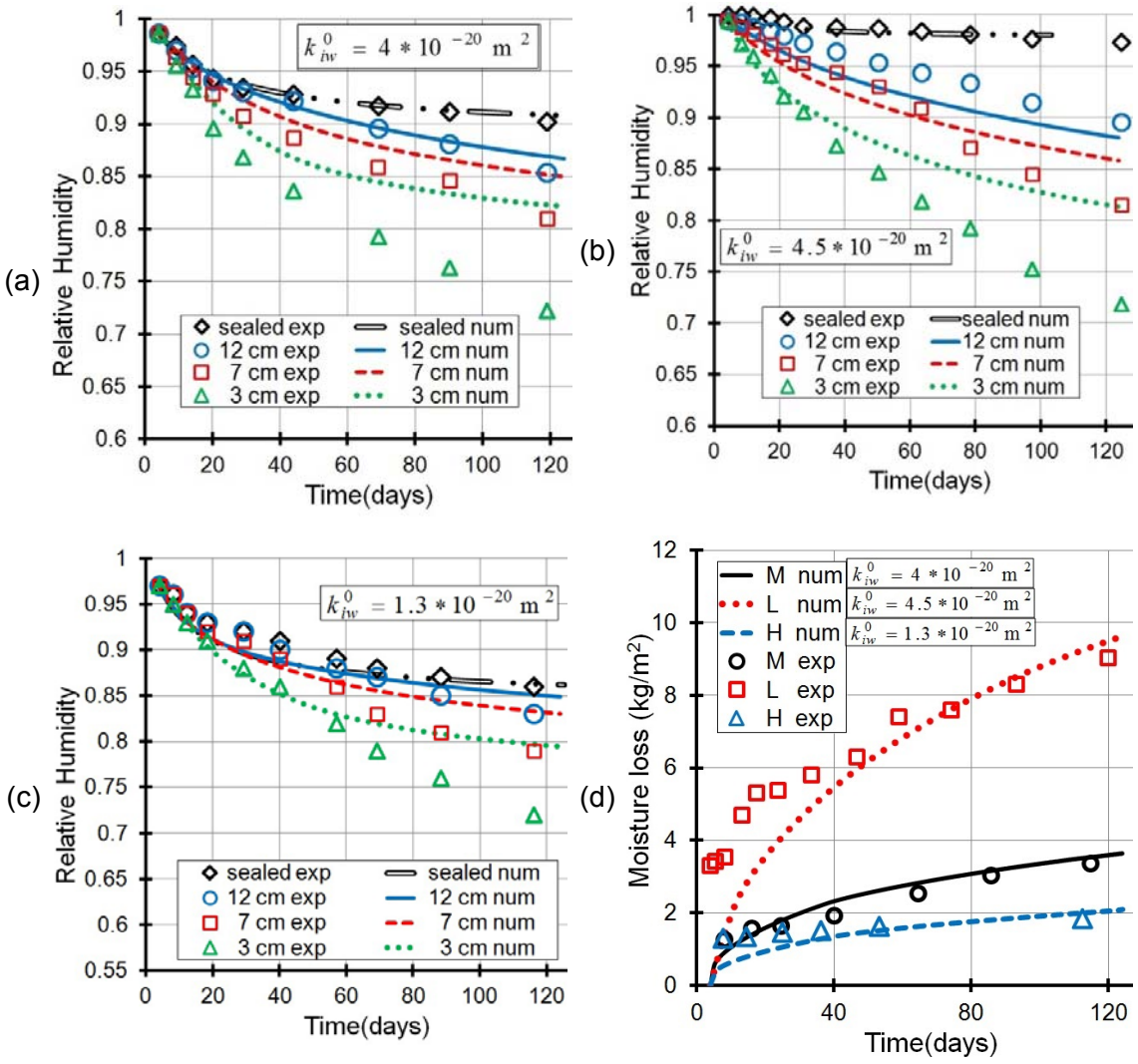

Figure 6.14 Example 3 – variant 2: Evolution of *RH*s and moisture losses; (a) *M*, (b) *L* and (c) *H*.

In this case, the match between the numerical evolution of w_{moist_loss} from diagram Figure 6.14 (d) and the values reported by Kim and Lee (1999) is much more satisfactory. The variation in time of the relative humidities shifts towards a more saturated state, but essentially it does not improve too much. As a general rule, the

drying in all the three locations is less intense and a better correspondence of *RH*s values is observed at 12 cm.

6.3 Conclusions

The purpose of this chapter was to validate the theoretical formulations describing the thermo-hygral behaviour of the ordinary cementitious materials. The model simulating the transport processes of both fluids and heat is composed of a *TH* boundary value problem which replicates the change of moisture and entropy in space and time that uses the porosity development provided by a microstructural model that simulates the hydration reaction of the ordinary Portland cements.

Three main sets of simulations with different types of curing conditions were performed. In the first two examples, the simulations of the self-desiccation and the external drying of a hardened cement paste and a concrete mix were compared with laboratory measured results. The numerical findings were found to be in close agreement with the experimental values and confirmed that when the samples are submitted to a lower environmental *RH*, a moisture gradient between the core and the cover of the specimen appears that is smaller for the cement paste than for the concrete. The last example investigated the humidity distribution of three types of concrete subjected to sealed and unsealed boundary conditions. Although the model response has successfully demonstrated that the hygral behaviour is replicated fairly well during self-desiccation, it has certain limitations in terms of accurately modelling the spread of the humidity levels during external drying.

Chapter 7. Validation of the Self-Healing Model for Cementitious Materials

7.1 Introduction

The overall thermo-hygro-chemical response observed during the self-healing of cementitious materials brings to the fore complex physical and chemical processes that are linked directly to the phenomenon of crack bridging and indirectly to the regain of strength. The self-healing in the first weeks after casting is thought to be a result of ongoing hydration rather than a result of carbonation (Van Tittelboom and De Belie, 2013; Jacobsen et al., 1995; Granger et al., 2007). The efficiency of crack recovery is dependent not only on the crack opening, but also on the mix characteristics and the starting time of the self-healing phenomenon (Hosoda et al., 2009; Sisomphon et al., 2011). The speed of the crack recovery is affected by the moisture content, the ambient temperature and the amount of unreacted cement grains existing in the paste (Neville, 2002; Granger et al., 2007).

The majority of the available strategies for numerical self-healing modelling are developed at microscale and investigate the hydration kinetics of some spherical elements dispersed in an aqueous medium (Ye and van Breugel, 2007). The alternative to this approach is to enlarge the modelling scale and to account for the moisture, the temperature and the solute transfer using a mechanistic representation. It is this latter approach that will be explored in the current chapter.

The finite element method, as outlined in Chapter 4, is implemented here to model the self-healing mechanisms. The physical laws describing the reactive transport of the unreacted cement particles are calibrated so as to provide numerical results comparable to available laboratory data.

Section 7.2 describes briefly the chosen experimental study and its conclusions related to the *THC* behaviour of the investigated samples. In addition it discusses the effect of the laboratory procedure upon the modelling approach and presents some required adjustments of the theoretical formulations. Section 7.3 shows how the finite element discretisation was performed and presents comparisons between the laboratory and

the numerical findings, whilst section 7.4 provides the conclusions from all the above work.

7.2 Review of the Experimental Study

An experimental programme undertaken in Cardiff University and dedicated to the autogenous healing of cementitious materials was selected for the validation of the *THC* model (Davies, 2014). Its primary scope was to provide information about the mechanical properties of the filler located in the crack in order to simulate mechanical recovery of the damaged cementitious material. However, some data, related to the transport and chemical mechanisms occurring during self-healing, is also available and has been used in the present work. The observations made in these experiments were not wholly consistent and had high variability; therefore they are used tentatively for the model validation. In these circumstances it is more appropriate to say that the current chapter is aimed to establish the "functionality" of the *THC* model rather than its validity.

7.2.1 Description of the Experimental Setup

A plain mortar (CEM II/B-V 32.5R + sand) sample of 255 X 75 X 75 mm was poured in a wooden mould in order to cast a beam with a narrow preformed central notch in the lower face as in Figure 7.1. The notch was intended to replicate a uniform width crack of 0.2 mm and it was obtained by first embedding and then removing a steel shim.

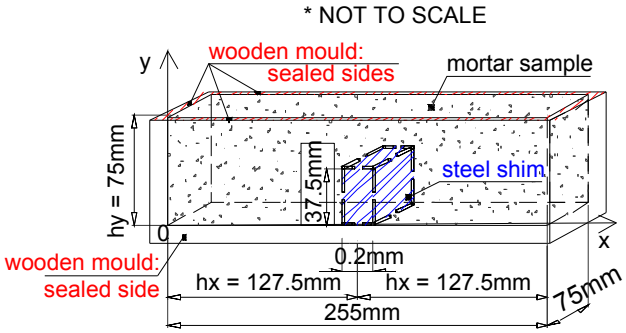

Figure 7.1 Schematic representation of the experimental setup

The metal plate was introduced uncoated, to prevent any undesired chemical reactions between the mould release oil and the paste, and after its removal (at 6 hours after casting) the crack was prevented from dry out by covering the beam with wet hessian sack. The sample was demoulded after approximately one day (26 hours) and was

immediately immersed in water for 14, 27 and 41 days. At the end of these curing periods the sample was broken by means of a three-point bending test in order to measure the gain in strength and also to look for visual and chemical evidence of self-healing. Camera images of the beam cross section were taken and chemical probes with the new deposited material were collected for chemical investigation. On the external surface of the crack a white crystalline substance appeared, but the crack reduction was not measured since it was not considered “a reliable way of achieving repeatable experimental observations”. On the other hand, a ridge of material build up having the same colour as the bulk sample was formed on the crack surface. In addition, a white crystalline material, believed to be calcium carbonate, could often be distinguished in a distinctive pattern by the naked eye. This substance became more visible once the fractured surface of the crack was exposed to the air. The *SEM* tests detected portlandite, ettringite and calcium-silicate-hydrate in the composition of the deposited material, while the *XRD* tests identified portlandite, silica and calcite. Davies (2014) concluded that “continued hydration is the dominant process taking place in the narrow notched cracks”.

7.2.2 The Effect of the Experimental Procedure upon the Modelling Approach

Considering the above laboratory procedure, it can be concluded that the investigated sample is subjected to two different types of curing conditions that divide the experiment into two main stages. The first represents a classical drying process similar to the examples discussed in Chapter 5, whilst the second triggers a transport process in almost saturated conditions that activates the reactive transfer of the unhydrated cement particles. In these circumstances, during the first type of curing, the solute transport is neglected in the *THC* model, while, during the second type of curing, the boundary conditions take into account the fact that the elements located in the narrow notch are always saturated. For this region of the modelled sample, the amount of water penetrating the notch diminishes in time due to the deposition of new material and for this reason the porosity function defined in (7.1) is adopted in the crack zone:

$$\eta_j(\Gamma, V_P) = 1 - \frac{V_P}{V_{crack}} \tag{7.1}$$

where V_P is the volume of self-healed material precipitated in the crack and V_{crack} is the initial volume of the crack. During each time step V_P is evaluated according to:

$$V_P = \frac{m_P}{\rho_P} \tag{7.2}$$

in which m_P – the mass of precipitated material – is equivalent to the term m_ω from (3.78) and is therefore equal to:

$$m_P = m_\omega = \alpha_P \omega^{\beta_P} m_{CW} \tag{7.3}$$

In the above equation m_{CW} quantifies the mass of capillary water, as follows:

$$m_{CW} = \underbrace{S_w^{cap} \eta_{cap} V_{tot}}_{V_{CW}} \rho_w \tag{7.4}$$

It should be also stated that the microstructural model *STOICH_HC2,* which was used in the previous chapter to estimate the water forms, was designed to investigate only the hydration of the clinker minerals. This limitation requires the introduction of an additional coefficient (c_{FA}^j) that increases the porosity when fly ash is present:

$$\eta_j(\Gamma, V_P) = \begin{cases} \dfrac{w - \Gamma \cdot c_{FA}^j \cdot \sum_i w_i^{ult}}{w - \Gamma_0 \sum_i w_i^{ult}} \eta_j(\Gamma_0) & , \Gamma < \Gamma_0 \\ \dfrac{\dfrac{w}{c} + \dfrac{\rho_w V_{ea}}{c} - \left[V_s(\Gamma) \dfrac{\rho_w}{c} + \Gamma \cdot c_{FA}^j \cdot C_{\eta\_S}^j \right]}{\dfrac{\rho_w}{\rho_c} + \dfrac{w}{c} + \dfrac{\rho_w V_{ea}}{c} + \dfrac{\rho_w \sum V_{agg}}{c} + \dfrac{\rho_w \sum V_{SCM}}{c}} & , \Gamma \geq \Gamma_0 \end{cases} \tag{7.5}$$

The cement type CEM II/B-V 32.5R is obtained by adding 65 to 79 % clinker and 21 to 35 % siliceous fly ash, which is composed mainly of siliceous, aluminium and ferric oxides. The latent hydraulic properties of the fly ash are activated by portlandite during the pozzolanic reactions as can be seen below (Stefanović et al., 2007):

$$2S + 3CH \rightarrow C_3S_2H_3 \tag{7.6}$$

$$C_3A + C\bar{S}H_2 + 10CH \rightarrow C_4A\bar{S}H_{12} \tag{7.7}$$

$$A + C\bar{S}H_2 + 3CH + 7H \rightarrow C_4A\bar{S}H_{12} \tag{7.8}$$

$$A + 4CH + 9H \rightarrow C_4AH_{13} \tag{7.9}$$

Chindaprasirt et al. (2005) have examined the effect of this type of cement replacement on the porosity and obtained the results from Figure 7.2. Under the assumption of a 30% by weight Portland cement replacement, the plots from Figure 7.2 were used in the current investigation in an interpolation-based procedure to identify the ratio between the porosity of the pure Portland cement paste and the porosity of the blended cement paste. The coefficients c_{FA}^j were established by fitting the computed ratios with the porosity function (7.5). Doing so resulted in the values c_{FA}^{cap} = 0.4 and c_{FA}^{tot} = 0.1.

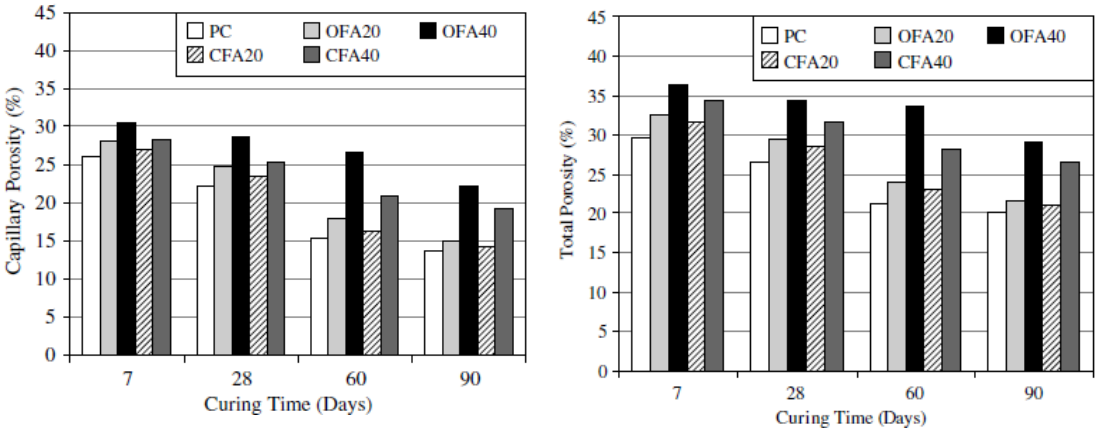

Figure 7.2 Capillary and total porosity evolution of various cement blends measured by Chindaprasirt et al. (2005)

7.3 Numerical Modelling of the Experimental Study

7.3.1 Numerical Model Conditions for Stage 1 (Moist Air Curing)

The mould oil, used to facilite demoulding, effectively seals (with respect to moisture transport) three sides of the specimen and enables unidirectional moisture flow. The coverage of the beam with a hessian sack during the first 26 hours is taken into account in the modelling by considering an external relative humidity equal to 50%. In terms of heat flow, the environmental temperature is set to T_{env} = 20°C.

The domain is divided into 20 X 10 equally sized 4-noded planar finite elements having two active degrees of freedom per node (S_w^{cap} and T). A schematic representation of the chosen mesh configuration is illustrated in Figure 7.3.

The time discretisation uses steps of 3600 seconds and a convergence tolerance of $1*10^{-3}$ for the Newton-Raphson iterations, based on an L2 norm of the error in the governing equations. The initial values of the principal variables were T_0 = 293°K and

$$S_{w\ 0}^{cap} = \frac{\frac{w}{\rho_w}}{\frac{w}{\rho_w} + V_{ea}}$$ = 0.95. The numerical analysis starts at Γ_0 ≈ 0 by taking the initial time equal to 1 second.

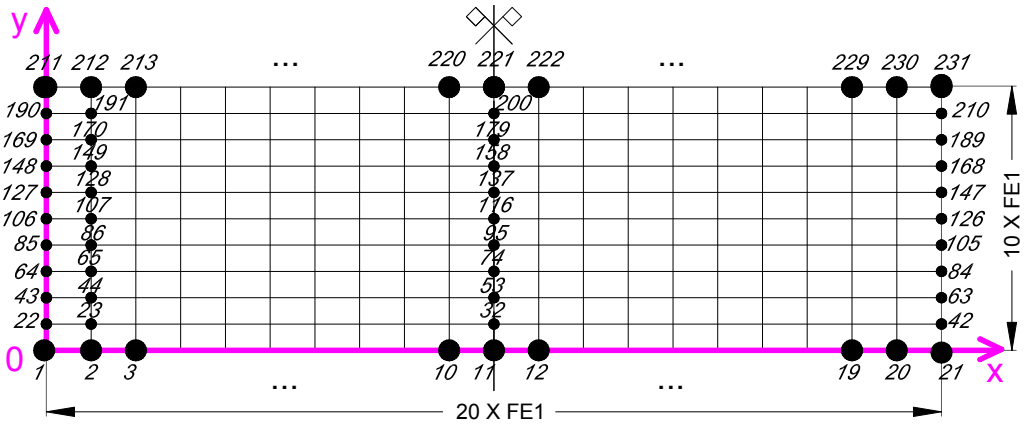

Figure 7.3 Meshing used for the stage 1 of curing; node numbers are written in italics

During the first stage of curing, no experimental results describing the heat and moisture development in the mortar beam were available. Consequently, it was decided to adopt the drying parameters of the concrete used in the numerical example discussed in section 6.2. Their values are enumerated in Table 6.1 and Table 6.2. The cement composition of *BO,* given in Table 5.3, was also employed in this numerical examination of autogenous healing.

Additionally, in both stages of the current simulation:

- the mortar paste has the mix characteristics given in Table 7.1;

Table 7.1 Mix characteristics of the mortar paste *SH*

	$\frac{w}{w_b}$	w_b	c	w_{FA}	w	w_{fagg}	ρ_c	ρ_{FA}	ρ_{fagg}	ρ_{dry}	V_{ea}
		[kg/m^3]									[m^3/m^3]
SH	0.500	571.4	400	171.4	285.7	1200	3168	2330	2400	1770	0.015

- the hydration model developed by Schindler and Folliard (2005) has the following parameters accounting for the contribution of the fly ash: f_{FA} = 30%, f_{FA-CaO} = 12.67%, h_{FA} = 209 J/g and f_{cem} = 70% and
- the required output from the *STOICH_HC2* model equals to: $C^{cap}_{\eta\_S}$ = 0.279 and $C^{tot}_{\eta\_S}$ = 0.144 (w^{ult}_{CBW} = 69.140, $w^{ult}_{AW+ILW+IGW}$ = 27.924, w^{ult}_{SGP} = 36.959, w^{ult}_{LGP} = 29.919, w^{ult}_{CW} = 121.772) and Γ_{ult} = 1.

7.3.2 Results and Discussions

The moisture and temperature distributions after 26 hours of curing are presented in Figure 7.4 and Figure 7.5. The existing difference in relative humidity between the external surroundings and the interior of the paste triggers an expected desiccation process.

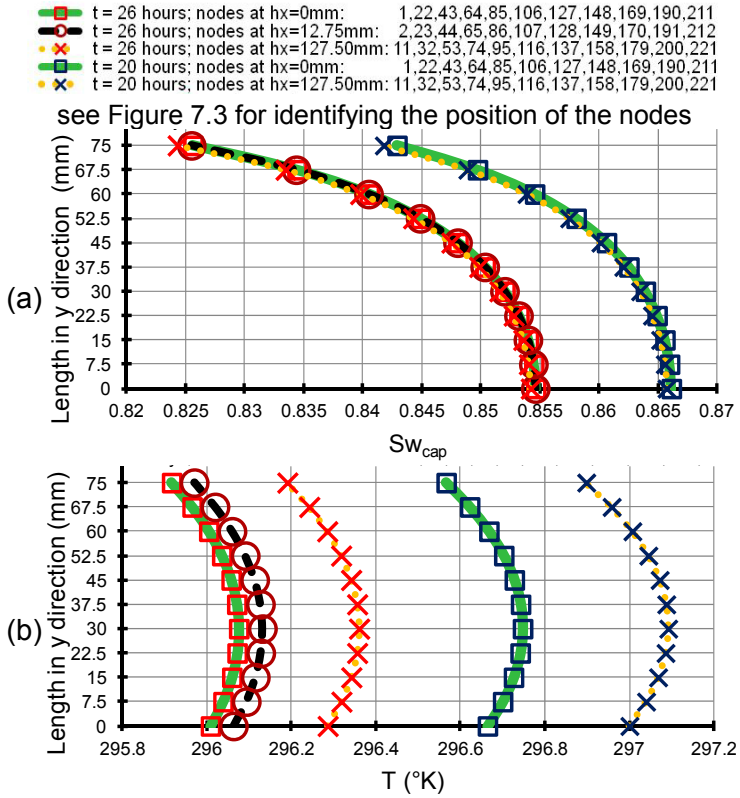

Figure 7.4 Distribution of (a) S_w^{cap} and (b) T in y direction at 20 and 26 hours after casting

A part of the initial volume of capillary water is either consumed by the hydration or evaporates during the external drying. Figure 7.4 (a) and Figure 7.5 (a) indicate, on one hand, an almost uniform distribution of the moisture content along the length of the sample and on the other hand, a positive gradient in S_w^{cap} between the notched bottom and its corresponding opposite side. This trend however is not followed by the temperature variation presented in Figure 7.4 (b) and Figure 7.5 (b) because the applied thermal boundary conditions are different. Instead, in this case, the magnitude of the heat gradients in both longitudinal and transversal directions is comparable.

Before passing to the description of the model conditions employed in the second type of curing, it must be also mentioned that the current thermo-hygral state reached at 26 hours after casting represents the starting point of the *TH* evolution in the effective self-healing process simulated in the following section.

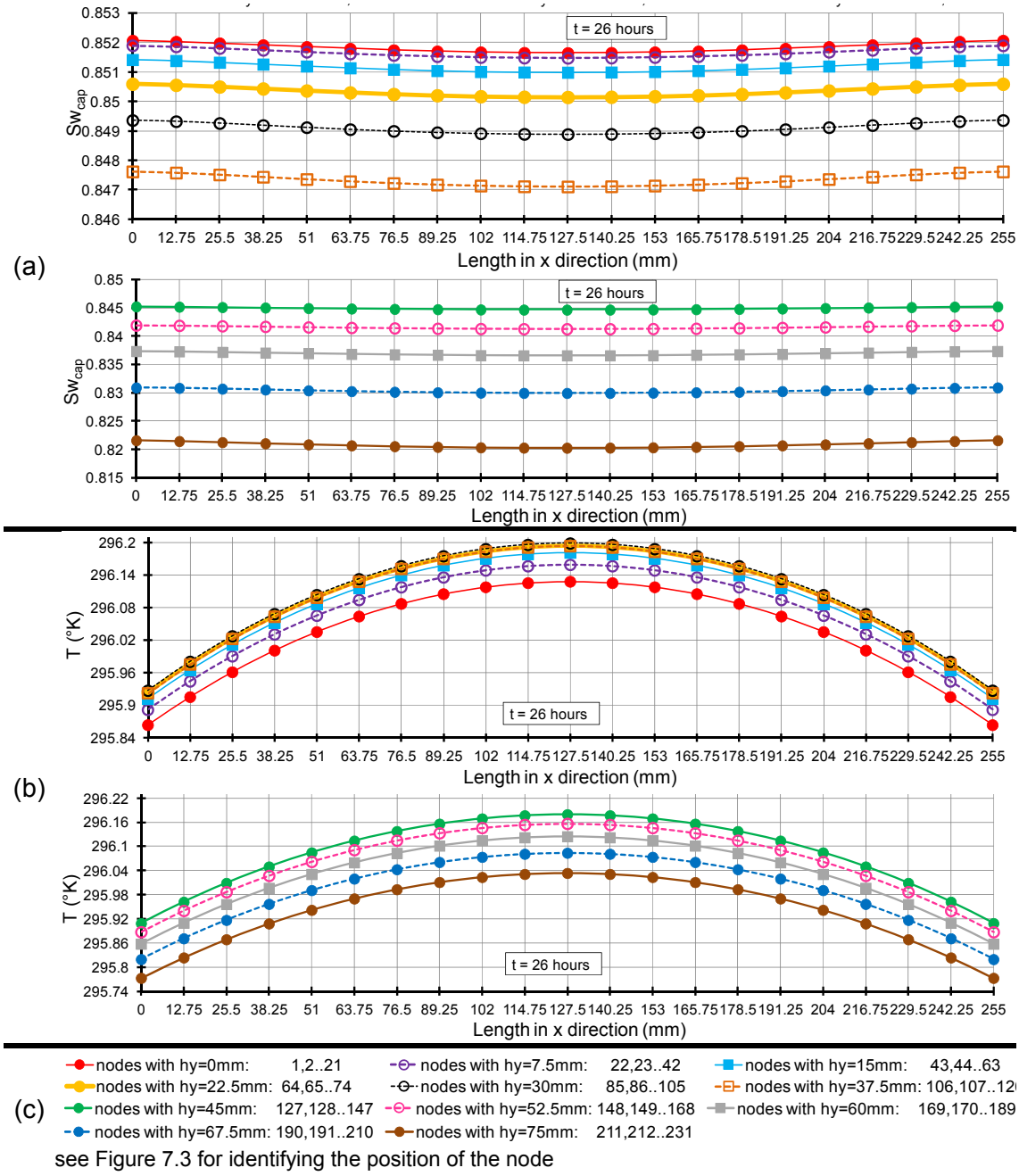

Figure 7.5 Distribution of (a) S_w^{cap} and (b) T at the end of stage 1 along the x direction

7.3.3 Numerical Model Conditions for Stage 2 (Immersed Water Curing)

In the second stage of the experimental study, the mortar beam was immersed in water, its sides were continuously saturated and the crack was filled with H_2O due to the capillary rise effect as it is showed in Figure 7.6 (a). Since the environmental conditions were symmetrical with respect to the middle cross section of the specimen and since the attention in this thesis is focused on the healing effect, the discretisation is done solely for the beam section included in the detail B from Figure 7.6 (b). This

beam section is divided into two parts. The first part, which has a volume equal to 127.4 X 37.5 X 75 mm, is filled with mortar and is discretised into 10 X 5 4-noded planar finite elements. The second part, representing the notch filled with water, is filled in time with hydrates and is split into other 10 X 5 4-noded planar finite elements. A schematic representation of the mesh is illustrated in Figure 7.7.

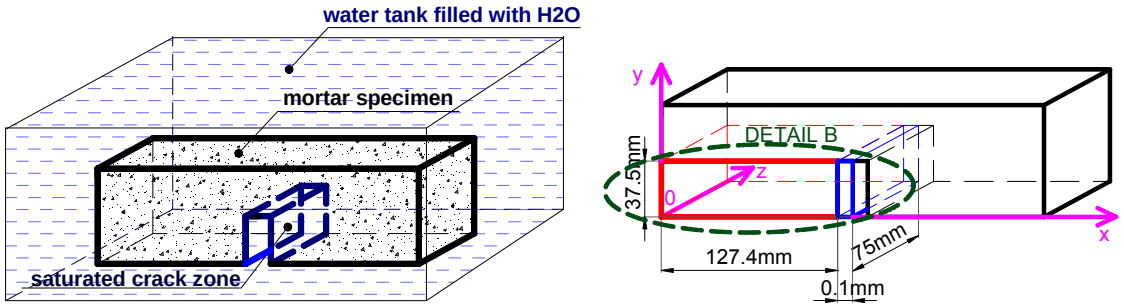

Figure 7.6 Schematic representation of the stage 2 of curing

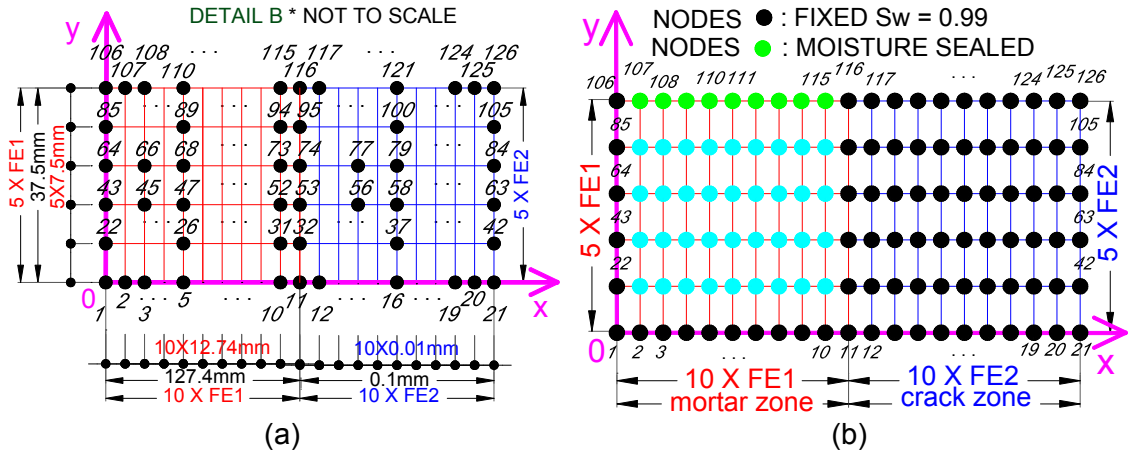

Figure 7.7 Meshing used for the stage 2 of curing; node numbers are written in italics

Due to the distinct nature of the internal structure of the materials and, having in mind the previous observations regarding the porosity function, it was decided to split the used finite elements into two categories as can be seen in Figure 7.7 (a) and (b). In the case of *FE1* elements, employed in the mortar region, the initial nodal values of S_w^{cap} and T are exactly the values returned by the *THC* model at the end of stage 1, while ω_0 is the ratio between the mass of unreacted cement particles – equation (7.11) – and the mass of the capillary water – equation (7.12) – existing at the initial time of the analysis t_0:

$$\omega_0 = \frac{m_{UCP}}{m_{CW}} \tag{7.10}$$

$$m_{UCP} = n_{UCP}\left(1-\Gamma_0\right)\left(c+m_{FA}\right) \tag{7.11}$$

$$m_{CW} = M_{CW}\Gamma_0 \tag{7.12}$$

where n_{UCP} is the mass fraction of unhydrated cement particles that can be transported through the capillary pore network. For this category of elements a fixed hygral boundary condition (S_w^{cap} = 0.99) is applied on the peripheral black nodes visible in Figure 7.7 (b), whilst the green nodes, which are in contact with the mortar paste, are free from any type of boundary constraint.

In the case of *FE2* elements, employed in the crack zone, it is assumed that the pores are always full of water and so the nodes have a fixed S_w^{cap} = 0.99 along the entire modelling period. The two remaining degrees of freedom have the following initial values, T_0 = 293°K and Γ_0 = 10^{-6}, but are free to change in time.

Regarding the spatial discretisation, varying time steps of:

$$\Delta t = \begin{cases} 3600s, & 1 < itime \le 250 \\ 7200s, & 250 < itime \le 350 \\ 12000s, & 350 < itime \end{cases} \tag{7.13}$$

and a constant convergence tolerance (10^{-3}) were used during the numerical analysis.

Next, Table 7.2 provides the values of the parameters used to characterise the reactive transport of the unreacted cement grains. It is important to specify at this point that the magnitudes of α_P, β_P, α_L, D_{mol}, δ_ω are calibrated such as to obtain a satisfactory estimation of the self-healing phenomenon at the end of the longest curing period (41 days).

Table 7.2 Parameters used in the reactive transport

m_ω equation (3.78)	α_P		2.5
	β_P		0.07
$\overline{\rho C}_p$ equation (3.86)	C_p^P	[J/(°K*kg)]	840
	C_p^{FA}	[J/(°K*kg)]	713
	ρ_P	[kg/m^3]	2600
D_{mdisp}^{ij} and D_{mdiff}^{ij} equations (3.76) and (3.77)	α_L	[m]	5*10^{-3}
	D_{mol}	[m/s]	10^{-8}
initial volume of precipitated material	V_{P0}	[m^3/ m^3]	10^{-9}
equation (4.14)	δ_ω	[kg/(s*m^2)]	10^{-6}
ω_0 equation (7.10)	n_{UCP}		30%

7.3.4 Results and Discussions

Before presenting the results of the proposed *THC* model, a short discussion regarding the available experimental evidences is needed. The images from (Davies, 2014) with the healed cross-sections of the artificially created narrow notches (see the blue region in Figure 7.6) are processed using ImageJ, a Java-based image processing program developed at the National Institutes of Health (Schneider et al., 2012) in order to obtain relevant quantities. The degree of self-healing in terms of area fraction of deposited material is established using the Analyze Particles command. Prior to running this command, the two dimensional healed zones are manually selected by means of brightness and colour-based criteria following the steps enumerated in ImageJ (2013). Examples of experimental and processed images are shown in Figure 7.8, while the summary of the visual analysis is presented in Table 7.3. The rest of the processed images are included in the Appendix B.

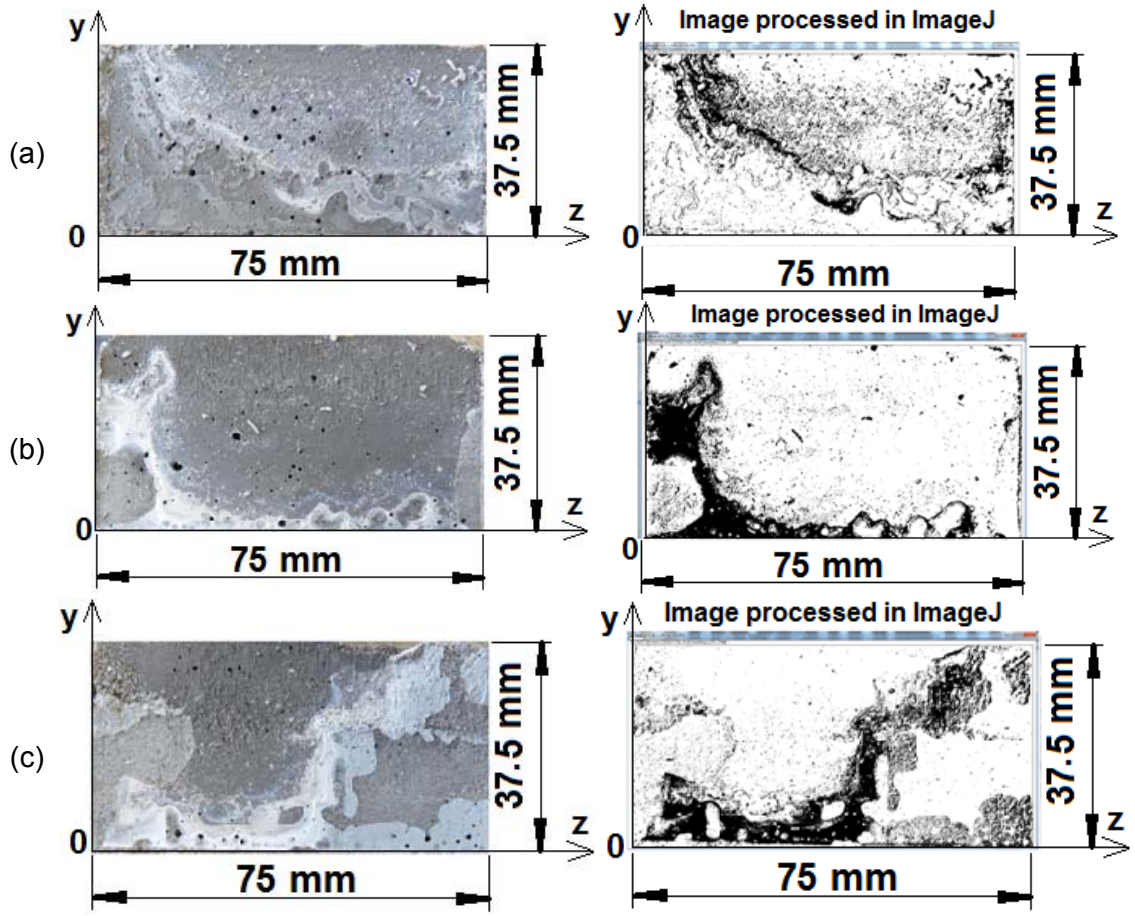

Figure 7.8 Self-healed area fractions at 13 days: (a) 18.33%; (b) 17.62%; (c) 21.17%; all the cross sections are positioned at 127.4mm on x direction

The proposed *THC* model estimates only the concentration of the *UCP* and the volume of precipitated material that appears during the crack recovery. No experimental data was available regarding the thickness of the self-healed area and therefore, in the

current investigation it is assumed that within the self-healed region of the cross section, the notch is completely bridged by the new deposited material. In this context the numerical estimation of the self-healed area fraction produces the values reported in Table 7.3 which are indicating an ascending trend of crack recovery which is in agreement with the experimental observations.

Table 7.3 Experimentally based data regarding the self-healing process

Duration of the self-healing process		13 days	27 days	41 days
Experimentally evaluated self-healed area fraction	[%]	19.04	21.15	24.89
Numerically evaluated self-healed area fraction	[%]	23.80	24.39	24.60

The values from the above mentioned table indicate that, when the calibration of the model targets the accurate estimation of the most prolonged self-healing condition (41 days), the filling of the crack is overestimated at the intermediate time periods (13 and 27 days). However, Figure 7.9 to Figure 7.12 confirm that the proposed *THC* model is able to predict a realistic trend for the crack recovery. The volume of precipitated material increases in time throughout the sample, but the magnitude of the deposition is significantly higher in the crack region as can be easily seen in Figure 7.10. Another interesting observation is that the mass accumulation is always intensified in the early-age period of the self-healing process. Regarding the spatial distribution of the filler, Figure 7.9 and Figure 7.11 show that in the transverse direction of the mortar zone there is a predominantly higher quantity of precipitated substance towards the mid height (i.e. at h_y=37.5 mm), whilst in the transverse direction of the notch the deposition occurs towards the opposite side. From Figure 7.12 it is apparent that in the longitudinal direction, the accumulation process in the mortar region changes in time towards a uniform distribution state. It is evident that the volume gradient along the length of the sample, visible at the 13th day of water immersed curing (Figure 7.12 (a)), reduces dramatically during the following 2 weeks and then stabilises in time (Figure 7.12 (b) and (c)). On the other hand, from Figure 7.9 (b) and (c) and Figure 7.11 (b) it is clear that in the crack zone the new material builds up in the same percentage in all the nodes located at the same height.

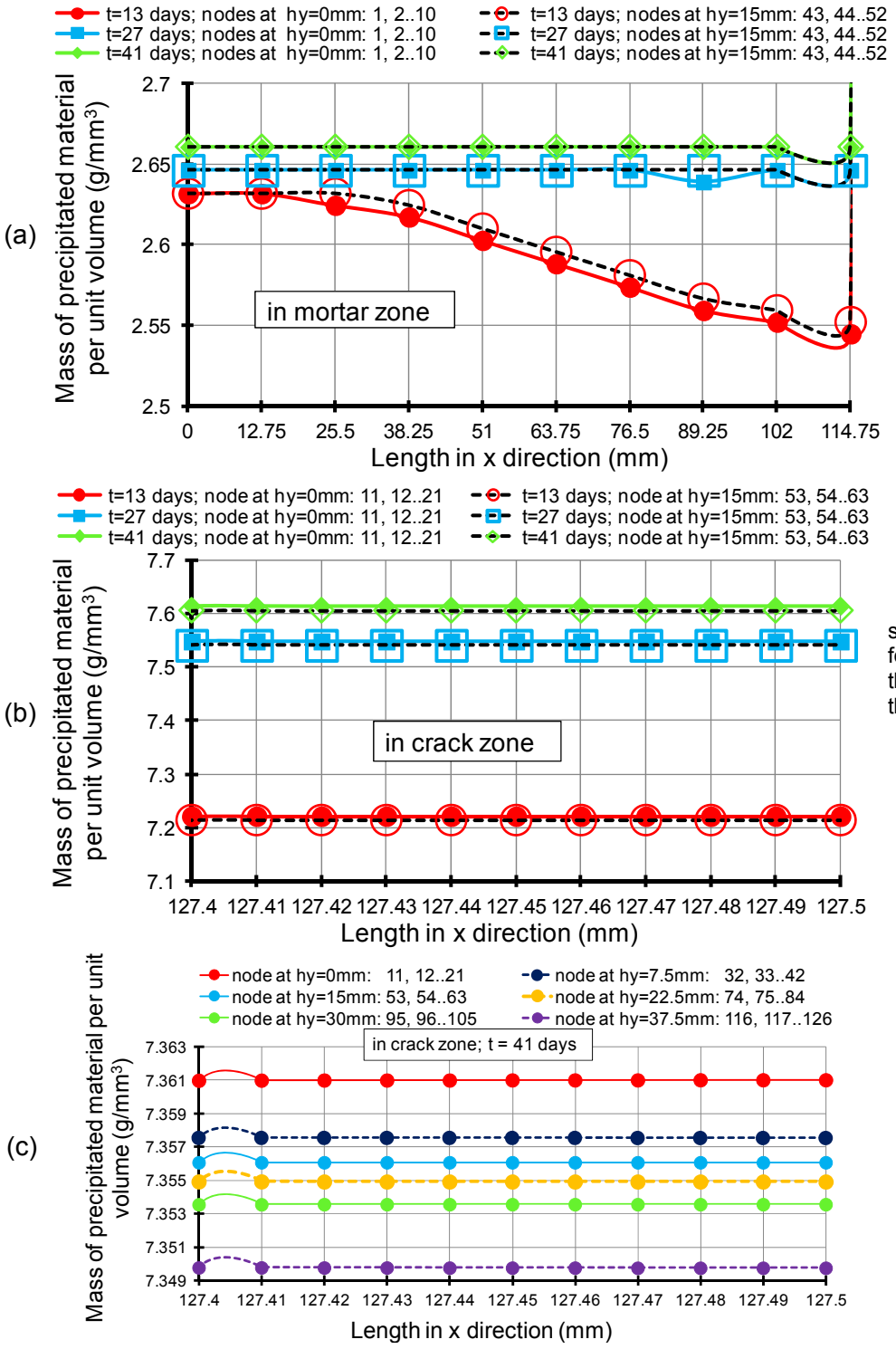

see Figure 7.7 for identifying the position of the nodes

Figure 7.9 Distribution of m_P per unit volume in x direction

(a)

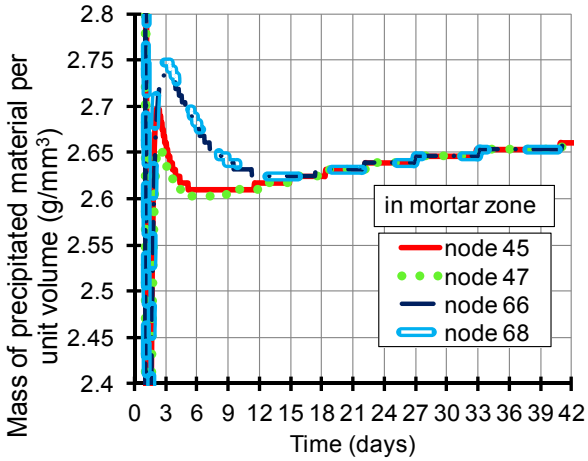

(b)

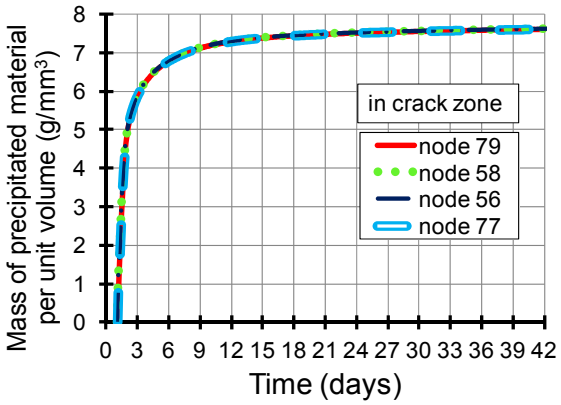

see Figure 7.7 for identifying the position of the nodes

Figure 7.10 Evolution of m_P per unit volume during the modelled self-healing process

(a)

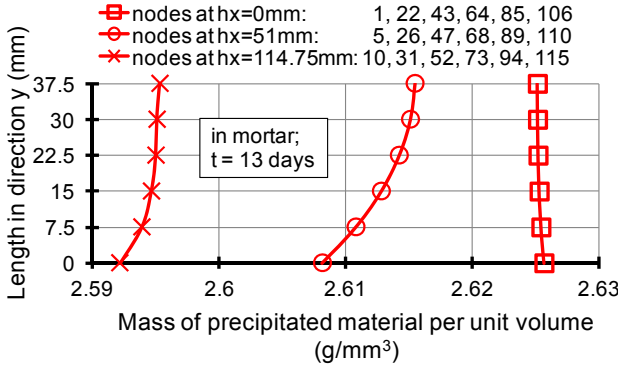

(b)

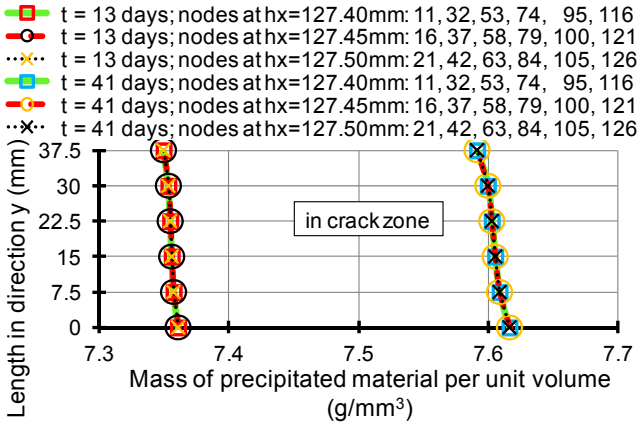

see Figure 7.7 for identifying the position of the node

Figure 7.11 Distribution of m_P per unit volume in y direction

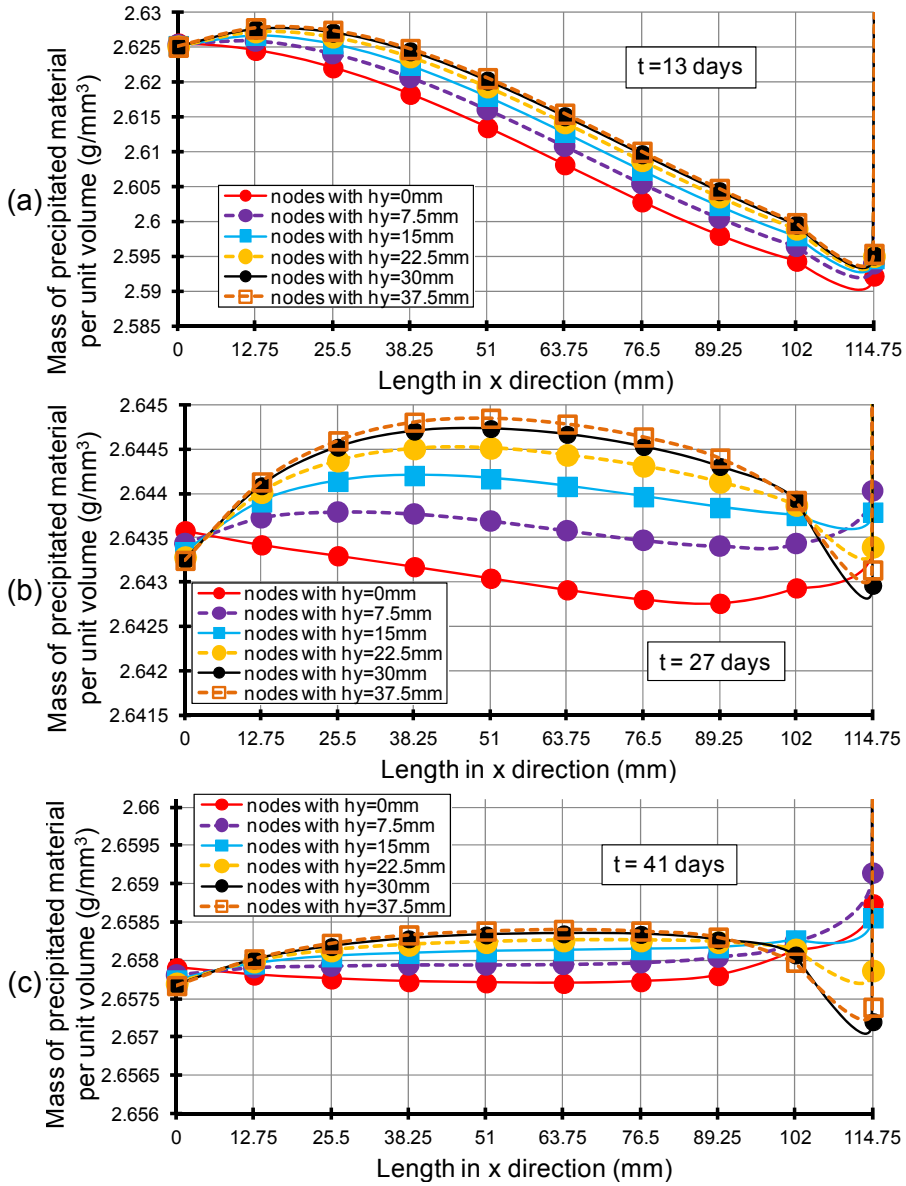

Figure 7.12 Evolution of m_P per unit volume in x direction in the mortar zone

7.4 Conclusions

The objective of this chapter was to demonstrate that a comprehensive *THC* model proves to be a useful tool in predicting the autogenous healing capacity of cementitious materials. In order to fulfil this task an experimental study, in which an artificially induced crack is filled with precipitates under specific curing conditions, was simulated. The numerically results were reasonably encouraging even if it is acknowledged that there is still room for improvement.

The *THC* model assumes that the crack recovery of the cementitious materials is due to the ongoing hydration of the *UCP* that can be transported within the saturated capillary network via advective and diffusive-dispersive fluxes driven by the gradients of the total water potential and chemical concentration. The model offers a macroscale image of the reactive transport mechanisms since its focus is not the movement of the dissolved clinker ions, but the movement of the unreacted cement particles as a whole. The nature of the modelling approach is mechanistic and requires several laboratory derived parameters to describe the reactive transport of the solute which were unavailable in this initial phase of the research. To overcome this shortcoming, the simulation consisted in effect of an inverse parameter identification exercise that enabled a qualitative validation of the theoretical considerations underlying the proposed *THC* model. A greater experimental focus on the reactive transport mechanisms could produce interesting findings that may considerably improve the predicted crack recovery capacity.

The simulation of the self-healing process was carried out within the framework of the finite element method which allows the application of a complete range of boundary conditions. It is envisaged that in the future a micromechanical model to be included into the existing finite element method in order also asses the mechanical strength gain. Taken together, this numerical investigation represents the starting point towards a holistic thermo-hygro-chemo-mechanical model that can predict the healing capacity of cementitious materials.

Chapter 8. Conclusions

The present study was conducted to develop a computational code that can satisfactorily simulate the autogenous healing of cementitious materials. A coupled *THC* model, that is specifically designed to account for crack recovery from the durability point of view, has been described in Chapters 3 and 4. In the following paragraphs the conclusions corresponding to the proposed computational developments are synthesised and suggestions are made for further research and developments.

The conclusions that can be drawn are directly linked to the aims of the current research highlighted in the first chapter. The study presented in this thesis involved :

1. The development of a reliable theoretical model for the coupled transport of moisture and temperature that is capable of simulating the early-age and long term thermo-hygral behaviour of ordinary cementitious materials;
2. The integration of a microstructural model into the proposed *TH* framework in order to realistically reproduce the hydration reaction and the evolution of the pore network;
3. The investigation of the coupled *TH* model under different curing conditions and the comparison of the results with experimental findings;
4. The coupling of the theoretical principles describing the reactive transport of solutes to the *TH* model and thereby the development of a novel thermo-hygro-chemical model for the autogenous healing of cement-based materials;
5. The simulation by means of the finite element method of the autogenous healing process and the validation of the results against laboratory data.

In respect to the first three objectives, that provide the spatial and temporal evolution of moisture and heat within the porous network, the following conclusions were reached:

- The proposed mass and entropy balance equations, in which the transport mechanism of moisture is assumed to occur at the capillary pore level, allow a wide range of cementitious materials types and curing conditions to be considered. The mathematical formulation accounts for consumption of capillary water due to hydration, for water adsorption/desorption by the unsaturated aggregate and for water desorption from the gel pores at low relative humidities. The model gives good predictions of the early age and long term thermo-hygral

behaviour of cement-based materials subjected to self-desiccation and external drying, but additional experimental work is required in order to correctly determine the material parameters related to the transport mechanisms of moisture and heat. In this connection, a high priority should be given to the thorough investigation of the effect of porosity development upon the constitutive law between the capillary pressure and the water saturation degree.

- The accuracy of the simulated *TH* behaviour depends greatly on the correlation between hydration kinetics and porosity evolution. The innovative proposed microstructural model, that incorporates a colloidal model for the *C-S-H* gel pores together with the hydration kinetics and stoichiometry of Portland cement, provides realistic estimates of the volume fractions of pores and hydrates. The model is capable of identifying the minimum *w/c* ratio necessary for the complete hydration of Portland cement and suggests a linear variation of both total and capillary porosity with respect to the degree of hydration. Nevertheless, further development of this microstructural model is needed in order to capture the effect of the addition of cement replacement materials (fly ash, ground-granulated blast-furnace slag cement and others) upon the porosity development and also the effect of the curing conditions upon the reaction rates of the clinker minerals.
- The experimental procedure designed to examine the water absorption of the aggregate has shown that the quantity of bulk water transferred from the mix into the unsaturated pores of the aggregate may be considered second order in comparison with the quantity of water used in hydration.

In respect to the last two objectives of the thesis, the conclusions are as follows:

- The proposed self-healing model represents a promising tool for assessing the durability improvement of damaged concrete structures. The numerical investigation focused mainly on simulating the deposition of new materials in cracks, since the available experimental measurements allowed only the validation of this process. Whilst the accumulation of precipitates in the empty or water filled pores is likely to decrease the permeability of the hardened concrete, and thus improve their durability, this needs to be confirmed in future work.
- Although the qualitative predictions are good, there is scope for the accuracy of these predictions to be improved. An inverse parameter identification exercise, aimed at validating the theoretical assumptions underlying the proposed *THC* model, was performed in this study. A logical further step would be a

comprehensive investigation of the reactive transport mechanisms, which should be supported by detailed experimental evidence. The model assumed the movement of the unreacted cement particles towards the crack location as a whole, but in the context of new data regarding the reactive transport, it might be necessary to narrow the scale of the modelling towards the movement of the dissolved clinker ions.

- The finite element method has proved to be an effective numerical framework for the *THC* model which gives accurate predictions of moisture contents, entropy distributions and chemical concentrations . Its limitations related to the computational cost may be overcome by developing an efficient equation solution method. Moreover, the *FEM* is a suitable choice because it facilitates the future coupling of a mechanical component that can simulate the strength recovery and, in certain circumstances, the enhancement of healed cementitious composites.
- The ability of the proposed *THC* model to capture self-healing behaviour due to ongoing hydration of Portland cement serves as further evidence of its flexibility and augurs well for its future application at capturing other healing phenomena.

References

Acker, P. and Ulm, F.-J. (2001). Creep and shrinkage of concrete: physical origins and practical measurements. *Nuclear Engineering and Design* 203, pp. 143–158.

Aldea, C.M., Shah, S.P. and Karr, A. (1999). Permeability of cracked concrete. *Materials and Structures* 32, pp. 370–376.

Balonis, M. and Glasser, F.P. (2009). The density of cement phases. *Cement and Concrete Research* 39, pp. 733–739.

Barbarulo, R., Marchand, J., Snyder, K.A. and Prené, S. (2000). Dimensional analysis of ionic transport problems in hydrated cement systems. *Cement and Concrete Research* 30, pp. 1955–1960.

Baroghel-Bouny, V. (1994). *Caracterisation des pates de ciment et des betons : Methodes, analyse, interpretations*. PhD Thesis. Paris: Laboratoire central des Ponts et Chaussees.

Baroghel-Bouny, V. (1997). Experimental investigation of self-desiccation in high-performance materials - comparison with drying behaviour. In: Persson, B. and Fagerlund, G. eds. *Self-desiccation and its importance in concrete technology*. Lund, pp. 72–88.

Baroghel-Bouny, V. (2007). Water vapour sorption experiments on hardened cementitious materials. Part II: Essential tool for assessment of transport properties and for durability prediction. *Cement and Concrete Research* 37, pp. 438–454.

Baroghel-Bouny, V. and Chaussadent, T. (1995). Pore structure and moisture properties of cement-based systems from water vapor sorption isotherms. *Mater. Res. Soc. Symp. Proc.* 370, pp. 245–254.

Baroghel-Bouny, V., Mainguy, M., Lassabatere, T. and Coussy, O. (1999). Characterization and identification of equilibrium and transfer moisture properties for ordinary and high-performance cementitious materials. *Cement and Concrete Research* 29, pp. 1225–1238.

Baroghel-Bouny, V., Thiéry, M. and Wang, X. (2011). Modelling of isothermal coupled moisture–ion transport in cementitious materials. *Cement and Concrete Research* 41, pp. 828–841.

Bary, B., de Morais, M.V.G., Poyet, S. and Durand, S. (2012). Simulations of the thermo-hydro-mechanical behaviour of an annular reinforced concrete structure heated up to 200°C. *Engineering Structures* 36(0), pp. 302–315.

Bary, B., Ranc, G., Durand, S. and Carpentier, O. (2008). A coupled thermo-hydro-mechanical-damage model for concrete subjected to moderate temperatures. *International Journal of Heat and Mass Transfer* 51, pp. 2847–2862.

Baur, I., Keller, P., Mavrocordatos, D., Wehrli, B. and Johnson, C.A. (2004). Dissolution-precipitation behaviour of ettringite, monosulfate, and calcium silicate hydrate. *Cement and Concrete Research* 34, pp. 341–348.

Bear, J. and Bachmat, Y. (1991). *Introduction to modeling of transport phenomena in porous media*. Dordrecht; Boston: Kluwer Academic Publishers.

Bentz, D.P. (2007). Transient plane source measurements of the thermal properties of hydrating cement pastes. *Materials and Structures* 40, pp. 1073–1080.

Bentz, D.P., Snyder, K.A. and Stutzman, P.E. (1997). Hydration of Portland cement: the effects of curing conditions. In: Justness, H. J. ed. *10th International Congress on the Chemistry of Cement. Vol. 2. 2-6 June, 1997*. Göteborg: Amarkai AB and Congrex, p. 2ii078.

Bernard, O., Ulm, F.-J. and Lemarchand, E. (2003). A multiscale micromechanics-hydration model for the early-age elastic properties of cement-based materials. *Cement and Concrete Research* 33, pp. 1293–1309.

Boudreau, B.P., Meysman, F.J.R. and Middelburg, J.J. (2004). Multicomponent ionic diffusion in porewaters: Coulombic effects revisited. *Earth and Planetary Science Letters* 222(2), pp. 653–666.

Van Breugel, K. (1991). Simulation of hydration and formation of structure in hardening cement-based materials. PhD Thesis,. Delft University Press.

Brouwers, H.J.H. (2004). The work of Powers and Brownyard revisited: Part I. *Cement and Concrete Research* 34, pp. 1697–1716.

Buenfeld, N.R. and Okundi, E. (1999). Release of air from unsaturated aggregate during setting of concrete. *Construction and Building Materials* 13(3), pp. 143–147.

Bullard, J.W., Enjolras, E., George, W.L., Terrill, J.E. and Satterfield, S.G. (2010). A parallel reaction-transport model applied to cement hydration and microstructure development. *Modelling and Simulation in Materials Science and Engineering* 18, pp. 1–16.

Bullard, J.W., Jennings, H.M., Livingston, R.A., Nonat, A., Scherer, G.W., Schweitzer, J.S., Scrivener, K.L. and Thomas, J.J. (2011). Mechanisms of cement hydration. *Cement and Concrete Research* 41, pp. 1208–1223.

Carino, N.J. and Lew, H.S. (2001). The maturity method: from theory to application. In: Chang, P. C. ed. *Structures 2001*. Washington D.C.: American Society of Civil Engineers, pp. 1–19.

Cembureau (2014). *Activity report 2013 [Online]*. [Online] http://www.cembureau.eu/2013-activity-report [Accessed: September 2014].

Cerny, R. and Rovnonikova, P. (2002). *Transport processes in concrete*. London: Spoon Press.

Chindaprasirt, P., Jaturapitakkul, C. and Sinsiri, T. (2005). Effect of fly ash fineness on compressive strength and pore size of blended cement paste. *Cement and Concrete Composites* 27, pp. 425–428.

Cleall, P.J. (1998). *An investigation of the thermo/hydraulic/mechanical behaviour of unsaturated soils, including expansive clays*. PhD Thesis, Cardiff University.

Clear, C.A. (1985). The effects of autogenous healing upon the leakage of water through cracks in concrete. *Cement and Concrete Association* Tech Rpt., pp. 1–31.

Cook, R.A. and Hover, K.C. (1999). Mercury porosimetry of hardened cement pastes. *Cement and Concrete Research* 29, pp. 933–943.

Damidot, D., Nonat, A. and Barret, P. (1990). Kinetics of tricalcium silicate hydration in diluted suspensions by microcalorimetric measurements. *Journal of the American Ceramic Society* 73(11), pp. 3319–3322.

Davie, C., Pearce, C. and Bićanić, N. (2010). A fully generalised, coupled, multi-phase, hygro-thermo-mechanical model for concrete. *Materials and Structures* 43(1), pp. 13–33.

Davie, C.T., Pearce, C.J. and Bićanić, N. (2012). Aspects of permeability in modelling of concrete exposed to high temperatures. *Transport in Porous Media* 95(3), pp. 627–646.

Davie, C.T., Pearce, C.J. and Bićanić, N. (2014). Fully coupled, hygro-thermo-mechanical sensitivity analysis of a pre-stressed concrete pressure vessel. *Engineering Structures* 59, pp. 536–551.

Davies, R.D. (2014). Micromechanical modelling of self-healing cementitious materials. PhD Thesis, Cardiff University.

Domone, P.L.J. and Illston, J.M. (2010). *Construction materials: their nature and behaviour*. fourth ed. London: Spon Press.

Double, D.D., Hellawell, A. and Perry, S.J. (1978). The hydration of Portland cement. *Proc. R. Soc. Lond. A* 359, pp. 435–451.

Dry, C. (1994). Matrix cracking repair and filling using active and passive modes for smart timed release of chemicals from fibers into cement matrices. *Smart Materials and Structures* 3, pp. 118–123.

Edlefsen, N.E. and Andersen, A.B.. (1943). Thermodynamics of soil moisture. *Hilgaria* 15(2), pp. 1–298.

Edvardsen, C. (1999). Water permeability and autogenous healing of cracks in concrete. *ACI Materials Journal* 96, pp. 448–454.

Feldman, R., Chan, G., Brousseau, R. and Tumidajski, P. (1994). *Investigation of the Rapid Chloride Permeability Test*.

Feldman, R.F. (1973). Helium flow characteristics of rewetted specimens of dried hydrated Portland cement paste. *Cem. Concr. Res* 3, pp. 777–790.

Fujii, K. and Kondo, W. (1986). Kinetics of hydration of calcium sulphate hemihydrate. *Journal of the Chemical Society, Dalton Transactions* (4), pp. 729–731.

Fujii, K. and Kondo, W. (1974). Kinetics of the hydration of tricalcium silicate. *Journal of the American Ceramic Society* 54, pp. 492–497.

Galerkin, B.G. (1915). Series solution of some problems in elastic equilibrium of rods and plates. *Vestnik inzhenerov i tekhnikov* 19, pp. 897–908.

Gallucci, E., Mathur, P. and Scrivener, K. (2010). Microstructural development of early age hydration shells around cement grains. *Cement and Concrete Research* 40, pp. 4–13.

Gardner, D.R., Jefferson, A.D. and Lark, R.J. (2008). An experimental, numerical and analytical investigation of gas flow characteristics in concrete. *Cement and Concrete Research* 38, pp. 360–367.

Garrault, S., Finot, E., Lesniewska, E. and Nonat, A. (2005). Study of C-S-H growth on C3S surface during its early hydration. *Materials and Structures* 38, pp. 435–442.

Garrault-Gauffinet, S. and Nonat, A. (1999). Experimental investigation of calcium silicate hydrate (C-S-H) nucleation. *Journal of Crystal Growth* 200, pp. 565–574.

Gartner, E.M. (1997). A proposed mechanism for the growth of C-S-H during the hydration of tricalcium silicate. *Cement and Concrete Research* 27, pp. 665–672.

Gawin, D., Majorana, C.E. and Schrefler, B.A. (1999). Numerical analysis of hygro-thermal behaviour and damage of concrete at high temperature. *Mechanics of cohesive-frictional materials* 4, pp. 37–74.

Gawin, D., Pesavento, F. and Schrefler, B.A. (2006a). Hygro-thermo-chemo-mechanical modelling of concrete at early ages and beyond. Part I: hydration and hygro-thermal phenomena. *International Journal for Numerical Methods in Engineering* 67(3), pp. 299–331.

Gawin, D., Pesavento, F. and Schrefler, B.A. (2006b). Hygro-thermo-chemo-mechanical modelling of concrete at early ages and beyond. Part II: shrinkage and creep of concrete. *International Journal for Numerical Methods in Engineering* 67(3), pp. 332–363.

Gawin, D., Pesavento, F. and Schrefler, B.A. (2009). Modeling deterioration of cementitious materials exposed to calcium leaching in non-isothermal conditions. *Computer Methods in Applied Mechanics and Engineering* 198, pp. 3051–3083.

Gawin, D., Pesavento, F. and Schrefler, B.A. (2008). Modeling of cementitious materials exposed to isothermal calcium leaching, considering process kinetics and advective water flow. Part 1: Theoretical model. *International Journal of Solids and Structures* 45, pp. 6221–6240.

Gawin, D., Pesavento, F. and Schrefler, B.A. (2011a). What physical phenomena can be neglected when modelling concrete at high temperature? A comparative study. Part 1: Physical phenomena and mathematical model. *International Journal of Solids and Structures* 48(13), pp. 1927–1944.

Gawin, D., Pesavento, F. and Schrefler, B.A. (2011b). What physical phenomena can be neglected when modelling concrete at high temperature? A comparative study. Part 2: Comparison between models. *International Journal of Solids and Structures* 48(13), pp. 1945–1961.

Van Genuchten, M.T. (1980). A closed form equation for predicting the hydraulic conductivity of unsaturated soils. *Soil Science Society of America Journal* 44, pp. 892–898.

Granger, S., Loukili, A., Pijaudier-Cabot, G. and Chanvillard, G. (2007). Experimental characterization of the self-healing of cracks in an ultra high performance cementitious material: Mechanical tests and acoustic emission analysis. *Cement and Concrete Research* 37(4), pp. 519–527.

Hadley, D.W., Dolch, W.L. and Diamond, S. (2000). On the occurrence of hollow-shell hydration grains in hydrated cement paste. *Cement and Concrete Research* 30, pp. 1–6.

Halamickova, P., Detwiler, R.J., Bentz, D.P. and Garboczi, E.J. (1995). Water permeability and chloride ion diffusion in portland cement mortars: Relationship to sand content and critical pore diameter. *Cement and Concrete Research* 25, pp. 790–802.

Harmathy, T.Z. (1970). Thermal properties of concrete at elevated temperatures. *Journal of Materials* 5, pp. 47–44.

He, H. (2010). *Computational Modelling of Particle Packing in Concrete*. PhD Thesis. Technische Universiteit Delft.

He, H., Guo, Z., Stroeven, P., Stroeven, M. and Sluys, L.J. (2007). Self-healing capacity of concrete - computer simulation study of unhydrated cement structure. *Image Anal Stereol* 26, pp. 137–143.

Hearn, N. (1998). Self-sealing, autogenous healing and continued hydration: What is the difference? *Materials and Structures* 31, pp. 563–567.

Hearn, N. and Morley, C.T. (1997). Self-sealing property of concrete—Experimental evidence. *Materials and Structures* 30(7), pp. 404–411.

Ter Heide, N. (2005). Crack healing in hydrating concrete. Msc Thesis, Delft University of Technology.

Ter Heide, N. and Schlangen, E. (2007). Selfhealing of early age cracks in concrete. In: van der Zwaag, S. ed. *Proceedings of the First International Conference on Self Healing Materials.* Noordwijk aan Zee, 18-20 April 2007,: Springer, pp. 1–12.

Hilloulin, B., Grondin, F., Matallah, M. and Loukili, A. (2013). Numerical modelling of autogenous healing and recovery of mechanical properties in ultra-high performance concrete. In: De Belie, N., Van der Zwaag, S., Gruyaert, E., Van Tittelboom, K., and Debbaut, B. eds. *ICSHM 2013: Proceedings of the 4th International Conference on Self-Healing Materials*. Ghent, 16-20 June, 2013: Ghent: Magnel Laboratory for Concrete Research, pp. 414–417.

Hosoda, A., Komatsu, S., Ahn, T., Kishi, T., Ikeno, S. and Kobayashi, K. (2009). Self healing properties with various crack widths under continuous. In: Alexander, M. G., Beushausen, H.-D., Dehn, F., and Moyo, P. eds. *Concrete Repair, Rehabilitation and Retrofitting II*. London: Taylor & Francis Group, pp. 221–227.

Hou, P., Kong, D., Kawashima, S., Qian, J., Corr, D. and Shah, S. (2013). A novel evidence for the formation of semi-permeable membrane surrounding the Portland cement particles during the induction period. *Journal of Thermal Analysis and Calorimetry* 113(2), pp. 881–884.

Huang, H. and Ye, G. (2012). Simulation of self-healing by further hydration in cementitious materials. *Cement and Concrete Composites* 34(4), pp. 460–467.

Huang, H. and Ye, G. (2011). The mechanism of self-healing in high performance concrete. In: Palomo, A., Zaragoza, A., and Agüí, J. C. L. eds. *13th International Congress on the Chemistry of Cement.* Madrid, 3-8 July, 2011, p. 365.

Huang, H., Ye, G. and Damidot, D. (2013). Characterization and quantification of self-healing behaviors of microcracks due to further hydration in cement paste. *Cement and Concrete Research* 52, pp. 71–81.

Hubler, M.H., Thomas, J.J. and Jennings, H.M. (2011). Influence of nucleation seeding on the hydration kinetics and compressive strength of alkali activated slag paste. *Cement and Concrete Research* 41, pp. 842–846.

ImageJ (2013). *Tutorials and Examples*. [Online] Available at http://imagej.nih.gov/ij/docs/examples/index.html%20%5BAccessed%20%20%5BAccessed%2009/2014%5D [Accessed September 2014].

Jacobsen, S., Marchand, J. and Hornain, H. (1995). SEM observations of the microstructure of frost deteriorated and self-healed concretes. *Cement and Concrete Research* 25(8), pp. 1781–1790.

Jacobsen, S. and Sellevold, E.J. (1996). Self healing of high strength concrete after deterioration by freeze/thaw. *Cement and Concrete Research* 26, pp. 55–62.

Jaffer, S. and Hansson, C. (2008). The influence of cracks on chloride-induced corrosion of steel in ordinary Portland cement and high performance concretes subjected to different loading conditions. *Corrosion Science* 50, pp. 3343–3355.

Jennings, H.M. (2008). Refinements to colloid model of C-S-H in cement: CM-II. *Cement and Concrete Research* 38, pp. 275–289.

Jennings, H.M. and Pratt, P.L. (1979). An experimental argument for the existence of a protective membrane surrounding portland cement during the induction period. *Cement and Concrete Research* 9(4), pp. 501–506.

Jennings, H.M. and Thomas, J.J. (2009). *Materials of Cement Science Primer: The Science of Concrete*. Infrastructure Technology Institute for TEA.

Joseph, C., Gardner, D., Jefferson, T., Isaacs, B. and Lark, B. (2010). Self-healing cementitious materials: a review of recent work. *Proceedings of the ICE - Construction Materials* 164(1), pp. 29 –41.

Joseph, C., Lark, R., Diane, G. and Jefferson, T. (2009). *Potential application of self-healing materials in the construction industry*. Cardiff University.

Kang, S.-T., Kim, J.-K., Lee, Y., Park, Y.-D. and Kim, J.-S. (2012). Moisture diffusivity of early age concrete considering temperature and porosity. *KSCE Journal of Civil Engineering* 16, pp. 179–188.

Kantro, D.L., Weise, C.H. and Brunauer, S. (1966). Paste hydration of beta-dicalcium silicate, tricalcium silicate and alite. *Portland Cement Association. Research and Development Laboratories* 209, pp. 309–327.

Kim, J.-K. and Lee, C.-S. (1999). Moisture diffusion of concrete considering self-desiccation at early ages. *Cement and Concrete Research* 29(12), pp. 1921–1927.

Kjellsen, K.O. and Lagerblad, B. (2007). Microstructure of tricalcium silicate and Portland cement systems at middle periods of hydration-development of Hadley grains. *Cement and Concrete Research* 37, pp. 13–20.

Knudsen, T. (1980). On particle size distribution in cement hydration. In: *The 7th international congress on the chemistry of cement*. Paris, pp. 170–175.

Koenders, E.A.B. (1997). *Simulation of volume changes in hardening cement-based materials*. PhD Thesis, Delft University Press.

Kondo, R. and Ueda, S. (1968). Kinetics and mechanisms of the hydration of cements. In: *5th International Congress on the Chemistry of Cement. Part 2*. pp. 203–255.

Koniorczyk, M. (2010). Modelling the phase change of salt dissolved in pore water - Equilibrium and non-equilibrium approach. *Construction and Building Materials* 24, pp. 1119–1128.

Koniorczyk, M. (2012). Salt transport and crystallization in non-isothermal, partially saturated porous materials considering ions interaction model. *International Journal of Heat and Mass Transfer* 55, pp. 665–679.

Koniorczyk, M. and Gawin, D. (2008). Heat and Moisture Transport in Porous Building Materials Containing Salt. *Journal of Building Physics* 31, pp. 279–300.

Koniorczyk, M. and Gawin, D. (2012). Modelling of salt crystallization in building materials with microstructure - Poromechanical approach. *Construction and Building Materials* 36, pp. 860–873.

Kuhl, D. and Meschke, G. (2003). Computational modeling of transport mechanisms in reactive porous media – application of calcium leaching of concrete. *Computational Modelling of Concrete Structures, EURO-C 2003*, pp. 473–482.

Kuhl, D. and Meschke, G. (2007). Numerical analysis of dissolution processes in cementitious materials using discontinuous and continuous Galerkin time integration schemes. *International Journal for Numerical Methods in Engineering* 69, pp. 1775–1803.

Lauer, K.R. and Slate, F.O. (1956). Autogenous healing of cement paste. *ACI JOURNAL* 52, pp. 1083–1097.

Lewis, R. and Schrefler, B. (1998). *Finite Element Method in the deformation and consolidation of porous media*. second ed. Chichester: John Wiley & Sons.

Li, K., Li, C. and Chen, Z. (2009). Influential depth of moisture transport in concrete subject to drying–wetting cycles. *Cement and Concrete Composites* 31(10), pp. 693–698.

Li, V.C., Lim, Y.M. and Chan, Y.-W. (1998). Feasibility study of a passive smart self-healing cementitious composite. *Composites Part B: Engineering* 29, pp. 819–827.

Li, V.C. and Yang, E. (2008). Self Healing in Concrete Materials. In: van der Zwaag, S. ed. *Self Healing Materials SE - 8*. Springer Series in Materials Science. Springer Netherlands, pp. 161–193.

Livingston, R.A., Schweitzer, J.S., Rolfs, C., Becker, H.-W. and Kubsky, S. (2001). Characterization of the induction period in tricalcium silicate hydration by nuclear resonance reaction analysis. *Journal of Materials Research* 16(3), pp. 687–693.

Locher, F.W. (1966). Stoichiometry of tricalcium silicate hydration. In: National Research Council (U.S.) ed. *Symposium on Structure of Portland Cement Paste and Concrete*. Washington, D.C: Highway Research Board: Washington : Highway Research Board, Division of Engineering, National Research Council, National Academy of Sciences-National Academy of Engineering, pp. 300–308.

Lokhorst, S.J. (1999). *Deformational behavior of concrete influenced by hydration related changes of the microstructure*. Research Report, Delft University of Technology.

Lura, P., Jensen, O.M. and Van Breugel, K. (2003). Autogenous shrinkage in high-performance cement paste: An evaluation of basic mechanisms. *Cement and Concrete Research* 33, pp. 223–232.

Di Luzio, G. and Cusatis, G. (2009). Hygro-thermo-chemical modeling of high performance concrete. I: Theory. *Cement and Concrete Composites* 31, pp. 301–308.

Lv, Z. and Chen, H. (2012). Modeling self-healing efficiency for cracks due to unhydrated cement nuclei in hardened cement paste. *Procedia Engineering* 27, pp. 281–290.

Lv, Z. and Chen, H. (2013). Self-healing efficiency of unhydrated cement nuclei for dome-like crack mode in cementitious materials. *Materials and Structures* 46(11), pp. 1881–1892.

Marsavina, L., Audenaert, K., Schutter, G. De, Faur, N. and Marsavina, D. (2009). Experimental and numerical determination of the chloride penetration in cracked concrete. *Construction and Building Materials* 23, pp. 264–274.

Martys, N.S. (1995). *Survey of Concrete Transport Properties and their Measurements*. Gaithersburg: U.S. Department of Commerce.

McCutcheon, S.C., Martin, J.L. and Barnwell, T.O.J. (1993). Water quality. In: Maidment, D. R. ed. *Handbook of hydrology*. McGraw-Hill, pp. 346–414.

Minard, H., Garrault, S., Regnaud, L. and Nonat, A. (2007). Mechanisms and parameters controlling the tricalcium aluminate reactivity in the presence of gypsum. *Cement and Concrete Research* 37, pp. 1418–1426.

Mindess, S., Young, J.F. and Darwin, D. (2003). *Concrete*. Upper Saddle River: Prentice Hall PTR.

De Morais, M.V.G., Bary, B., Ranc, G., Pont, S.D. and Durand, S. (2009). Comparative analysis of coupled Thermo-Hydro-Mechanical models for concrete exposed to moderate temperatures. *Numerical Heat Transfer, Part A: Applications* 55(7), pp. 654–682.

Mualem, Y. (1976). A new model for predicting the hydraulic conductivity of unsaturated porous media. *Water Resources Research* 12, pp. 513–522.

Neville, A. (2002). Autogenous healing: a concrete miracle? *Concrete International*, pp. 76–82.

Neville, A.M. and Brooks, J.J. (2003). *Concrete Technology*. Singapore: Pearson Education Ltd.

Ngab, A.S.. and Nilson, A.H. (1981). Shrinkage and Creep of High-Strength Concrete. *ACI JOURNAL Proceedings* 78, pp. 255–261.

Office for National Statistics (2013). *Construction statistics - no. 14, 2013 Edition*. [Online] http://www.ons.gov.uk/ons/publications/re-reference-tables.html?edition=tcm%2525253A77-324202%20%255BAccessed:%2009/2014%255D%20%5BAccessed:%2009/2014%5D [Accessed September 2014].

Office for National Statistics (2014). *Construction statistics - no. 15, 2014 Edition*. [Online] http://www.ons.gov.uk/ons/publications/re-reference-tables.html?edition=tcm%25253A77-360369%20%5BAccessed:%2009/2014%5D [Accessed September 2014].

Onsager, L. and Fuoss, R.M. (1931). Irreversible processes in electrolytes. Diffusion, conductance and viscous flow in arbitrary mixtures of strong electrolytes. *The Journal of Physical Chemistry* 36(11), pp. 2689–2778.

Otieno, M., Alexander, M. and Beushausen, H. (2010). *Transport mechanisms in concrete. Corrosion of steel in concrete. Assessment of corrosion*. Cape Town: Concrete Materials ans Structural Integrity Research Group.

Pesavento, F., Gawin, D., Wyrzykowski, M., Schrefler, B.A. and Simoni, L. (2012). Modeling alkali–silica reaction in non-isothermal, partially saturated cement based materials. *Computer Methods in Applied Mechanics and Engineering* 225-228, pp. 95–115.

Peterson, V.K., Neumann, D.A. and Livingston, R.A. (2005). Hydration of tricalcium and dicalcium silicate mixtures studied using quasielastic neutron scattering. *The journal of physical chemistry. B* 109, pp. 14449–14453.

Pimienta, P. and Chanvillard, G. (2004). Retention of the mechanical performances of Ductal® specimens kept in various aggressive environments. In: *Fib — Symposium 2004*. Avignon, 26-28 April, 2004.

Poursaee, A. and Hansson, C.M. (2008). The influence of longitudinal cracks on the corrosion protection afforded reinforcing steel in high performance concrete. *Cement and Concrete Research* 38, pp. 1098–1105.

Powers, T.C. (1964). The physical structure of Portland cement paste. In: Taylor, H. F. W., Ogburn, C., Fuller, S., Chandler, J., and Hardin, T. eds. *The chemistry of cements*. London: Academic Press, pp. 391–416.

Powers, T.C. and Brownyard, T.L. (1948). Studies of the physical properties of hardened portland cement paste. *PCA Bulletin Portland Cement Association* 43, pp. 1–356.

Pratt, P.L., Ghose, A., Skalny, J. and Hewlett, P.C. (1983). Electron microscope studies of Portland cement microstructures during setting and hardening. *Phil. Trans. R. Soc. Lond.* 310, pp. 93–103.

Qian, S., Zhou, J., de Rooij, M.R., Schlangen, E., Ye, G. and van Breugel, K. (2009). Self-healing behavior of strain hardening cementitious composites incorporating local waste materials. *Cement and Concrete Composites* 31, pp. 613–621.

Reinhardt, H.-W. and Jooss, M. (2003). Permeability and self-healing of cracked concrete as a function of temperature and crack width. *Cement and Concrete Research* 33, pp. 981–985.

Remmers, J.C. and de Borst, R. (2008). Numerical modelling of self healing mechanisms. In: van der Zwaag, S. ed. *Self Healing Materials SE - 17*. Springer Series in Materials Science. Springer Netherlands, pp. 365–380.

Rodriguez, O.G. and Doug Hooton, R. (2003). Influence of cracks on chloride ingress into concrete. *ACI Materials Journal* 100(2), pp. 120–126.

Şahmaran, M., Beskin, S.B., Ozerkan, G. and Yaman, I.O. (2008). Self-healing of mechanically-loaded self consolidating concretes with high volumes of fly ash. *Cement and Concrete Composites* 30, pp. 872–879.

Samson, E. (2003). Calculation of ionic diffusion coefficients on the basis of migration test results. *Materials and Structures* 36, pp. 156–165.

Samson, E., Marchand, J., Snyder, K.A. and Beaudoin, J.J. (2005). Modeling ion and fluid transport in unsaturated cement systems in isothermal conditions. *Cement and Concrete Research* 35, pp. 141–153.

Scherer, G.W. (1990). Theory of Drying. *Journal of the American Ceramic Society* 73, pp. 3–14.

Schindler, A.K. and Folliard, K.J. (2005). Heat of hydration models for cementitious materials. *ACI Materials Journal* 102(1), pp. 24–33.

Schlangen, E. and Joseph, C. (2009). Self-healing processes in concrete. In: Ghosh, S. W. ed. *Self-healing Materials. Fundamentals, Design Strategies, and Applications*. Weinheim: Wiley-VCH Verlag GmbH & Co. KGaA, pp. 141–179.

Schlangen, E. and Sangadji, S. (2013). Addressing infrastructure durability and sustainability by self healing mechanisms - Recent advances in self healing concrete and asphalt. *Procedia Engineering* 54(0), pp. 39–57.

Schneider, C.A., Rasband, W.S. and Eliceiri, K.W. (2012). NIH Image to ImageJ: 25 years of image analysis. *Nature Methods* 9, pp. 671–675.

Sciumè, G., Benboudjema, F., De Sa, C., Pesavento, F., Berthaud, Y. and Schrefler, B.A. (2013). A multiphysics model for concrete at early age applied to repairs problems. *Engineering Structures* 57, pp. 374–387.

Scrivener, K.L. and Pratt, P.L. (1984). Microstructural studies of the hydration of C 3 A and C 4 AF independently and in cement paste. In: *F.P. Glasser (Ed.), Brit. Ceram. Proc. 35, Stoke-on-Trent, British Ceramic Society*. pp. 207–219.

Sedighi, M. (2011). *An investigation of hydro-geochemical processes in coupled thermal,hydraulic, chemical and mechanical behaviour of unsaturated soils*. PhD Thesis, Cardiff University.

Shaeffer, R.E. (1992). *Reinforced concrete: preliminary design for architects and builders*. McGraw-Hill Companies.

Singh, N.B. and Middendorf, B. (2007). Calcium sulphate hemihydrate hydration leading to gypsum crystallization. *Progress in Crystal Growth and Characterization of Materials* 53, pp. 57–77.

Sisomphon, K., Çopuroğlu, O. and Fraaij, A.L.A. (2011). Durability of blast-furnace slag mortars subjected to sodium monofluorophosphate application. *Construction and Building Materials* 25(2), pp. 823–828.

Stefanović, G., Ćojbašć, L., Sekulić, Ž.˘ and Matijašević, S. (2007). Hydration study of mechanically activated mixtures of Portland cement and fly ash. *Journal of the Serbian Chemical Society* 72, pp. 591–604.

Steffens, A., Li, K. and Coussy, O. (2003). Aging approach to water effect on alkali–silica reaction degradation of structures. *Journal of Engineering Mechanics* 129(1), pp. 50–59.

Stein, H.N. and Stevels, J.M. (1964). Influence of silica on the hydration of 3 CaO,SiO2. *Journal of Applied Chemistry* 14(8), pp. 338–346.

Stroeven, M. and Stroeven, P. (1999). SPACE system for simulation of aggregated matter application to cement hydration. *Cement and Concrete Research* 29, pp. 1299–1304.

Taylor, H.F.W. (1997). *Cement chemistry*. second ed. London: Thomas Telford.

Tennis, P.D. and Jennings, H.M. (2000). A model for two types of calcium silicate hydrate in the microstructure of Portland cement pastes. *Cement and Concrete Research* 30, pp. 855–863.

Van Tittelboom, K. and De Belie, N. (2013). Self-Healing in cementitious materials—A review. *Materials* 6, pp. 2182–2217. Available at: http://www.mdpi.com/1996-1944/6/6/2182/.

Turner, L. (1937). The autogenous healing of cement and concrete: Its relation to vibrated concrete and cracked concrete. In: *International Association for Testing Materials*. The Autoge. p. 344.

U. S. Geological Survey (2009). *Mineral commodity summaries 2009*. pp. 1-195.

Verbeck, G. and Landgren, R. (1960). Influence of physical characteristics of aggregates on frost resistance of concrete. *AMERICAN SOCIETY FOR TESTING MATERIALS* 60, pp. 1063–1079.

Wagner, E.F. (1974). Autogenous healing of cracks in cement-mortar linings for grey-iron and ductile-iron water pipes. *Journal of the American Water Works Association* 66, pp. 358–360.

Wan, X., Wittmann, F., Zhao, T. and Fan, H. (2013). Chloride content and pH value in the pore solution of concrete under carbonation. *Journal of Zhejiang University SCIENCE A* 14(1), pp. 71–78.

Xi, Y., Bazant, Z.P. and Jennings, H.M. (1994). Moisture diffusion in cementitious materials Adsorption isotherms. *Advanced Cement Based Materials* 1, pp. 248–257.

Ye, G. and van Breugel, K. (2007). Potential use of the HYMOSTRUC cement hydration model for self-healing of microcracks in cementitious materials. In: *Proceedings of the First International Conference on Self Healing Materials*. Noordwijk aan Zee, The Netherlands, pp. 1–8.

Young, J.F. and Hansen, W. (1987). Volume relationships for C-S-H formation based on hydration stoichiometries. *Materials Research Society Symposium Proceedings* 85, pp. 313–322.

Zienkiewicz, O.C. and Chan, A.H.C. (1989). Coupled problems and their numerical solution. In: Doltsinis, I. S. ed. *Advances in Computational Nonlinear Mechanics SE - 4*. International Centre for Mechanical Sciences. Springer Vienna, pp. 139–176.

Zienkiewicz, O.C., Taylor, R.L. and Zhu, J.Z. (2013). *The Finite Element Method. Its basis and fundamentals*. 7th ed. Elsevier Butterworth-Heinemann.

Appendix A. Input for the Microstructural Model

Table A. 1 Stoichiometric reactions for ordinary Portland cements

Process	Stage	Stoichiometry of the reaction
Hydration C_3A	I	$\mathbf{C_3A + 3C\bar{S}H_2 + 26H \rightarrow C_6A\bar{S}_3H_{32}}$ [a,b] $C_3A + 3C\bar{S}H_2 + (z_1 - 6)H \rightarrow C_6A\bar{S}_3H_{z_1}$
	II	$\mathbf{2C_3A + C_6A\bar{S}_3H_{32} + 4H \rightarrow 3C_4A\bar{S}H_{12}}$ [a,b] $2C_3A + C_6A\bar{S}_3H_{z_1} + (3z_2 - z_1)H \rightarrow 3C_4A\bar{S}H_{z_2}$
	III	$\mathbf{C_3A + C_4A\bar{S}H_{12} + CH + 12H \rightarrow 2C_3A(C\bar{S},CH)H_{12}}$ [b] $C_3A + C_4A\bar{S}H_{z_2} + CH + (2z_3 - z_2)H \rightarrow 2C_3A(C\bar{S},CH)H_{z_3}$ --- $\mathbf{C_3A + CH + 12H \rightarrow C_4AH_{13}}$ [a] $C_3A + CH + (z_4 - 1)H \rightarrow C_4AH_{z_4}$
Hydration C_3S		$\mathbf{C_3S + 5.3H + \rightarrow C_{1.7}SH_4 + 1.3CH}$ [c] $C_3S + (1.3 + y)H + \rightarrow C_{1.7}SH_y + 1.3CH$
Hydration C_2S		$\mathbf{C_2S + 4.3H + \rightarrow C_{1.7}SH_4 + 0.3CH}$ [c] $C_2S + (0.3 + y)H \rightarrow C_{1.7}SH_y + 0.3CH$
Hydration of C_4AF	I	$\mathbf{0.75C_4AF + 3C\bar{S}H_2 + 27.5H \rightarrow C_6(A,F)\bar{S}_3H_{32} + 0.5(F,A)H_3}$ [b,d] $0.75C_4AF + 3C\bar{S}H_2 + (z_5 + 0.5z_6 - 6)H \rightarrow$ $\rightarrow C_6(A,F)\bar{S}_3H_{z_5} + 0.5(F,A)H_{z_6}$
	II	$\mathbf{1.5C_4AF + C_6(A,F)\bar{S}_3H_{32} + 7H \rightarrow 3C_4(A,F)\bar{S}_3H_{12} + (F,A)H_3}$ [b,d] $1.5C_4AF + C_6(A,F)\bar{S}_3H_{z_5} + (3z_7 + z_6 - z_5)H \rightarrow$ $\rightarrow 3C_4(A,F)\bar{S}_3H_{z_7} + (F,A)H_{z_6}$
	III	$\mathbf{C_4AF + 2CH + 10H \rightarrow 2C_3(A,F)H_6}$ [c] $C_4AF + 2CH + (2z_8 - 2)H \rightarrow 2C_3(A,F)H_{z_8}$

bolted reactions = saturated stoichiometry

[a]: (Taylor, 1997); [b]: (Mindess et al., 2003); [c]: (Tennis and Jennings, 2000);

[d]: (Jennings and Thomas, 2009)

Table A. 2 Stoichiometric coefficients used for saturated and partially saturated hydration reactions

	RH range			
	***i*4** **[60%, 40%)**	***i*3** **[40%,11%)**	***i*2** **[11%,0%)**	***i*1** **≈0%**
Expelled water form	*LGP* bulk water	*SGP* constraint water	*AW+ILW+IGW*	*CBW*
y	4[a]	3.15[a]	2.10[a]	1.30[a]
z_1	32	25.06*	14.41*	7[b]
z_2	12	10.89*	9.19*	8[b]
z_3	12	9.75*	6.30*	4.40*
z_4	13	10.56*	6.83*	4.23*
z_5	32	26*	16.80*	10.40*
z_6	3	2.43*	1.58*	0.98*
z_7	12	9.75*	6.30*	3.90*
z_8	6	4.88*	3.15*	1.95*
Density [kg/m^3]	1000	1200	1200	1200

[a] – (Jennings, 2008); [b] – (Powers and Brownyard, 1948; Tennis and Jennings, 2000);

* - linear interpolation

Table A. 3 Kinetics parameters for the investigated Portland cements

Kinetics parameters	$\frac{w}{c}$	**Hydration curve**	**Clinker mineral**			
			C_3S	**C_2S**	**C_3A**	**C_4AF**
k_X	0.5	*HC1*	0.25	0.46	0.28	0.26
		HC2	$k_X = \frac{1}{K_X \tau_X}$			
	0.348		0.05	0.02	0.02	0.02
	0.487		0.04	0.01	0.02	0.02
	0.4		0.05	0.02	0.02	0.02
			0.04	0.01	0.02	0.02
t_X^I	0.5	*HC1* [hours]	0.9	0	0.9	0.9
		HC2 [days]	$t_X^I = \tau_X \Gamma_X^I$			
	0.348		0.24	0	1.97	8.56
	0.487		0.26	0	2.23	10.26
	0.4		0.24	0	1.99	8.71
			0.25	0	2.14	9.68
K_X	0.5	*HC1*	1.72	0.96	1.00	2.30
		HC2	0.70	0.12	0.77	0.55
	0.348		1.83	1.07	1.11	2.40
	0.487		1.73	0.97	1.01	2.31
	0.4		1.79	1.03	1.07	2.37
Γ_X^I		*HC2*	0.02	$1*10^{-6}$	0.04	0.4
Γ_X^D		*HC2*	0.27	0.21	0.19	0.45
$\tau_{X,0}$	0.5	*HC2*	11.90	60.90	49.20	21.40
	0.348		13.12	68.73	55.66	25.66
	0.487		12.00	61.60	49.80	21.80
	0.4		12.70	66.05	53.45	24.20
$t_{X,0}^D$ [hours]	0.5	*HC2*	deduced from equation (3.5)**Error! Reference source not found.**			
			10.16	12.98	9.96	22.09
	0.348		12.37	18.90	14.15	28.23
	0.487		10.34	13.43	10.28	22.59
	0.4		11.59	16.73	12.61	26.06
D_X [cm^2/hours]		*HC2*	$2.5*10^{-12}$	$8*10^{-13}$	$4*10^{-12}$	$9*10^{-13}$
R_{ck} [cm]		*HC2*	$2.51*10^{-4}$			

Table A. 4 Densities of reactants and reaction products

Compound	C3A	C3S	C2S	C4AF
Density [kg/m^3]	3030[a]	3150[a]	3280[a]	3730[a]

Compound	$C_3A(C\bar{S},CH)H_{12}$	C_4AH_{13}	$C_{1.7}SH_4$	$C_6(A,F)\bar{S}_3H_{32}$
Density [kg/m^3]	2030[c]	2044[b]	2040[d]	1804[b]

Compound	$(F,A)H_3$	$C_3(A,F)H_6$	CH	$C_6A\bar{S}_3H_{32}$
Density [kg/m^3]	2711[b]	2670[b]	2240[a]	1750[a]

Compound	$C\bar{S}H_2$	$C_4(A,F)\bar{S}H_{12}$	$C_4A\bar{S}H_{12}$
Density [kg/m^3]	2320[a]	2089[b]	1990[a]

[a]: (Tennis and Jennings, 2000)
[b]: (Balonis and Glasser, 2009): individual aluminate and ferrite phases
[c]: (Balonis and Glasser, 2009): average of $C_4A\bar{S}H_{12}$ and C_4AH_{13}
[d]: (Bernard et al., 2003)

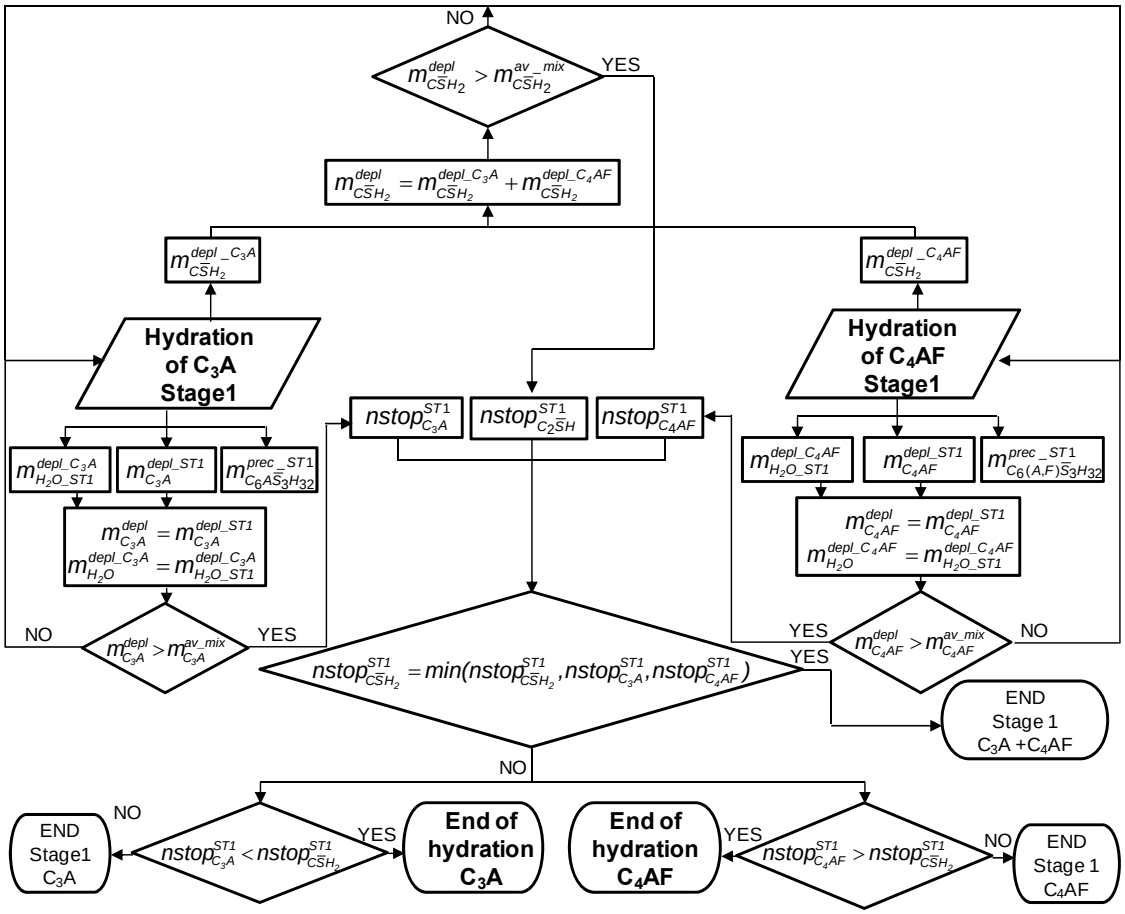

Figure A. 1 Algorithm for modelling the hydration of C_3A and C_4AF (Stage 1)

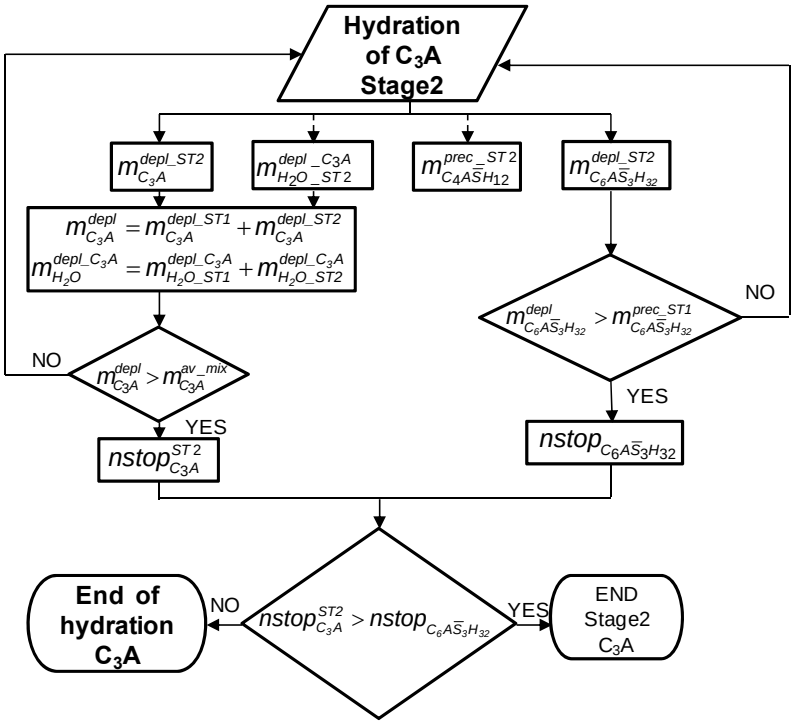

Figure A. 2 Algorithm for modelling the hydration of C_3A (Stage 2)

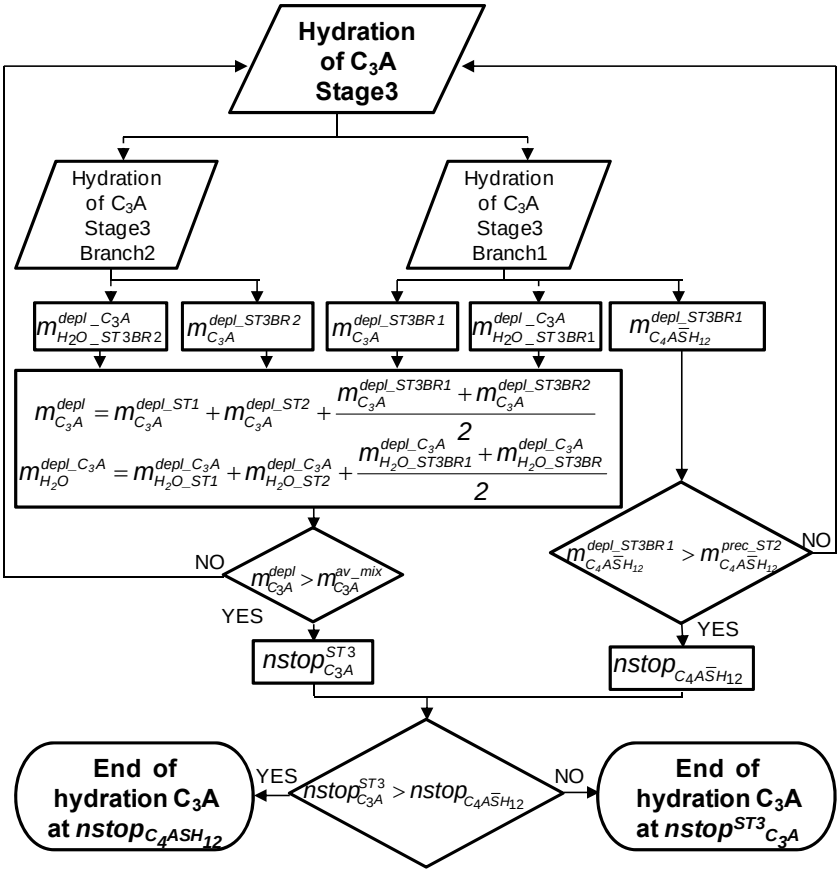

Figure A. 3 Algorithm for modelling the hydration of C_3A (Stage 3)

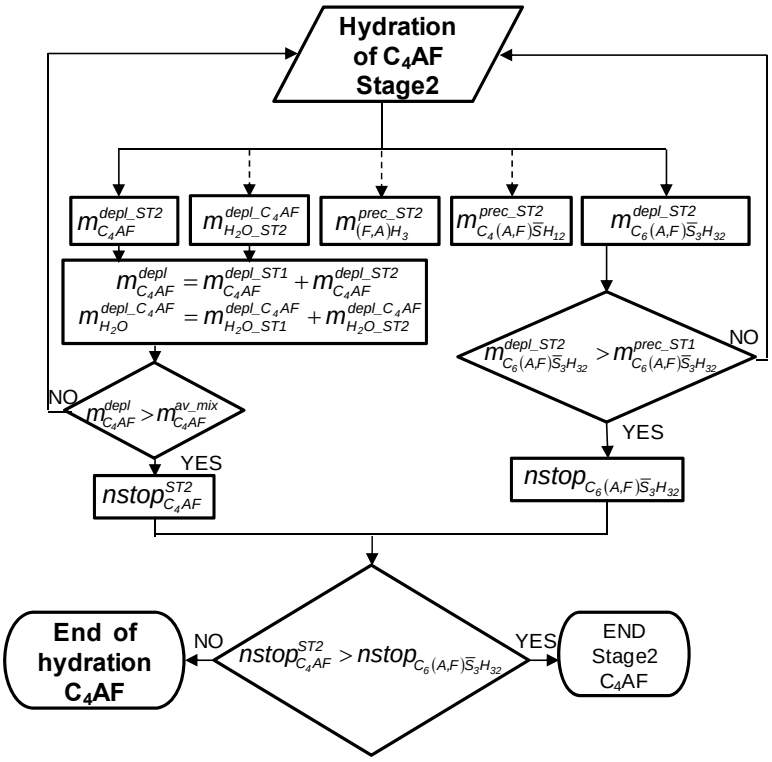

Figure A. 4 Algorithm for modelling the hydration of C_4AF (Stage 2)

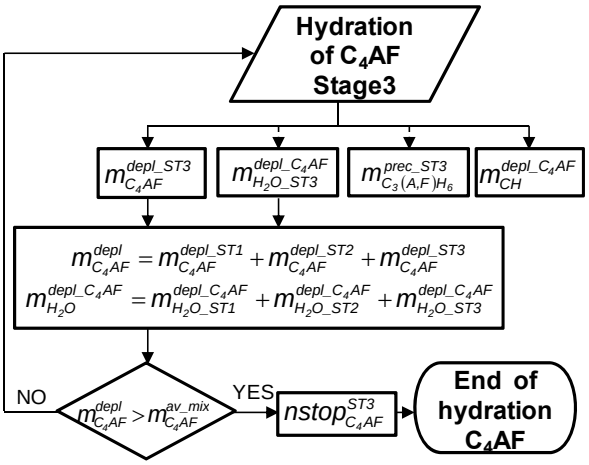

Figure A. 5 Algorithm for modelling the hydration of C_4AF (Stage 3)

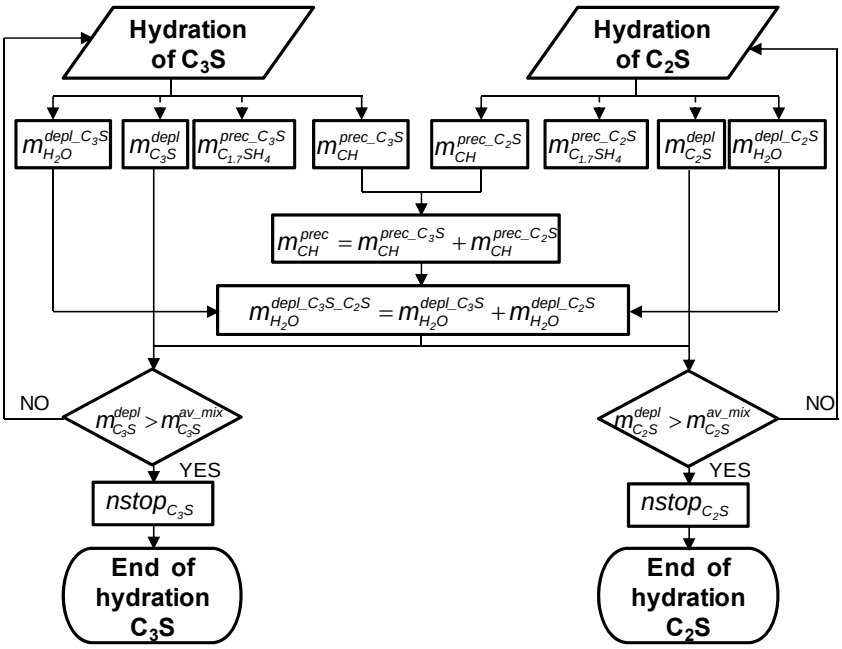

Figure A. 6 Algorithm for modelling the hydration of C_3S and C_2S

Appendix B. Processed Experimental Data for the Self-healing Model

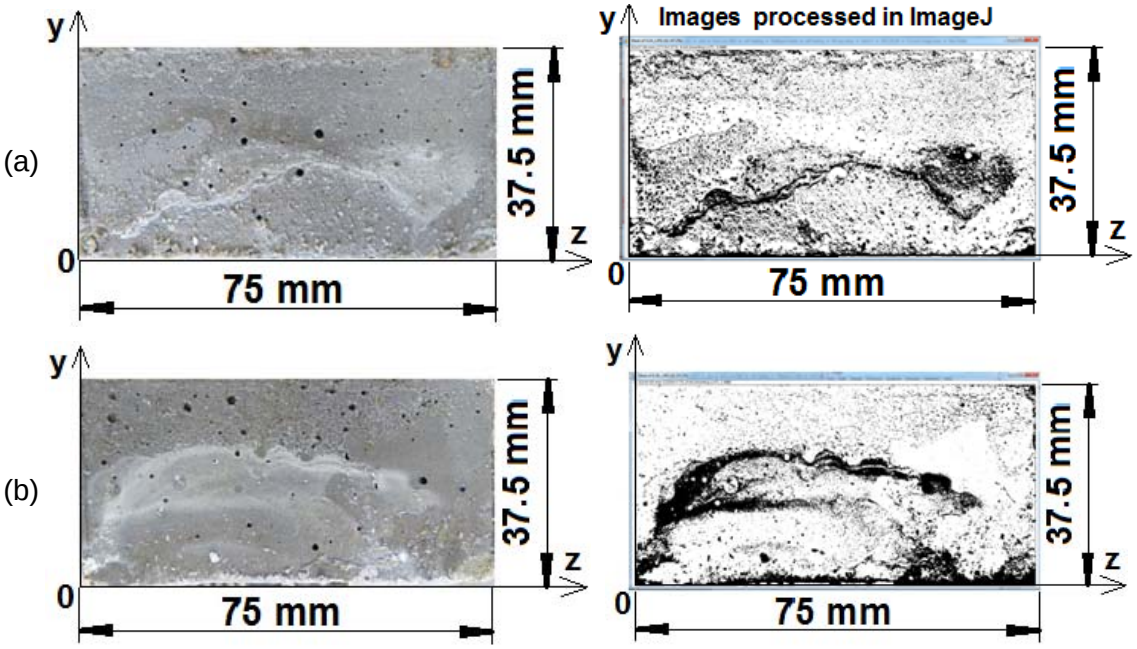

Figure B.1 Self-healed area fractions at 27 days: (a) 22.76%; (b) 21.55%; all the cross sections are positioned at 127.4mm on x direction

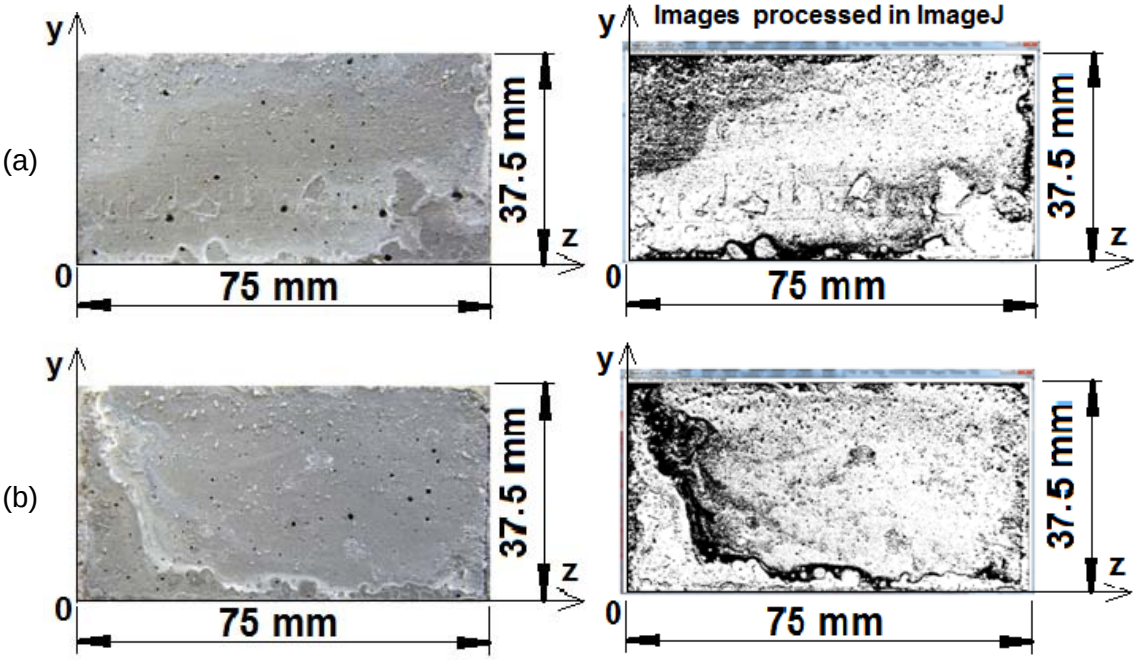

Figure B.2 Self healed area fractions at 41 days: (a) 24.27%; (b) 25.51%; all the cross sections are positioned at 127.4mm on x direction